J. R. DAVIDSON

COMPOSITE STRUCTURAL PROGRAM

RENSSELAER POLYTECHNIC INSTITUTE TROY, N.Y. 12181

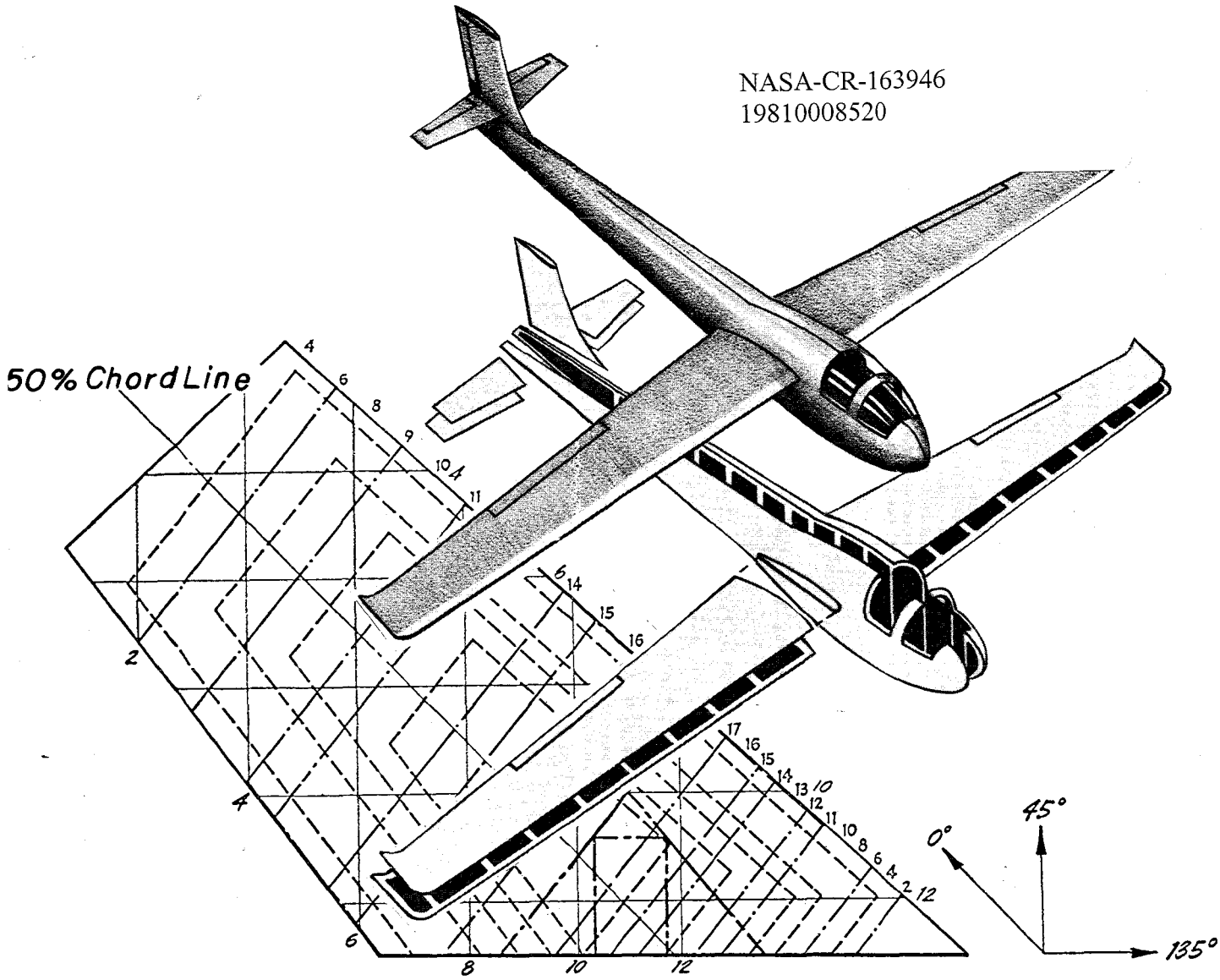

SKIN DESIGN

SPONSORED BY NASA/AFOSR

Semi-Annual Progress Report

May 1980 - September 1980

COMPOSITE STRUCTURAL MATERIALS

Air Force Office of Scientific Research
and
National Aeronautics and Space Administration
Grant No. NGL 33-018-003

Co-Principal Investigators:

George S. Ansell
Dean, School of Engineering

Robert G. Loewy
Institute Professor

and

Stephen E. Wiberley
Professor of Chemistry

Rensselaer Polytechnic Institute
Troy, New York 12181

NASA Technical Officer

Leonard A. Harris
Materials and Structures Division
NASA Headquarters

39th Semi-Annual Report January 1981

CONTENTS

LIST OF TABLES

LIST OF FIGURES

INTRODUCTION

INTRODUCTION

The promise of filamentary composite materials, whose development may be considered as entering its second generation, continues to generate intense interest. Such interest is well founded, since it is based on the possibility of using brittle materials with high modulus, high strength, but low density in composites which fail in a non-catastrophic manner. Such fiber reinforced composite materials offer substantially improved performance and potentially lower costs for aerospace hardware.

Much progress has been achieved since the initial developments in the mid 1960's. Only a very few applications to primary aircraft structure have been made, however, and those are in a material-substitution mode and - with the exception of experiments only just now being conducted on large passenger airplanes - on military aircraft.

To fulfill the promise of composite materials more completely, requires a strong technology base. NASA and AFOSR have realized that to fully exploit composites in sophisticated aerospace structures the technology base must be improved. This, in turn, calls for expanding fundamental knowledge and the means by which it can be successfully applied in design and manufacture. Not the least of this effort is to learn how to design structures specifically to capitalize on the unique properties of composite materials.

It also calls for expanding the body of engineers and scientists competent in these areas. As part of their approach to accomplishing this, NASA and AFOSR have funded the current composites program at Rensselaer. The purpose of the RPI composites program is to develop advanced technology in the areas of physical properties, structural concepts and analysis, manufacturing, reliability and life prediction. Concommitant goals are to educate engineers to design and use composite materials as normal or conventional materials. A multifaceted program has been instututed to achieve these objectives. The major elements of the program are:

1. CAPCOMP (Composite Aircraft Program Component). CAPCOMP is primarily a graduate level project being conducted in parallel with a composite structures program sponsored by NASA and performed by a private, aerospace manufacturing contractor. The first component redesign is being done in conjunction with the Boeing Commercial Airplane Company. The main spar/rib region on the Boeing 727 elevator, near its actuator attachment point, was selected, with Boeing's advice and the concurrence of NASA/AFOSR, for study in CAPCOMP. The magnitude of the project - studying, designing, fabricating and testing of a relatively small but highly stressed region on the elevator - is both consistent with Rensselaer's capabilities and a significant challenge. The selection of a portion of a full-scale flight hardware structure assures relevance to this project's direction.

Visits to Boeing were conducted by Professor Hoff and several of his students, and the first serious design work began on two alternative designs. Each was pursued to the point of preliminary analysis and testing. One of these was selected for more detailed analysis, redesign, complete fabrication and testing. Completion of fabrication facilities, the first complete part and test fixture development are reported in Part I.

2. CAPGLIDE (Composite Aircraft Program Glider). This undergraduate demonstration project has as its objectives the design, fabrication and testing of a foot-launched, ultralight glider using composite structures. A flight vehicle was selected to maximize student interest and to provide the students with a broad-based engineering experience. For those students continuing with graduate work at RPI, CAPGLIDE is intended to provide natural progression to CAPCOMP. The progress on the CAPGLIDE project to date has been very good. Seven professors and approximately 30 students were actively engaged in the project during this period; that is, the Spring '80 semester and summer period. High point of the project to date was initial flight testing of the glider, dubbed "RP-1", and first public flight demonstration on September 16, 1980. A description of the status of the CAPGLIDE project at the end of the current reporting period is given in Part II.

3. COMPAD (Computer Aided Design). A major thrust of

the composites program is to develop effective and efficient tools for the analysis and design of composite structures. Rensselaer and NASA Langley have jointly implemented the use of the SPAR code on minicomputers, and the work at Rensselaer has made "virtual memory" available to those using SPAR. Special RPI software has been developed to make existing programs more useful, particularly as regards graphics. Attention for the current period has focused on preprocessor and postprocessor developments; details are reported in Part III.

4. Composites Fabrication and Test Facility. Structural design engineers, educated only by course work and design projects limited to paper, often fail to sense or appreciate problems involved in fabrication. The actual fabrication and testing of composite structural components provides this training and the final validation for the designs in our CAP projects. RPI's Composites Fabrication and Test Facility is located in the laboratory and high bay areas of the Jonsson Engineering Center. Equipment is available for compression molding parts as large as 19" x 19" and vacuum bagging parts of much larger size. Panels, approximately 4' x 20', have been made by vacuum bagging. A pressure vessel for long narrow parts, such as spars, has been designed and built. All of these techniques and facilities have been used in the CAPGLIDE part of the project, described in Part II. A second vessel capable of fabricating shorter but wider

parts at higher pressures was designed and completed in the current period. More information on this development is contained in Part I, CAPCOMP.

5. INSURE (Innovative and Supporting Research). The criteria for selecting research projects to be conducted under this program include the following: (a) they must anticipate critical problem areas which may occur in the CAP or NASA/AFOSR programs or (b) solutions to existing problems are not yet satisfactorily in hand. During the reporting period six such projects were conducted as part of the program. Results from the ongoing projects are reported in Part IV.

6. Curriculum Revisions. The goal of educating engineers to think of composites as normal or conventional materials has required changes in curriculum. Since the initiation of this program, almost all Rensselaer engineers take introductory courses which incorporate the concepts of anisotropy and composite materials. In addition, six specialized courses in composites have been offered during the past three years to develop those special skills required of students involved in the composites program. A new course was introduced in the Fall of '78 semester on composite design and analysis using programmable hand calculators, a central mini and full frame computers. A new graduate level advanced topics course with the title "Advanced Finite Elements" was offered for the first time in September 1979.

The additions of the SAP and SPAR computer codes and the growing availability of interactive computer graphics under our COMPAD program element have reached the point where our engineering students are using these facilities as everyday working tools for design, analysis and visualization purposes. We have thus achieved one of the principal goals of the curriculum development activities.

Two continuing education special courses, outgrowths of the composite materials and structures program, were presented during the month of July. They were "Composite Materials & Structures" and "The Finite Element Approach in Structural Analysis". Each course lasted a week, and they were run serially so that a participant might come for both on the same trip. The level of the material was planned to be suitable for graduate engineers and useful to managers of engineering structures activities who are involved in technical work but who may not have taken courses for several years. Because of the wide variety of special courses available throughout the United States dealing with this subject matter, only rather unique aspects justify additional offerings in these areas. Our programs were planned to be unusual in the respect that "hands-on" experiences were inherent and required for completion of each course. Use of hand-held programmable calculators, application of optimization programs using computer graphics, lay-up and cure of a simple part in graphite epoxy and testing tensile, shear and

compression coupons to failure were all part of the first course. As part of the second course, workshop sessions were held in RPI's Computer Graphics Center. In these sessions students defined, "constructed" and analyzed their own finite element models on refresh graphics terminals.

Faculty-staff and student attendees for the courses are as follows:

Composite Materials & Structures

Program Director:

R. G. Loewy
Institute Professor
Rensselaer Polytechnic Institute

Faculty:

R. Judd Diefendorf
Professor, Materials Eng.
Rensselaer Polytechnic Inst.

H. Gunter Helwig
Asst. Research Professor
Aeronautical Eng., Mechanical Eng. and Mechanics
Rensselaer Polytechnic Inst.

B. Walter Rosen
President
Materials Sciences Corp.

Stephen W. Tsai
Chief, Mechanics and Surface Interactions Branch
Air Force Materials Lab.
Wright-Patterson AFB

Dick J. Wilkins
Sr. Engineering Specialist
General Dynamics

Students:

Cecil G. Armstrong
Research Engineer
Rensselaer Polytechnic Inst.

David J. Brangwin
Senior Engineer
Harris Corporation

Richard H. Cole
Mechanical Engineer
Benet Laboratory
Watervliet Arsenal

Michael J. Dennis
Specialist II, Structures Technology
Boeing Vertol

John H. Kelbel
Mechanical Engineer
Nurad Inc.

William L. Poesch
Member of Technical Staff
MRJ, Inc.

J. B. Senior
Project Stress Engineer
Rolls-Royce Ltd.
Derby, UK

Alan Servoz
Engineer
Aerospatiale
Toulouse, France

The Finite Element Approach in Structural Analysis

Program Director:

Mark S. Shephard
Assistant Professor
Civil Engineering
Rensselaer Polytechnic Inst.

Faculty:

Richard H. Gallagher
Dean, College of Engineering
University of Arizona

John A. Swanson
President
Swanson Analysis Systems, Inc.

Students:

Richard Adkins
Design Engineer
Ashland Petroleum Co.

Frank P. Hill
Manager, Analytical Eng.
Combustion Engineering Inc.

John P. Housprup
Instructional Consultant
Combustion Engineering Inc.

Robert Jankowski
Sr. Structural Engineer
Brumman Aerospace

Edward Kirchner
Research Engineer
Farrel Corporation/Div. USM

William Lewis
Mechanical Engineer
Mechanical Technology Inc.

Sudhir C. Mehrotra
Research Scientist
Vigyan Research Associates, Inc.

Gary S. Miller, Sr.
Staff Engineer
General Physics Corporation

Joyceann Montini
Associate Engineer
Boeing Vertol

Charles A. Pagel
Mechanical Engineer
Naval Weapons Support Center

Alan Servoz
Engineer
Aerospatiale
Toulouse, France

John Stimpson
Mechanical Engineer
Raytheon Company

John Talbourdet
Structural Engineer
Honeywell Electro Optics Systems Center

Roger Weseloh
Sr. Design Engineer
Westinghouse

Reaction to these offerings on the part of the attendees was highly favorable, and we plan to give the courses again in 1981.

7. Technical Interchange.

a) Mr. Hiromitsu Otsuka, who joined the faculty at RPI as a Visiting Research Associate in Mechanical Engineering, Aeronautical Engineering and Mechanics, returned to Japan in July 1980. Mr. Otsuka is a member of the staff of the Industrial Products Research Institute of the Ministry of International Trade and Industry, where he was engaged in developing a light weight wheelchair of fiber reinforced plastic materials. At RPI he conducted acoustic emission studies of composites under load, together with RPI's Professor H. Scarton, during this period. The results of this work are reported in Part IV, INSURE.

b) Technical Meetings: Technical meetings, on- and off-campus, provide important opportunities for interchange of technical information. Because of the large number of composites meetings, a central catalog with all upcoming meetings is being maintained and distributed periodically. In this way we help assure that a Rensselaer staff member will participate in important meetings. The calendar for this reporting period is shown in Table 1. Meetings attended by RPI composites program faculty/staff during the reporting period are shown in Table 2. Some meetings particularly relevant to composites, held on-campus with off-campus

TABLE 1

CALENDAR OF COMPOSITES-RELATED MEETINGS

for the period May '80 to September '80

5/6-8	25th National SAMPE Symposium and Exhibition, San Diego, CA. "Sponsored by SAMPE."
5/12-14	21st Structures, Structural Dynamics and Materials Conference, Seattle, WA. "Sponsored by AIAA/ASME."
5/13-15	Annual Forum, Washington, D. C. "Sponsored by AHS."
5/14-15	Impact for the '80's (Materials/Structures Panel), Cleveland, OH.
5/15-16	Analysis of USAF Aircraft Engine Structural Durability and Damage Tolerance, Seattle, WA. "Sponsored by AIAA."
5/19-23	4th International Conference on Pressure Vessel Technology, London, England. "Sponsored by ASME."
5/27-30	IUTAM Symposium on Physical Non-Linearities in Structural Analysis, Senlis, France.
5/28-29	M.A.B. Meeting: Committee on High Temperature Metal and Ceramic Matrix Composites, Washington, D. C.
6/2-5	IUTAM Symposium on Three Dimensional Constitutive Relationship and Ductile Fracture, Dourdan, France.
6/4-8	1980 SIAM National Meeting, Alexandria, VA.
6/30-7/4	Carbon '80, Baden-Baden, Germany.
8/11-13	7th Atmospheric Flight Mechanics Conference (includes Aeroelastic Tailoring of Flexible Aircraft), Danbers, MA. "Sponsored by Battelle, Columbus Labs."
8/17-23	15th International Congress of Theoretical and Applied Mechanics, Toronto, Canada. "Sponsored by AIAA."
8/25-30	3rd International Conference on Composite Materials, Paris, France. "Sponsored by AIAA."
9/1-5	8th International Conference on Rheology, Naples, Italy.
9/2-3	International Conference on Vibrations in Rotating Machinery, Cambridge, England. "Sponsored by ASME."
9/3-5	USA-USSR Symposium on Fracture of Composite Materials Bethlehem, PA.
9/10-12	Mechanics of Non-Destructuve Testing, Blacksburg, VA. "Sponsored by ARO-D; NSF and V.P.I."

TABLE 1 (continued)

9/15-17	1st Chautauqua on Finite Element Modeling, Harwichport, MA.
9/15-19	Composite Materials Processing and Quality Assurance, Los Angeles, CA.
9/16-17	4th Meeting, Commission on Acoustic Emission from Reinforced Plastics, Montery, CA. "Sponsored by Lawrence Livermore National Lab. and Acoustic Emission Tech. Corp."
9/16-17	6th European Rotorcraft and Powered Lift Aircraft Forum, Bristol, England.
9/17-19	IPAD National Symposium, Denver, CO. "Sponsored by NASA."
9/24-27	4th International Symposium on Composite Materials, Rydzyna, Poland.
9/30	Carbon/Carbon: Composite Technology, Dallas, TX.
9/30-10/2	Army Symposium on Solid Mechanics, Yarmouth, MA. "Sponsored by Army Materials and Mechanics Research Center."

TABLE 2

COMPOSITES-RELATED TECHNICAL MEETINGS ATTENDED OFF-CAMPUS

for the period May '80 to September '80

5/11-15	21st Structures, Structural Dynamics and Materials Conference (Prof. Helwig), Seattle, WA.
5/27-30	IUTAM Symposium on Physical Non-Linearities in Structural Analysis (Prof. Diefendorf), Senlis, France.
5/28-29	M.A.B. Meeting: Committee on High Temperature Metal and Ceramic Matrix Composites, (Prof. Diefendorf), Washington, D.C.
6/2-5	IUTAM Symposium on Three Dimensional Constitutive Relationship and Ductile Fracture (Prof. Krempl), Dourdan, France.
6/4-8	1980 SIAM National Meeting, (Prof. Brunelle*), Alexandria, VA.
6/30-7/4	Carbon '80 (Prof. Diefendorf), Baden-Baden, Germany.
8/25-30	3rd International Conference on Composite Materials (Prof. Diefendorf), Paris, France.
9/1-5	8th International Conference on Rheology (Prof. Diefendorf), Naples, Italy.
9/15-17	1st Chautauqua on Finite Element Modeling (Profs. Feeser and Shephard**), Harwichport, MA.
9/16-17	4th Meeting, Commission on Acoustic Emission from Reinforced Plastics (Prof. Scarton), Montery, CA.
9/24-27	4th International Symposium on Composite Materials (Prof. Diefendorf), Rydzyna, Poland.
9/30	Carbon/Carbon: Composite Technology (Prof. Diefendorf), Dallas, TX.

---

* Presented a paper titled, "The Use of a Double Affine Transformation to Obtain a Class of Generalized Elastodynamic Solutions for Orthotropic Plates".

** Presented a paper titled, "RPIFEP - An Interactive Finite Element Package".

speakers, are listed in Table 3. A list of composite-related visits to relevant organizations by RPI faculty/staff/students, with the purpose of each visit outlined, is presented in Table 4.

In summary, the NASA/AFOSR Composites Aircraft Program is a multi-faceted program whereby aeronautical, mechanical and materials engineers must interact to achieve its goals. "Hard-nosed" engineering of composite aircraft structures is balanced against research aimed at solving present and future problems. In the following sections, detailed descriptions of the CAPCOMP, CAPGLIDE, COMPAD and INSURE programs are presented.

TABLE 3

COMPOSITES-RELATED MEETINGS/TALKS HELD AT RPI

(May '80 - September '80)

Topic	Date	Speaker(s)
F-16 and Other Developments at General Dynamics	7/17/80	Dick J. Wilkins Sr. Engin. Specialist General Dynamics Fort Worth, TX
Bending-Torsion Coupling Effects in Cascade Flutter	7/29/80	Oddvar O. Bendiksen Dir. of Project Engin. Pacific Airmotive Corp. Burbank, CA
A Hierarchy of Conforming Timoshenko Beam Elements	9/22/80	Alexander Tessler Northrop Aircraft Los Angeles, CA
Oscillating Cascade Fluid Energy Extractor	9/30/80	Lee Arnold Emeritus Professor of Applied Science New York University New York, NY

TABLE 4

COMPOSITES-RELATED VISITS TO RELEVANT ORGANIZATIONS

by RPI Faculty/Staff/Students

Visited	Date	by Prof(s)	Purpose
G. E. Space Division Dr. Carl Zweben	9/25/80	R. G. Loewy	To review composite structures activities
Drexel University Professors: P. C. Chou D. Mortimer J. Awerback A. Wang J. Rose G. Harlow	9/25/80	R. G. Loewy	To discuss programs in composites research and visit laboratories

PART I

CAPCOMP (Composite Aircraft Program Component)

CAPCOMP (Composite Aircraft Program Component)

(N. Hoff, R. Loewy)

CAPCOMP is a program to design flight critical structures to take the maximum advantage of composite materials. By combining the efforts of experienced faculty with bright and well trained but inexperienced graduate students in an environment relatively free of traditional design and manufacturing processes, we intend to devise new and hopefully useful design concepts.

There is sufficient information available to prove that many structural elements can be made lighter by using advanced composites today than by using metals. But if such elements have to be joined by methods other than adhesive bonding, difficulties and uncertainties arise which can be eliminated only through conservative designs with their attendent penalties in weight or by extensive and expensive programs of "cut and try". This stands as one important impediment to full adoption of composites by the aerospace industry.

On the basis of these considerations Rensselaer Polytechnic Institute began, as the first task aimed at new structural concepts, the design using composites of a joint used in an airplane elevator. To make the design realistic, an existing metal airframe component was chosen for redesign in composites. The existing design chosen was that of the Boeing 727 elevator actuator attachment. We conceive of

this work as carrying forward a Structures Demonstration Program using the actuator attachment joint of the 727 elevator, paralleling that of NASA and its aerospace contractor, the Boeing Commercial Airplane Company. Our design, fabrication and test effort emphasizes designs using advanced composite construction for the purpose of minimizing the weight of the structure, but on a scale consistent with the university context and funding level. The staff of RPI is very grateful to the Boeing Company and its engineers for their wholehearted support of this work at RPI.

During the last reporting period, one of two different designs reported previously (July and December 1979) as suitable for replacing the largely metal attachment produced by Boeing was selected for further analysis, redesign, fabrication and testing. We call it the "Berg Design", and it makes use of quasi-isotropic, graphite-epoxy laminates. The second design, called the "Muser Design", which made a deliberate attempt to use uniaxial graphite-epoxy tape to as great an extent as possible, was suspended. It has led, however to more generic research efforts to maximize the load carrying ability of pin-loaded holes in composite membranes and plates. These efforts are directed at improving the design of the attachment of the rib flanges to the elevator skin through mechanical (i.e., pin-type) fasteners and at maximizing the efficiency of the movable, heavily loaded, actuator attachment points in CAPCOMP. In addition, however,

and increasingly, these generic effects are motivated by the general and widespread utility that will result from improvements in pin-loaded hole designs for composites.

These efforts have been jointly directed by Dr. Nicholas J. Hoff, in part time arrangement and by Dr. Robert G. Loewy. They are further described in the following paragraphs.

1. The Elevator and Its Attachment

To place the progress reported here in proper context, some descriptions used in earlier reports are repeated. The conventional aluminum alloy elevator of the Boeing 727 is shown in the upper half of Figure I-1. The lower half of the figure is the new version of the elevator redesigned by Boeing in graphite epoxy; it is evident from the pictures that the latter is composed of fewer parts than the former. However, the actuator fitting of the new design is still manufactured of aluminum alloy. This fitting is shown in Figure I-2. The fitting is attached to outboard and inboard portions of a new graphite-epoxy spar and to a graphite-epoxy nomex-honeycomb rib as indicated in Figure I-3.

The attachment was designed by Boeing to carry loads up to 19,000 pounds. The direction of the load varies as the elevator rotates over an angle of 28 degrees from the full-down to the full-up position.

2. Berg's Design

(R. Loewy)

Berg's design for the elevator rib is shown in Figure I-4

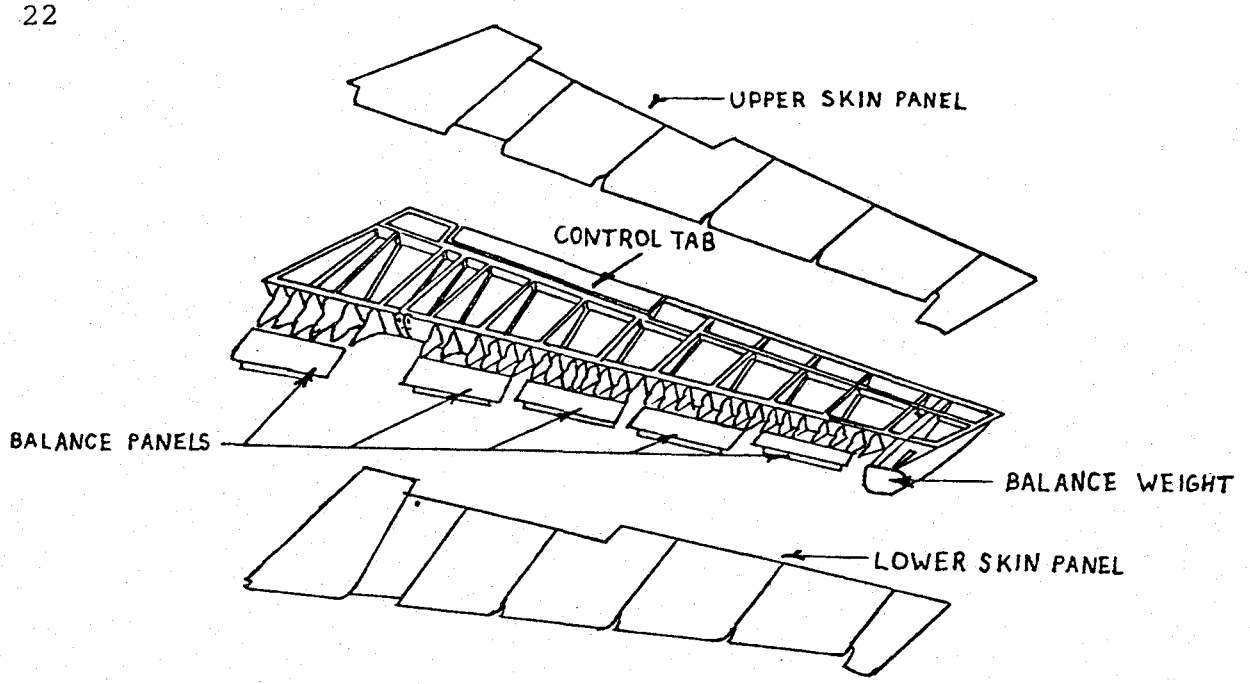

Conventional Aluminum Elevator

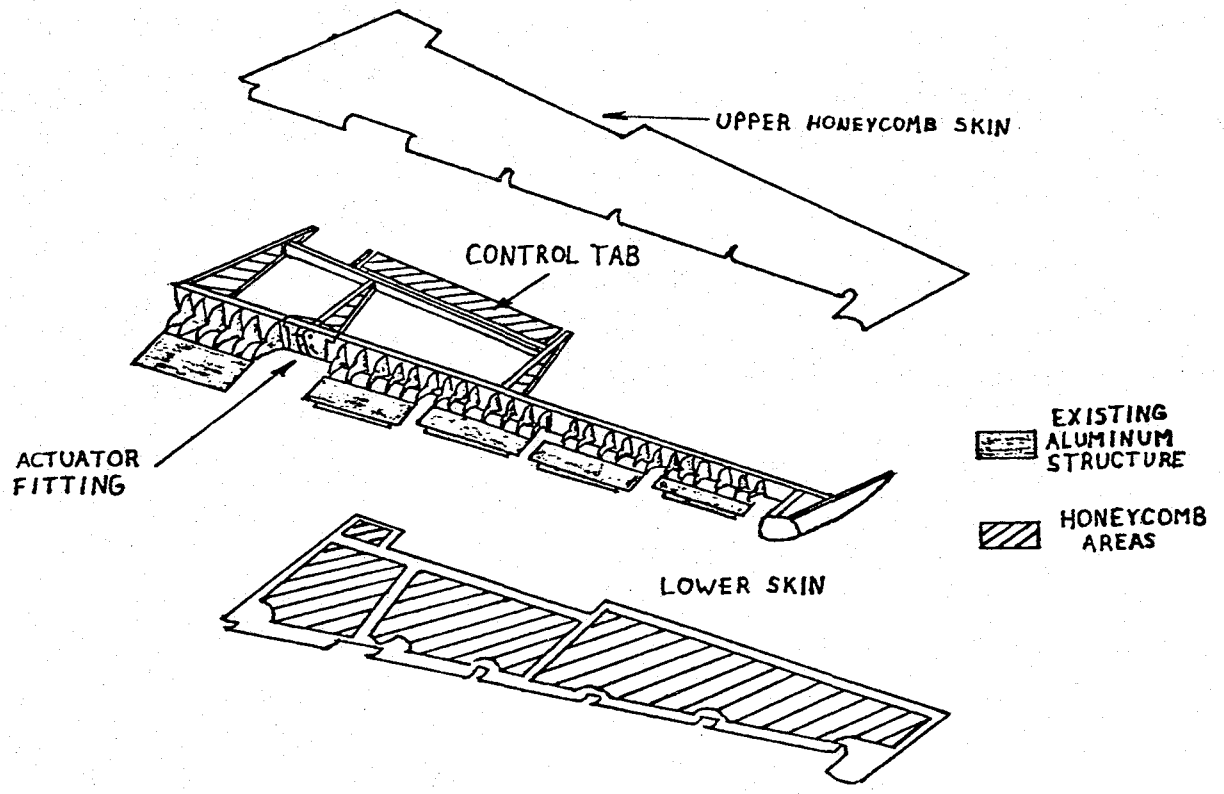

Advanced Composite Elevator

BOEING ELEVATOR ASSEMBLY

Figure I-1

ALUMINUM ACTUATOR FITTING (Boeing Design)

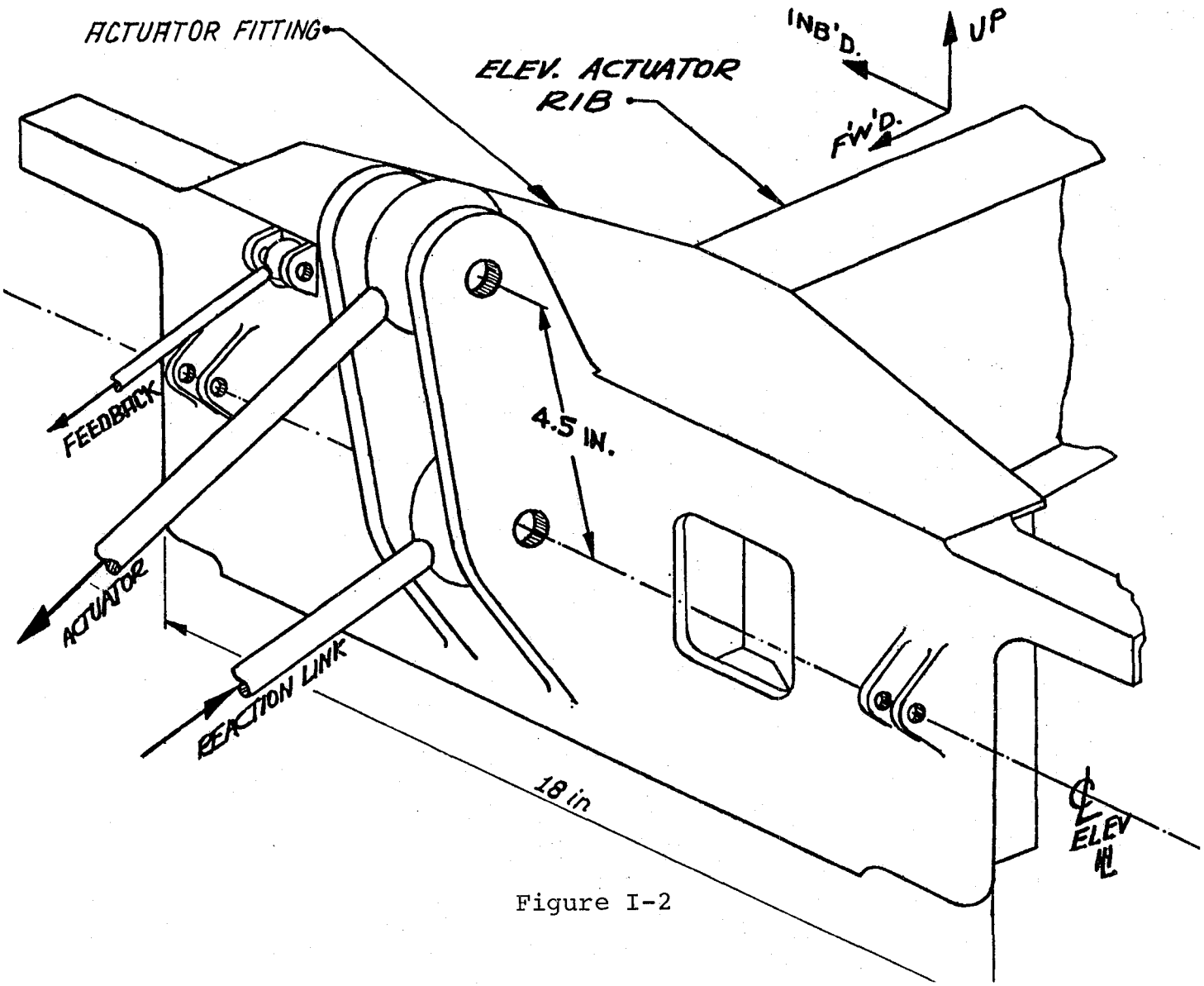

Figure I-2

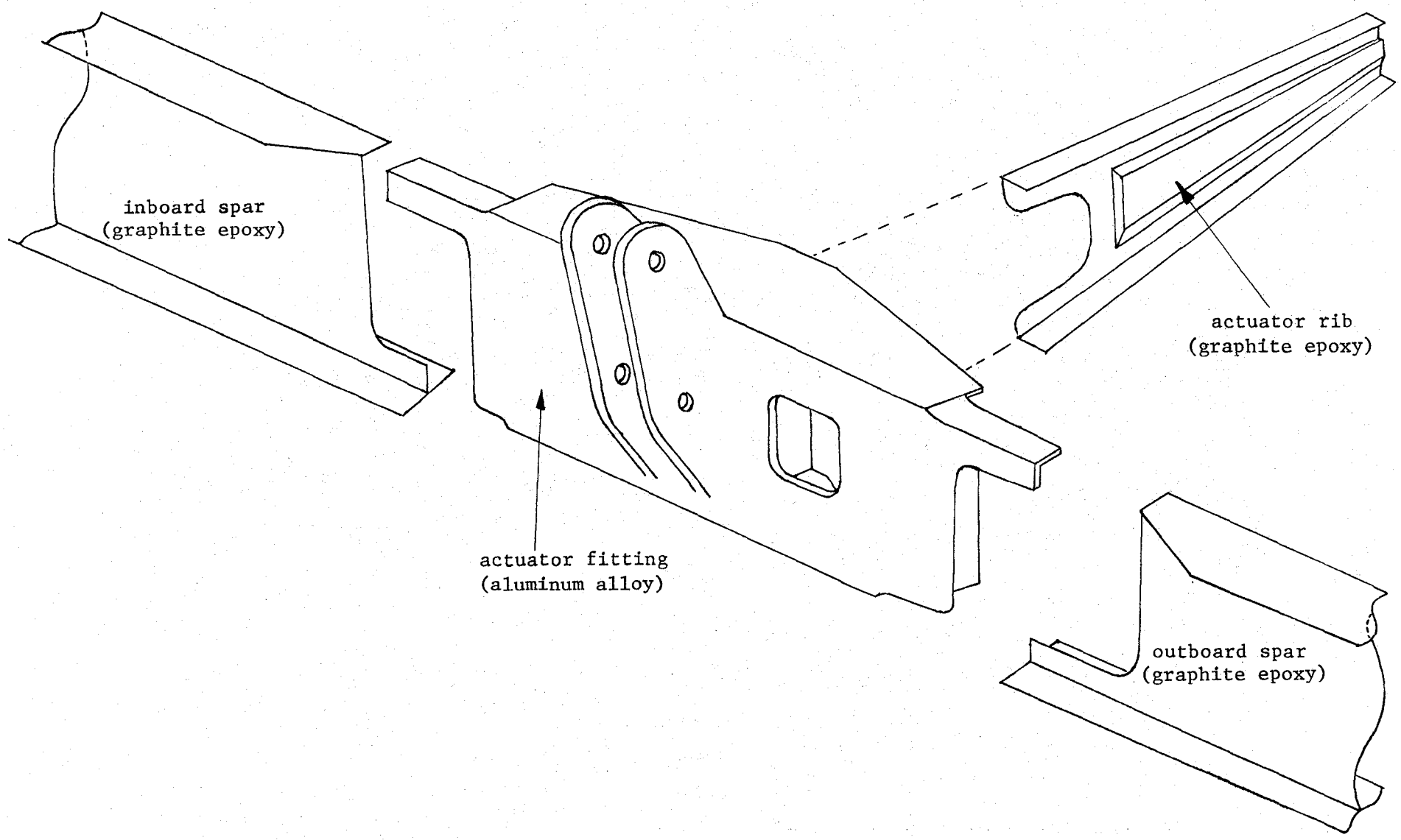

COMPOSITE ELEVATOR ACTUATOR ASSEMBLY (Boeing Design)

Figure I-3

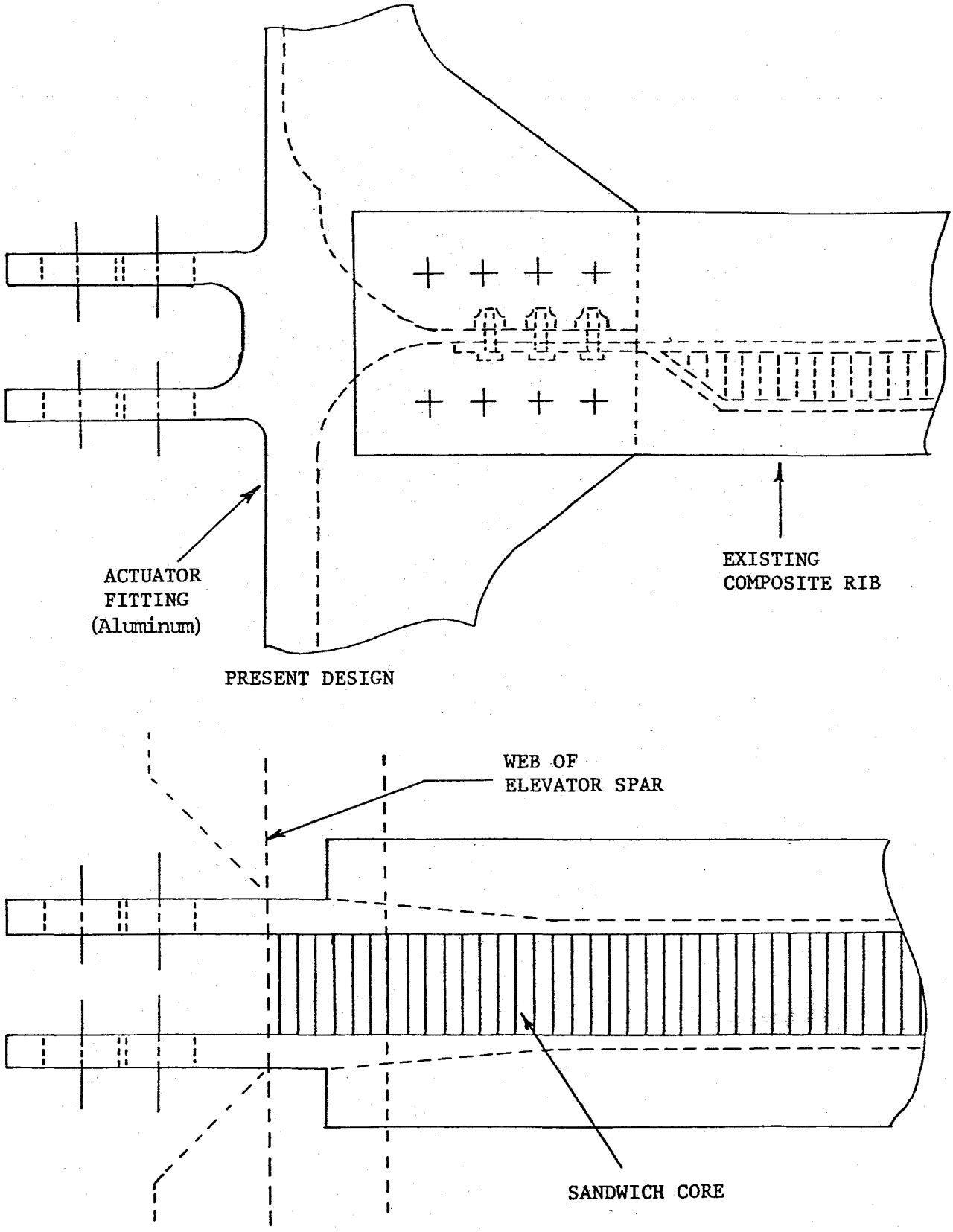

ACTUATOR LUG TO RIB TRANSITION - TOP VIEW

Figure I-4

and I-5. The first of these figures compares the Boeing composite design with Berg's design; both are shown. Figure I-5 shows both how the spar and new actuator rib would be assembled and also the build-up of thickness in the lug areas anticipated as needed to provide the required bearing strength. Note that the edges of some of the layers are bent 90 degrees to form flanges to which the upper and lower skins of the elevator can be attached. Attachment of flanges to elevator skins will be by means of titanium Hi-Loc fasteners. The right-hand and left-hand graphite-epoxy webs are stabilized by a layer of nomex-honeycomb between them.

The design analyses described in the previous reports led to an elevator attachment rib with a variable thickness web. The distribution of thickness was chosen using successive finite element calculations to produce a relatively uniform stress level. It is shown in Figure I-6.

During the current period a new pressure vessel, designed and fabricated especially for fabricating carbon-epoxy components in the CAPCOMP size category, was completed. Its useful dimensions are 7'8" x 18" diameter, gage pressures of 90 psi are available from the compressed air supplies in our Composites Fabrication Laboratory, and internal temperatures of up to 140°F can be generated by electrical conduction heating elements powered by a Thermac cure-cycle controller. Figure I-7 is a photograph of the completed pressure vessel.

The Berg Design, composite 727 aircraft elevator actuator

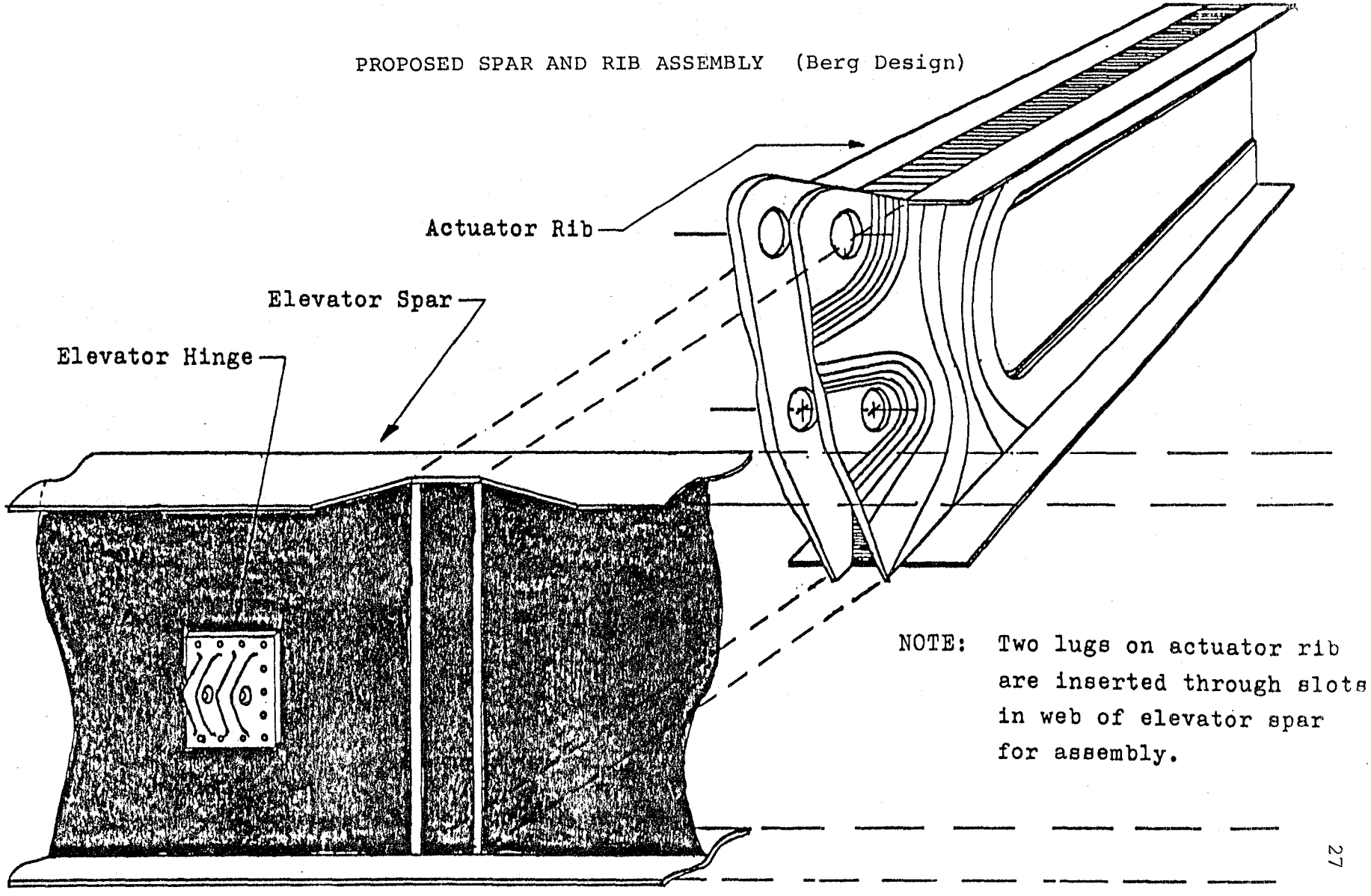
PROPOSED SPAR AND RIB ASSEMBLY (Berg Design)
Actuator Rib
Elevator Spar
Elevator Hinge
NOTE: Two lugs on actuator rib are inserted through slots in web of elevator spar for assembly.

Figure I-5

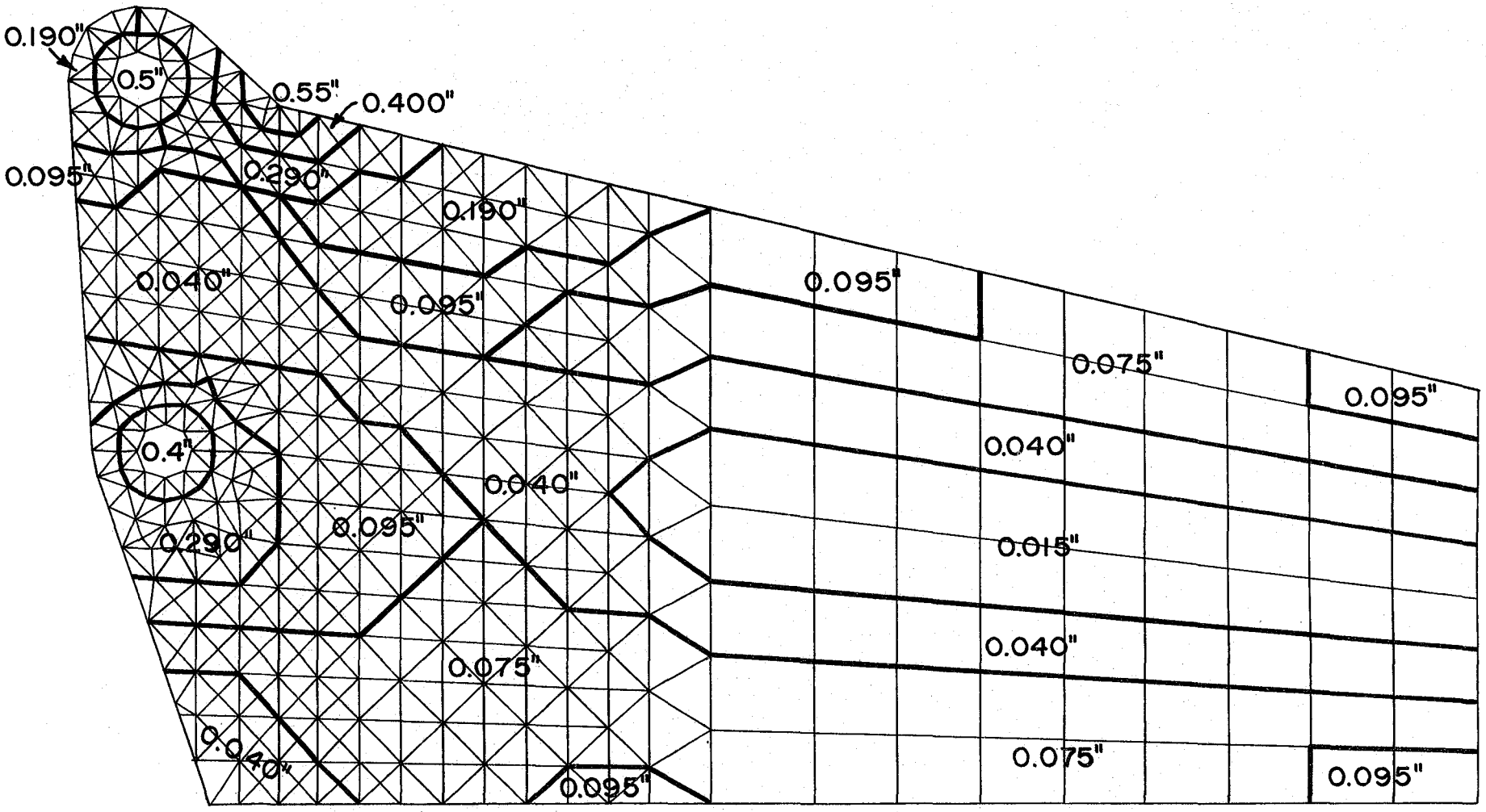

VARIABLE THICKNESS FINITE ELEMENT MESH

Figure I-6

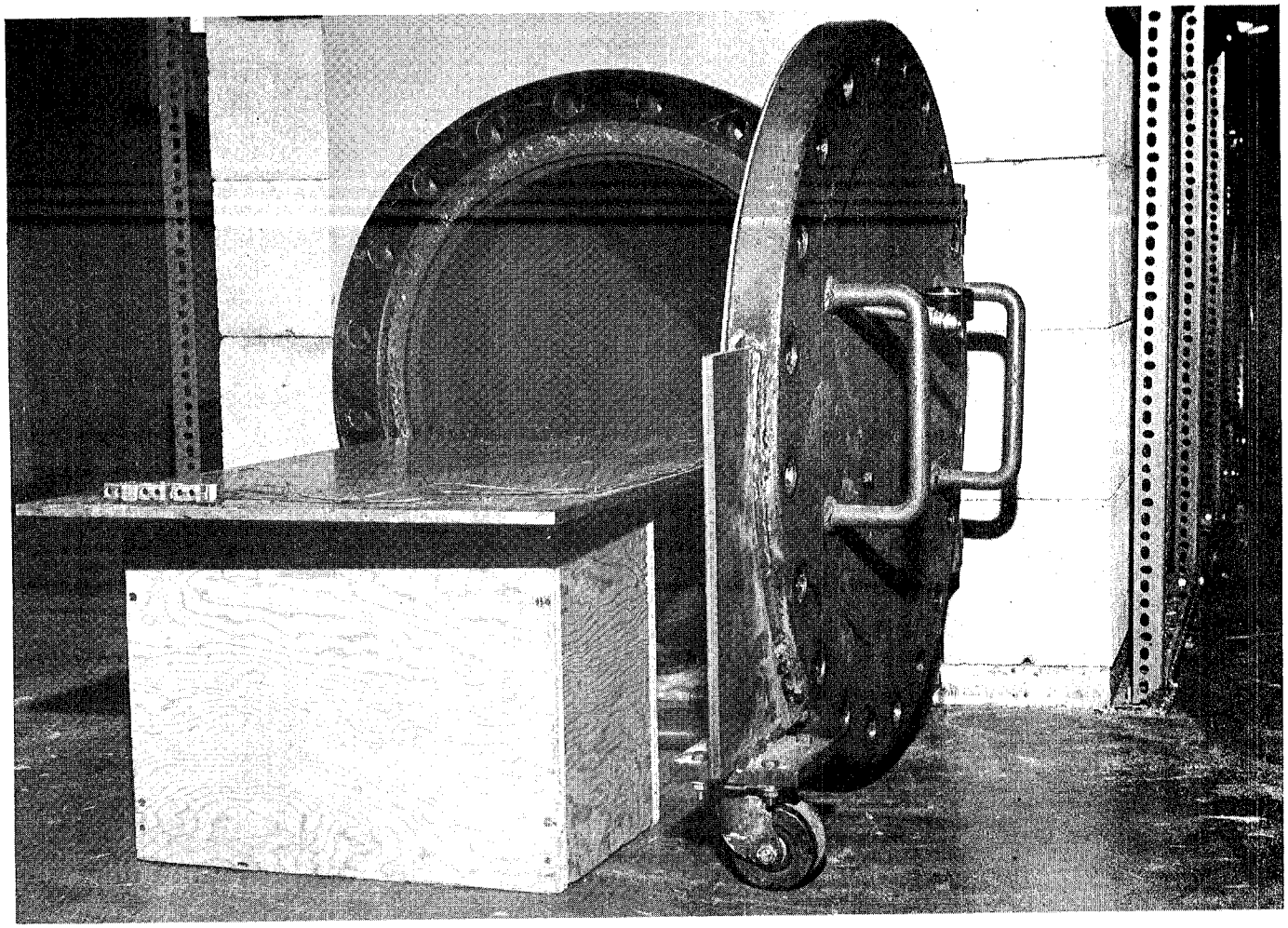

Figure I-7

18" Inner Diameter Pressure Vessel Showing Access Door

attachment rib is shown in various stages of assembly (see Figures I-8a, -8b and -8c).

As noted in the last report, the Boeing Commercial Airplane Company provided a full description of the testing procedures they used to qualify their 727 elevator actuator attachment structure. Figure I-9 shows the Boeing test set-up; note that two hydraulic cylinders (mounted horizontally) provide the actuator load and reaction through a vertical bar which is bolted to the two elevator actuator attachment points. In the absence of such mobile hydraulic load generators at RPI, we plan to generate the equivalent loadings in an Instron testing machine through linkages as shown in Figure I-10. In the campus test set-up, loads will be applied vertically to a bar oriented horizontally which transmits the loads through two bolts to the elevator actuator attachment lugs. This linkage arrangement, which provides the equivalent of the Boeing load test, has been stress-checked and fabrication has been completed during this reporting period.

Also shown in Figure I-10 is the "strong-back" structure (items 9, 10, and 11) and the reinforcements of the elevator rib (items 12 and 13) to ensure reaction-load transfer to the "strong-back" structure. These test fixtures (i.e., items 9, 12 and 13) and the aft elevator skin reinforcements (item 14) are essentially those used in the Boeing test. Their fabrication also was completed in this current reporting period.

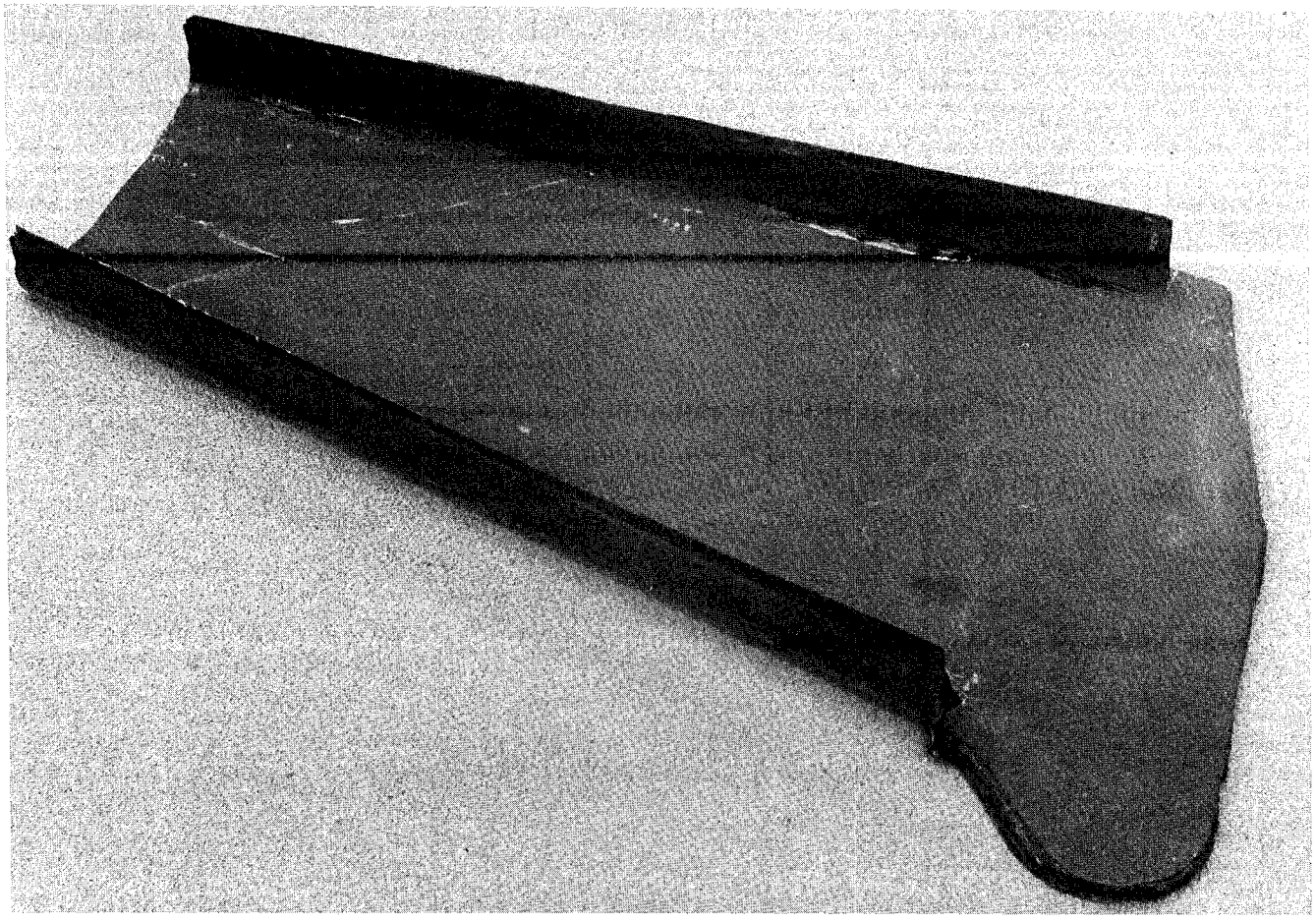

Figure I-8a

Left-Hand Member Elevator Actuator Attachment Rib

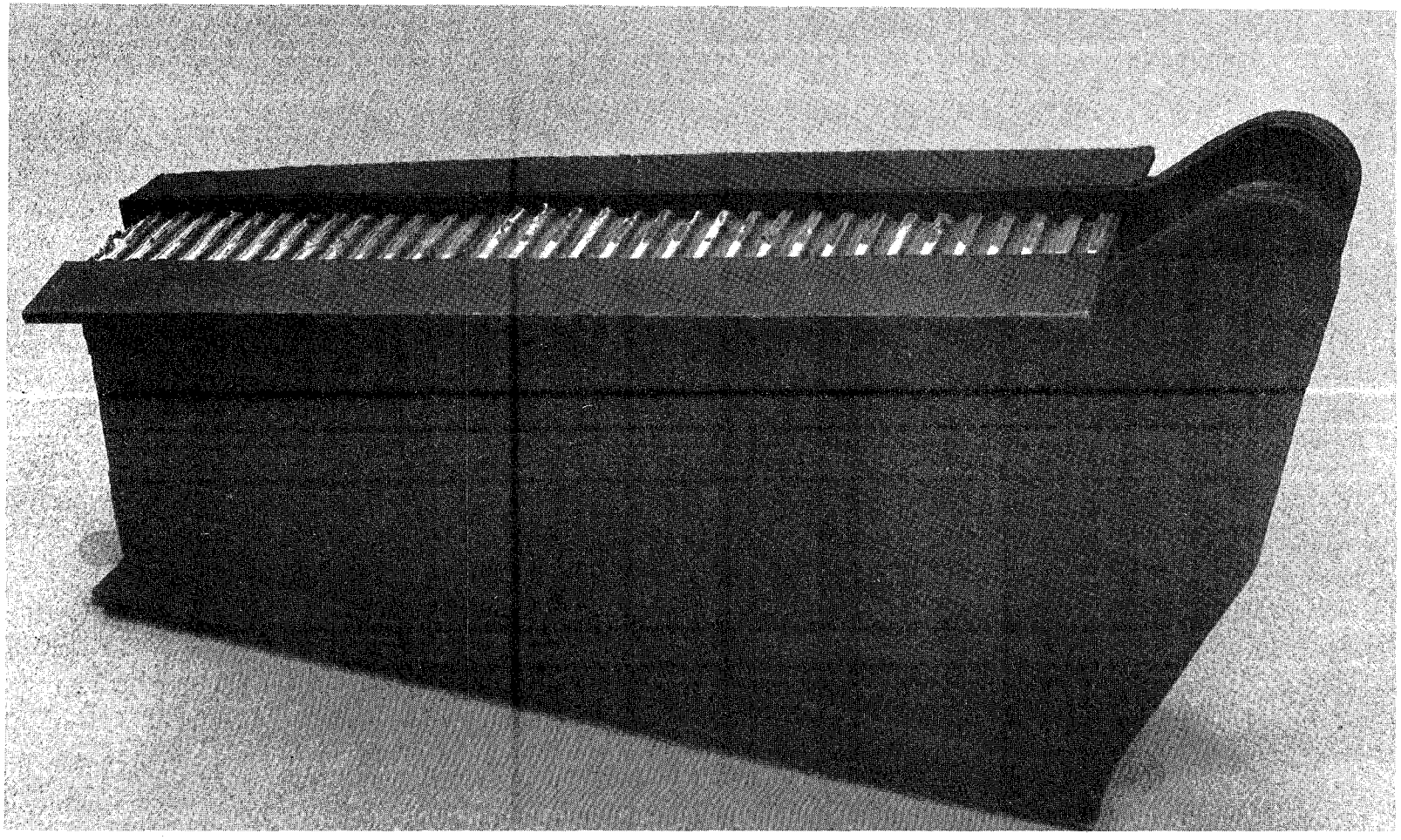

Figure I-8b

Elevator Attachment Rib Assembly

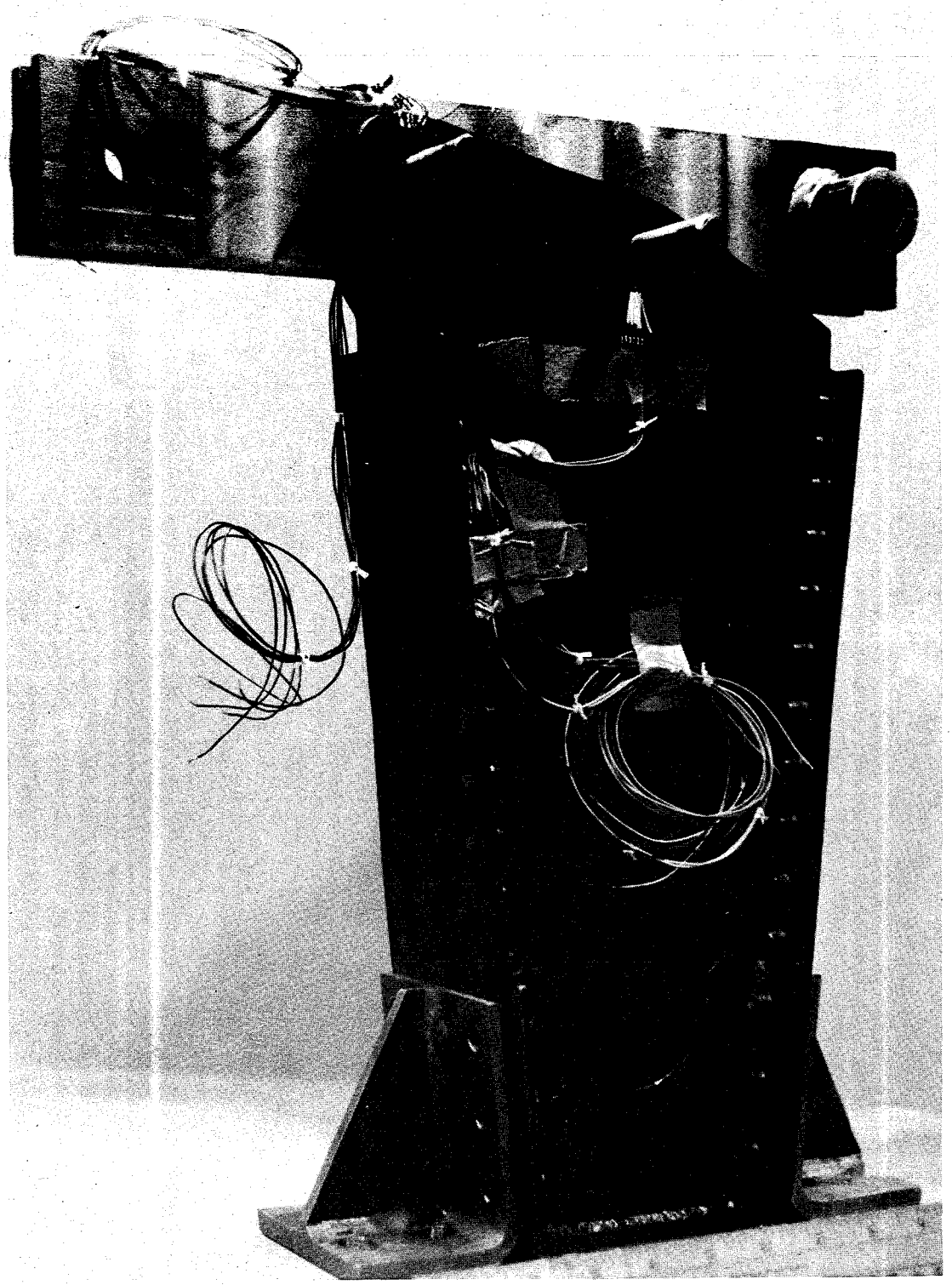

Figure I-8c

Elevator Attachment Rib Assembly Mounted and Instrumented for Testing

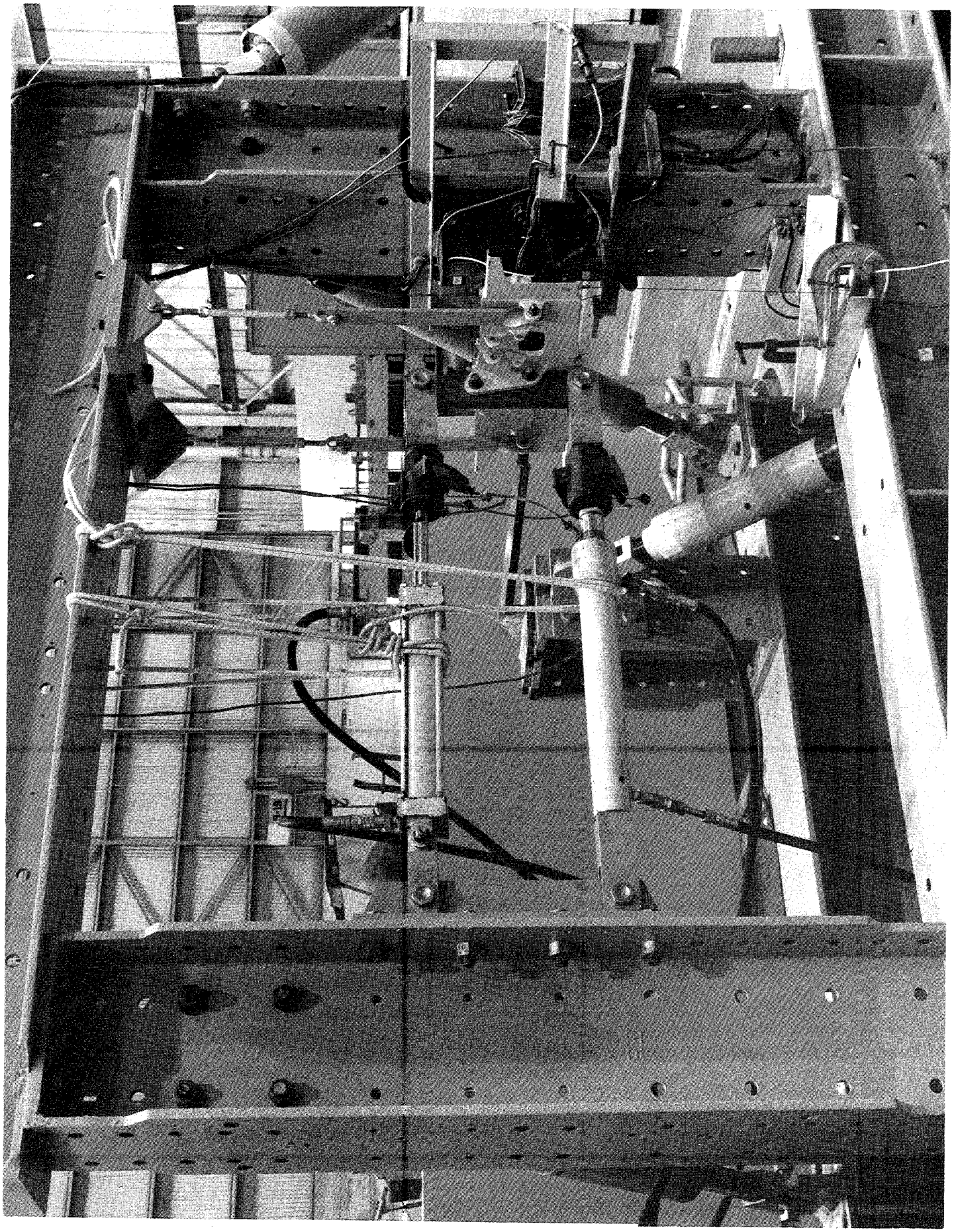

Figure I-9 Advanced Composite Elevator Rib Test (BAC/NASA 727)

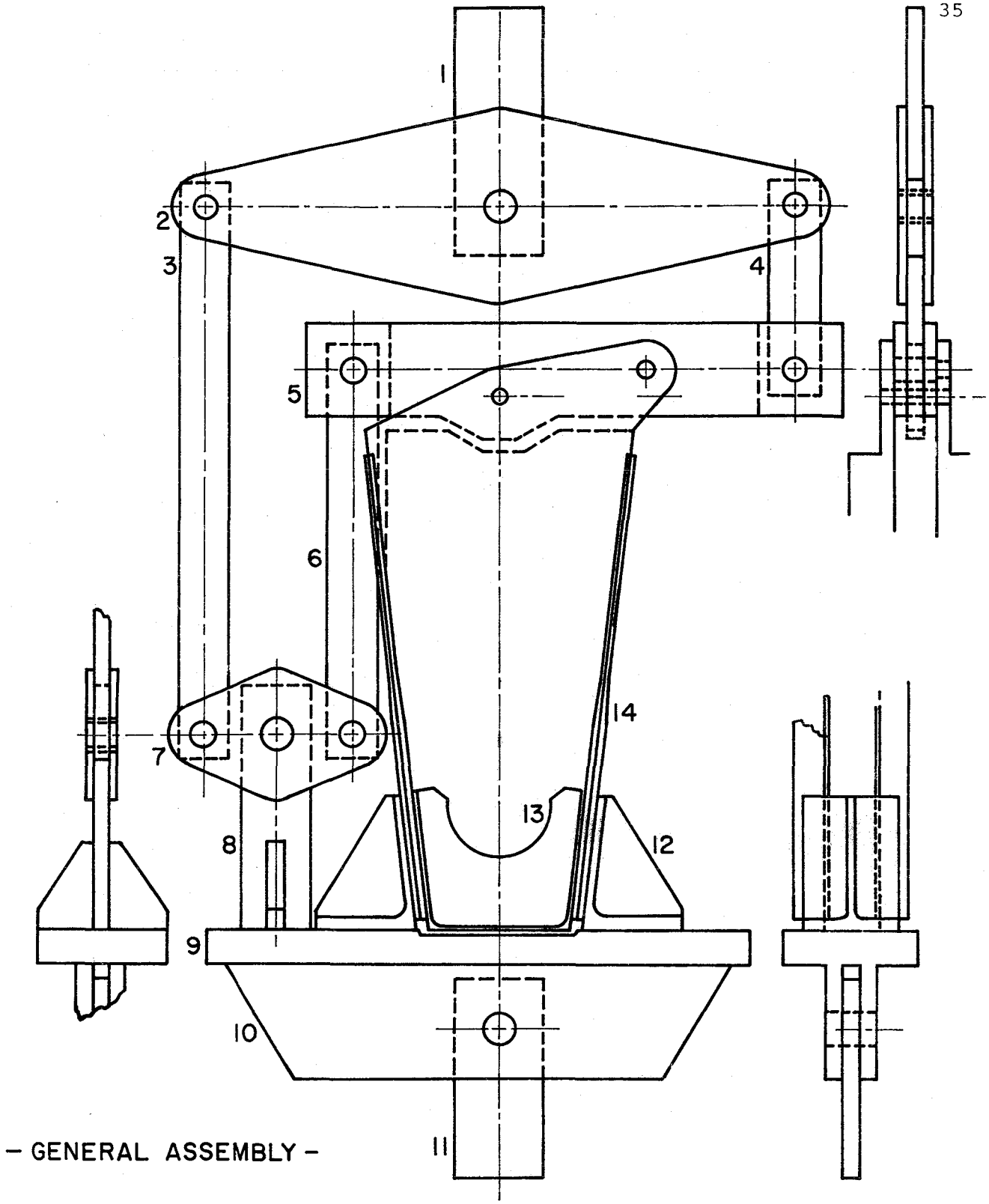

Figure I-10 Rib Test Fixture

From equilibrium of moments in item 5 in Figure I-10 (see free-body diagrams in Figure I-11), it is clear that $P'\ell = [P/2]3\ell$. Thus $P = 2/3P'$. To achieve full design load on the elevator actuator rib attachment point (19,000#), therefore, the RPI Instron (maximum capacity 28,000#) need develope only $P = 2/3(19,000) = 12,666^{\#}$. Further, as designed, the moment equilibrium on the "strong-back structure" (items 8, 9, 10, 12 and 13) will be achieved, since this requires that $M = P'\ell = 3/2P\ell = P\Lambda$, and, in fact, $3/2\ell = 6.638"$ and $\Lambda = 6.638"$.

We expect the first proof load tests to failure of the Berg design actuator attachment rib to be conducted early in the next reporting period. Both strain gage and acoustic emission data will be taken during these tests.

3. Optimizing Fiber Orientations in the Vicinity of Heavily Loaded Joints

(N. Hoff)

A. Introduction

The purpose of this work is to find ways of arranging fibers in a composite structure that lead to high load-carrying capacity-to-weight ratios in the neighborhood of discontinuities such as mechanical joints and openings. The paucity of theoretical information of this kind and the scarcity of long-time practical experience with composite joints have compelled designers to use metals for fittings rather than composites in most highly loaded cases. It is believed that composites offer the possibility of saving weight in such joints and thus merit a detailed investigation.

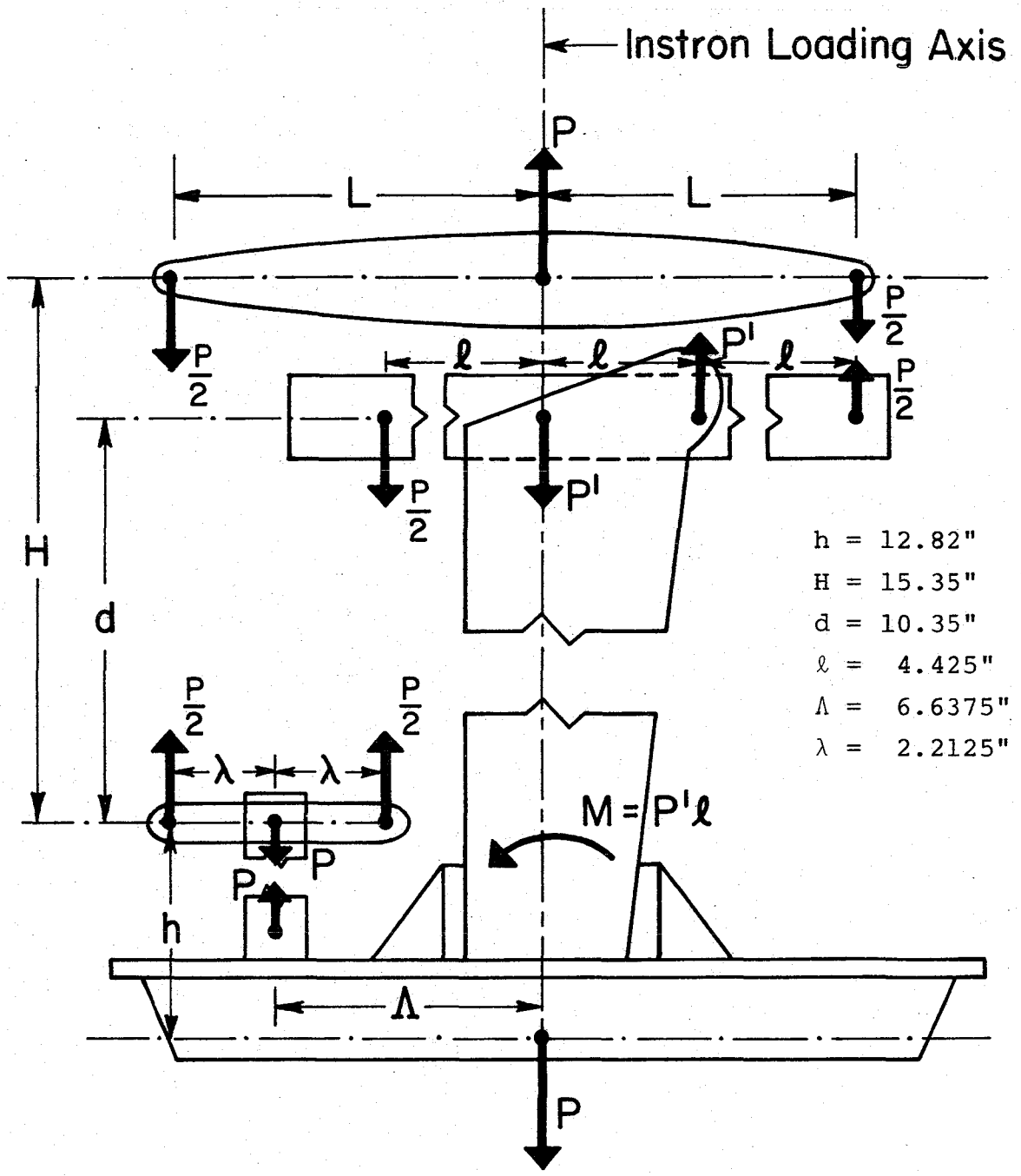

Figure I-11

Free-Body Diagram of the RPI CAPCOMP Loading Linkage

B. Work Completed before May 1

As described in the previous Semi-Annual Progress Report, a manufacturing technique has been developed for tensile specimens incorporating a hole, with fiber arrangements varying with distance from the hole in a manner intended to reduce stress concentration factors. A few specimens were built and tested to failure.

A start was made toward the establishment of a theory of the stress distribution around empty holes when uniform uniaxial tension is applied to the specimen far away from the hole. Such a theory has existed for many years in the case of orthotropy in a Cartesian system of coordinates, but no solutions have been known in the case when the plate is orthotropic in a polar coordinate system (cylindrical orthotropy). Yet this kind of orthotropy promises to reduce the stress concentrations.

Our earlier investigations discovered the fact that a uniform state of tension cannot exist, even far away from the hole, in a cylindrically orthotropic plate under edge loading when properties are independent of distance from the hole, except in the special case when the compliances are connected by the equation

$$2\bar{S}_{rr} - 2\bar{S}_{r\theta} - \bar{S}_{66} = 0$$

where $\bar{S}_{rr} = S_{rr}/S_{\theta\theta}$; $\bar{S}_{r\theta} = S_{r\theta}/S_{\theta\theta}$; and $\bar{S}_{66} = S_{66}/S_{\theta\theta}$.

(In the middle of pg. 54* the term $\bar{S}_{66}$ was written as $\bar{S}_{\theta\theta}$

*Pg. 54 of 38th Semi-Annual Progress Report on Composite Structural Materials.

through a typing error.) In this case it was found possible to derive a closed-form solution for the circumferential stress at the edge of the hole. This solution is the next equation on pg. 54 (see footnote on previous page). No solution of the problem was given in the general case.

C. Progress Made during Reporting Period

During the present reporting period our effort was concentrated on obtaining analytical solutions for the case where properties are independent of distance from the hole, and we have made significant progress in this direction. Complete closed-form solutions have been found for the stresses around the hole for any arbitrary combination of the values of the compliances S_{rr}, $S_{r\theta}$, $S_{\theta\theta}$ and S_{66} as long as these values are constant.

One interesting result of the analysis is that the four compliances can be combined into two parameters in such a manner that the stress concentration factor becomes a function only of these parameters and not of the four individual compliances. One of the parameters is the ratio $\overline{S}_{rr}$ of the compliances for extension in the radial and circumferential directions:

$$\overline{S}_{rr} = S_{rr}/S_{\theta\theta}.$$

The other parameter $\overline{S}$ is defined as

$$\overline{S} = 2\overline{S}_{r\theta} + \overline{S}_{66} = 2(S_{r\theta}/S_{\theta\theta}) + (S_{66}/S_{\theta\theta}).$$

The earlier conclusion that a uniform state of stress cannot exist in the cylindrically orthotropic plate, except

when the values of the compliances are related according to a particular condition, has been confirmed.

The analytical work shows that the solution depends strongly on the values of the two parameters defined earlier. In the first range of the parameters the stress function and the expressions for stress and strain are exponential functions of the radial distance r with real exponents. Naturally these can be combined into hyperbolic functions of real argument.

In another range of the parameters the exponents are complex and the solutions are products of hyperbolic functions with trigonometric functions of real argument. Finally, in a third range the solutions are products of trigonometric functions of real argument.

Even within these ranges the stress-concentration factors show different patterns of behavior. In one subrange the factors remain finite when the outer radius R of the circular plate analysed increases beyond all bounds. In a second subrange the factors approach zero signifying that the tractions applied to the outer edge of the plate are in equilibrium in a boundary layer parallel to the loading and excluding the hole and cause no finite stresses in the vicinity of the central circular hole.

In a third subrange the stress-concentration factor approaches infinity if the outer radius R of the plate is allowed to increase beyond all bounds. Although strange at

first reading, this behavior is not contrary to any of the laws of mechanics. After all, infinite plates are a mathematical fiction. In the physical world no one has yet built an infinite plate, nor has he loaded it at infinity.

The manuscript of a full report on this phase of our investigations has been completed and is now ready for typing in its final form. It is entitled, "Stress Concentrations in Cylindrically Orthotropic Composite Plates with a Circular Hole". In addition to the mathematical derivations, the report also contains physical explanations of the various behavior patterns observed.

A good start has also been made with an investigation of the stress-concentration factors in cylindrically orthotropic plates when the compliances are functions of the radial distance r. In this case the compliances have the form

$$S_{ij} = S_{ij}^{*} + S_{ij}^{*} e_i r^{2h}$$

where h is an integer and S_{ij}^{*} and e_i are determined by the prescribed properties at the hole (r = 1) and at the outer edge (r = R). The solution for the stresses in such a plate is based on the procedure described earlier, where the compliances are <u>not</u> a function of the radius r, and it involves power series. To test the calculation method, the distribution of circumferential stress along the radius was determined using a pocket calculator. Compliances were chosen as follows: at the hole (r = 1) values are set for composites with ±45° fibers only; at the outer boundary (r = R = 10) the

properties are made those of a nearly quasi-isotropic material with a fiber arrangement $(0^\circ_{25}/45^\circ_{25}/-45^\circ_{25}/90^\circ_{26})$. Since a state of plane stress is assumed the stacking sequence is not important for the calculations. Two composite materials were chosen for the examples. One case is a typical glass epoxy, where the compliances do not change greatly from r = 1 to r = 10, and the other is a typical graphite epoxy where the compliances exhibit a large variation in the end points, that is the values at r = 1 as compared to r = 10. Values of compliance between the end points were not calculated based on variations of fiber lay-ups as might be expected in practice. Rather, simple power series were picked which could be expected both to be tractable and, at the same time, provide for realistic values. Figure I-12 shows for the property $S_{\theta\theta}$ this behavior of the compliances. Two different variations of S_{ij} are shown for glass epoxy and one for graphite epoxy. All values are nondimensionalized. The overall geometry of the loaded plate is shown in Figure I-13.

The distribution of circumferential stress along the radius r at $\theta = \pi/2$ for glass epoxy is plotted in Figure I-14. The two curves for a different variation of S_{ij} with the radius r, may be compared with the one where the plate consists of ±45° fibers only. The difference in the stress distribution occurs mainly in the vicinity of the hole and somewhat at the outer boundary. The stress concentration factors differ from the value of 3 encountered with isotropic materials, as expected.

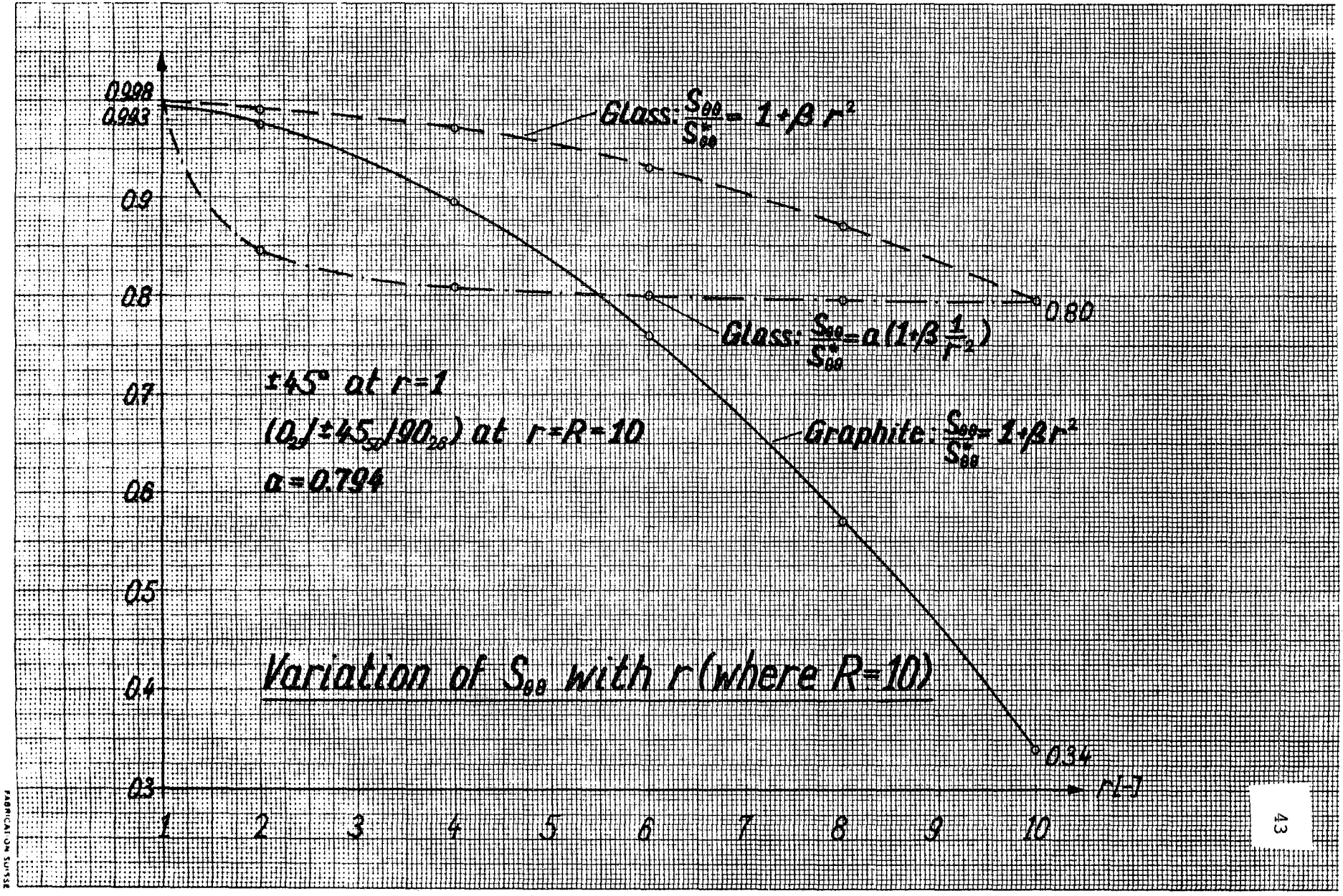
0.998
0.993
0.9
0.8
0.7
0.6
0.5
0.4
0.3
Glass: $\frac{S_{\theta\theta}}{S^*_{\theta\theta}} = 1+\beta r^2$
0.80
Glass: $\frac{S_{\theta\theta}}{S^*_{\theta\theta}} = a(1+\beta\frac{1}{r^2})$
±45° at r=1
$(0_2/\pm 45_{5D}/90_{2S})$ at r=R=10
a=0.794
Graphite: $\frac{S_{\theta\theta}}{S^*_{\theta\theta}} = 1+\beta r^2$
Variation of $S_{\theta\theta}$ with r (where R=10)
0.34
r/L-1
1
2
3
4
5
6
7
8
9
10
43

Figure I-12

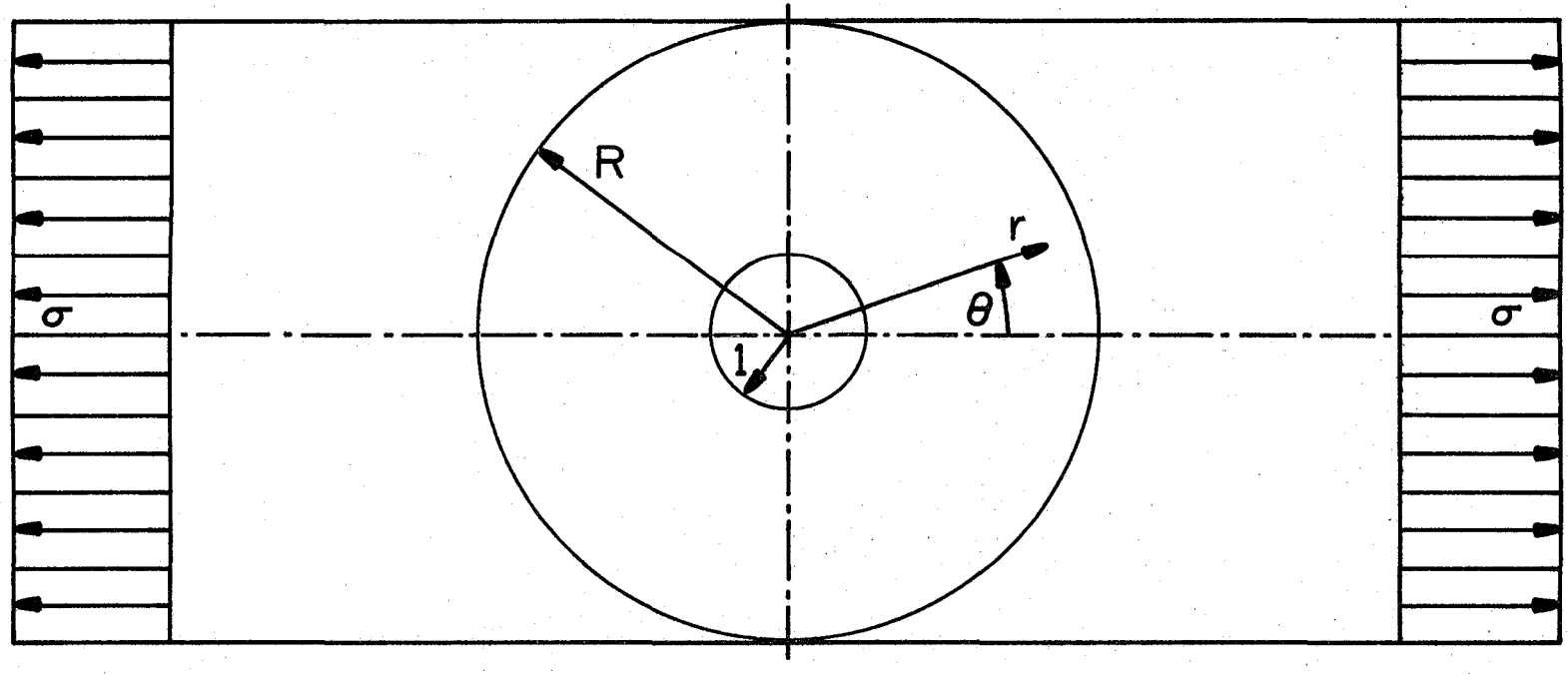

Geometry of axially loaded plate

Figure I-13

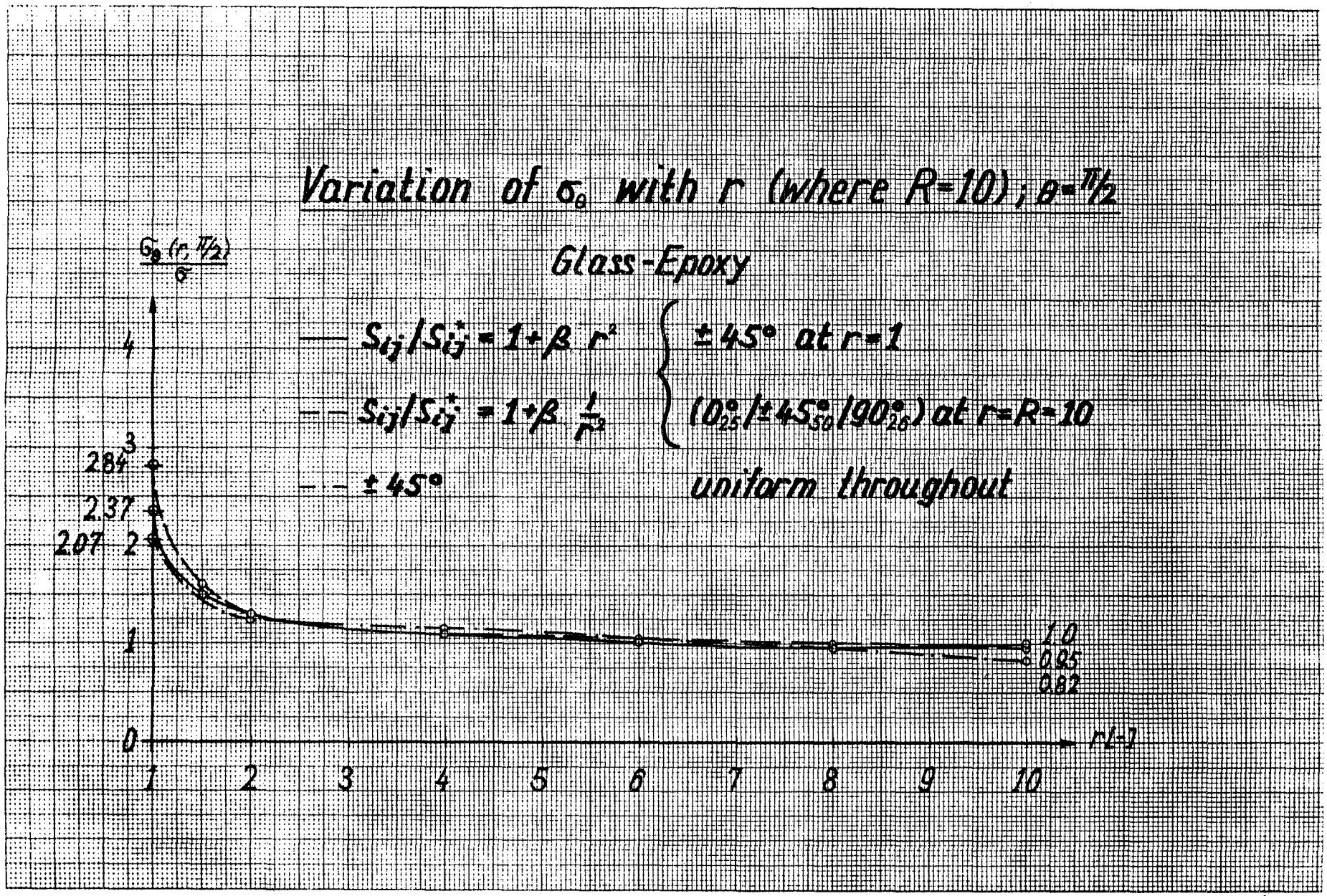
Variation of σ_θ with r (where R=10); $\theta=\pi/2$
$\frac{\sigma_\theta(r,\pi/2)}{\sigma}$
Glass-Epoxy
$S_{ij}/S_{ij}^* = 1+\beta r^2$ ± 45° at r=1
$S_{ij}/S_{ij}^* = 1+\beta \frac{1}{r^2}$ $(0^\circ_{25}/\pm 45^\circ_{50}/90^\circ_{26})$ at r=R=10
± 45°
uniform throughout
4
3
2.84
2.37
2.07
2
1
0
1.0
0.95
0.82
r/a-1
1
2
3
4
5
6
7
8
9
10

Figure I-14

The curves for circumferential stress in the case of graphite epoxy are shown in Figure I-15. Note that when the compliances are a function of the radius r, the stresses do not differ greatly from a uniform average stress distribution. The two stress concentrations, here, are smaller than unity, and the highest stress occurs not at the hole but at a point one or two radii away from the hole. These maximum stress concentration values are about 1.5. It is noted that, in the case of ±45° fibers throughout, the stresses near the hole have a negative sign, indicating compression.

A more thorough treatment of this problem where the compliances are a function of the radius will be the subject of follow-up research. We consider this study of great importance because, as noted earlier, in the optimal plate most likely the fibers near the hole will be arranged differently from those far away from the hole.

D. Plans for Upcoming Period

1. The manufacturing effort and the testing of specimens described in the previous report will be continued.
2. Graphs will be prepared to show the stress-concentration factors as a function of the two parameters $\bar{S}_{rr}$ and $\bar{S}$. Values will be computed from the expressions already derived; they should prove useful in practical design.
3. The investigation of the stress-concentration factors will be continued for cases

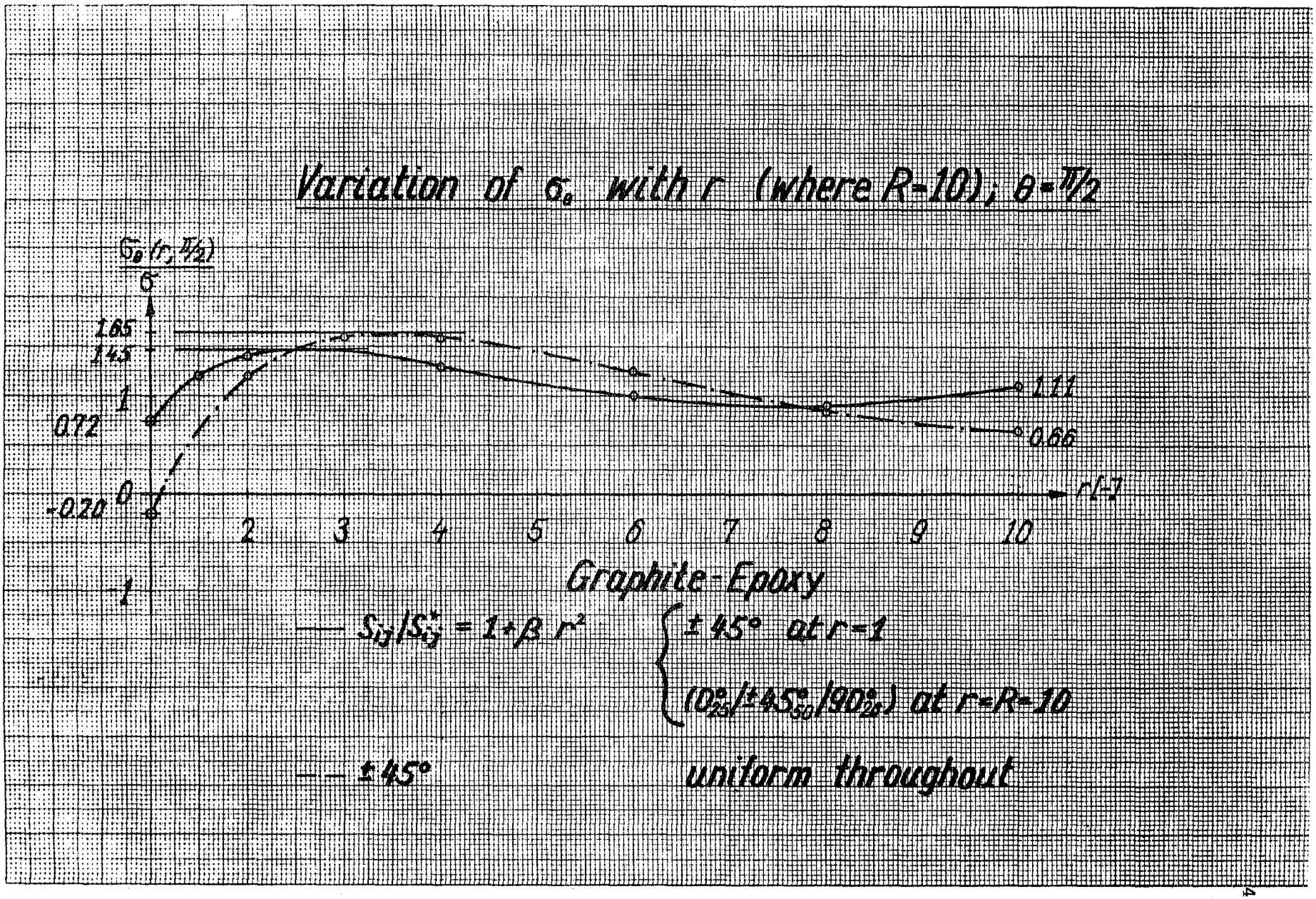
Variation of σ_θ with r (where R=10); $\theta=\pi/2$
$\sigma_\theta(r,\pi/2)$
σ
1.65
1.45
1
0.72
0
-0.20
-1
2
3
4
5
6
7
8
9
10
1.11
0.66
r/-7
Graphite-Epoxy
$S_{ij}/S_{ij}^* = 1+\beta r^2$
$\pm 45°$ at r=1
$(0^\circ_{25}/\pm 45^\circ_{50}/90^\circ_{25})$ at r=R=10
$\pm 45°$
uniform throughout

Figure I-15

when the compliances (and thus the parameters $\bar{S}_{rr}$ and $\bar{S}$) are functions of the radial distance r. It is expected that a technical report covering this work will become available by the end of the upcoming period.

4. Supporting Research on Lightly Loaded Mechanical Joints

(R. Loewy)

A. Introduction

The work of graduate student Wonsub Kim continued to concentrate on stress distributions around pin-loaded holes in composite membranes and plates with no special fiber arrangements around the hole and the associated bearing strength and failure mechanisms.

B. Status

Three different approaches outlined in the previous report are being pursued in parallel, as a way to increase understanding of the behavior of plates subjected to bearing loads. Of these, emphasis during the past months was directed to finite element numerical computations and correlation with photoelastic analysis.

It will be recalled that the finite element model shown in Figure I-16 has been postulated. A constant strain, triangular shaped element is used and a 345 element model with 212 nodes was generated by the program. The plan we formulated was to use several constraint equations to simulate the loaded edge condition. If we can match the strain distribution from one of the finite element solutions with the

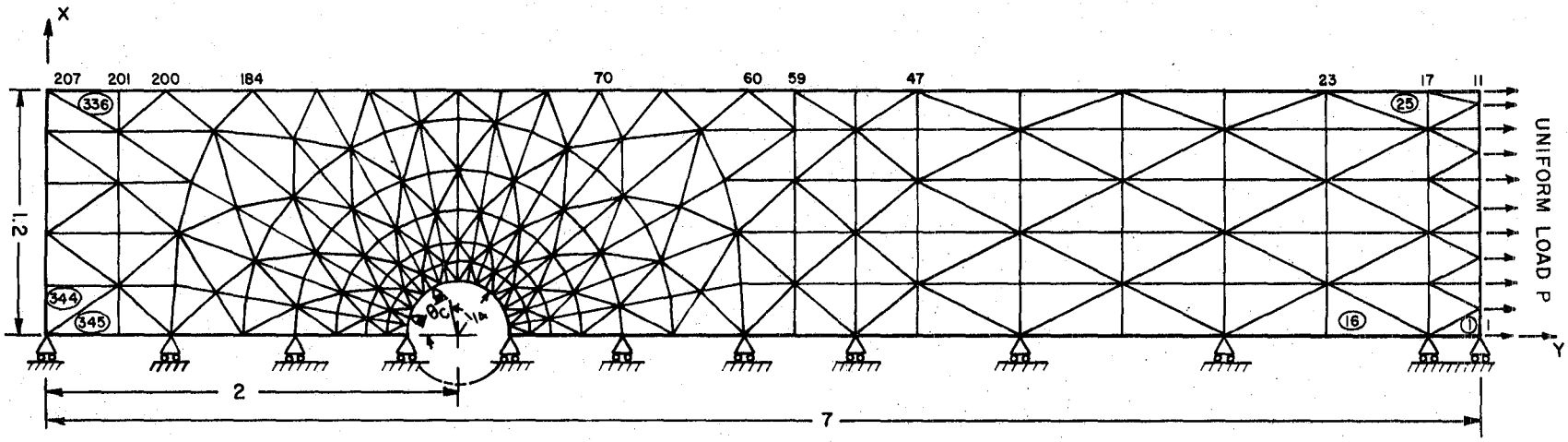

Figure I-16 Finite Element Idealization and Boundary Conditions

fringes from the photoelastic experiment, we will then know the contact zone assumed between the loading pin and the edge of the hole in the corresponding computation was correct. If successful, this will be a linear solution to an essentially non-linear problem.

C. Progress During Reporting Period

To put our model for the finite element analysis of a pin-loaded composite plate into the main analysis program, considerable time has been spent in data preparation. The output and input of the main program are in terms of element coordinates. It was, therefore, necessary to transform all the material information, which is related to principle material axes, to each elemental coordinate system. To transform the material orientation given in terms of a global x - y coordinate system into each elemental coordinate, the following preliminary calculation was used.

Given nodal positions of an element, x and y, then the transformation angle ϕ is

$$\phi = \mathrm{Tan}^{-1}\left(\frac{y_j - y_i}{x_j - x_i}\right)$$ as shown in Figure I-17,

where, subscripts i, j correspond to the nodes numbered I and J, respectively. Since we know the global fiber direction angle α,

$$\beta = \alpha - \phi.$$

These transformations were performed for 345 elements and 3 fiber orientations (45°/90°/-45° -- the same as the photoelastic specimen, Ph - C type) by a preprocessor. This

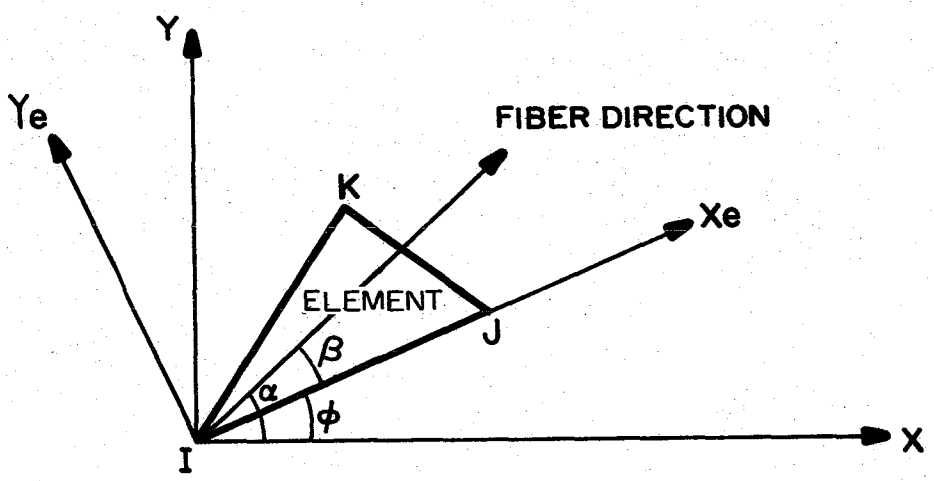

Figure I-17
Transformation Diagram from Elemental to Global Coordinates

data preparation has now been completed and checked.

The variable contact area between pin and hole, as load is changed, was simulated by using constraint equations at particular nodes on the loaded boundary of the hole. In our first computation/correlation attempt, eight nodes out of a total of nineteen around the half circle of the hole with which the pin could make contact were constrained to have free displacement in the circumferential direction only. That corresponds to a contact angle of 80 degrees. All the nodes along the axis of symmetry were assumed to be simply supported. Along the loaded edge of the model, a uniform displacement field was used as a forced boundary condition. The value of the displacement imposed was 0.02 inch in the y direction (parallel to the axis of the symmetry).

The output from the main analysis program is also in terms of element coordinate systems. Such output includes three principal stresses (maximum and minimum normal stresses and maximum shearing stresses) at the centroid of the triangular elements and three stresses along the material axes (longitudinal, transverse and shearing) on each layer.

The following procedure was used to check the consistency of the equations used in the program.

1) Using the stress output along the material axes and the strains in terms of the same coordinates,

$$\{\varepsilon_o\} \equiv [D_o]\{\sigma_o\}$$

Where,

$$\{\sigma_o\} \equiv \begin{Bmatrix} \sigma_L \\ \sigma_T \\ \tau_{LT} \end{Bmatrix}, \quad \{\varepsilon_o\} \equiv \begin{Bmatrix} \varepsilon_L \\ \varepsilon_T \\ \gamma_{LT} \end{Bmatrix}$$

and

$$[D_o] \equiv \begin{bmatrix} \frac{1}{E_L} & \frac{-\nu_{LT}}{E_L} & 0 \\ -\frac{\nu_{LT}}{E_L} & \frac{1}{E_T} & 0 \\ 0 & 0 & \frac{1}{G_{LT}} \end{bmatrix}$$

again, where the subscripts L and T represent the fiber and transverse directions, respectively. But from the general strain tensor,

$$[\varepsilon_o] = \begin{bmatrix} \varepsilon_L & \frac{1}{2}\gamma_{LT} \\ \frac{1}{2}\gamma_{LT} & \varepsilon_T \end{bmatrix}$$

The characteristic equation for the eigen functions which determine principal strains is

$$\lambda^2 - (\varepsilon_L + \varepsilon_T)\lambda + (\varepsilon_L\varepsilon_T - \tfrac{1}{4}\gamma_{LT}^2) = 0$$

from which the eigen values are

$$\lambda = \tfrac{1}{2}\left[\varepsilon_L + \varepsilon_T \pm \sqrt{(\varepsilon_L + \varepsilon_T)^2 - 4(\varepsilon_L\varepsilon_T - \tfrac{1}{4}\gamma_{LT}^2)}\right]$$

2) Accordingly, the direction of the maximum value ψ is

$$\psi = \mathrm{Tan}^{-1}\left[\frac{2}{\gamma_{LT}}(\varepsilon_{max} - \varepsilon_L)\right]$$

where, obviously, $\varepsilon_{max} \equiv \lambda_{max}$ in this case, and the maximum shear strain γ_{max} is

$$\gamma_{max} = \varepsilon_{max} - \varepsilon_{min}$$

3) Using the laminated plate theory and strains calculated above, principal stresses were computed and compared with those from the program output. The results were identical.

As noted earlier in this section of the report, strain contours are the principal means of correlating with the photoelastic results. To plot the strain contours, the following procedure was used. The maximum shearing strains at the elements' centroids were determined using the calculation method described above. These centroidal values were then used to compute values at the nodes, by a weighted least-squares fit. The assumed fitting function was the second order, two dimensional polynomial

$$P(x,y) = a_0 + a_1x + a_2y + a_3x^2 + a_4xy + a_5y^2$$

and the weighting function was,

$$F_{w_i}(x,y) = \frac{f_i(x,y)}{r^4}$$

where $f_i(x,y)$ is the centroidal value of the element i, and

$$r = \sqrt{(x - x_i)^2 + (y - y_i)^2}.$$

The least square approximation technique to get the constants a_i (where $i = 0;\cdots 5$) was checked with a one-dimensional case on the IMLAC graphics terminal. The resulting agreement was excellent; the curve passed through all the arbitrarily generated data points and was smooth in the regions outside of the end points. Furthermore, no extra calculations such as an extrapolation were needed to calculate values at the nodes on the edge of the model. After getting the nodal values of strain, contour lines were drawn on the graphics terminal screen, by applying a linear interpolation method locally, based on the three nodal values of each element.

A first sample calculation was completed during this period, and the plot shown in Figure I-18 exhibits patterns of maximum shearing strain distribution encouragingly similar to those of the photoelastic fringes. The photoelastic pictures show half fringes (Figure I-19a) and full fringes (Figure I-19b). The fringe number 1 is equivalent to a maximum shearing strain value

$$\gamma_{max} = 0.18917 \times 10^{-2} \text{ inch/inch.}$$

This is the same scaling factor used in the contour plotting of analysis results. Thus, a fringe number 2 corresponds to a γ_{max} value of 0.37834×10^{-2} inch/inch. The half fringe number 1 on the photoelastic picture in Figure I-19a is equivalent to $\gamma_{max} = 0.09458 \times 10^{-2}$ inch/inch. The load applied in the photoelastic experiments was 1500 pounds, and the post-calculated load of the finite element model was 1480 pounds.

Although the fringe patterns are similar, the finite element analysis results show almost exactly twice as many fringes as the photoelastic pictures show. The reasons for this are not yet clear. The somewhat different shape of the fringes may be caused by one or more of the following reasons.

1) Possible Material Differences. The material information used in the finite element analysis may differ from the characteristics of that used in photoelastic tests. Careful coupon testing would be required to resolve this; "sensitivity checks" using arbitrary

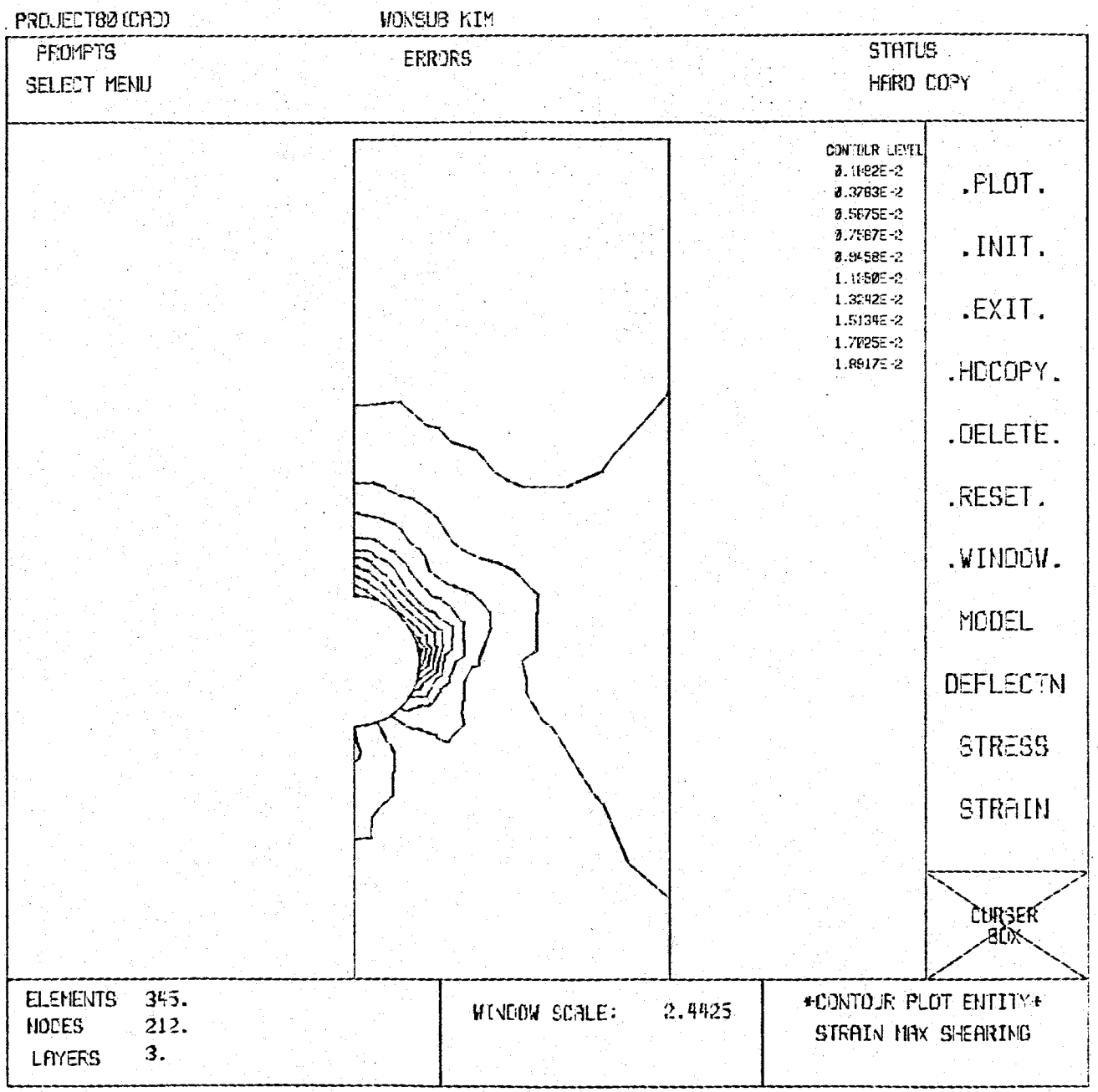

Figure I-18

Contour Plot of Maximum Shear Strain
from the Finite Element Analysis
(applied load, 1480 lbs.)

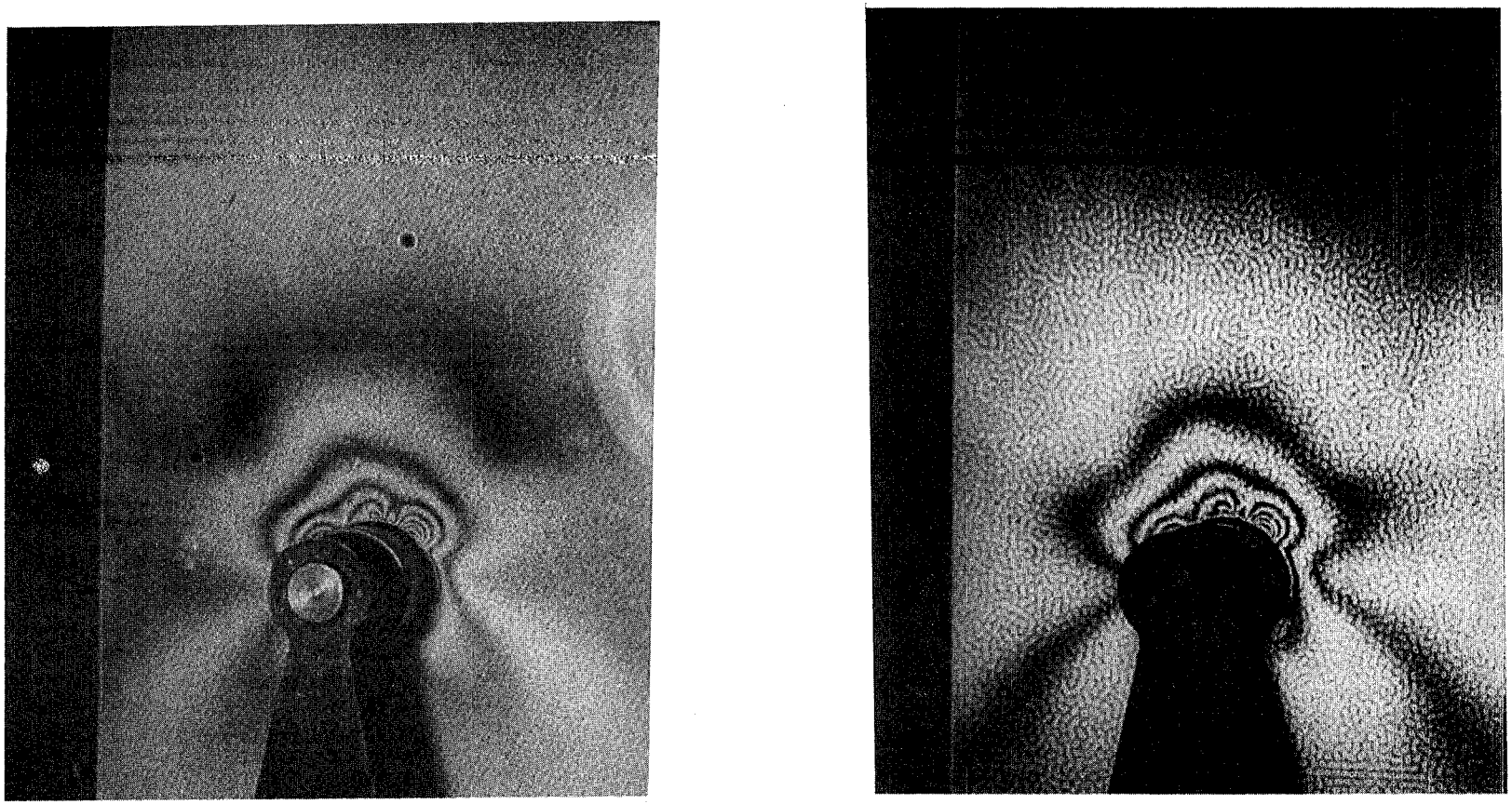

a) Half fringes

b) Full fringes

Figure I-19
Photoelastic Fringes (applied load, 1500 lb.)
(1 fringe corresponds to γ_{max} = 0.0018917 in/in)

variations of material properties in the analysis, however, may be worthwhile.

2) Contact Angle. The contact angle corresponding to the analytical contour plot has not been iterated. It would be extremely fortuitous if the assumed contact angle of 80° was correct. It is the purpose of this research to arrive at the correct contact angle by iteration, and this will be done.

3) Slightly Different Model Size. The width of the analysis model is 2.4 inches and for the photoelastic specimen 2.48 inches. The distance from the center of the hole to the free end is 2.0 inches for analysis model and 2.35 inches for the specimen plate; thickness was the same for both models.

4) Other Experimental Inaccuracies. Calibration of photoelastic coating, effect of grips, etc.

D. Plans for Upcoming Period

For the immediate furture, we will attempt to verify the material properties of the model and explore other potential sources of discrepancy between the fringes in the photoelastic results and those of our finite element analysis.

PART II

CAPGLIDE (Composite Aircraft Program Glider)

CAPGLIDE (Composite Aircraft Program Glider)
(R. J. Dienfendorf, H. J. Hagerup, G. Helwig)

FAA certification in the "experimental" category was obtained for the first all-composite ultra-light glider, the RP-1, on August 25, 1980. A series of increasingly extended automobile tows from turf was then conducted at Schenectady County Airport, Schenectady, N. Y. during late July and August. The first public flight demonstration took place on September 16, 1980 with extensive media coverage. From first lift-off to public demonstration, the aircraft has made a total of sixteen successful flights using automobile-tow with release altitudes up to 700 feet. Significant gain in altitude above the release point was observed on at least one flight, although no attempt was made in these early trials to achieve soaring flight. Airplane traffic at the airport caused the tower to restrict all RP-1 flights to a relatively small area; this prevented a search for thermals. Mr. M. McCarron, a professional pilot, has piloted all flights to date. His reaction to the aircraft has been very positive, emphasizing its good inherent stability characteristics and responsive control. Photographs of these activities at Schenectady County Airport are reproduced in Figures II-1 through 6.

The only untoward incident was experienced when the attempt to launch the fourteenth flight was abandoned, and a relatively mild, partial ground loop followed which produced minor structural damage to the skid assembly. We believe

Figure II-1 RP-1 Unloaded From Trailer, Ready for Assembly

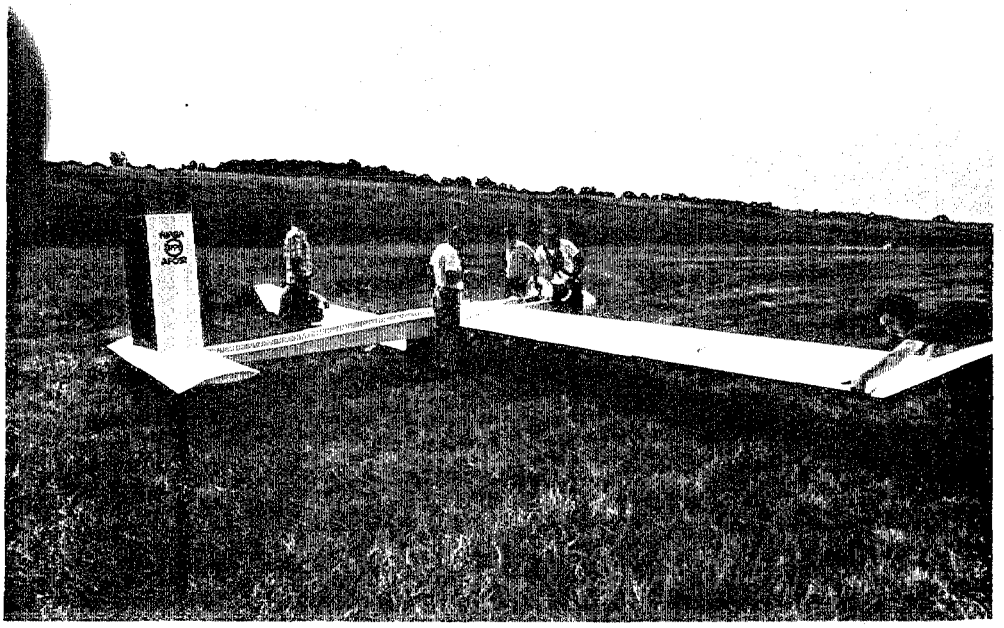

Figure II-2 RP-1 Being Assembled

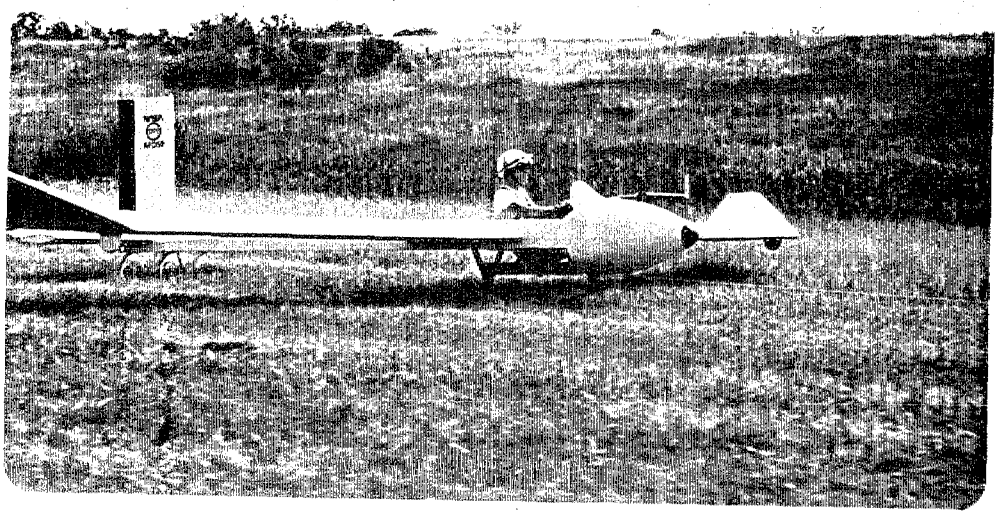

Figure II-3 RP-1 Ready for Tow Initiation

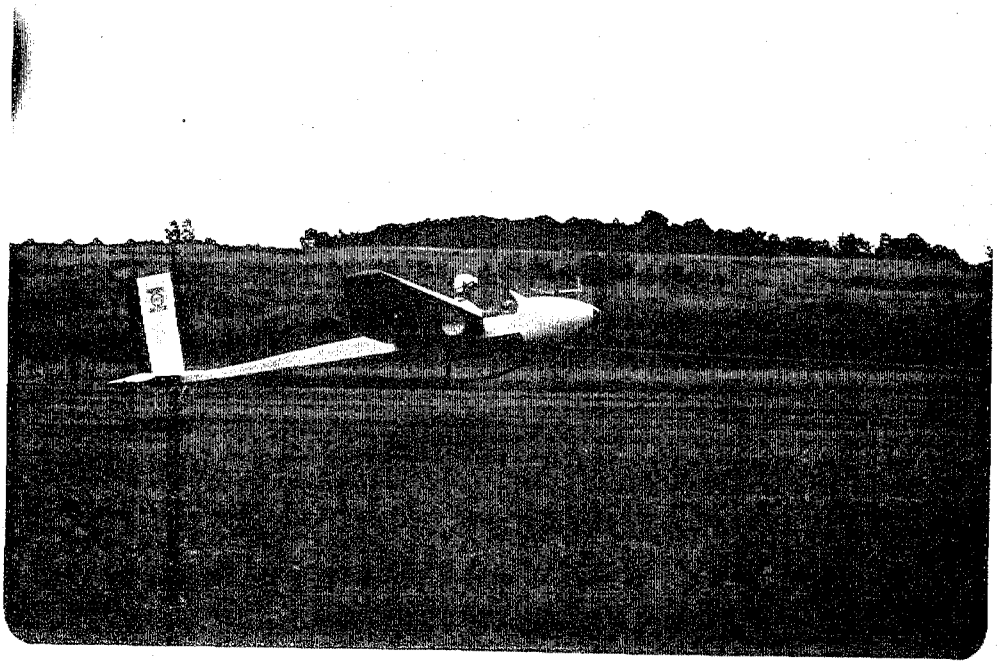

Figure II-4 RP-1 Airborne

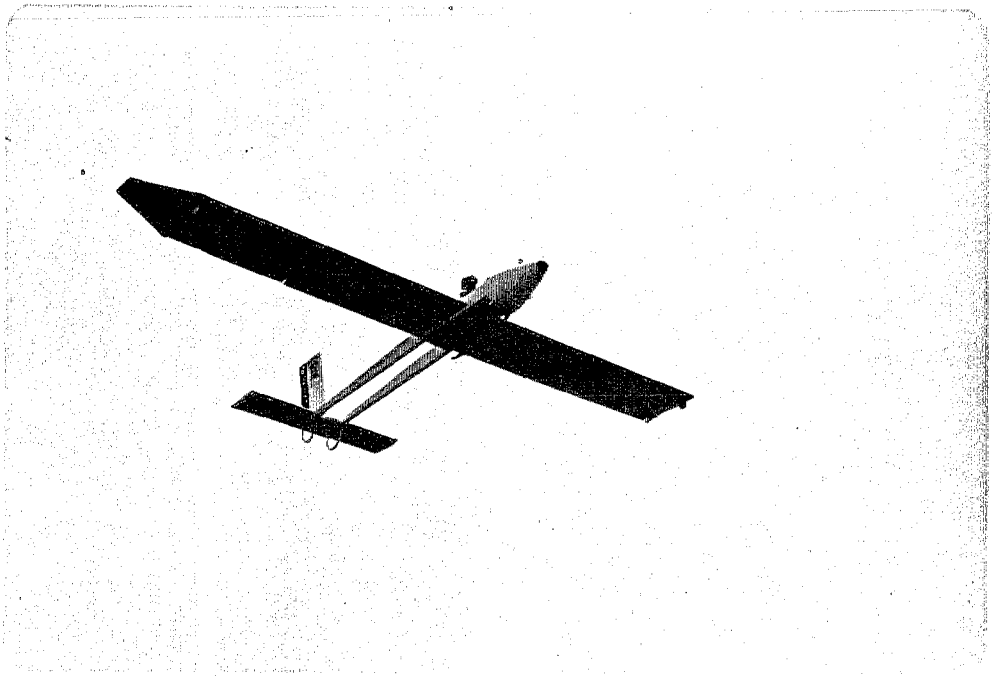

Figure II-5 RP-1 Gaining Altitude

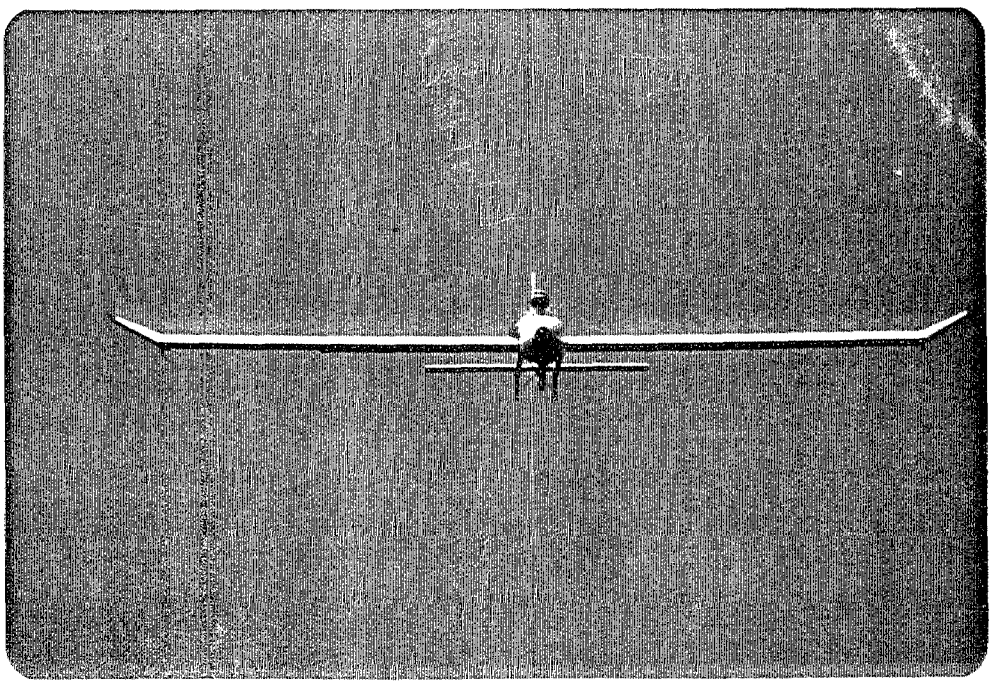

Figure II-6 RP-1 Free Flight

that the difficulty was due to the use of an excessively elastic tow rope and too-rapid tow acceleration technique. Calculations confirmed that this caused the cable-aircraft combination to act somewhat like a slingshot, causing the glider to surge forward following the abrupt drop of friction from static to sliding during the first acceleration of the automobile. Then, after the potential energy in the cable was exhausted and tension in the cable dropped to zero, the glider momentarily slowed down. The pilot, sensing yaw and a reduction in directional control at that point, released from the tow rope. The aircraft yawed left, coming to rest in an area of sparse tall grass, which was probably the direct cause of the final ground loop. The damage to the skid assembly was quickly repaired, however, and the flight test program continued with a conscious effort to accelerate the tow car quickly only after the glider was seen to move.

Operations are presently being moved to another site where winch tow to higher release altitudes will be possible, and there will be fewer restrictions on operating areas. The RP-1 landing gear is being modified to incorporate a wheel, thus facilitating launch by winch-tow. Release altitudes up to 1400 feet are expected. This second phase of the flight test program is designed to obtain performance data such as stall speed and glide polar for the RP-1. These tests can be performed safely only at considerable altitude.

Meanwhile, work on the conceptual design and the preliminary design of the second aircraft has started. It now

appears that the RP-2 will be a 44-foot span tapered wing, ultra-light, all-composite sailplane with a fully-enclosed conventional fuselage. The aircraft, in order to ultimately have a self-launch capability, is being designed with space and structural provisions for an auxiliary engine. We expect to conduct, however, initial test flights without an operational engine installed. The airfoil will be the thick version of the variable geometry airfoil developed by Boeing in cooperation with RPI and reported in the last semi-annual progress report. Preliminary experiments indicate that a structural design for the RP-2 wing, consisting of one-sided Kevlar-on-foam sandwich skins, will have the necessary strength and stiffness. This design approach allows a very simple fabrication technique. The one-sided sandwich skins can be laid up flat and cured and then bonded to the rib-spar-shear-webs internal wing structure. The lower bending stiffness of the cured, one-sided sandwich skins allows them to take the shape of the ribs to which they are bonded. Wing-molds of the type used in the construction of the RP-1 will thus not be necessary, saving time and effort. A preliminary three-view drawing of the RP-2 is shown in Figure II-7, and a preliminary version of the V-n diagram defining the loads envelope appears in Figure II-8.

Activity in the Composites Fabrication Laboratory during the present reporting period has again been focused on composites structural techniques, with each student individually,

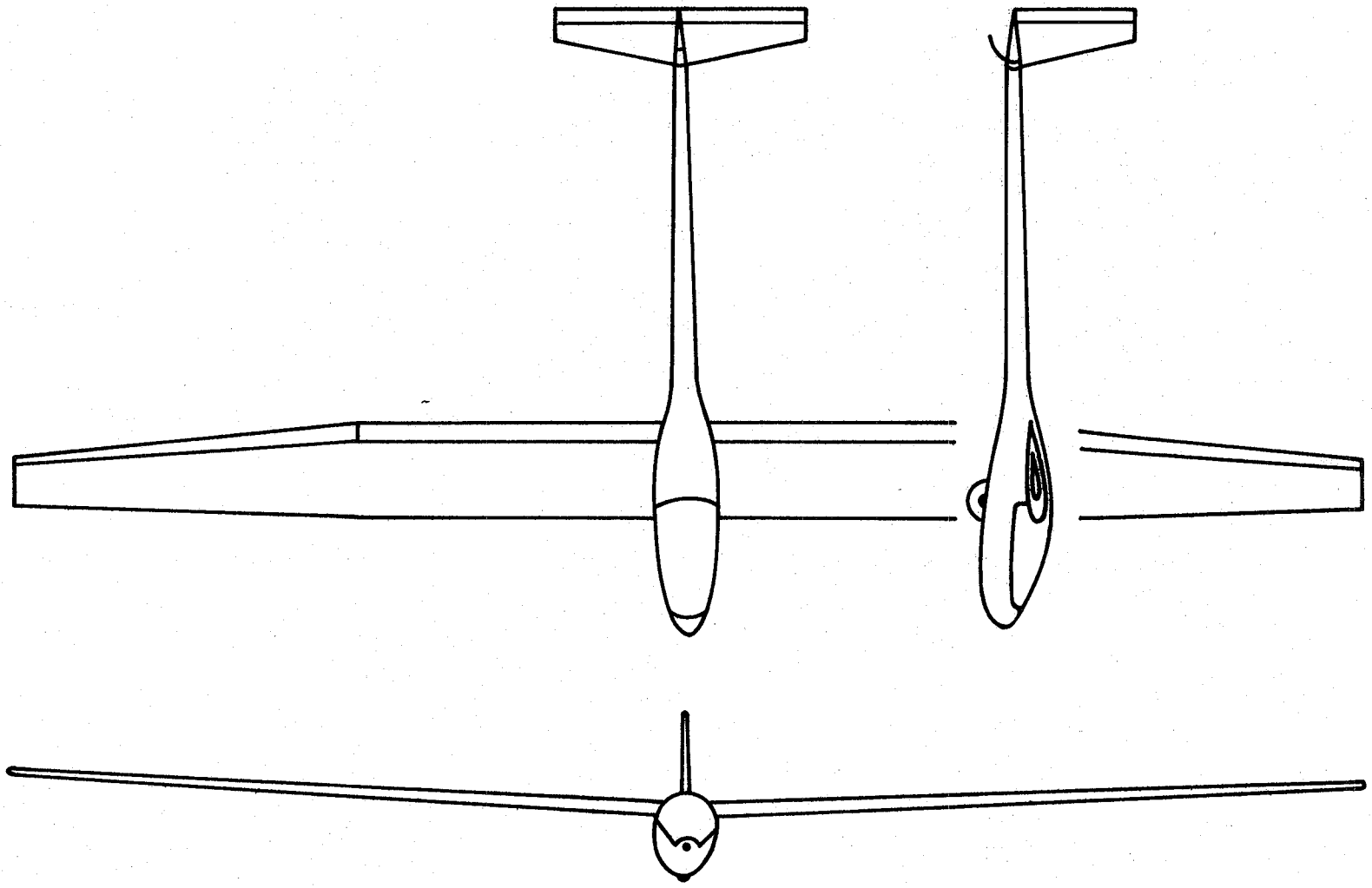

Figure II-7
Three-View Preliminary Design of Glider, RP-2

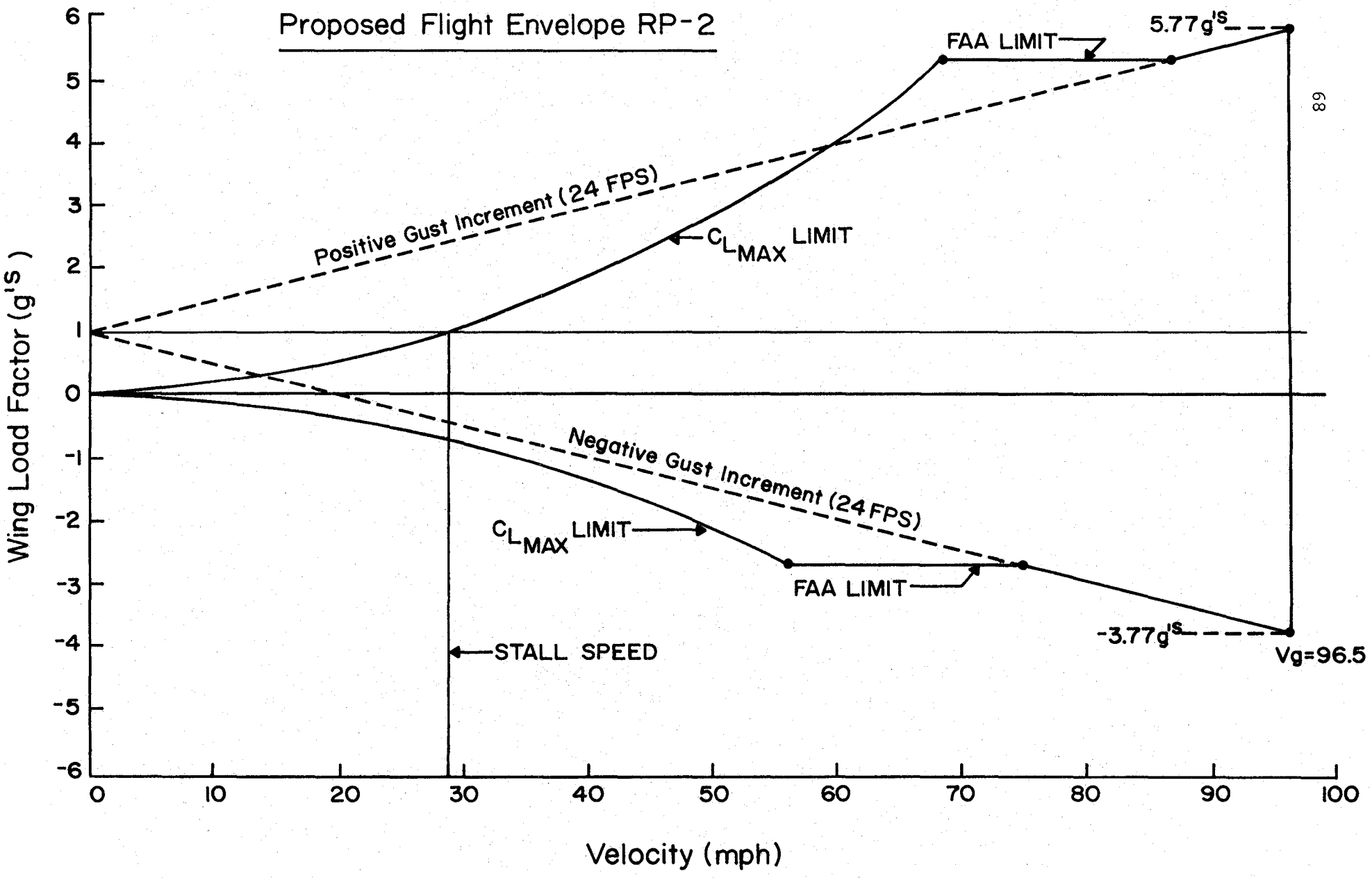
Proposed Flight Envelope RP-2
FAA LIMIT
5.77g's
Positive Gust Increment (24 FPS)
$C_{L_{MAX}}$ LIMIT
Negative Gust Increment (24 FPS)
$C_{L_{MAX}}$ LIMIT
FAA LIMIT
-3.77g's
Vg=96.5
STALL SPEED
Wing Load Factor (g's)
Velocity (mph)
6
5
4
3
2
1
0
-1
-2
-3
-4
-5
-6
0
10
20
30
40
50
60
70
80
90
100

Figure II-8

or as a member of a team, undertaking a one-semester project. Generally, each project involves design, fabrication and testing. A partial listing of project topics selected for the Fall Semester follows:

1. Tapered graphite tubes
2. Graphite-Kevlar hybrid leading edge
3. Variable camber wing section
4. Fire-retarding composite materials
5. Filament winding
6. Shear test procedures
7. Foreign object damage
8. Honeycomb sandwich
9. Aeroelastic box-beam wing

Some of the projects are described in additional detail as follows:

Project 1 will apply fabrication techniques and test data developed in the small-scale project work last year to construct a full-scale, circular cross-section, tapered fuselage boom. This is the type of construction which we anticipate using for the aft portion of the RP-2 fuselage. The boom will consist of 0° and ±45° layers of graphite prepreg for bending and torsion stiffness respectively, the number of layers to be determined from deflection and stress calculations for the boom when it is subjected to the design tail loads. The weight of the boom is expected to be approximately 10 pounds.

Project 2 explores the feasibility of replacing the present balsa wood leading edges by graphite-Kevlar hybrids. Kevlar cloth is laid up between two layers of 0° graphite

prepreg, and curing takes place in a mold incorporating the desired leading edge contour. The result should be a tough, light weight and easy-to-fabricate leading edge.

Project 9 continues work from last year to predict coupled bending and twisting in a box-beam wing. As a result of model construction and tests of such a wing last year, this coupling is now well understood and can be predicted using the classical equations for orthotropic plates or finite element analysis. The next step is to apply the concept to a forward swept wing so as to increase bending-torsion divergence speed to an acceptable level without extensive internal structure and/or added weight.

PART III

COMPAD (Computer Aided Design)

COMPAD (Computer Aided Design)
(M. S. Shephard)

The objective of the computer aided portion of the composites project is to provide computer "tools" for the analysis and design of composite structures. COMPAD's major thrust has been in the finite element area with effort directed toward implementing and improving the efficiency of existing analysis codes at RPI, developing our own inhouse analysis codes and developing interactive computer graphic preprocessing and postprocessing capabilities. The majority of recent effort has been in the development of the interactive computer graphics programs because they represent the type of user interface that is required for effective use of advanced analysis techniques in the design of composites. That is, the importance of making new programs available is secondary to the effective use of those in operation at this time.

The status of the RPI finite element software system is best indicated by the fact that several analysis programs (one inhouse program and several outside programs implemented on the RPI computer systems), an interactive two-dimensional finite element preprocessor and an associated postprocessor exist and are being used more or less routinely.

Several requests have been made to change the acronym of the software system from RPIFEP to something that can be articulated more easily. Therefore, the acronym POFES has been

adopted; this stands for People Oriented Finite Element Software.

Effort during the current reporting period has been concentrated in the following three areas:

1. Implementation of a nodal resequencing algorithm for use in reducing finite element solution times.
2. Development of an interactive graphic two-dimensional postprocessor.
3. Development of an interactive graphic attribute editor for the insertion of material properties, applied loads and boundary conditions to the finite element models generated with the two-dimensional preprocessor.

The first two areas above have been completed to the point that versions of the programs are available for general use, while the last item is in the early stages of development. Further details of the progress made in each of these areas are given in the following sections.

1. Nodal Resequencing Algorithm

Efficient solution of the algebraic equations for a finite element model requires that the equation solver used accounts for the sparse and banded nature of the coefficient matrix. All general purpose finite element codes employ equation solvers that operate on the bandwidth[i],

---

[i] Bandwidth $\triangleq$ the maximum spread in rows or columns of non-zero elements on either side of the main diagonal of the matrix.

wavefront[i] or skyline[ii] of the coefficient matrix. The solution time required for a model is more or less proportional to the square of the bandwidth, wavefront or skyline. The size of these parameters is dependent on the ordering of the unknowns in the coefficient matrix which is, in turn, defined by the ordering of the node or element numbers of the finite element model. For most problems, excepting those with unusually regular geometries, the numbering of nodes or elements that yields maximum solution efficiency is not obvious. Therefore, it is desirable to have an automatic means for ordering the node or element numbers that will minimize solution time.

Several approaches have been taken in the development of reordering algorithms, with those based on graph theory being the most efficient and versatile. The algorithm chosen for implementation in POFES was developed by Gibbs, Poole and Stockmeyer[iii]. The implementation of this algorithm is general, so it can be used to renumber node numbers or element numbers, depending on the finite element code chosen to analyze the problem. This program runs very quickly and has

---

[i] Wavefront = the profile of first non-zero elements, viewing the matrix from left to right and row by row.

[ii] Skyline = the profile of first non-zero elements, viewing the matrix from top to bottom and column by column.

[iii] Gibbs, N. E., W. G. Poole, Jr. and P. K. Stockmeyer, "An Algorithm for Reducing Bandwidth and Profile of a Sparse Matrix", Siam J. on Num. Analysis, Vol. 13, No. 2, April 1977, pp. 236-250.

been found to result in large time savings in all but very small problems.

2. Two-Dimensional Postprocessor

The function of this postprocessor is to make it easier for the user to obtain a graphical representation of the results of a finite element analysis. The basic capabilities of the postprocessor include deformed shapes, contour plots of various stress components and the ability to interactively obtain selected numerical output. In addition, the user has the option to have the results of the problem sent to the line printer.

The postprocessor has been designed to interface with the two-dimensional preprocessor to obtain the basic model definition and to interface with several analysis programs for their output. At the current time the postprocessor is only linked to our inhouse program FEPROQ, but it has been designed so that it can also be interfaced to other analysis programs such as SPAR, SAP-IV and ANSYS.

The way we plan to use the postprocessor is best explained by an example. Consider a bracket of uniform thickness (Figure III-1) fixed at the left end and loaded along the right-hand edges of both the hole and hook. Figure III-2 shows a close-up of the right-hand portion of the bracket with the undeformed mesh in dashed lines and the displaced mesh (with a scale factor of six applied) in solid lines. In addition to displaying the displaced shape in terms of the

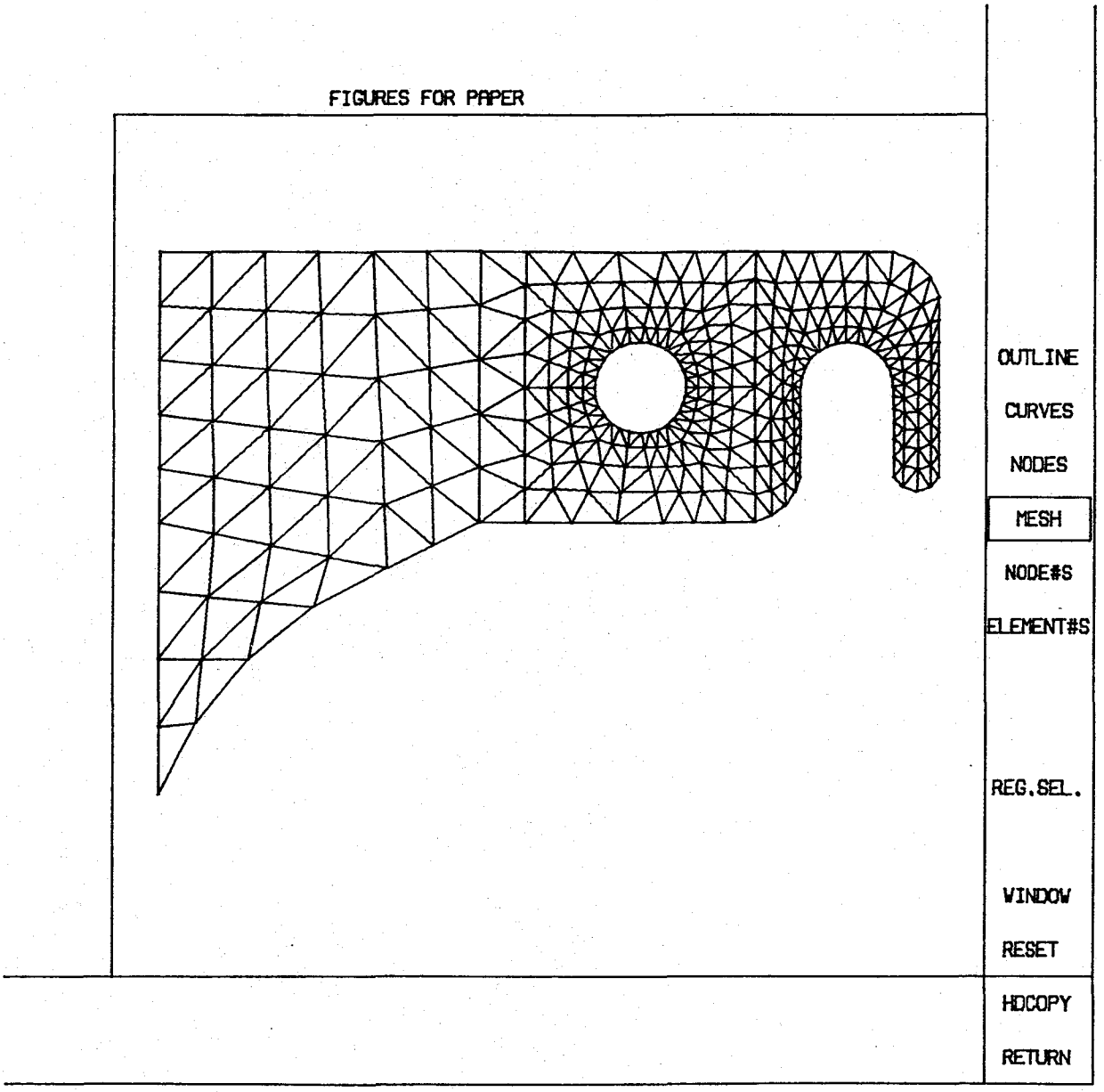

Figure III-1
Bracket Example

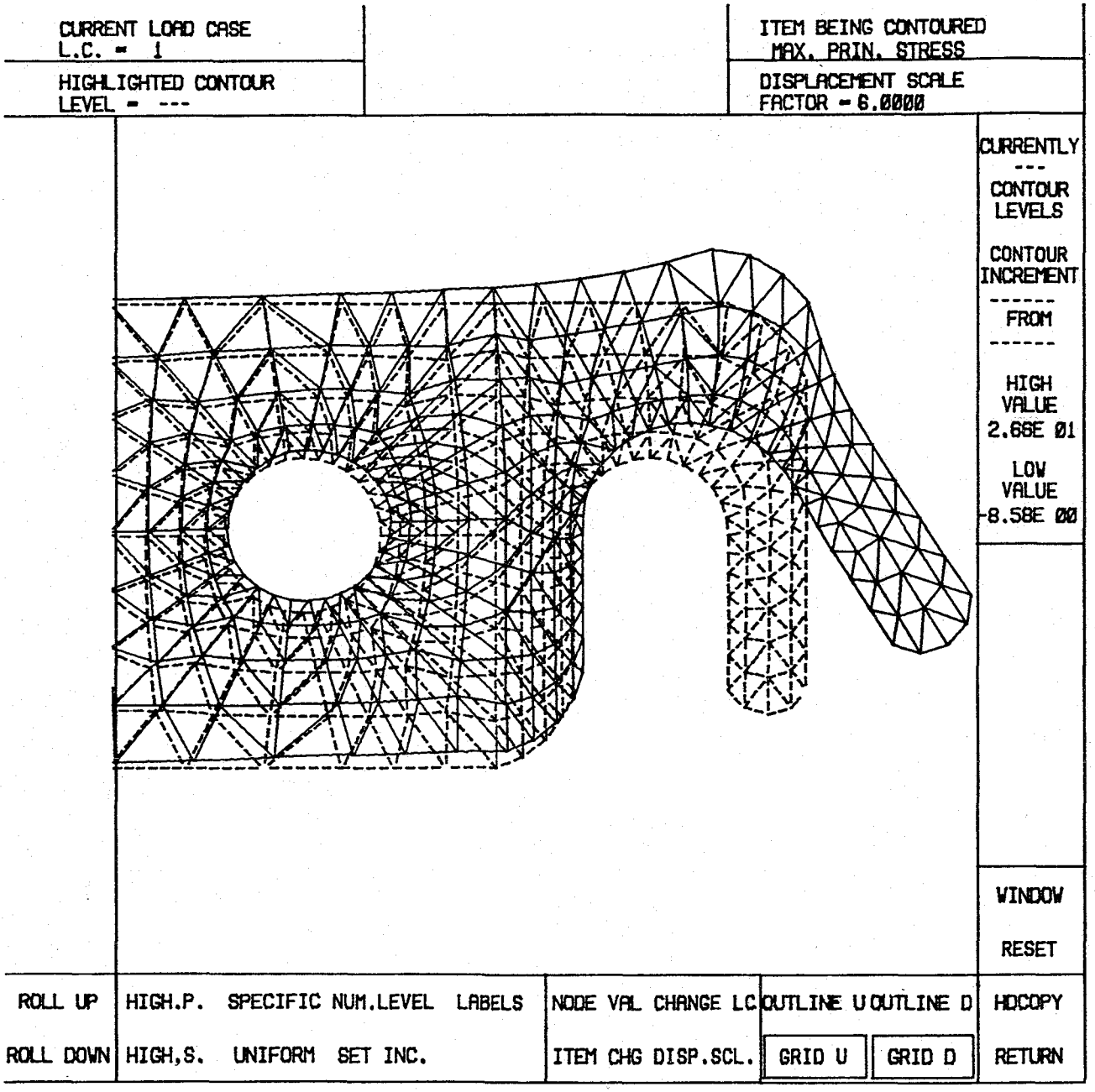

Figure III-2

Deformed Mesh Superimposed on Undeformed Mesh

meshes, the deformed and undeformed outlines of the object can be shown. The user can also interactively change the scale factor applied to the deformed shape.

The numerical values of the displacements and stresses at the node points of the element mesh are also available to the user interactively. Figure III-3 demonstrates the use of this option. This figure shows a close-up of the right-hand portion of the bracket with a deformed mesh superimposed on an undeformed outline. This plot indicates that the maximum displacements occur at the bottom of the hook. Thus the user has interactively selected (by pointing with the light-pen which placed a "box" around it) the node that has the numerical values of displacement and stress which are desired. These values are printed to the far right under the associated node number for that point.

To obtain more information on the stress field throughout an object, the user can view contour plots of the maximum principle stresses (Figure III-4), minimum principle stresses (Figure III-5) and maximum shear stresses (Figure III-6). The user can specify the contour level values in three ways; (1) the specific values of stress levels to be contoured, (2) a number of desired levels (Here the values for that number of equally spaced contours and their locations will be shown.) or (3) a starting value and increments of x and y coordinates and have the other levels determined at each point, incrementing in both directions till the maximum and minimum values of x and y on the body are passed.

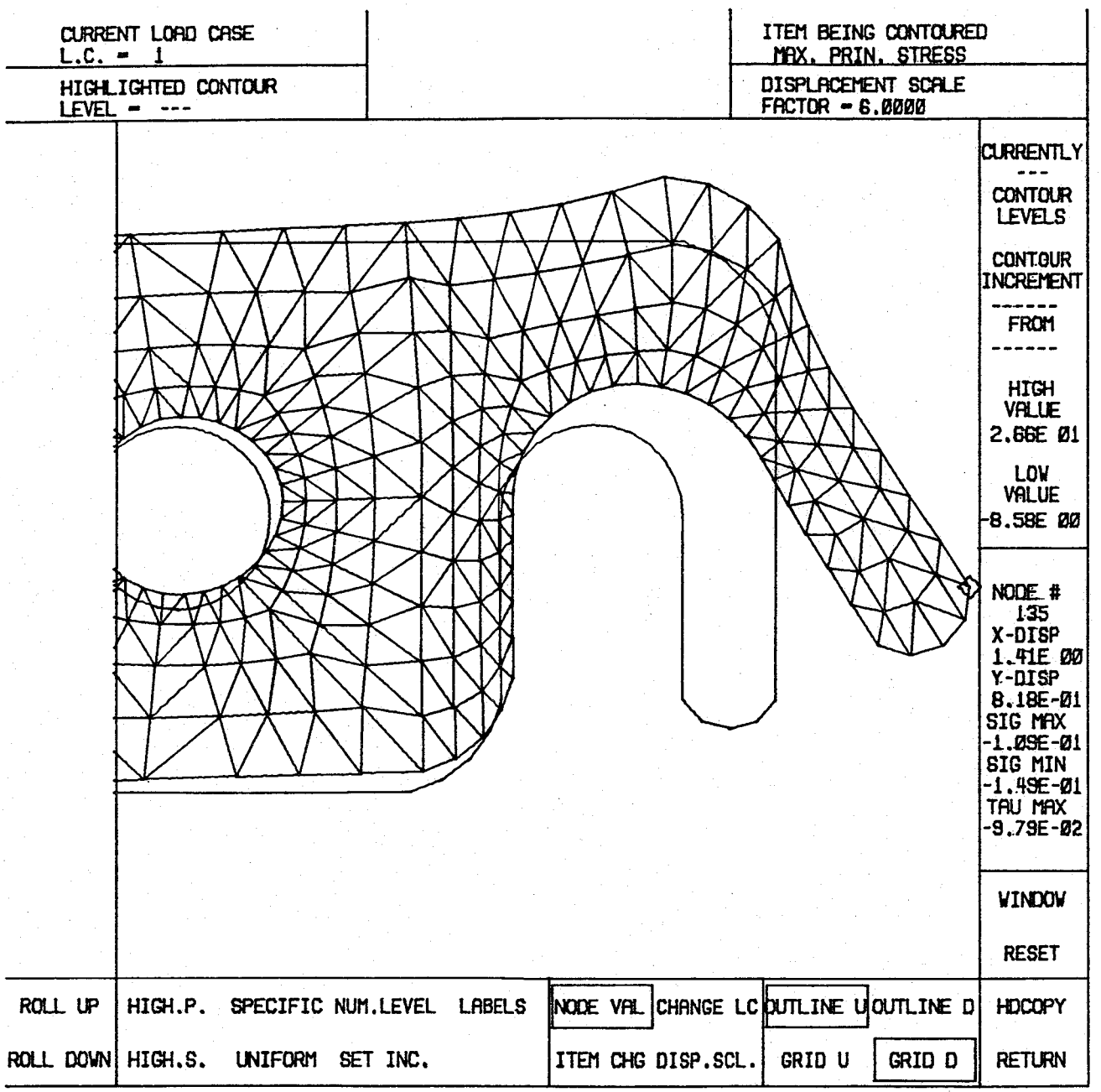

Figure III-3

Obtaining Selective Numerical Output

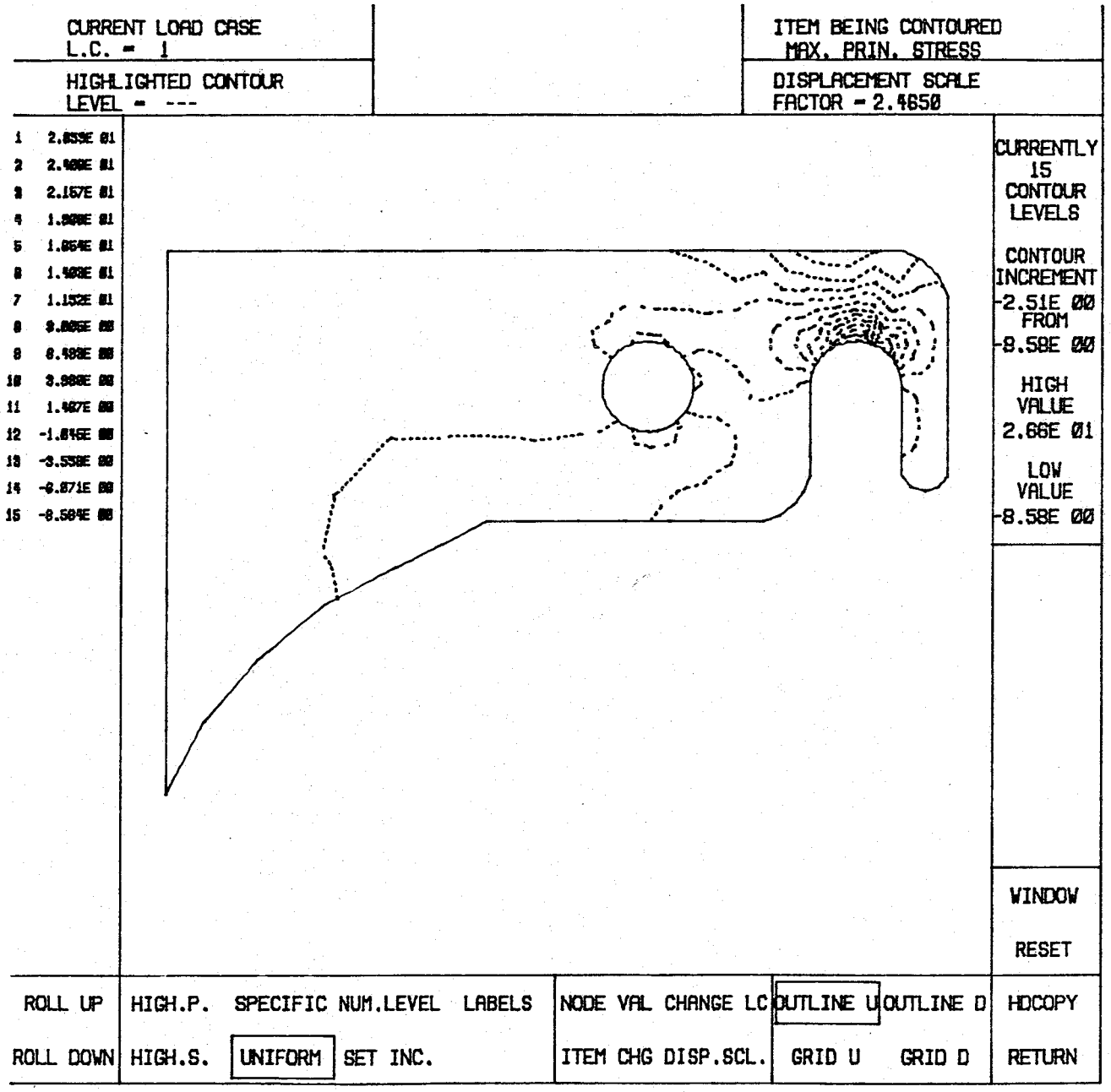

Figure III-4

Maximum Principle Stresses

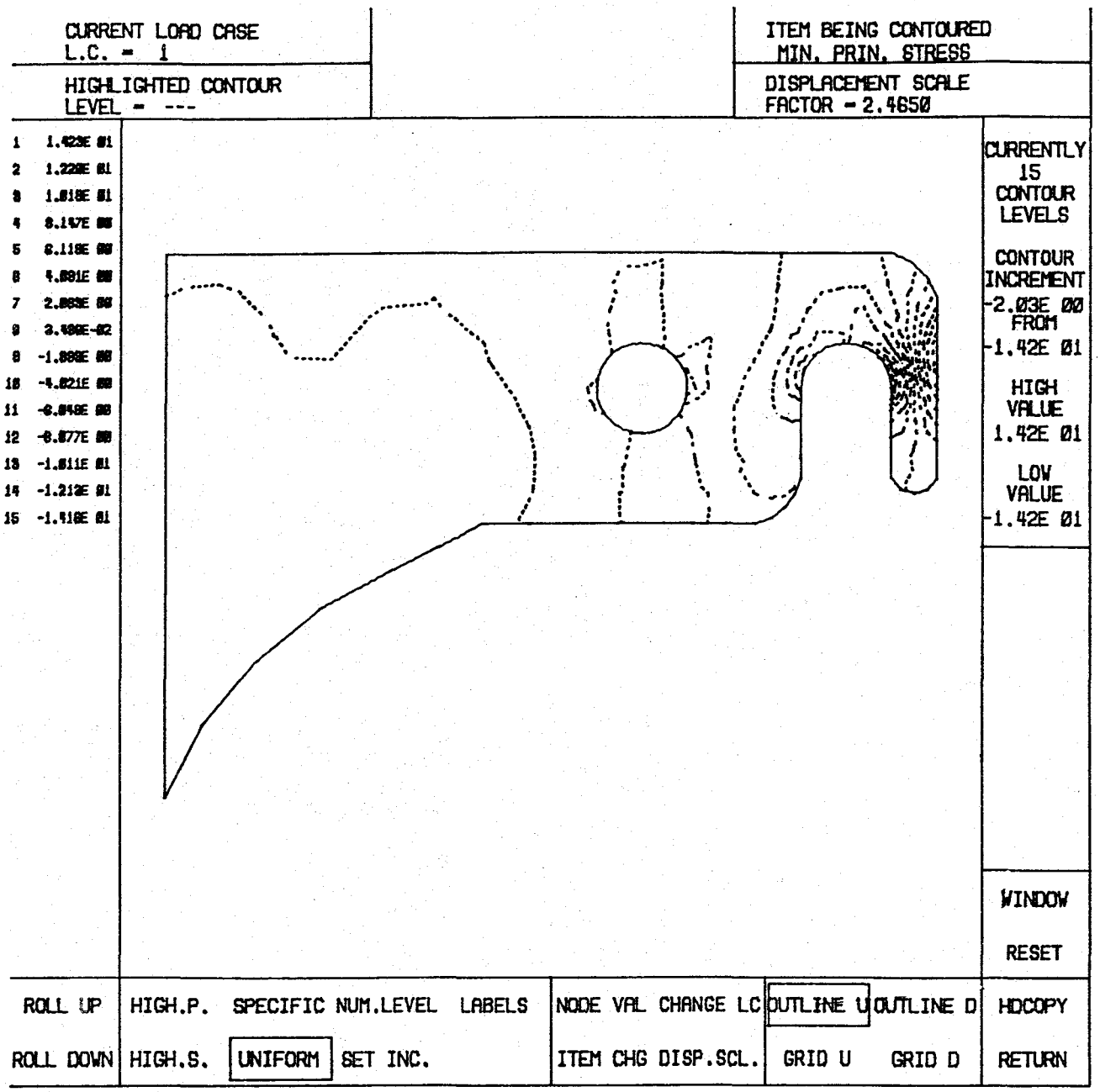

Figure III-5

Minimum Principle Stresses

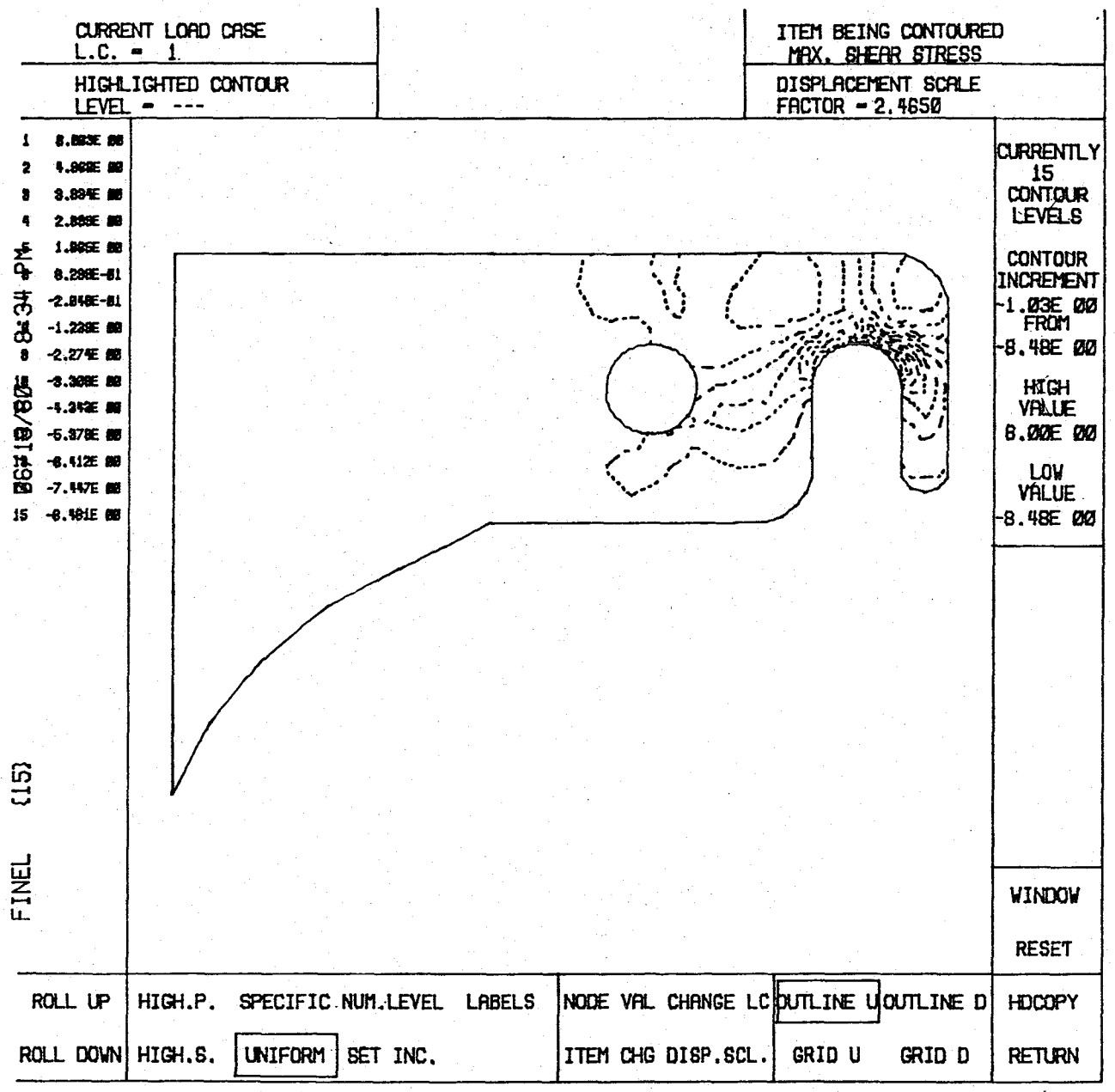

Figure III-6

Maximum Shear Stresses

Although these contour plots indicate the basic trends, they can be enhanced to yield more information. Figure III-7 demonstrates two features available for doing this. The first is the labels that have been placed on the contour levels. The values of the contours are shown in the far left portion of the figure. The second feature is the ability to highlight a contour level by pointing at it. This has been done for contour 11 in Figure III-7.

Details of the means by which contours are obtained may be described as follows:

a) Starting with the set of nodal values describing an element, the element is broken up into a set of triangles. (The three-noded element is represented as a single triangle, the four-noded element is represented as four triangles, the six-noded element is represented by 36 or 64 triangles and the eight-noded element is represented by 64 or 128 triangles.)

b) The values of the stress component being contoured are calculated at each of the triangles' vertices on the element. (The above two operations are efficiently accomplished in the natural coordinate systems used in the finite element representations of the elements.)

c) Positions of portions of the desired contours of the chosen stress are then determined as intersection points of that value with the triangle's edges. The locations of these intersections are based on a linear interpolation of the corner values. Each of the

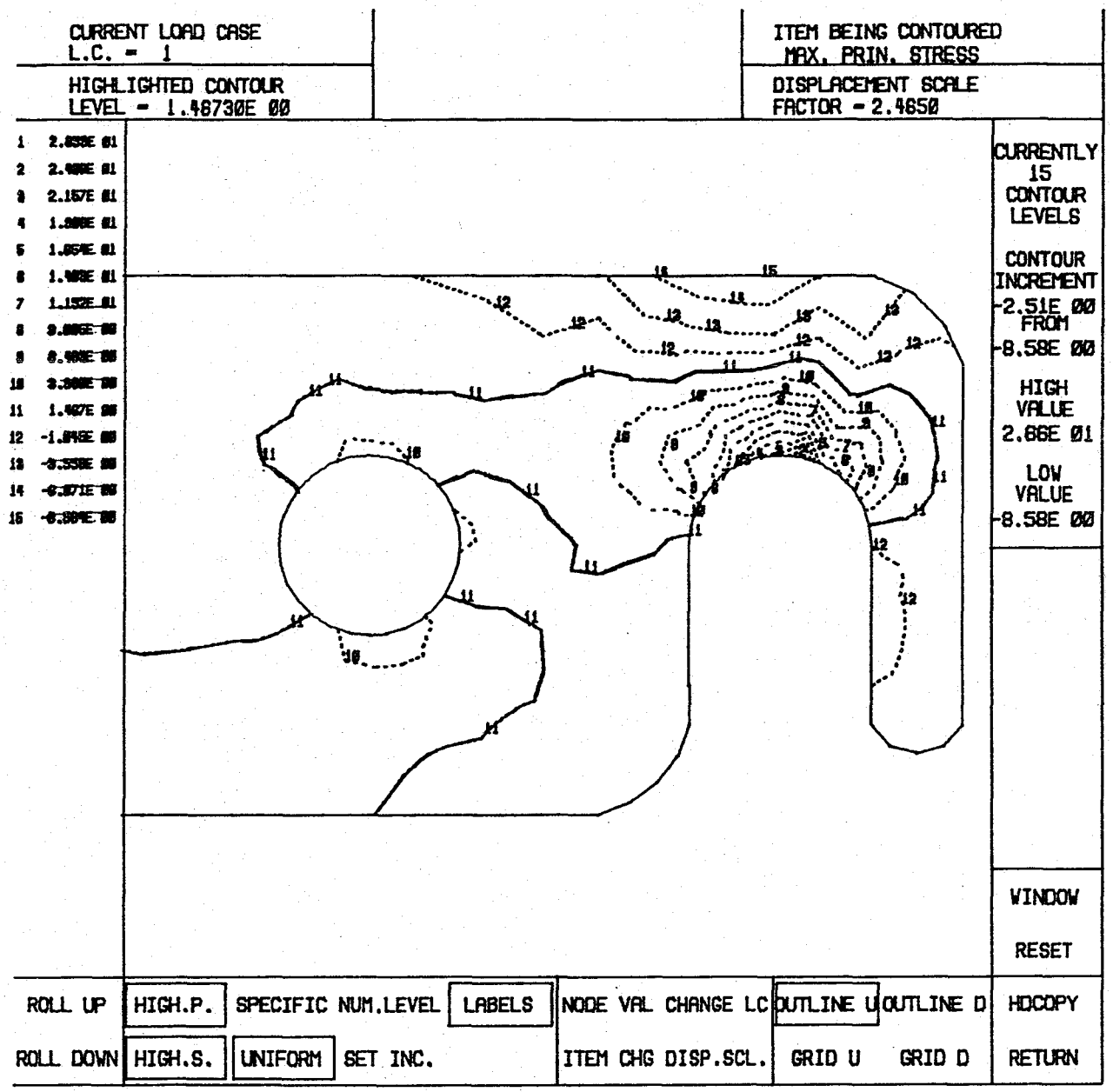

Figure III-7

Close-Up of Contour Plot Showing the Use of Labels and Highlighting

> detected intersections is then properly connected to the intersection of that value on one of the other two edges. Since the three corner values of a triangle uniquely define a plane in terms of the value of stress being contoured, there is no problem determining the proper connections of intersections.

One must exercise caution when determining the values of nodal stresses used by the contouring algorithm. It is well known that the direct evaluation of nodal stresses, by use of stress-displacement matrices, yields very poor stress values. In addition, the element by element evaluation of the nodal stresses will result in discontinuous contours at the element boundaries because the values at the nodes along an edge will be different for the two elements. The second problem can be overcome by a simple averaging of the nodal values for each element sharing a node. This averaging would yield continuous but inaccurate contours, due to the first problem.

It is also well known that the most accurate values of the stresses are obtained by evaluating them at the locations of the numerical integration points. However, the only points that prove convenient for use by a contouring algorithm are the node points. Therefore, a method for obtaining accurate nodal values based on the values at the numerical integration points is needed. There are two satisfactory means of doing this. The first and most accurate is referred to as "global stress smoothing". The computations required

to do this, however, are more extensive than the original finite element analysis and cannot be justified for an interactive program. The second method* is sufficiently accurate but requires far less computation. In this procedure the stresses are first smoothed on the elemental level using a least squares fit, based to a shape function one order less than that used for the displacement field. Averaging is then performed for nodal values using all the elements meeting at that node.

3. Attribute Editor for The Two-Dimensional Preprocessor

The preprocessor discussed in the last two progress reports gives the analyst the ability to define finite element representations for any two-dimensional geometry. However, before a finite element analysis can actually be performed, information about the material properties, loads and boundary conditions must be specified for the object. Since this information is dependent on the class of problem, a seperate program (referred to as an "attribute editor") is required for each class. Effort is currently underway to develope an interactive attribute editor for stress analysis problems.

The operation of the attribute editor is controlled by a main control page (Figure III-8) that indicates the basic

---

*Hinton, E. and J. S. Campbell, "Local and Global Smoothing of Discontinuous Finite Element Functions Using a Least Squares Method", Int. J. Num. Meth. Engng., Vol. 8, 1974, pp. 461-480.

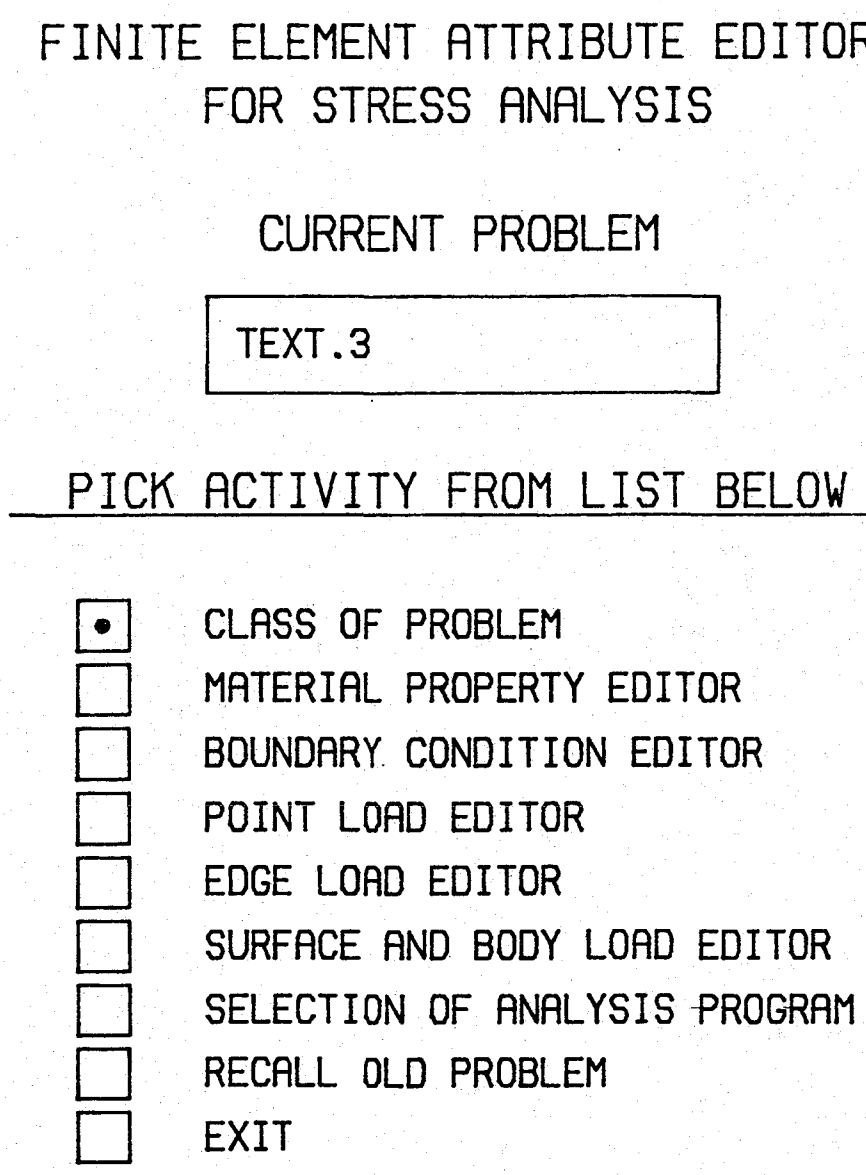

Figure III-8
Attribute Editor Control Page

program modules. Thus far the modules that have been started include the point load, boundary condition and material property editors.

The function of the material property editor is to give the user a means for specifying the material constants associated with the elements of the various subregions. Figure III-9 shows the use of the material property editor in the application of properties to a deep beam made-up of two different isotropic materials. This editor is being designed to allow composite materials' properties to be defined conveniently.

Boundary conditions are specified by means of the menu page shown in Figure III-10. The user can use this menu to interactively fix any of the possible translations or rotations (in bending problems) of the nodes; fixing one node at a time along a portion of an edge curve or in an entire mesh subregion. For the deep-beam example, the user has fixed both translations at the bottom-left corner and the vertical motion of the node next to that. He has also fixed the two nodes on the right edge of the bottom to simulate the beam sitting on bearing pads at either end.

The point load editor operates in much the same manner as the boundary condition editor with the only difference being the specification of the load value. Figure III-11 shows the display given after the application of point loads along a portion of the top of the beam.

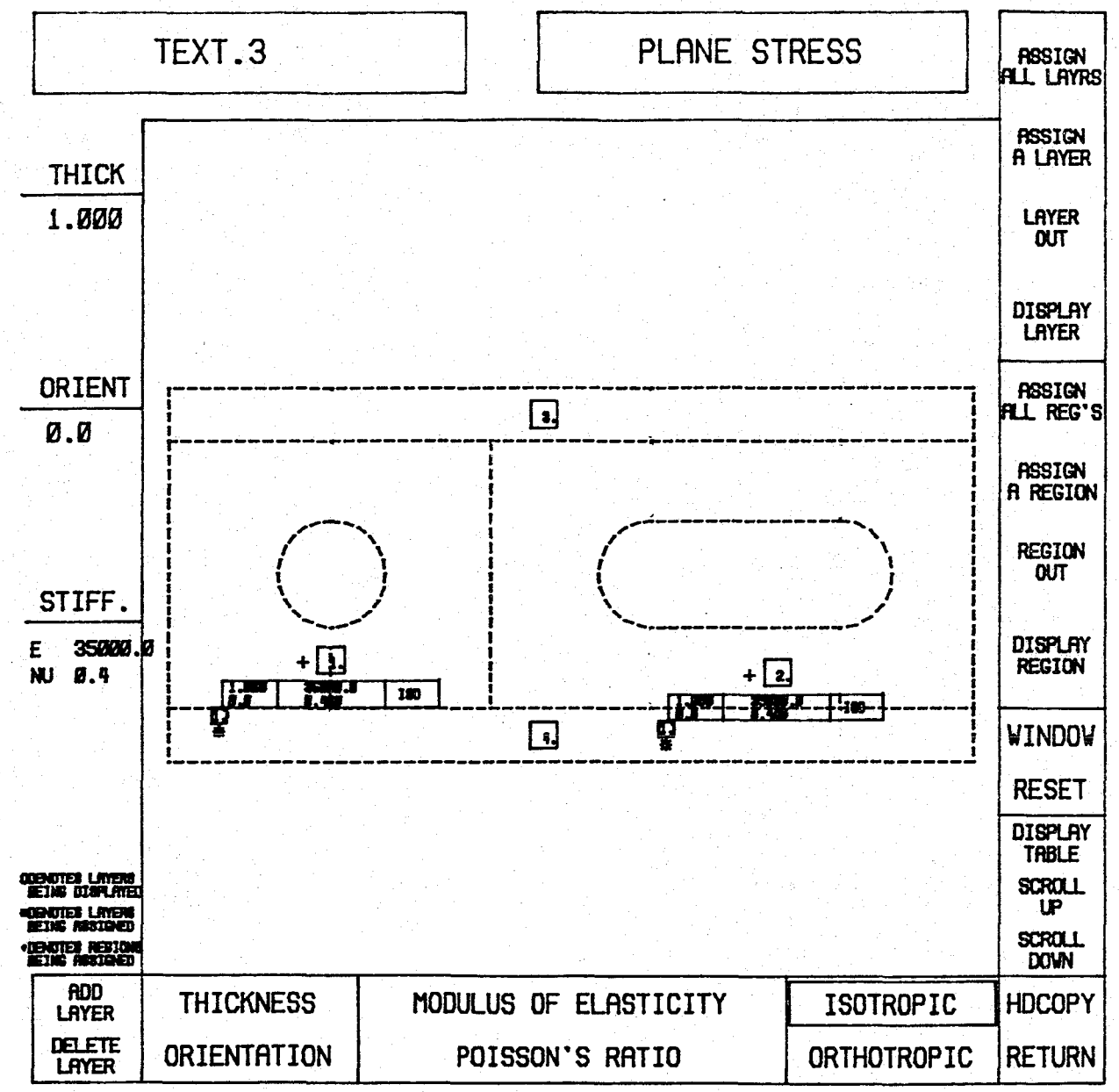

Figure III-9

Application of Material Properties

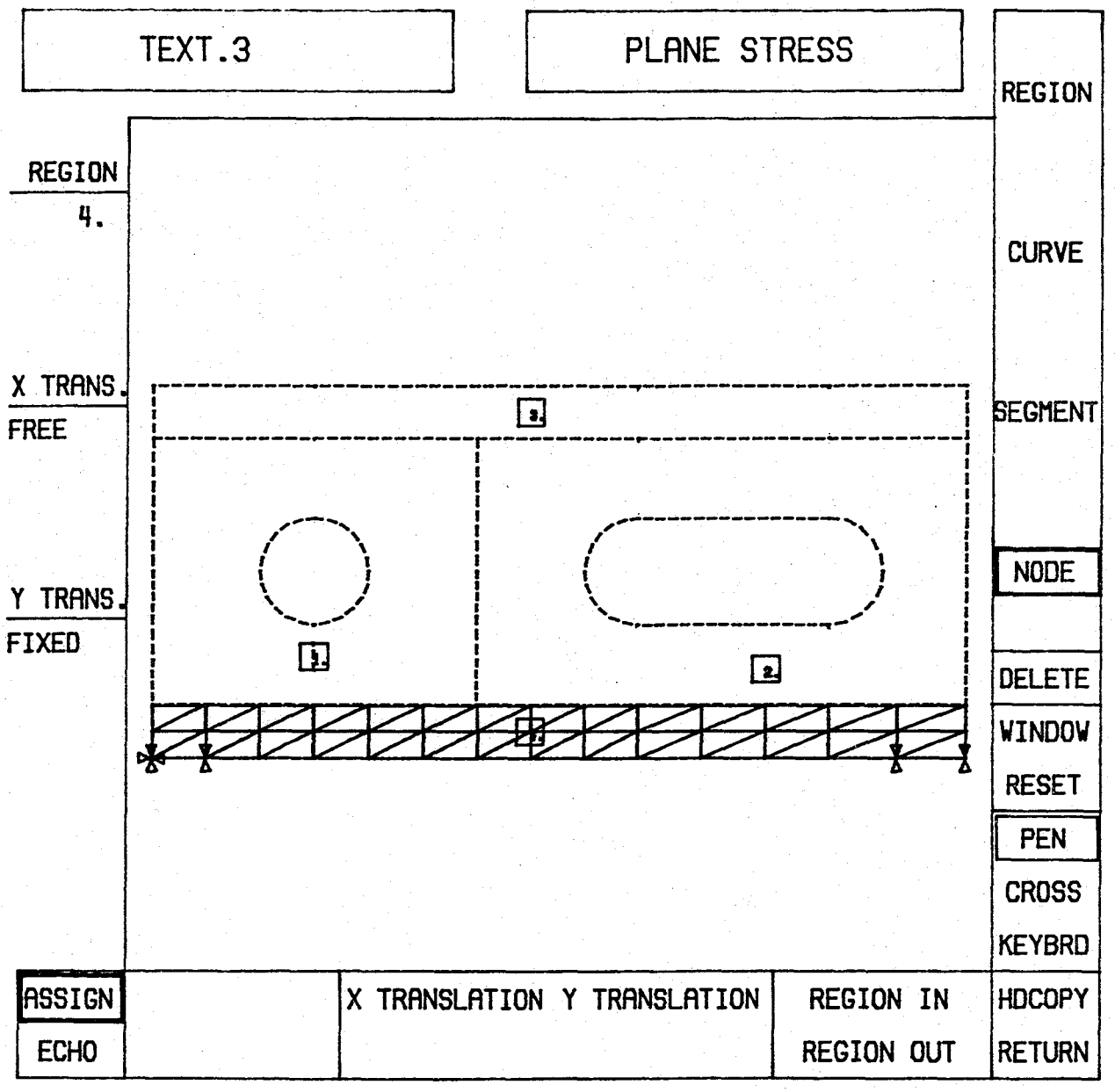

Figure III-10
Application of Boundary Conditions

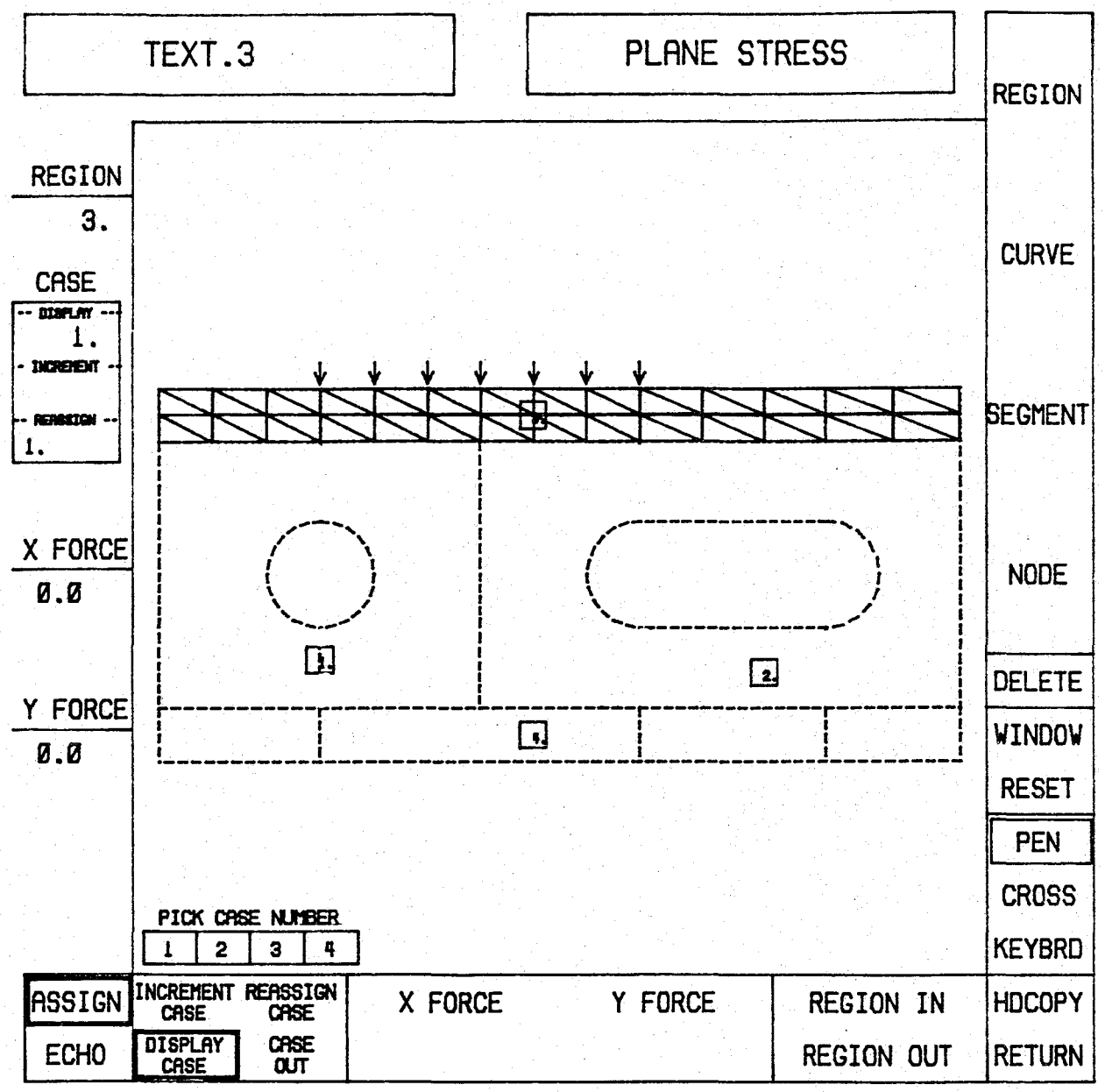

Figure III-11
Application of Boundary Conditions

Plans for the upcomming period call for the major effort to be placed on the stress analysis attribute editor. The portions requiring the most work are the material property editor, edge-load editor and surface-load editor. In addition, a program will be written to link the attribute editor to FEPROQ.

Although the postprocessor in its present form provides a useful capability, some additional features are desirable. One of these features which, however, will require substantial effort is the ability to properly contour stresses in the presence of material interfaces. Work is expected to be done in this area as well as on the attribute editor.

PART IV

INSURE (Innovative and Supporting Research)

A. Advanced Structural Analysis Methods for Composites, E. J. Brunelle.

B. Ultrasonic Non-Destructive Testing of Composite Structures, P. Das and H. F. Tiersten.

C. High Modulus Graphite Fiber Surface Modification for Improved Interaction with Matrices, R. J. Diefendorf.

D. Fatigue in Composite Materials, E. Krempl.

E. Acoustic Emission of Composite Materials Undergoing Fatigue, H. Otsuka and H. A. Scarton.

F. Resin Matrix Dependent Characteristics of Composites, S. S. Sternstein.

IV-A ADVANCED STRUCTURAL ANALYSIS METHODS FOR COMPOSITES

Senior Investigator: E. J. Brunelle

The filamentary composite lamina is the basic building block of almost all composite structures. Metaphorically it contains the genetic code that governs the general behavior of laminate assemblages. The specialized behavior of a particular composite structure (its deformation characteristics, etc.) is determined by its cellular structure (the stacking sequence) and by its phylum (beam, plate, shell, etc.). It is suggested that to completely understand the behavior of various composite structures one must back-track through the path of its creation and first understand the behavior of the individual lamina in as illuminating and as efficient a representation as possible. The correct representation, it is held, comes from two viewpoints, not one. The first viewpoint is that one must clearly understand the behavior of the lamina's constitutive constants under coordinate rotation since reflection and translation yield little useful information. Once this part of the representation is fully understood then one may move to the second viewpoint which holds that if the changes in response of the lamina to the systematic changes of external stimuli are understood (say by a very efficient and concise method of generating solutions to various stimuli) then one may claim to possess a valid representation of the behavior of a single lamina. To these ends, two broad avenues of investigation are being pursued.

1. Status

The major thrusts of the last two reporting periods (previous periods were not devoted to INSURE) were (a) the delineation of the rotational elastic properties of an orthotropic lamina, the key parameter being the nondimensional number $B = \frac{U_2}{4U_3}$, which predicts "regular" or "anomalous" rotational properties depending on whether $B > 1$, or $B < 1$ respectively. Extensions of this work to composite structures and its expected important role in off-design structural conditions was outlined and temporarily set aside to concentrate (b) on finding the most efficient representation of thin orthotropic structures and to find concise solutions for said structures. This work led to the useful concept of multiple affine transformations, several nondimensional numbers (the generalized rigidity $D^* = \frac{D_{12} + 2D_{66}}{\sqrt{D_{11}D_{22}}}$ being the most prominent one for plate structural solutions) and the existence of solution functional dependences for many classes of composite structures problems. The usual form of these dependences was $n^p f\left\{\frac{a_o n}{b_o m}\right\}$ were a_o/b_o is a length ratio in the affinely stretched coordinate system, m and n are positive integers, and p is a plus or minus integer. Finally (c), a systematic effort was undertaken (and is still in progress) to provide generic solutions for a wide variety of problems. The largest body of solutions to date presents elastic buckling coefficients of thin plates for a wide variety of loadings and boundaries;

the only parameter in most of these solutions being D*, which takes values in the range $o \leq D^* \leq 1$.

2. Progress During Report Period

Two more closed form exact solutions have been obtained. The first of these solutions yields buckling coefficients and vibration frequencies of uniaxially loaded simply supported rectangular plates bonded to a core material. The core is modelled as a Winkler Foundation (its inertial effects are not accounted for) thus the frequency expressions are valid only for the low-to-middle range of the usual classical vibration domain; for most practical purposes this will not be a problem. Both solutions come from the homogeneous partial differential equation (in affinely stretched x_o, y_c and t_o coordinates):

$$\frac{\partial^4 w}{\partial x_o^4} + 2D^* \frac{\partial^4 w}{\partial x_o^2 dy_o^2} + \frac{\partial^4 w}{\partial y_o^4} + \frac{P}{\sqrt{D_{11}}} \frac{\partial^2 w}{\partial x_o^2} + kw + \frac{\partial^2 w}{\partial t_o^2} = 0$$

where $\frac{\partial^2}{\partial t_o^2} = ph\frac{\partial^2}{\partial t^2}$ and k is the foundation (core) modulus. Defining a buckling coefficient $k_o = \left(\frac{b}{\pi}\right)^2 \frac{P}{\sqrt{D_{11}D_{22}}}$ and letting $w(x_o, y_o)$ assume the usual multiple half sine wave behavior in both the x_o and y_o direction (the time variable is suppressed) we find that

$$k_o - 2D^* = \left(\frac{mb_o}{a_o}\right)^2 + \left(\frac{a_o}{mb_o}\right)^2 \left[1 + \frac{K}{D_{22}}\left(\frac{b}{\pi}\right)^4\right]$$ and n = 1 with the following detailed information. The minimum $k_o - 2D^*$ values

are given by $(k_o - 2D^*)_{Min.} = 2\sqrt{K^*}$ where $K^* = \left[1 + \frac{k}{D_{22}}\left(\frac{b}{\pi}\right)^4\right] \geq 1$, and the corresponding values of a_o/b_o are given by $(a_o/b_o)_{Min.(k_o - 2D^*)} = \frac{m}{(K^*)^{\frac{1}{4}}}$ where m is the number of half-waves in the x_o direction. Furthermore, the values of a_o/b_o at which the buckling coefficients are equal are given by $(a_o/b_o)_m = m + 1 = \sqrt{\frac{m(m+1)}{\sqrt{K^*}}}$. These results are presented in Figures IV-A-1, -2 and -3. The dominant role of the core as it becomes progressively stiffer is quite evident. When the time variable is not suppressed and we let $w(x_o, y_o, t_o) = A \sin \frac{m\pi x_o}{a_o} \sin \frac{n\pi y_o}{b_o} e^{i\omega^o_{mn} t_o}$ a solution for the non-dimensional frequency $\Omega^2_{mno} = \left(\frac{b}{\pi}\right)^4 \frac{\left(\omega^o_{mn}\right)^2}{D_{22}}$ is found by utilizing the construction $k_o = 2(D^* + \sqrt{K^*})\xi$ where $o \leq \xi \leq 1$ (if only compressive loads are assumed). The result is

$$\left[\left(\Omega^2_{mn_o} + 1 - K^* - n^4\right)/n^4 K^*\right] = \left(\frac{mb_o}{K^{*\frac{1}{4}} n a_o}\right)^4 + 2\left[\frac{D^*}{\sqrt{K^*}} - \left(\frac{D^*}{\sqrt{K^*}} + 1\right)\frac{\xi}{n^2}\right]\left(\frac{mb_o}{K^{*\frac{1}{4}} n a_o}\right)^2$$

Noting that the maximum values of $\frac{D^*}{\sqrt{K^*}}$ and $\frac{\xi}{n^2}$ are unity, the coefficient they describe is very limited, thus the left hand side may be plotted versus $\frac{mb_o}{K^{*\frac{1}{4}} n a_o}$ with the limiting combinations of $\frac{D^*}{\sqrt{K^*}}$ and $\frac{\xi}{n^2}$ = (0, 0), (0, 1), (1, 0), (1, 1).

Some typical results obtained using the developments discussed above are shown in Figures IV-A-4 to -9. It should be reiterated that these graphs represent generic solutions; that

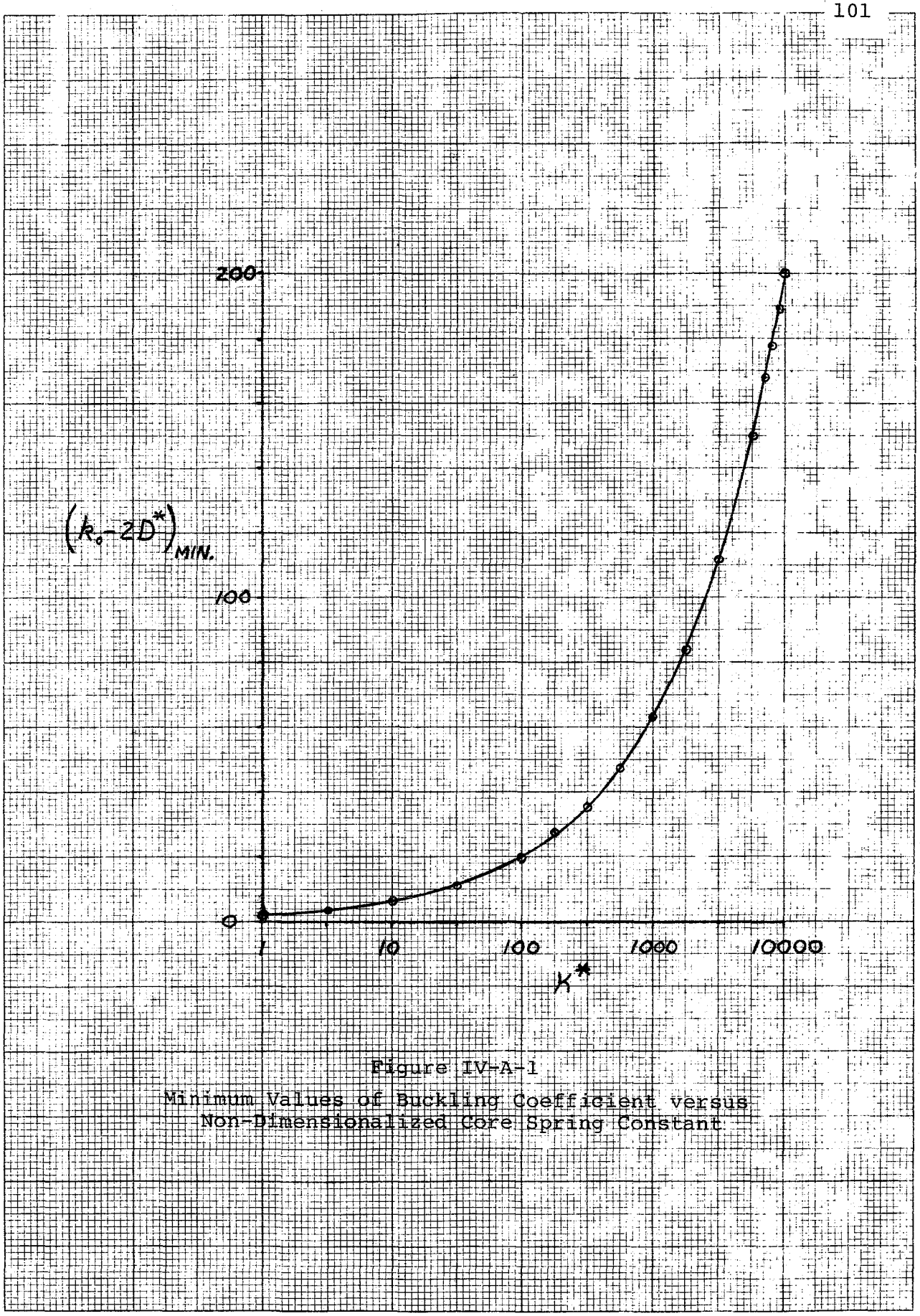

Figure IV-A-1
Minimum Values of Buckling Coefficient versus Non-Dimensionalized Core Spring Constant

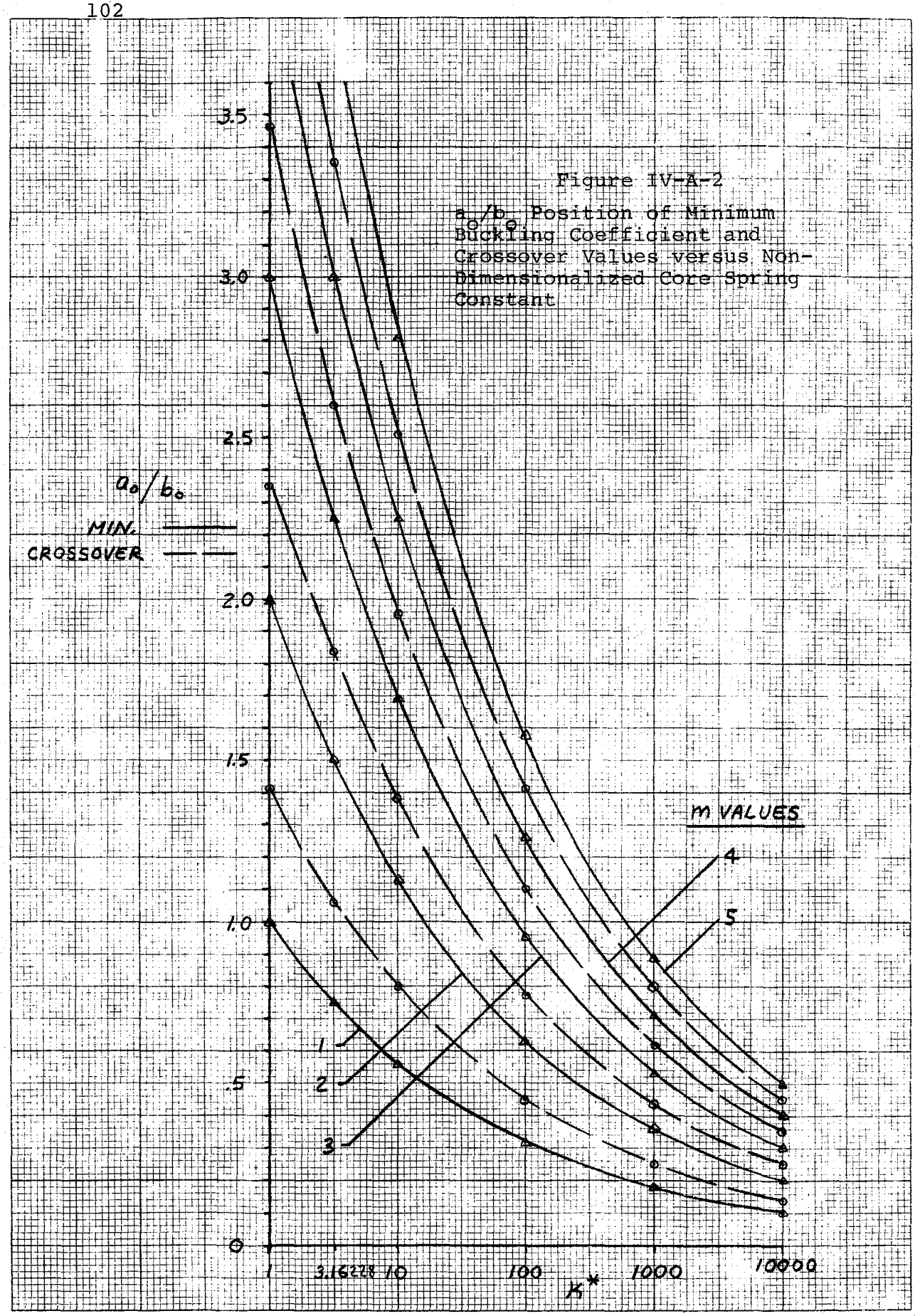

Figure IV-A-2

a_o/b_o Position of Minimum Buckling Coefficient and Crossover Values versus Non-Dimensionalized Core Spring Constant

Figure IV-A-3

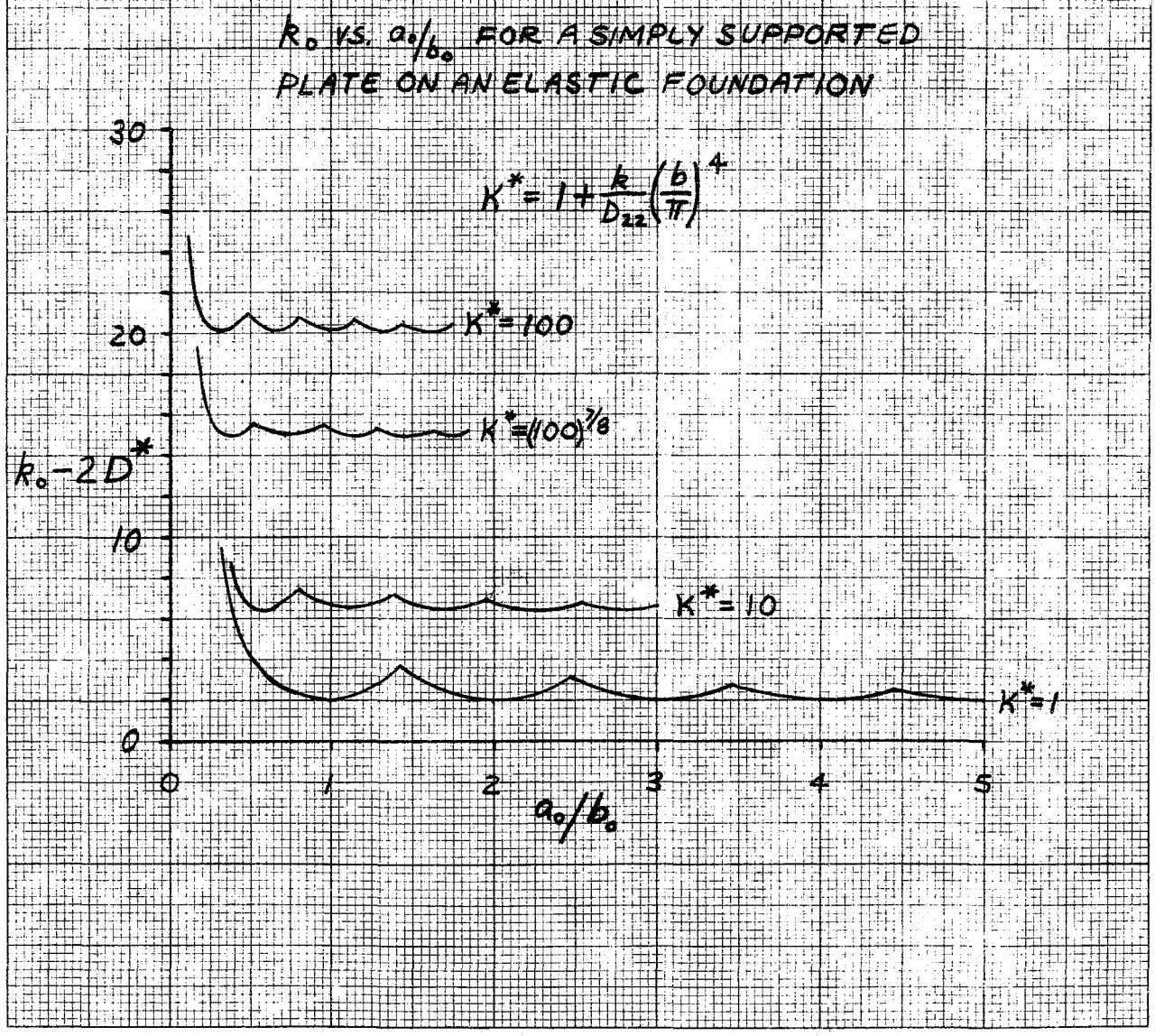
k_o VS. a_o/b_o FOR A SIMPLY SUPPORTED PLATE ON AN ELASTIC FOUNDATION
$K^* = 1 + \frac{k}{D_{22}}\left(\frac{b}{\pi}\right)^4$
30
20
10
0
$k_o - 2D^*$
$K^* = 100$
$K^* = (100)^{7/8}$
$K^* = 10$
$K^* = 1$
0
1
2
3
4
5
a_o/b_o

Figure IV-A-4

Stability Coefficient vs. Aspect Ratio of an Orthotropic Plate Compressed Between Opposite Hinged Edges with the Other Edges Free and Hinged. $\varepsilon = .3$

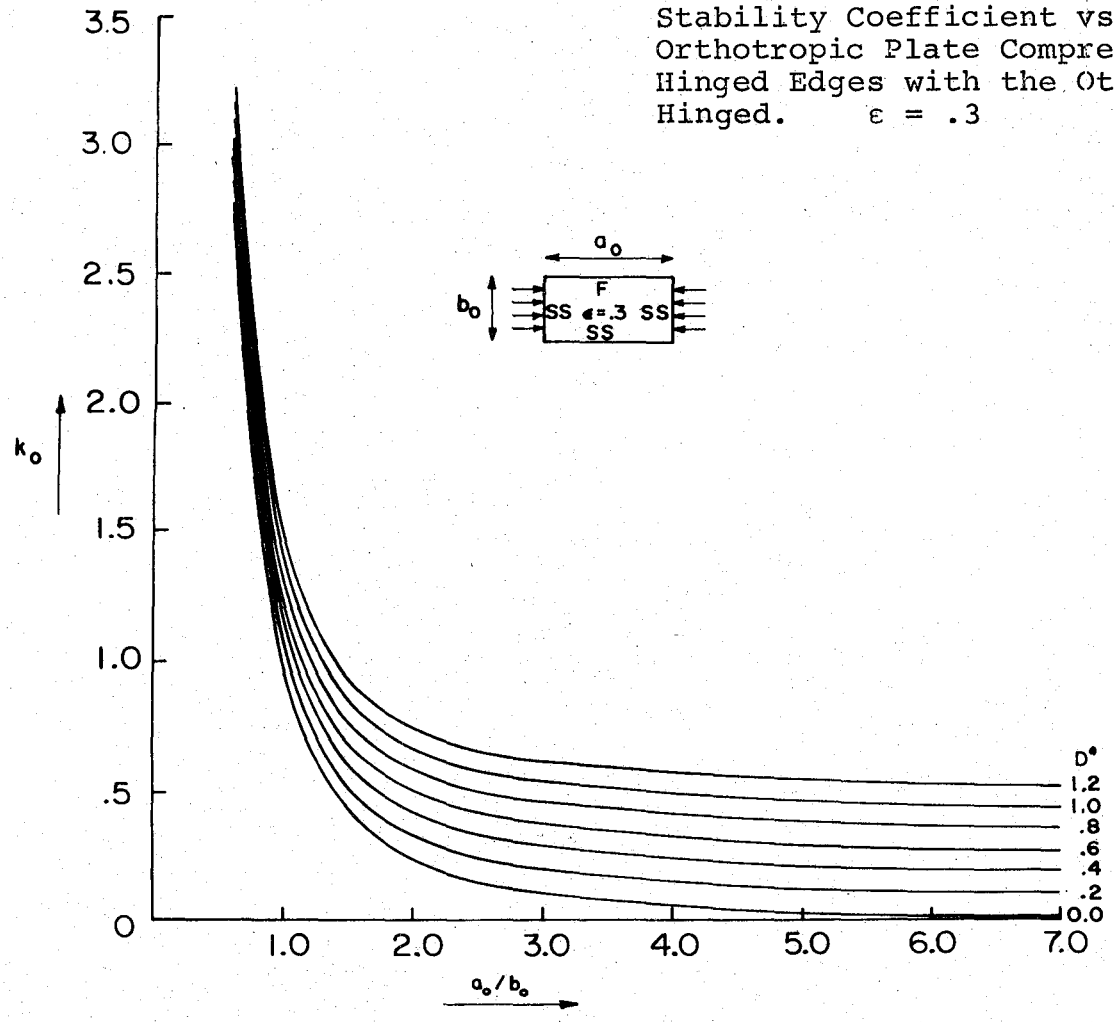

Figure IV-A-5

Stability Coefficient vs. Aspect Ratio of an Orthotropic Plate Compressed Between Opposite Hinged Edges with the Other Edges Clamped

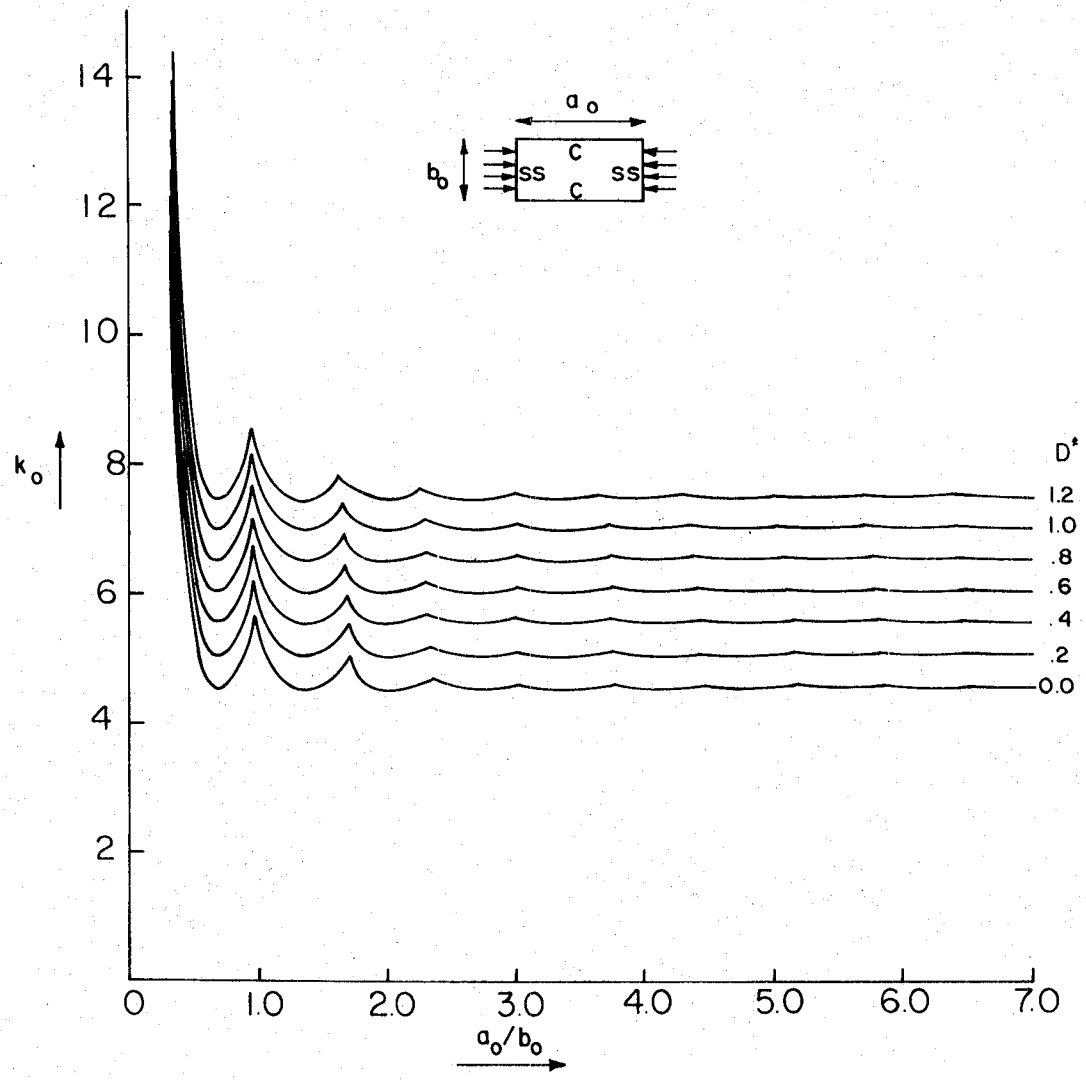

Figure IV-A-6

Stability Coefficient vs. Aspect Ratio of an Orthotropic Plate Clamped on All Edges and Compressed Between One Pair of Opposite Edges

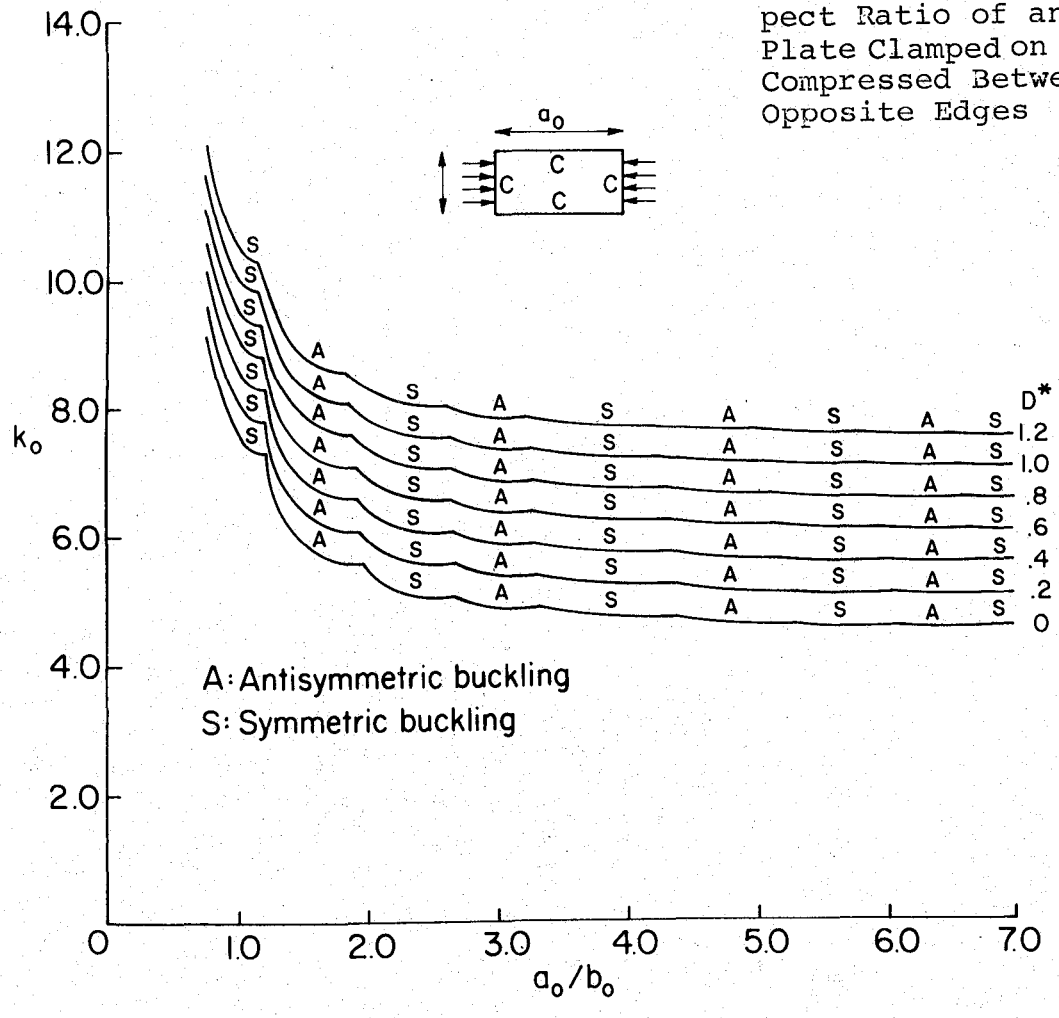

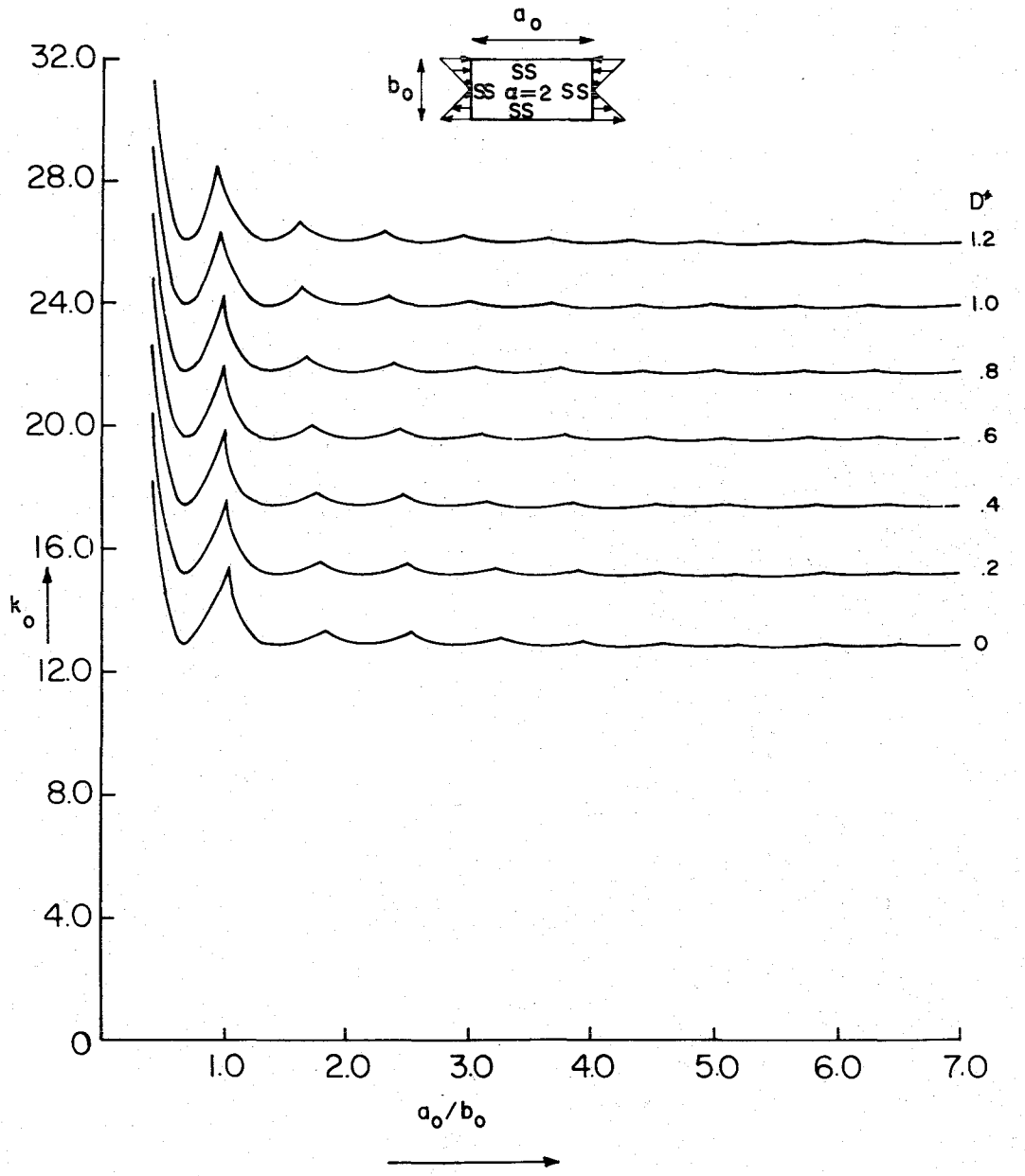

Figure IV-A-7

Stability Coefficient vs. Aspect Ratio of an Orthotropic Plate Hinged on All Edges with Pure Bending on a Pair of Opposite Edges

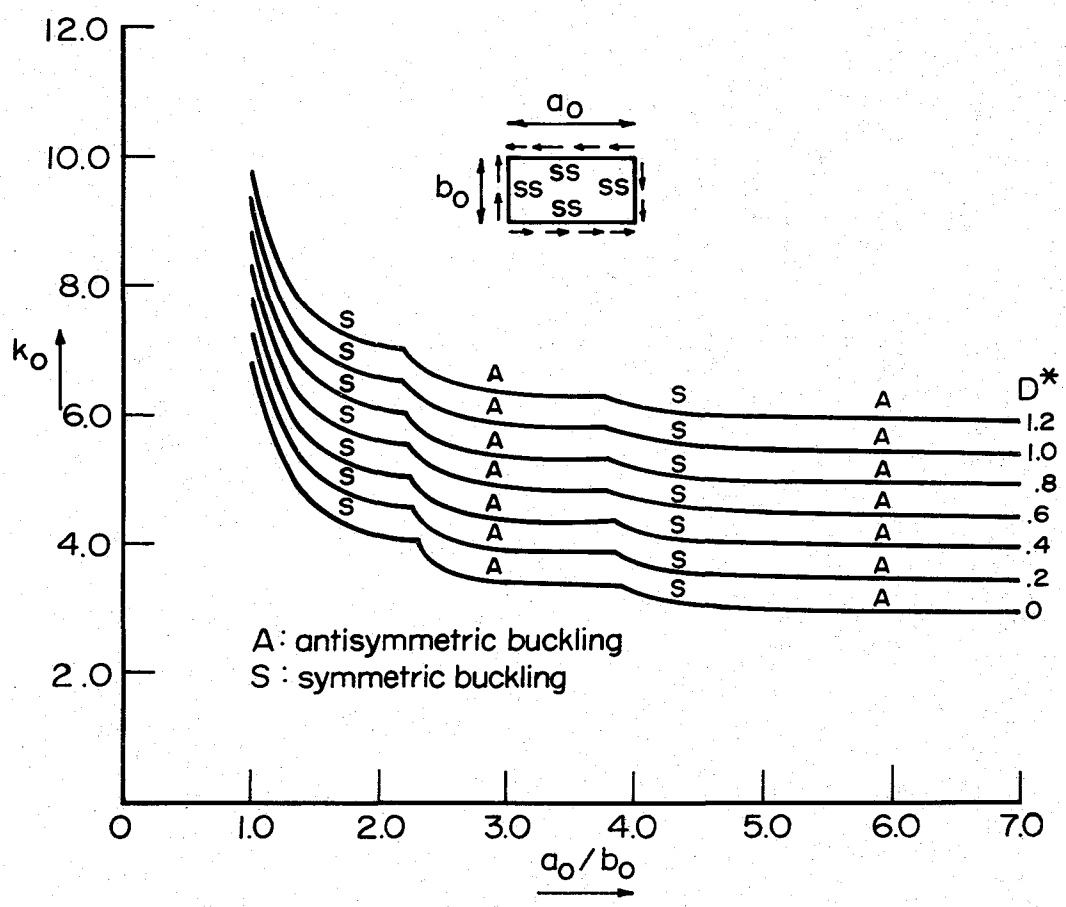

Figure IV-A-8

Stability Coefficient vs. Aspect Ratio of an Orthotropic Plate Hinged on All Edges with In-Plane Shear Forces on the Edges

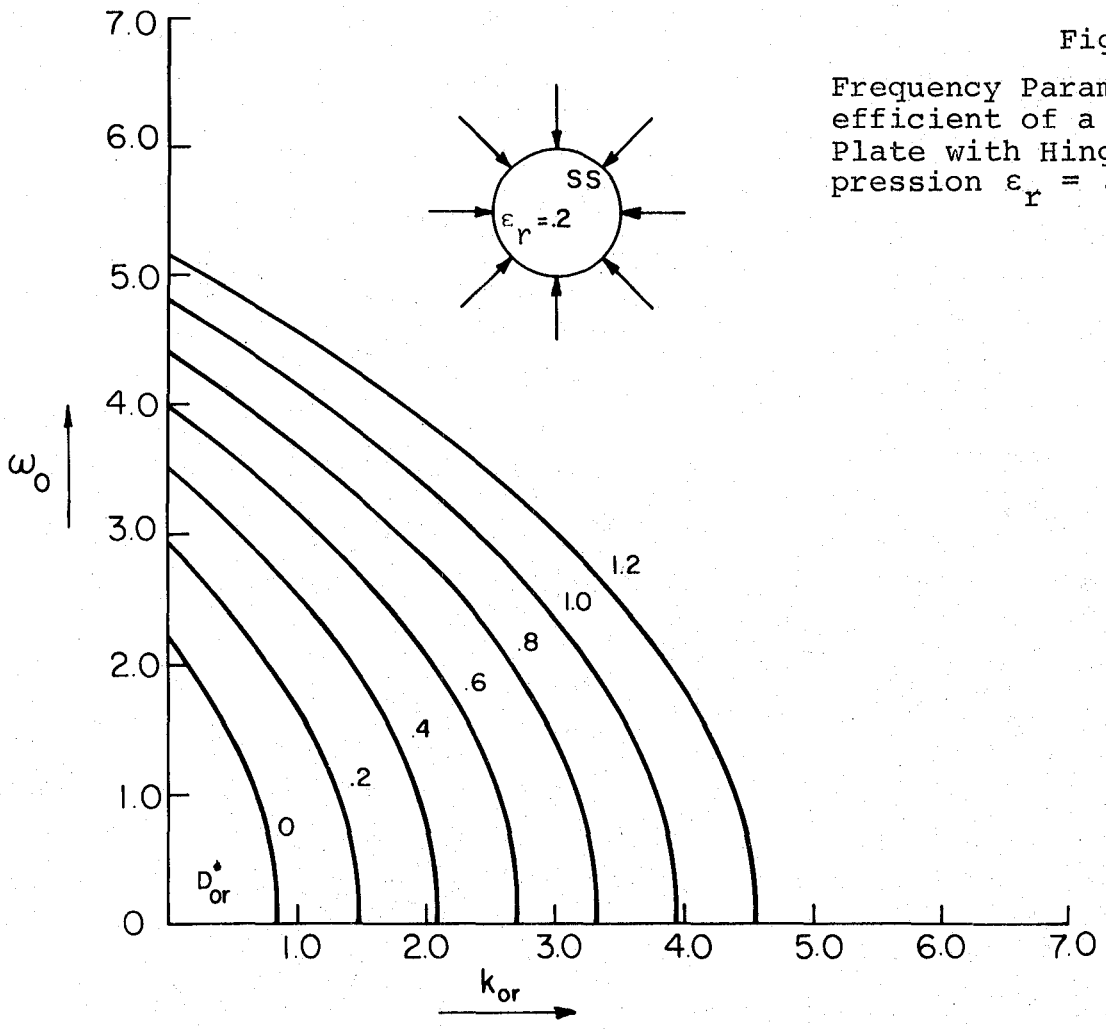

Figure IV-A-9

Frequency Parameter vs. Stability Coefficient of a Circular Orthotropic Plate with Hinged Edge Under Compression $\varepsilon_r = .2$

is, they are valid for any material and any dimension ratios for the specified rectangular or circular geometry in affinely stretched coordinates. During the process of checking these results with the existing particular solutions in the literature it was realized that by proper manipulation these existing particular solutions can be converted into generic solutions, thus greatly extending the usefulness of existing solutions (and eliminating the need to duplicate the corresponding generic results). For example Hearmon[1]* presents an energy solution for the center deflection u of a clamped plate under a uniform distributed load q as:

$$\frac{q}{292u} = \left(\frac{D_{11}}{a^4} + \frac{D_{22}}{b^4} + \frac{4}{7} \frac{(D_{12} + 2D_{66})}{a^2 b^2} \right)$$

A little algebra produces the generic result,

$$\frac{(a_o b_o)^2 q}{292u} - \frac{4}{7} D^* = \left(\frac{a_o}{b_o} \right)^2 + \left(\frac{b_o}{a_o} \right)^2$$

which is just a single curve in the variable a_o/b_o. Note now much more useful the second form is than the first form.

The second exact solution obtained in this period yields moisture diffusion results for a specially orthotropic slab. These results have been derived for the $x_3 = o,c$ faces at different equilibrium moisture concentrations at $t = o$ and at $t \to \infty$; i.e., the upper face goes from a moisture concentration Γ_u^o at time zero to Γ_u^∞ at steady state ($t \to \infty$). In a

---

*Bracketed numbers in this text refer to references on page 115

like fashion, the lower face goes from a moisture concentration Γ_{ℓ}° at time zero to Γ_{ℓ}^{∞} at steady state ($t \to \infty$). This allows the more typical condition of gases of different moisture concentrations to exist on each side of the slab and yields the essential case of a liquid/moist gas condition for treating submersible structures. It is easily shown that the one-dimensional and the three-dimensional solutions are related by multiplicative factors; long-time and short-time solutions are easily constructed, and an integration over the slab volume yields the total moisture content $G(t_o)$ as a function of non-dimensional time t_o. As is well known, the short-time (three-dimensional) solution for G(t) is linear in the square root of elapsed time [see, for example (2)]. In the variable t_o one has the counterpart relation $G(t_o) = m\sqrt{t_o}$ for short-times. The slope $m = \frac{4}{\sqrt{\pi}}\left[1 + \frac{c_o}{a_o}\left(1 + \frac{a_o}{b_o}\right)\right]$ is linear in both the thickness ratio $\frac{c_o}{a_o}$ and the aspect ratio a_o/b_o, where a_o, b_o and c_o are the slab dimensions in the affine space x_o, y_o, z_o and $t_o = t/c_o^2$ (see Figure IV-A-10). The affine transformations used in the moisture diffusion problem being $x_i = \sqrt{K_i}\chi_i$ where K_i are the moisture diffusion coefficients and the slab dimensions in real and affinely transformed space are related by:

$$a_o = a/\sqrt{K_1}\ , \qquad b_o = b/\sqrt{K_2} \qquad \text{and } c_o = c/\sqrt{K_3}.$$

Some brief solution details are given. Firstly, the equation governing moisture concentration Γ is given by $K_i \frac{\partial^2 \Gamma}{\partial \chi_i^2} = \frac{\partial \Gamma}{\partial t}$

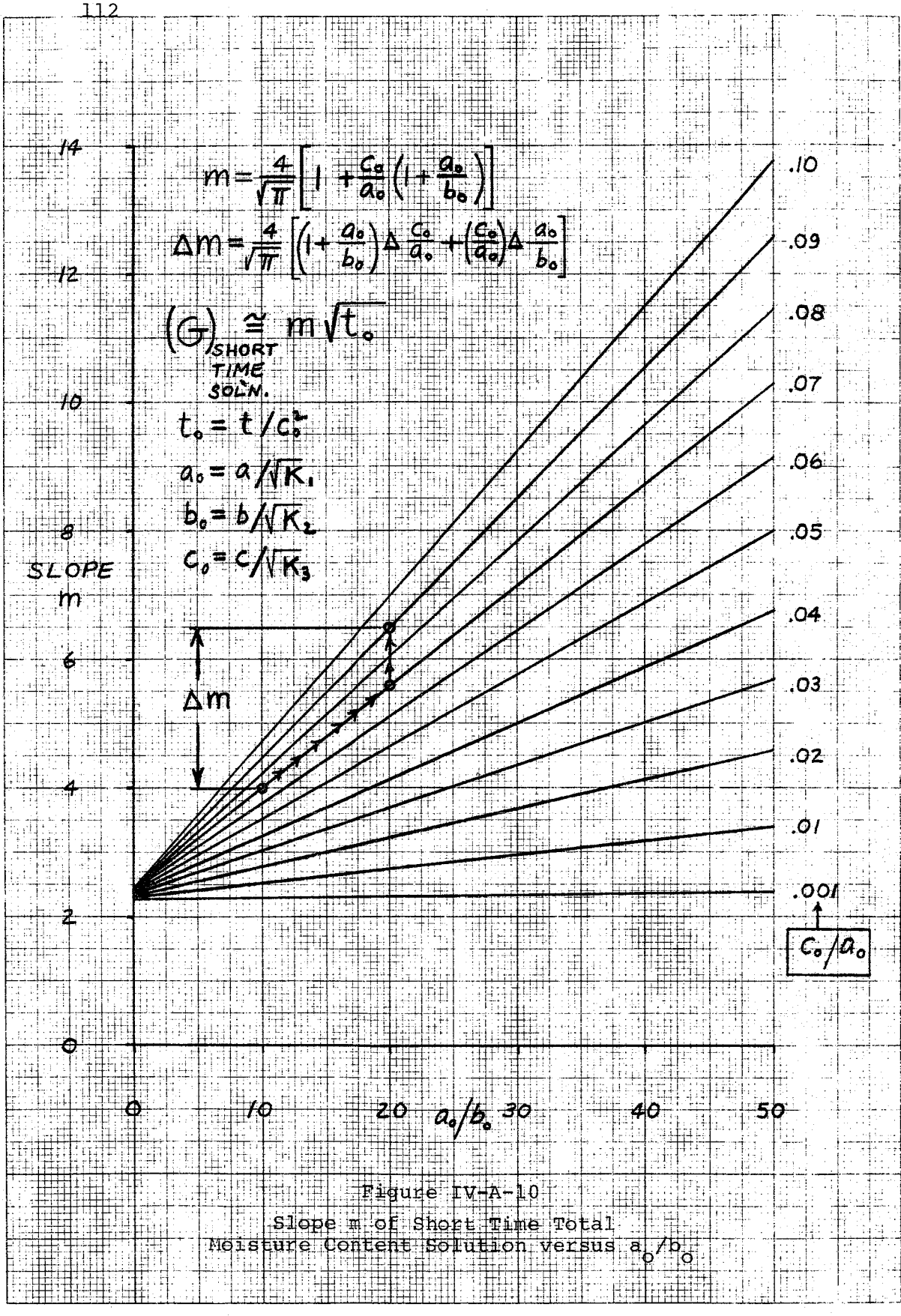

Figure IV-A-10
Slope m of Short Time Total Moisture Content Solution versus a_o/b_o

which is affinely transformed into χ_i space to yield,

$\frac{\partial^2 \Gamma}{\partial \chi_i \partial \chi_i} = \frac{\partial \Gamma}{\partial t}$ (t will be transformed to a suitable t_o later).

A solution is formed from the steady state solution as $t \to \infty$ and a transient solution. Thus, $\Gamma(\chi_i,t) = \Gamma_\infty(\chi_3) + \Gamma^T(\chi_i,t)$. From previous comments it is realized that $\Gamma_\infty = (\Gamma_u^\infty - \Gamma_\ell^\infty)\frac{\chi_3}{c_o} + \Gamma_\ell^\infty$, and one forms a separable representation of Γ^T as $\Gamma^T = \Gamma_1(\chi_1)\Gamma_2(\chi_2)\Gamma_3(\chi_3)T(t)$, where the value of Γ^T on all six faces must be zero at all times, and as $t \to \infty$, $\Gamma^T \to o$ throughout the entire space. When $t = o$, $\Gamma_o(\chi_3) = \Gamma_\infty(\chi_3) + \Gamma^T(\chi_i,o)$, where $\Gamma_o = (\Gamma_u^o - \Gamma_\ell^o)\frac{\chi_3}{c_o} + \Gamma_\ell^o$. Insuring these requirements leads to the desired result.

$$\Gamma(\chi_1, \chi_2, \chi_3, t_o) = \Gamma_\ell^\infty + (\Gamma_u^\infty - \Gamma_\ell^\infty)\frac{\chi_3}{c_o} +$$

$$+ \left(\frac{4}{\pi}\right)^3 \sum_{m=1}^{\infty} \sum_{n=1}^{\infty} \sum_{s=1}^{\infty} \frac{g - (-1)^s f}{(2m-1)(2n-1)(2s)} \sin(2m-1)\pi\frac{\chi_1}{a_o} \sin(2n-1)\pi\frac{\chi_2}{b_o} \sin s\pi\frac{\chi_3}{c_o} \cdot$$

$$\cdot \exp(-1)\left[\left(\frac{c_o}{a_o}\right)^2\left[(2m-1)^2 + (2n-1)^2\left(\frac{a_o}{b_o}\right)^2\right] + s^2\right]\pi^2 t_o$$

where $t_o = t/c_o^2$, $f = \Gamma_u^o - \Gamma_u^\infty$ and $g = \Gamma_\ell^o - \Gamma_\ell^\infty$.

An integration over the slab volume yields the total moisture content $G(t_o) = \int_V \Gamma(\chi_i, t_o)dV$, from whence the short time solution can be deduced. Also a one-dimensional solution for $G(t_o)$ can easily be deduced from the three-dimensional result. It is

$$\frac{G(t_o) - \frac{1}{2}(\Gamma_u^o + \Gamma_\ell^o)}{\frac{1}{2}\left[(\Gamma_u^\infty + \Gamma_\ell^\infty) - (\Gamma_u^o + \Gamma_\ell^o)\right]} = 1 - \frac{8}{\pi^2} \sum_{s=1}^{\infty} \frac{e - (2s-1)^2\pi^2 t_o}{(2s-1)^2}$$

3. Plans for the Upcoming Period

Two items appear to be logical areas for investigation. The first is to continue solving problems of importance which possess specially orthotropic constitutive relations. The second is the difficult one of trying to find the most efficient representation of solutions for problems with generally orthotropic constitutive relations. One remembers that a specially orthotropic plate has only four elastic constants whereas the generally orthotropic plate has six elastic constants and has its behavior complicated by the twist-coupling associated with D_{16} and D_{26}. The best generalization that one would dare hope for is that only one new "cluster constant" will appear, thus making generic solutions depend only on this new "cluster constant" and D*. From past R.P.I. research, however, one has an excellent idea of how solutions vary with D*. Therefore, it should be possible to concentrate on the solution variations with respect to just the (one) new cluster constant. If this speculation proves to be valid, then one should be able to predict directly the generic effects of changing individual plies upon the solution of a symmetric composite plate. This would appear to be a significant step forward in understanding the behavior of a large class of composite structures. In the upcoming period, this objective will be emphasized.

4. References

1) Hearmon, R. F. S., "An Introduction to Applied Anisotropic Elasticity", Oxford Press, 1961, p. 124.

2) Whitney, J. M., "Three-Dimensional Moisture Diffusion in Laminated Composites", AIAA J., Vol. 15, No. 9, September 1977, pp. 1356-1358.

5. Current Presentations by E. J. Brunelle on this Subject

1) "The Use of a Double Affine Transformation to Obtain a Class of Generalized Elastodynamic Solutions for Orthotropic Plates"

   Presented at the SIAM 1980 National Meeting, June 5-7, 1980, Ramada Inn - Old Town, Alexandria, VA.

2) "The Use of Affine Transformations in the Solution of Composite Structures Problems"

   To be presented at the 17th Annual Meeting of the Society of Engineering Science, Inc., December 15-17, 1980, Georgia Institute of Technology, Atlanta, Georgia.

IV-B ULTRASONIC NON-DESTRUCTIVE TESTING OF COMPOSITE STRUCTURES

Senior Investigators: H. F. Tiersten
P. Das

Ultrasonic waves are being expolited both in research and, increasingly, in routine non-destructive testing as a promising means of discovering and assessing manufacturing flaws and load-induced damage in composites. Our efforts in ultrasonic NDE are three-fold: improving image quality through data processing and display techniques, transducer development and material flaw image identification.

1. Status

Improvements in ultrasonic image quality have been obtained through use of a) a high resolution display monitor and b) color-coding of the intensity data. Both experimental and theoretical progress has been made in improving trapped energy mode mosaic ultrasonic transducers, including Fresnel lens types. Support of other project activity, using ultrasonic NDE is being provided on a service basis. Examples to date include delamination patterns around holes in bearing test specimens.

2. Progress During Report Period

To obtain high quality color-coded images, the raw stored data is now being routinely transferred to the Image Processing Laboratory which has a DEANZA image processor with

a PRIME host computer. The transferred data is being stored in the PRIME file system. For display or processing, the data is then transferred to the image refresh memory. The color coding of the data can now be achieved through a programmable intensity transformation table. The image is displayed in color on a high resolution monitor with zoom and scroll capability.

A series of ultrasound scans have been performed as a "blind test", i.e., a test in which the expected results of the scans were not known to the experimenter. The graphite composite samples were prepared and supplied by Professor S. Sternstein of the Materials Department at R.P.I., and this report presents the results which were obtained.

Six samples were used in the test. Each sample was a circular disk about 4.3 cm in diameter and .18 cm thick, with a mass of 2.5 gm (Figure IV-B-1). Since the samples appeared to be identical to the unaided eye, they were each identified by a code written on with a grease pencil. The codes were 1A, 1B, 2A, 2B, 3A and 3B. Also, an arrow was drawn on each disk to show the proper orientation for the scan. Although the meaning of these codes was not revealed until after the test results had been presented, they will be explained here for clarity.

The letter part of the code describes the physical construction of the sample while the number describes the degree of damage caused by stressing the sample. This is shown in Table IV-B-1. The samples were stressed prior to ultrasonic

inspection by supporting them around their circumference with a circular jig and applying a force directed perpendicular to the surface at the center of the disk. For ultrasonic testing, each of the samples was mounted in a plastic clamp that held the edge of the disk without stressing the sample. Figures IV-B-2 to 7 show the displays of the images resulting from ultrasonic scanning and image processing.

The degree of damage to each sample is readily apparent from the displays. Samples 1A, 1B, 2A and 2B show no damage. Samples 3A and 3B very clearly show a well-defined region of damage in the center of the disk, with the shape of the damaged area dependent on the construction of the disk. Also, 3A shows alternating bands of green and red, indicating some form of damage along the fiber lines. The failure mechanism that caused this has not yet been determined. In addition, the sensitivity of the ultrasound system is such that on many of the displays it is possible to see the code that was written on the sample.

The color coding scheme used shows heavily damaged areas in blue, while areas of lesser or no damage are shown in red and green, respectively. The coloring was chosen by examining a computer generated histogram of the image. The histogram shows the distribution of intensities in the image, and the coloring was adjusted to bring out as much detail as possible.

3. Plans for the Upcoming Period

In the next period we anticipate further development of our signal processing techniques, perhaps to include deconvolution. Transducer advances will include application of higher frequency ultrasound, from 5 to 15 MHz, for better resolution and further development of phased array transducers.

4. Current Publications or Presentations by Professors Das and/or Tiersten on this Subject

1. Das, P., S. Talley, R. Kraft, H. F. Tiersten and J. F. McDonald, "Ultrasonic Imaging Using Trapped Energy Mode Fresnel Lens Transducers, Acoustical Imaging, Vol. 9, Edited by Keith Y. Wang, Plenum Publishing Corp., 227 West 17th Street, New York, N. Y. 10011, 1980.

2. Webster, R. T., P. Das and R. Werner, "Ultrasonic Imaging for Nondestructive Evaluation of Composite Material with Digital Image Enhancement", to be presented at the 1980 Ultrasonic Symposium, Boston, MA, November 5-7, 1980.

TABLE IV-B-1

CODE FOR IDENTIFICATION OF "BLIND TEST SAMPLES"

Code	Construction
A	0-90 degree fiber lay-up
B	0-45 degree fiber lay-up
Code	**Damage**
1	no damage, unstressed
2	stressed, but not to failure
3	stressed to first failure

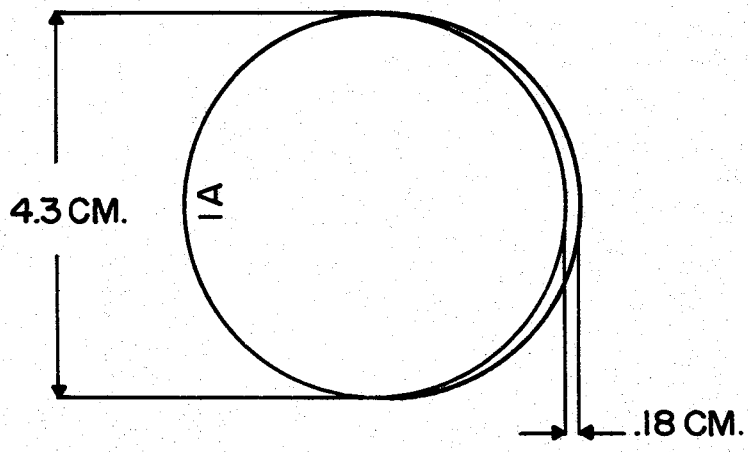

Fig IV B-1
SKETCH OF SAMPLE

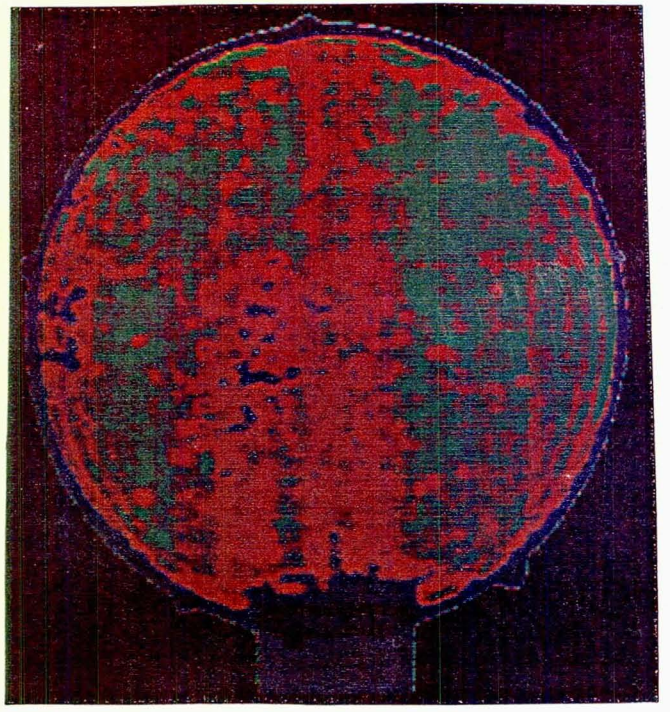

Figure IV B-2: Code 1A

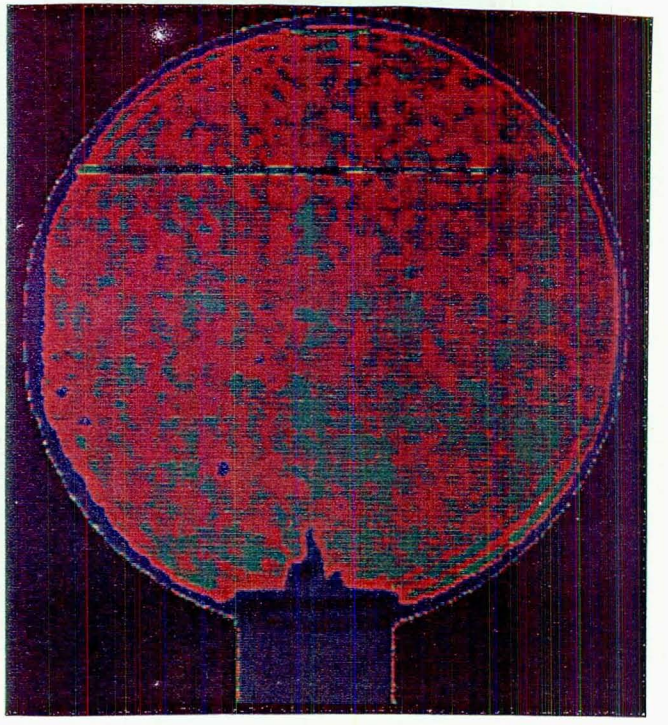

Figure IV B-3: Code 1B

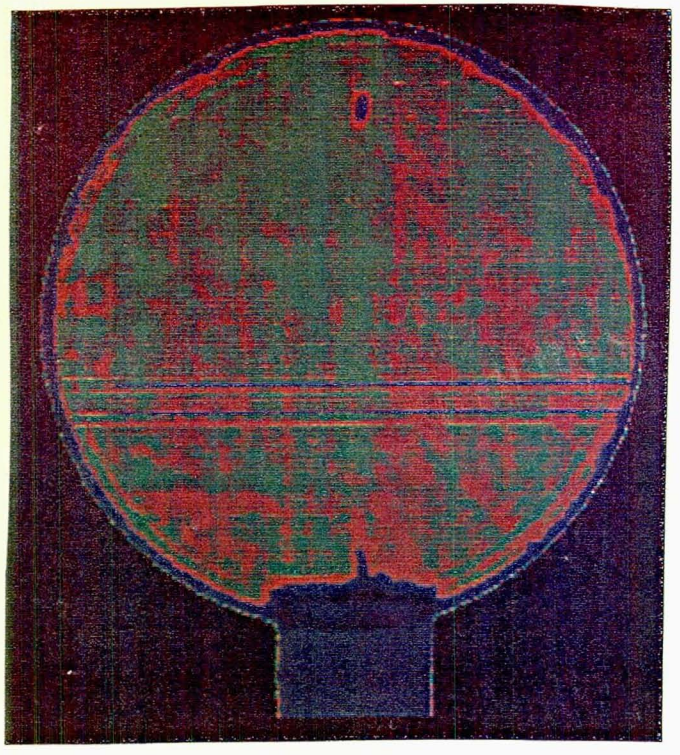

Figure IV B-4: Code 2A

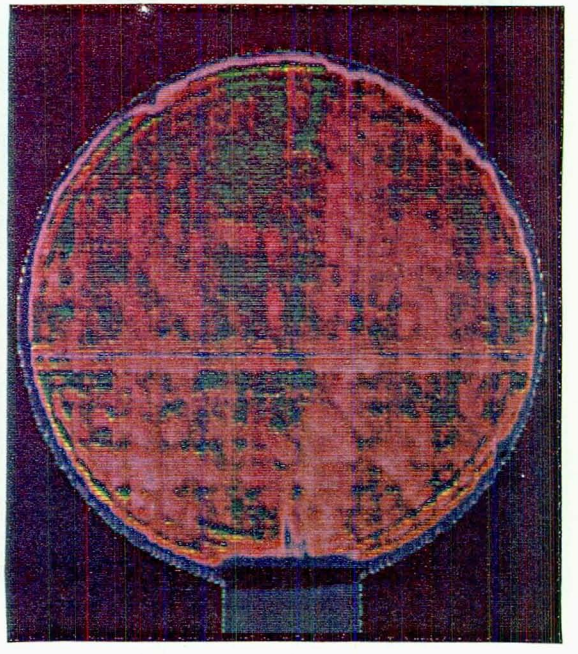

Figure IV B-5: Code 2B

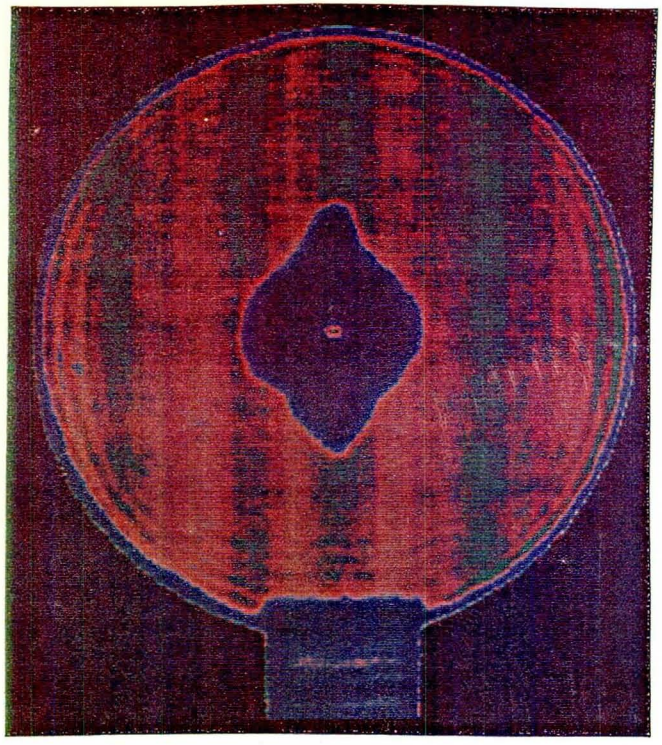

Figure IV B-6: Code 3A

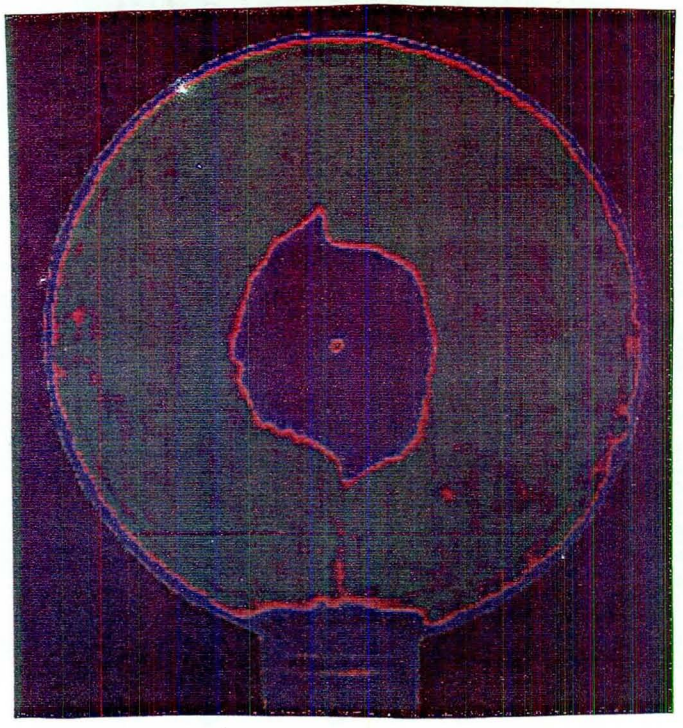

Figure IV B-7: Code 3B

IV-C HIGH MODULUS GRAPHITE FIBER SURFACE MODIFICATION FOR IMPROVED INTERACTION WITH MATRICES

Senior Investigator: R. J. Diefendorf

The mechanical properties of composite materials are strongly influenced by the strength and behavior of the interfacial region between the matrix and the fiber. Not only does the interfacial region determine whether an initiated crack will cause delamination or fiber breakage, it also will determine if a broken fiber will continue to reinforce.

1. Status

Goan[1]* and coworkers measured the short beam shear strength (SBSS) of composites using various high modulus graphite fibers and showed that the SBSS decreases with increasing fiber modulus. Moreover, for composites containing unsurface-treated fibers with moduli greater than 400 GPa, the SBSS drops to an unacceptably low value of about 15 MPa. This very low value of SBSS for a high modulus composite limits the application of these fibers in components where high shear loading may be present. While it can be argued that use of high modulus fibers may lead to composites with inherently lower SBSS, the high value of 125 MPa observed in boron fiber composites is direct evidence to the contrary.

---

*Numbers in parentheses in this section refer to the references listed on pages 154 and 155

Herrick[2] observed that etching the surface of high modulus carbon fibers resulted in composites with a remarkable increase in SBSS. However, the trend of decreasing SBSS with increasing fiber modulus remained. Although the absolute magnitude of SBSS increased, unfortunately the tensile strength often decreased by as much as thirty percent. In Herrick's other related work,[3] he concluded that surface functionality of the fiber was more important than the surface area in determining the SBSS of the resulting composite. More recent work on rayon precursor carbon fibers by Scola and Brooks[4] is in direct conflict with those of Herrick et al.

The purpose of this study is to elucidate the molecular nature and surface energetics of graphite fiber surfaces. This will be done so that the phenomena occurring at the matrix-fiber interfacial region may be characterized, and knowledge of these phenomena may be applied to improve composite materials.

2. Progress During Report Period

In this report the essential parameter used to study the surface energetics of graphite fibers was the wetting by various liquids. Wetting was evaluated by measuring the contact angle of various liquids in contact with the fibers. The immediate difficulty with this method is inherent with the fiber surface; that is

a) it is difficult to measure with reasonable accuracy the diameter [6 - 14μ] or perimeter of fibers, considering the fact that the cross-sectional area is not always circular. Also the cylindrical surface area per unit length varies from fiber to fiber.

b) The roughness and smoothness and polarity of fibers is strongly dependent on the conditions used in processing the fibers (including any final surface treatment rendered to the fiber surfaces).

It is well documented that the surface of high modulus fibers HMU, HMS carbon fibers and others with relatively low shear strength, have far smoother surfaces than low modulus (200 GPa) fibers with reasonably high shear strength (Figures IV-C-1 and -2).

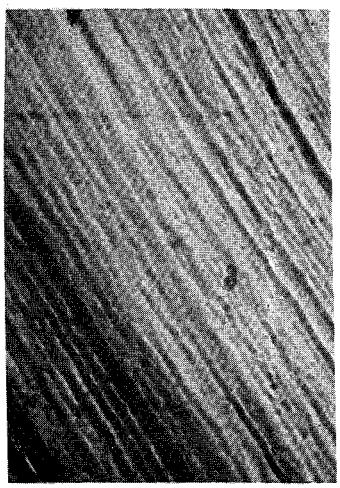

Figure IV-C-1

Scanning Electron Microscopy (SEM) of Longitudinal Surface of Low Modulus Fiber (E = 200 GPa). Magnification 20,000x.

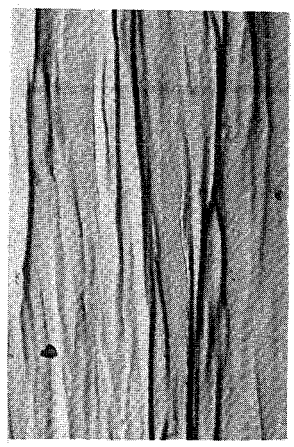

Figure IV-C-2

Transmission Electron Microscopy (TEM) of Longitudinal Surface of High Modulus Dogbone Fiber (E = 680 GPa). Magnification 66,700x.

In order to overcome the above difficulties, highly oriented pyrolytic graphite (HOPG) - the same as graphite monochromators used for x-ray and neutron analysis - was used to simulate the surface of high modulus fibers. While the average crystallite preferred orientation and perfection of high modulus carbon fibers is significantly lower than those of HOPG, TEM studies indicate that the outer-most layer of high modulus carbon fibers does not appear to be drastically different from HOPG. A comparison of some pertinent properties for HOPG versus Thornel P-75S is given in Table IV-C-1.

A subgoal of this study was to determine if HOPG could be used for simulation. The surface of HOPG (Figure IV-C-3) can be characterized as consisting of two major parts: a) the basal planes (0002) with low bonding ability, hence poor wetting and b) the very active edges with high surface energies with comparatively excellent wetting ability (schematically illustrated in Figure IV-C-4). The disparity in the behavior of the two areas is shown vividly in the sequential pictures of a drop of distilled water on a relatively pure basal region (Figure IV-C-5) and on the basal area containing some edges (Figures IV-C-6a through -6d).

The surface energetic of the basal planes of HOPG would be expected to be very similar to that of the surface of untreated high modulus fibers, because of the similarity of the basal plane orientation of HOPG to that of the outermost layers of high modulus fiber, Figures IV-C-3 and -7.

TABLE IV-C-1

SOME PROPERTIES OF HOPG AND HIGH MODULUS GRAPHITE FIBERS

Properties	Units	HOPG[15]*	Temp. Range Over Which Prop. Was Measured	Thornel P-75S[16] (Fiber Axis)	Temp. Range Over Which Prop. Was Measured
C_o	Å	6.710	Room	-----	-----
Filament diameter	μ	-----	-----	10μ	-----
Density	g/cm^3	2.266	Room	2.00	-----
Thermal conductivity	W/mK°	1700. (a)**	2-340°C	150	at 21°C
		8. (c)***	90-340°C		
Electrical resistivity	ohm/cm 10^{-4}	0.4 (a)	1-300	5	-----
		0.15 (c)	1-300		
Thermal expansion coefficient	$K^{\circ -1}$	Slightly negative (a)	300-1100	-1.1×10^{-6}	at 21°C
		28×10^{-6} (c)			
Tensile modulus	GPa	$C_{11} = 1060$	Room	500	-----
Carbon assay[17]	% Carbon	99.9996	-----	99	-----

*Bracketed numbers in this table refer to references on page 155

**Along the (a) axis of hexagonal lattice

***Along the (c) axis of hexagonal lattice

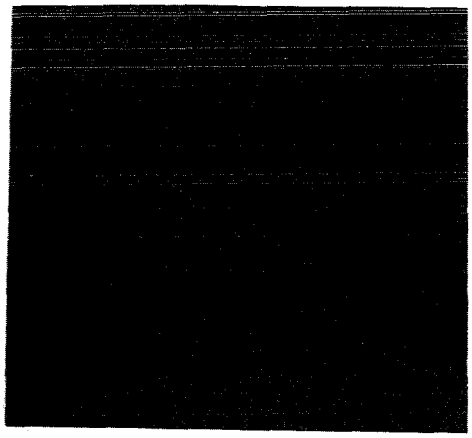

Figure IV-C-3

Surface of Freshly Cleaved HOPG (x100)

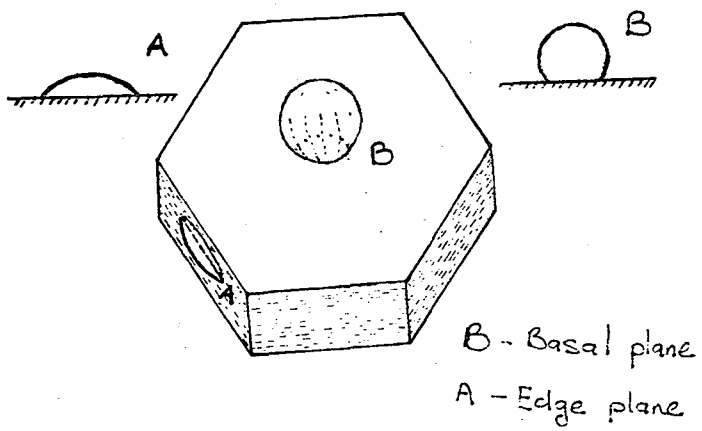

Figure IV-C-4

Schematics Illustrating Wetting Behavior
on Basal and Edge Portions of HOPG

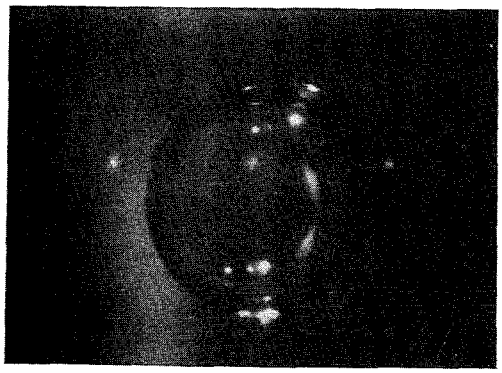

Figure IV-C-5

Poor Wetting of Water on Basal Plane of HOPG

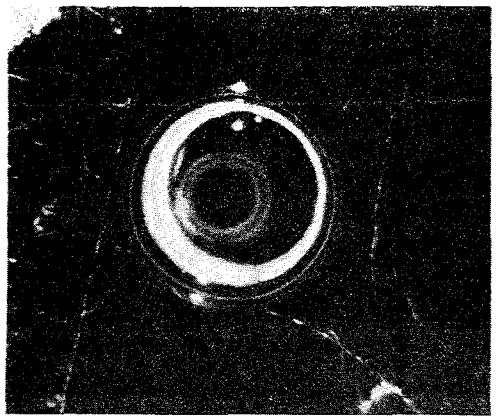

a) after 60 seconds x9

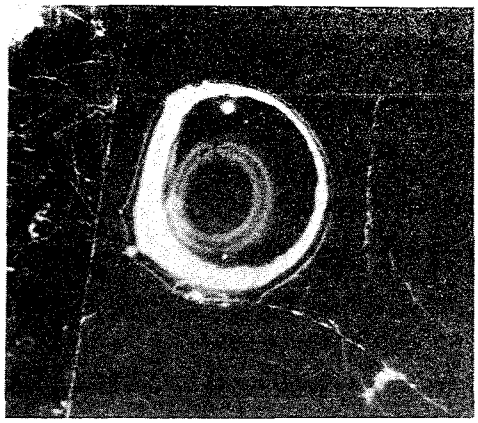

b) after 6 minutes x9

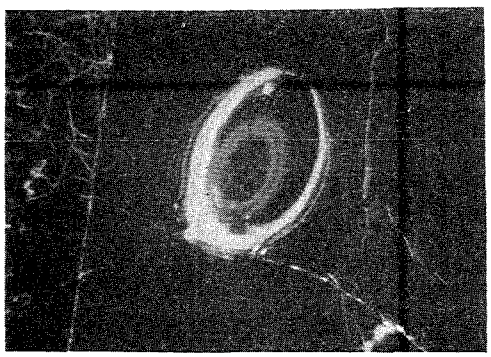

c) after 9 minutes x9

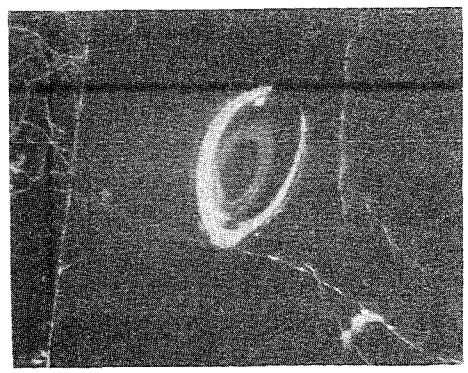

d) after 12 minutes x9

Figure IV-C-6
Distortion of Contact Angle of Water Due to Presence of Edges

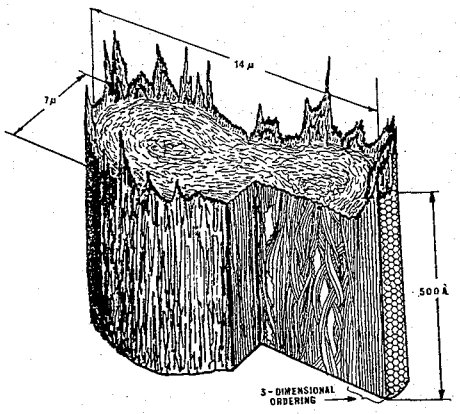

Figure IV-C-7

Model for High Modulus Graphite Fiber
(after R. J. Diefendorf and E. Tokarsky)

a) Experimental Technique

The surface of HOPG was carefully cleaved under a stereomicroscope to obtain a sufficiently large basal region on which the contact angle of resins, hardeners and various liquids of known and unknown polar and dispersive components could be measured by using a goniometer. The same experiments were replicated on the surface of polished polytetrafluoroethylene (PTFE). The polar and dispersive components of HOPG and PTFE were evaluated by determining the slope and intercepts of the Young-Fowkes relationship:

$$\text{Cos } \theta + 1 = \frac{2}{\gamma_L}\left(\sqrt{\gamma_L^d \gamma_S^d} + \sqrt{\gamma_L^p \gamma_S^p}\right)$$

where: γ_L refers to the equilibrium liquid-air surface energy of the contacting liquid, θ is the measured contact angle and γ_L^p and γ_L^d refer to the polar and dispersive components of the surface energy of the experimental liquid. Typical values for the liquids appear in Table IV-C-2. Similarly, γ_S^p and γ_S^d refer to the polar and the dispersive contributions of the solid surface energy γ_S. For the solid $\gamma_S = \gamma_S^p + \gamma_S^d$ and for the liquids $\gamma_L = \gamma_L^p + \gamma_L^d$. For a detailed derivation of this equation, see Kaeble[7].

Finally, the critical surface energy, γ_c, of HOPG and PTFE was evaluated using the Zisman plot[5, 7], and by using linear regression and measured contact angles, the surface energy of various hardeners and resins was estimated. A typical Zisman plot is shown in Figure IV-C-8.

TABLE IV-C-2

SURFACE ENERGY OF REFERENCE LIQUIDS AT 20°-25°C

Reference Liquids	Contact Angle θ on PTFE	Contact Angle θ on HOPG	γ_D [1] $\frac{erg}{cm^2}$	γ_P [2] $\frac{erg}{cm^2}$	γ_T [3] $\frac{erg}{cm^2}$
Water	112	60	51	21.75	72.75
Glycerol	95	50	37	26.4	63.4
Methylene iodide	75	17.5	48.4	2.4	50.4
Glycol	83	30	28.9	18.8	47.7

---

1 γ_D = Dispersive surface energy component

2 γ_P = Polar surface energy component

3 γ_T = Total, dispersive surface energy component and polar surface energy component

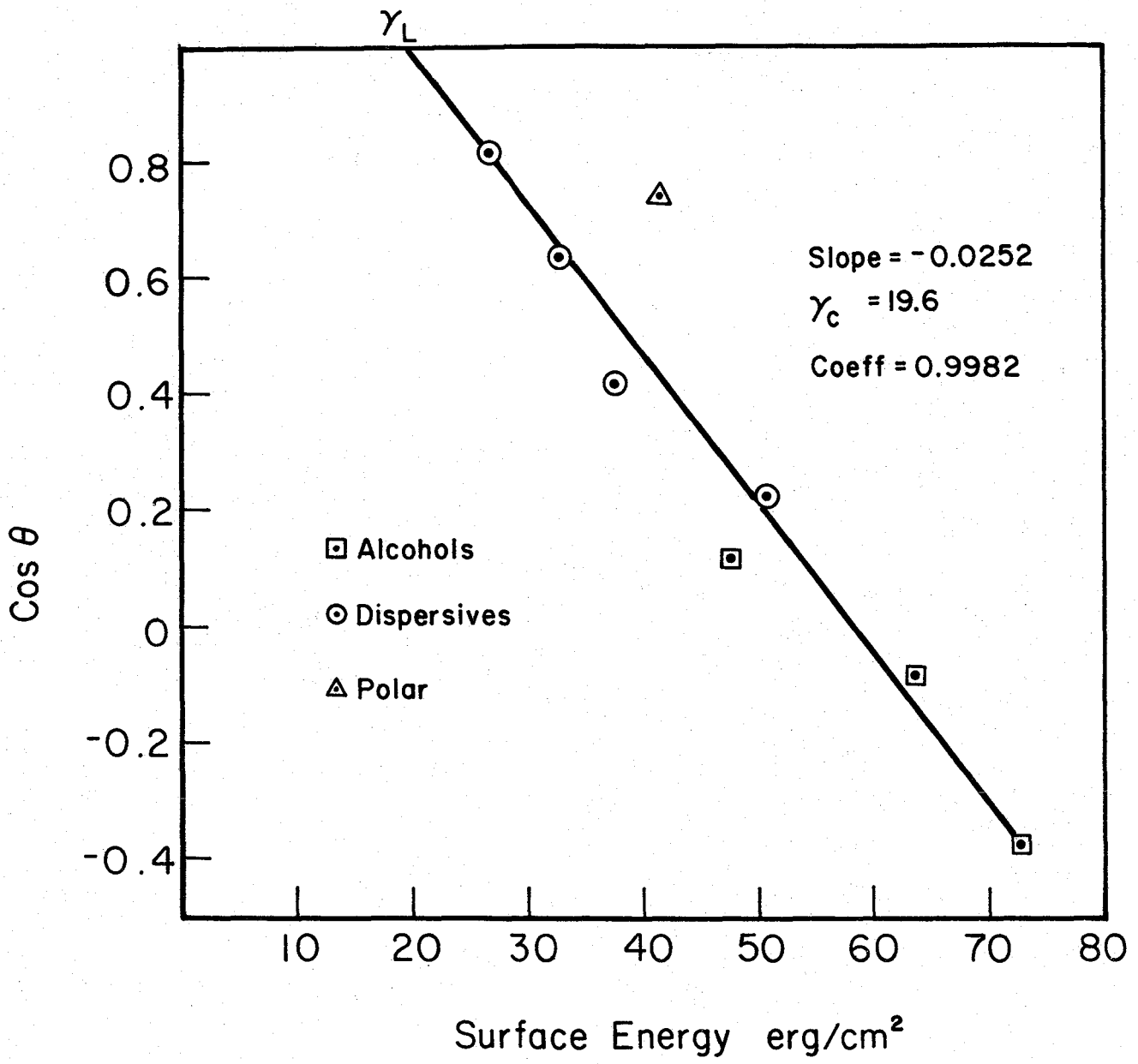

Figure IV-C-8

Zisman Wetability Plot of Various Liquids
on Polytetrafluoroethylene at 20°C

b) Results

By using the Young-Fowkes relationship again:

$$\text{Cos}\,\theta + 1 = \frac{2}{\gamma_L}\left(\sqrt{\gamma_L^d \gamma_S^d} + \sqrt{\gamma_L^p \gamma_S^p}\right)$$

where γ_L stands for the reference liquid total, d and p are the dispersive and polar components, respectively, and L and S are the liquid and solid, respectively. By rearranging the equation slightly:

$$\frac{\gamma_L(\text{Cos}\,\theta + 1)}{2\left(\gamma_L^d\right)^{\frac{1}{2}}} = \left(\gamma_S^d\right)^{\frac{1}{2}} + \left(\frac{\gamma_L^p}{\gamma_L^d}\right)^{\frac{1}{2}} \left(\gamma_S^p\right)^{\frac{1}{2}}$$

A plot of $\frac{\gamma_L(\text{Cos}\,\theta + 1)}{2\left(\gamma_L^d\right)^{\frac{1}{2}}}$ versus $\left(\frac{\gamma_L^p}{\gamma_L^d}\right)^{\frac{1}{2}}$ should be a straight line with $\left(\gamma_S^d\right)^{\frac{1}{2}}$ and $\left(\gamma_S^p\right)^{\frac{1}{2}}$ as intercept and slope, respectively. Such relations are shown in Figure IV-C-9. The data shown in Figure IV-C-10 was used to compile the information contained in Tables IV-C-3 and -4. A compendium of such data for a very wide range of resins, hardeners and liquids of interest in composites fabrication is presented in Table IV-C-5. These values were obtained with the methods reported here and from the literature. A summary of the surface energy of the solids PTFE and HOPG is given in Table IV-C-6 and compared with values in the literature.

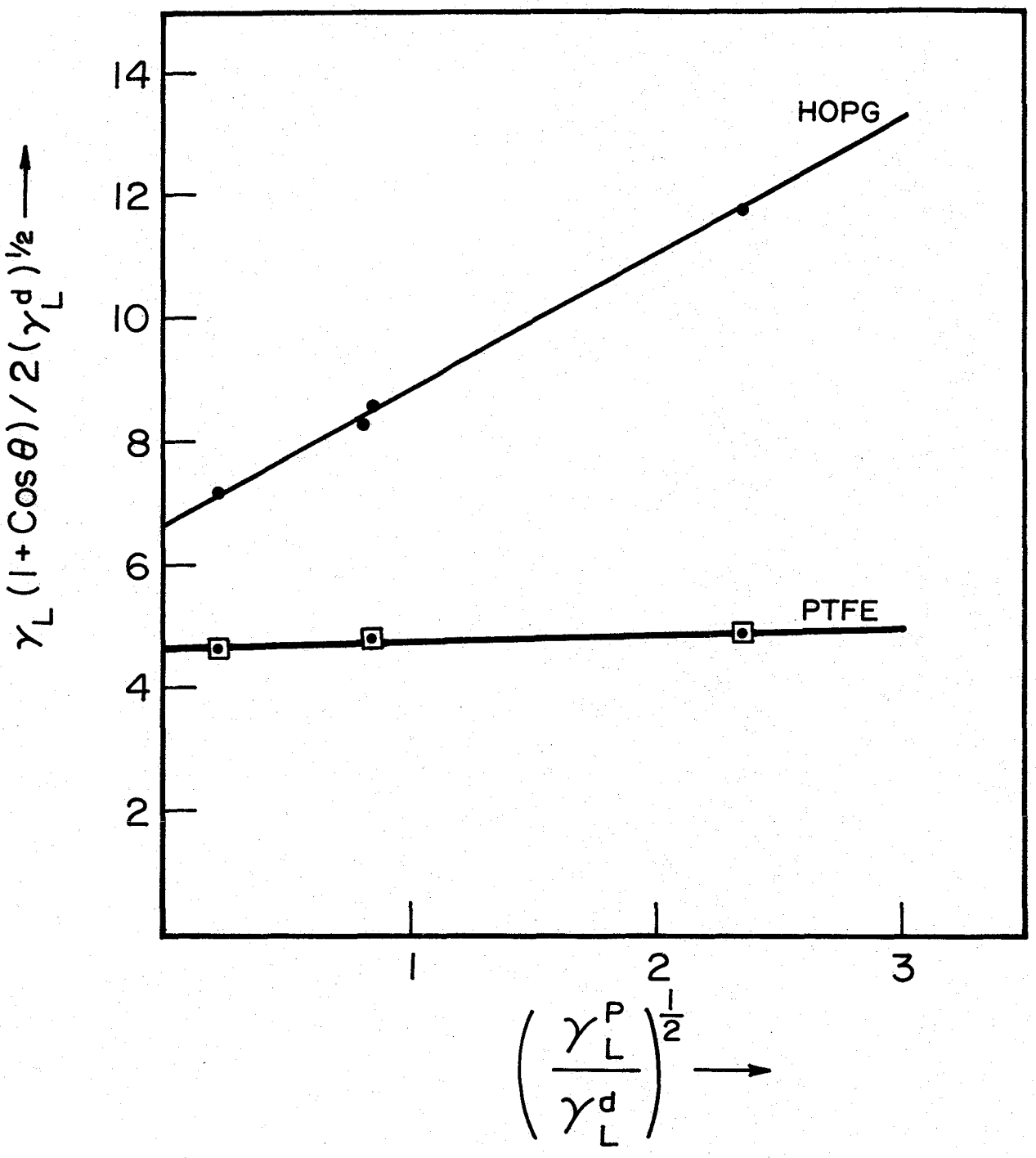

Figure IV-C-9

Determination of the Surface Energy Component of HOPG and PTFE at 20°C

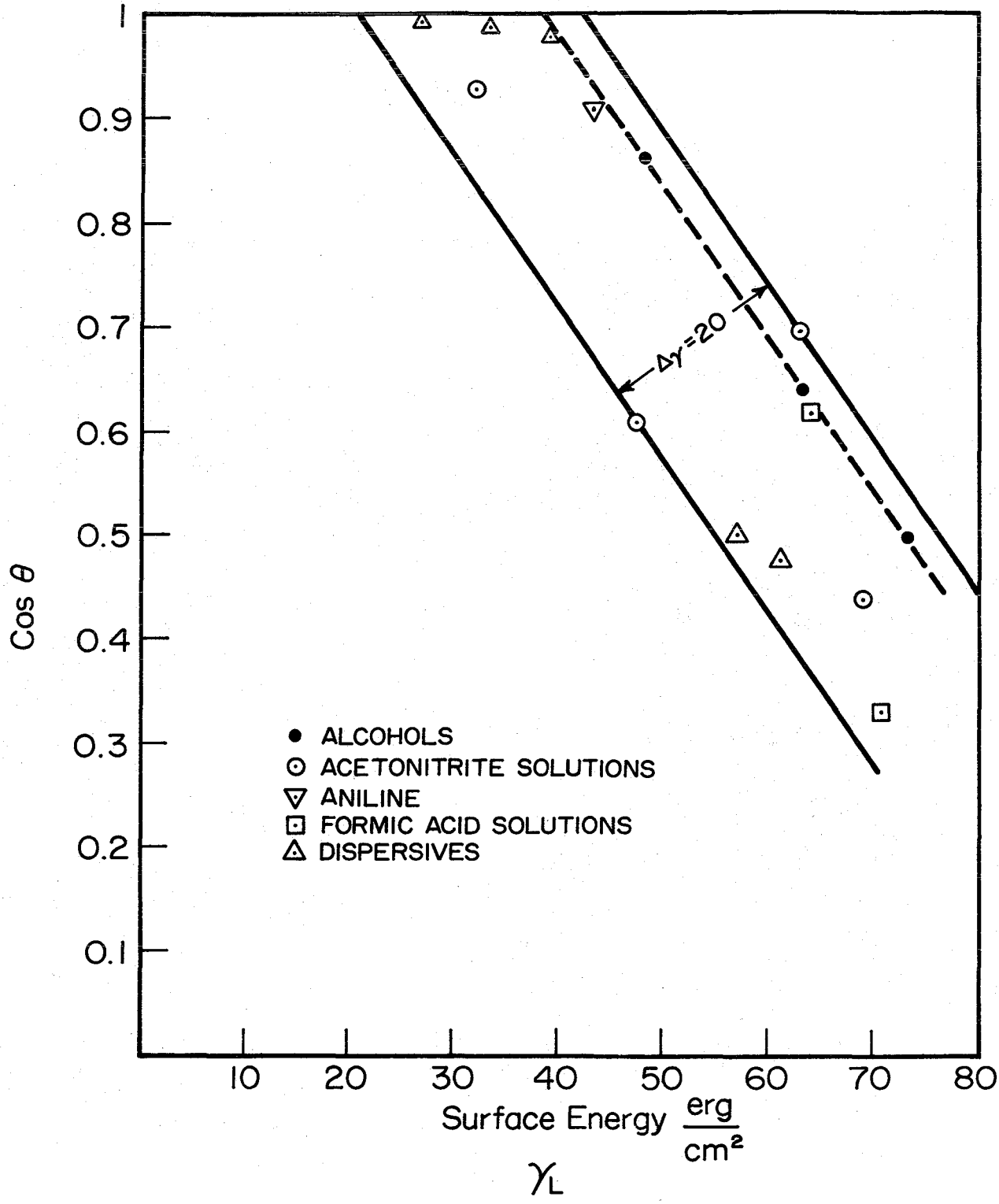

Figure IV-C-10

Zisman Wetability Plot of Various Liquids on HOPG at 20 - 25°C

TABLE IV-C-3

RESULTING DATA FOR SURFACE ENERGY COMPONENTS ON HOPG AND PTFE

Reference Liquids	$\left(\frac{\gamma_L^p}{\gamma_L^d}\right)^{\frac{1}{2}}$	PTFE $\frac{\gamma_L(1 + \cos\theta)}{2\left(\gamma_L^d\right)^{\frac{1}{2}}}$	HOPG $\frac{\gamma_L(1 + \cos\theta)}{2\left(\gamma_L^d\right)^{\frac{1}{2}}}$
Water	2.3448	11.7673	4.8778
Glycerol	0.8447	8.5613	4.7572
Glycol	0.8066	8.2756	----
Methylene iodide	0.2227	7.1330	4.5959

$(\gamma_{PTFE}^d)^{\frac{1}{2}} = 4.6034$ $\qquad$ $(\gamma_{HOPG}^d)^{\frac{1}{2}} = 6.6244$

$\gamma_{PTFE}^d = 21.2$ $\qquad$ $\gamma_{HOPG}^d = 43.9$

$(\gamma_{PTFE}^p)^{\frac{1}{2}} = 0.1232$ $\qquad$ $(\gamma_{HOPG}^p)^{\frac{1}{2}} = 2.1908$

$\gamma_{PTFE}^p = 0.015$ $\qquad$ $\gamma_{HOPG}^p = 4.78$

Corr. Coeff. = 0.9499 $\qquad$ Corr. Coeff. = 0.9991

≈ 0.95

$\gamma_{PTFE}^T = 21.2 \pm 0.35$ $\qquad$ $\gamma_{HOPG}^T = 48.7 \pm 3.2$

TABLE IV-C-4

ZISMAN EQUATION RESULTS FOR VARIOUS LIQUIDS ON PTFE AND HOPG

	PTFE		HOPG	
Liquids	Cos θ°	γ_{LV} $\frac{erg}{cm^2}$	Cos θ°	γ_{LV} $\frac{erg}{cm^2}$
Water	-0.3746	72.75	0.5	72.75
Glycerol	-0.0872	63.4	0.6428	63.4
Acetic anhydride	0.6428	32.7	0.9903	32.7
n-Butyric acid	0.8192	26.8	----	----
Acetonitrile	0.7547	29.3	----	----
Aniline	----	----	0.9063	42.9
Formic acid (9.76%)	----	----	0.6157	63.6

Linear Regression of Cos θ vs. γ_{LV}:

	PTFE	HOPG
γ_c (erg/cm^2)	19.6	33.5
Slope	-0.0252	-0.0125
Coeff. Corr.	0.9982	0.996
$\Delta\gamma$ (erg/cm^2)	----	20

TABLE IV-C-5

CONTACT ANGLE AND SURFACE ENERGY ESTIMATE FOR VARIOUS RESINS, HARDENERS AND LIQUIDS

		Contact Angle (Degrees)		$\gamma_L \frac{erg}{cm^2}$	$\gamma_L \frac{erg}{cm^2}$	$\gamma_L \frac{erg}{cm^2}$
		HOPG	PTFE	Estimate for PTFE	PTFE Corrected	Estimate for HOPG
	RESINS					
1.	Epon 828	15	85	54.8	49.1	36
2.	Epon 871 flexibilizing resin	10-12	67	42	37.6	34.9
3.	Epon 152 phenol Novolac	25	--	----	----	41
4.	Ciba MY-720 Cresole Novolac	32	92	59.6	53.4	45.7
5.	Ciba 179 cycloaliphatic resin	10-12	78	50	44.8	34.9
6.	Ciba 508	≤ 5	70	44	39	≤ 33.8
7.	Torlon 400 (Amoco) 20% imide in n-methyl pyrrolidone	50	99	64	57.4	62.2
8.	Kelpoxy G-272-100 epoxy terminated elastomeric copolymer	30-31	92	59.6	53.4	44
	HARDENERS					
9.	Nadic methyl anhydride (NMA)	9	50	32.9	29.5	34.5
10.	Dodecenyl succinic anhydride (DDSA)	8	50	32.9	29.5	34.2
	Amide					
11.	V-40 (Epon)	22	58	37.3	33.4	39.3
	Amines					
12.	Diethylene triamine (DTA)	30	80	51.4	46.1	44.2
13.	Tetraethylene pentamine (TPA)	30	80	51.4	46.1	44.2

TABLE IV-C-5 (Continued)

		Contact Angle (Degrees)		$\gamma_L \frac{erg}{cm^2}$	$\gamma_L \frac{erg}{cm^2}$	$\gamma_L \frac{erg}{cm^2}$
		HOPG	PTFE	Estimate for PTFE	PTFE Corrected	Estimate for HOPG
	HARDENERS					
	Coupling Agents					
	A) Coordinate Types (titanate complex)					
14.	KR44 (contains amine)	31-32	73	46.7	41.8	----
15.	KR46[B]	spreads	38	27.17	24.4	<33.5
16.	KR55	spreads	51	33.4	29.9	<33.5
	B) Chelate Types					
17.	KR-112S	8	--	----	----	34
18.	KR-134S	18	--	----	----	37.4
19.	Soap solution	splash spreads	--	----	----	<<33.5
	Oxidents					
20.	Hydrogen peroxide	30	--	----	----	44
21.	Nitric acid (70%)	15	--	----	----	36.2
22.	Titanium trichloride (20% solution)	55	--	----	----	----
	Dispersives					
23.	Acetic anhydride	8	50	32.9	29.5	34.2
24.	n-Butyric acid	<8	35	29.5	26.4	----
25.	Pyridine	spreads	--	----	----	----
26.	Methylene iodide*	17.5	75	48	43	37.2
27.	Aniline	25	--	----	----	----
28.	Bisphenol A**	50	--	----	----	62.2

*Literature Value = 50.4

**Melted at 160°C and cooled to room temperature

TABLE-IV-C-6

SUMMARY OF RESULTS

Solid		Surface Energy of Solids, erg/cm^2	Literature Values erg/cm^2
PTFE			
	Dispersive Component	γ_c = 19.6	18.5[a]; 19.5[b]; 19.6[g]
		γ^d = 21.2	23.9[f]; 22.6[c]; 22.5[d]
		$\gamma_{(c,\phi)}$ = 22.2[h]	19.1[c]
	Polar Component	γ^p = 0.015	2.0[g]
	γ Total	γ_T = 21.2 ± .35	21.6[g]
HOPG			
	Dispersive Component	γ_c = 33.5	
		γ^d = 43.88	33 ± 1.2[k]
		$\gamma_{(c,\phi)}$ = 41.7[h]	
	Polar Component	γ^p = 4.78	8.1 ± 3[k]
	γ Total	γ_T = 48.6 ± 3.2	41.1 ± 3

[a,b] Critical surface energy or surface tension $\left(\frac{\text{dynes}}{\text{cm}}\right)\gamma_c$ (6)(7)

[c,h] From equation of state, $\text{Cos}\ \theta = 2(\gamma_{c\theta}/\gamma_{LA})^{\frac{1}{2}} + 1$ (10)

[d] Obtained from harmonic mean equation (10)

[e] Obtained from geometric mean equation (10)

[f] From liquid homologous, molecular weight dependence (10)

[g] Kaeble (7)

[k] Drzal, L. T. (9), for HMU, i.e., high modulus fiber "un-surface-treated"

c) Discussion

The driving force for the adhesion of a liquid on any substrate is the work of adhesion, i.e., the reversible work required to separate a unit area of the liquid from the substrate. For the drop of any liquid on HOPG (see Figure IV-C-11):

$$W_a = \gamma_S + \gamma_L - \gamma_{SL} + \pi_e \qquad (1)$$

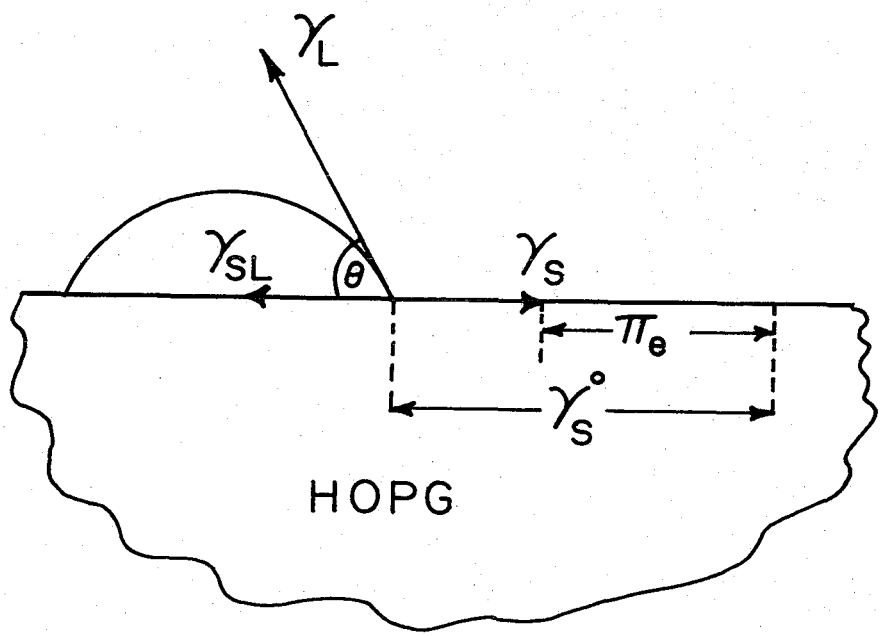

Figure IV-C-11
Contact Angle and Droplet Configuration

where γ_L = liquid-air surface tension

γ_{SL} = solid-liquid interfacial surface tension

γ_S = solid-air surface tension

γ_S^o = surface tension of HOPG in vacuum

π_e = the equilibrium spreading pressure

θ = contact angle between liquid and HOPG

For air-HOPG equilibrium:

$$\pi_e = \gamma_S^O - \gamma_S \qquad (2)$$

Using Young's equation, for HOPG-liquid-air equilibrium:

$$\gamma_L \text{Cos}\,\theta = \gamma_S - \gamma_{SL} \qquad (3)$$

Substituting (3) in (2) we obtain the Dupree-Young relation for work of adhesion:

$$W_a = \gamma_L(1 + \text{Cos}\,\theta) + \pi_e \qquad (4)$$

Assuming that as $\theta \to 0$, $\gamma_S \to 0$ and $\pi_e \to 0$ in orderly fashion,

$$W_a = \gamma_L(1 + \text{Cos}\,\theta) \qquad (5)$$

The work of cohesion W_c, i.e., the work required to produce two units of interfacial area from an original column of any liquid in air is given by

$$W_c = 2\gamma_L$$

The difference between work of adhesion of a liquid on a substrate and the work of cohesion is the spreading coefficient:

$$W_a - W_c = \gamma_L(1 + \text{Cos}\,\theta) - 2\gamma_L = S_{L/S}$$

a) When $W_a > W_c$, $S_{L/S}$ is positive, $\theta = 0$ and the liquid spreads spontaneously over the substrate to form a thin film.

b) When $W_a < W_c$, $S_{L/S}$ (spreading coefficient) is negative, the liquid does not spread over the substrate but forms droplets or lenses with finite contact angle θ.

c) When $W_c = W_a$,

$$\theta \to 0,\ \text{Cos}\,\theta = 1,\ S_{S/L} = 0$$

d) When $\theta = 180$,

$$W_a = 0,\ S_{S/L} = -2\gamma_L$$

$$\text{inefficiency factor} = \left|\frac{-2\gamma_L}{2\gamma_L}\right| \times 100 = 100.$$

Table IV-C-7 lists values calculated using the expressions for work of adhesion, W_a, spreading coefficient, $W_a - W_c$ and inefficiency factor

$$\left|\frac{W_a - W_c}{2\gamma_L}\right| 100, \text{ as given above.}$$

Close observation of the values in Table IV-C-7 shows the work of adhesion of the liquid resins on PTFE is in the range of 46 to 52 erg/cm^2 with a mean value of 48.1 erg/cm^2 while for HOPG, W_a is in the range of 72 to 98 erg/cm^2 with a mean value of 83.7 erg/cm^2. The inefficiency factor may be considered as the fraction of the cohesive strength of the liquid that did not contribute to adhesion. These results strongly demonstrate that adhesional wetting on HOPG is not only vastly superior to that on PTFE, but that the work of adhesion can be enhanced by a high value of γ_S; a high value of γ_L, at a low value for γ_{SL}; and a low value for spreading coefficient. Low spreading coefficient will occur when γ_S is roughly about the same as γ_L.

The critical surface energy γ_c of a solid is operationally defined by Zisman as

$$\text{Cos}\,\theta = 1 + b(\gamma_c - \gamma_L) \qquad (6)$$

TABLE IV-C-7

WORK OF ADHESION BETWEEN LIQUIDS, HOPG AND PTFE BASED ON CONTACT ANGLE MEASUREMENT

Material	Work of Adhesion γ_L^* (1 + Cos θ) [erg/cm^2]		Spreading Coefficient $S_{L/S} = W_a - W_c$ [erg/cm^2]		Inefficiency Factor $\left\|\frac{W_a - W_c}{2\gamma_L^*}\right\| 100$	
	HOPG	PTFE	HOPG	PTFE	HOPG	PTFE
Water	109	45	-36.5	-100.5	25	69
Glycerol	119	58	-26.5	87.5	21	62
Epon 828	83	46	-2.1	39	2.5	46
Epon 871	72	50	-0.5	23	0.7	31
Epon 152	78	--	-3.8	---	4.6	---
Ciba MY720	90	48	-9.1	-51	9.2	51.5
Ciba CY179	79	48	-0.7	-32	0.9	40
Ciba 508	$\leq$72	52	---	-26	---	33.5
Torlon 4000	98	50	-21.6	-69	18	57.5
Kelpoxy-G-272-100	90	47	-7.4	50.4	7.5	51.8

γ_L^* = Mean γ_L predicted from PTFE and HOPG

where b is a constant, and γ_L is the surface energy of the liquid. In all instances in which $\gamma_L < \gamma_c$, the equation predicts the contact angle will be zero, and the liquid will spread. Also, that for all $\gamma_L > \gamma_c$, the cosine of θ decreases in a linear manner.

Substituting (6) in (5), the work of adhesion becomes

$$W_a' = (2 + b\gamma_c)\gamma_L - b\gamma_L^2 \qquad (7)$$

which is a parabola. Equation (7) predicts that W_a' will display a maximum value at $\frac{dW'}{d\gamma_L} = 0$, $\gamma_L = \frac{1}{b} + \frac{1}{2}\gamma_c$ and that the maximum work that can be obtained from this surface will be given by

$$W_a'(\max) = \frac{1}{b} + \frac{1}{c} + \frac{1}{4}b\gamma_c \qquad (8)$$

A plot of maximum work obtainable from an HOPG surface with γ_c, critical surface tension, for various values of b, shows that for $W(\gamma_c = 33.5) = 80.3$ erg/cm^2 and $W(\gamma_c = 48.6) - 103.2$ erg/cm^2 for b = 0.0252, the work factor improved by 28 percent for a 45 percent increase in γ_c (Figure IV-C-12). This range compares favorably with the values in column 2 of Table IV-C-7 for the various epoxies. Equation (8) suggests that the only ways more work can be obtained from the HOPG basal plane surface are

a) decreasing the value of Zisman slope b and

b) increasing the critical surface energy of HOPG by oxidative activation of HOPG surface so that bonding reactions can occur with resin, etching or other techniques that may raise γ_c or the interaction between liquid and solid.

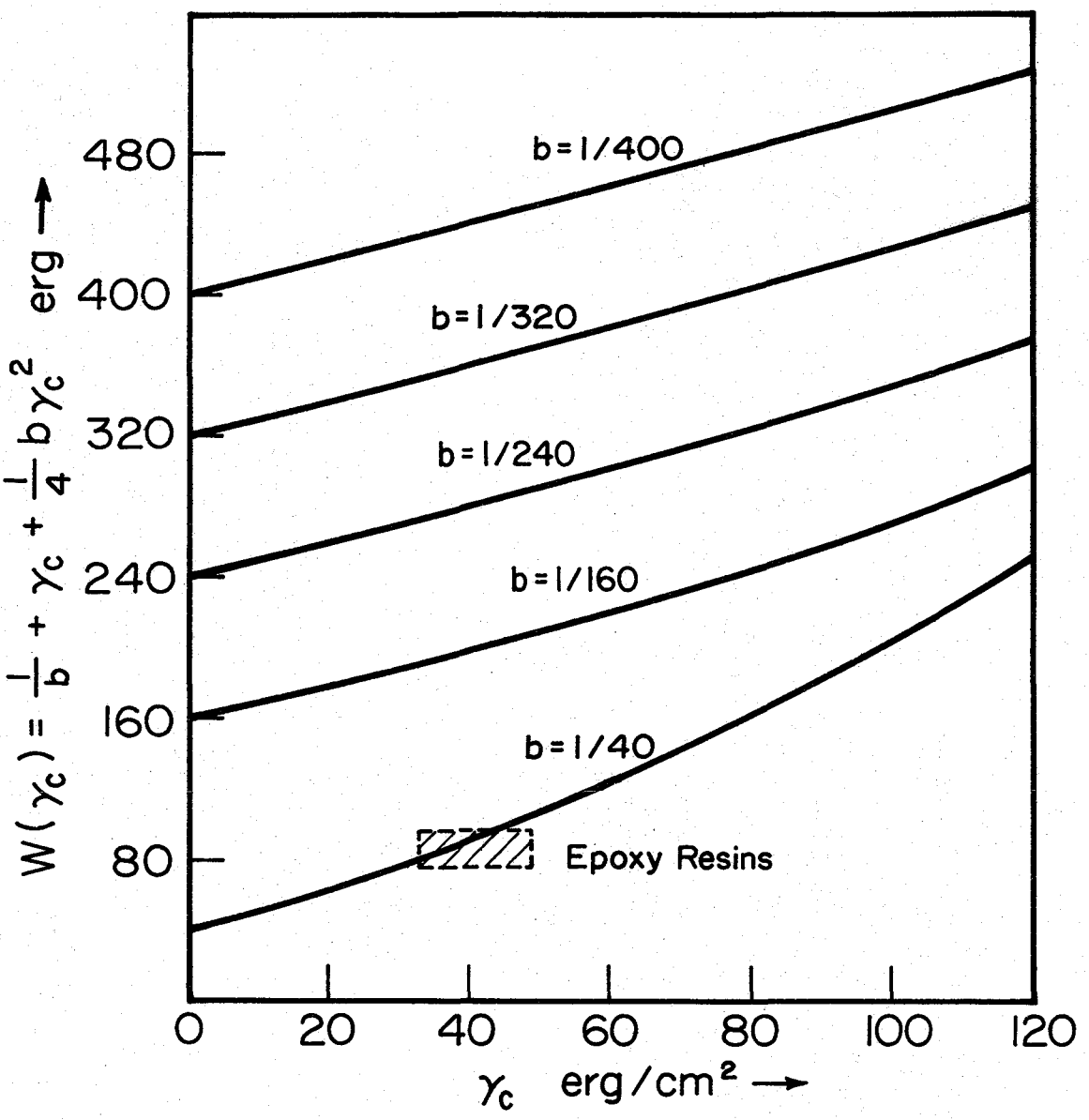

Figure IV-C-12

Plot of Maximum Work W(max) Obtainable on HOPG at Various Critical Surface Energy γ_c for Different b Values

In fact, it could be argued that b and γ_c are related and that any factor that will affect b also affects γ_c. The difficulty with etching HOPG surface or HM fibers to improve γ_c is that some of the highly oriented outermost layers are removed and also additional flaws may be introduced on the surface of the fibers. Hence, shear strength will increase at the expense of tensile strength of the composite.

The scatter γ_c = 20 erg/cm^2 in the Zisman plot could be traced to the following assumptions and reasons:

a) Liquids identical in chemical properties to a solid would have a zero contact angle on the solid, hence the same surface tension, γ_s.

b) All liquids with identical γ_L will display the same contact angle on any solid (converse of assumption "a").

c) Any liquid whose surface tension is below the critical surface tension of a solid will completely wet the solid.

d) There is a varying degree of adsorption of the various liquids on the HOPG surface, which leads to a hysteresis. This could be shown vividly in the case of diethylene-triamine on HOPG. (Figure IV-C-13)

e) Each surface of HOPG is slightly different, in terms of roughness of basal planes and 'fractional coverage' of non-basal planes with edges or high surface energy regions that could not be observed at 100X.

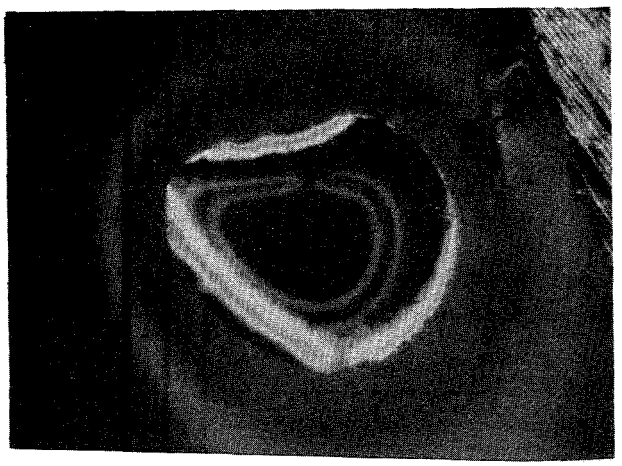

Figure IV-C-13
Drop of Diethylenetriamine on HOPG Surface

f) The polar surface energy components of the various liquids and HOPG were ignored.

The Zisman relation works well for homologous series of liquids, such as alcohol as shown in Figure IV-C-10. However, assumptions a) and b) above become particularly poor for non-homologous liquids. This is because it is the matching between both the polar and dispersive components of the liquid and HOPG that determines the contact angle. The empirical method of estimating γ_c may result in a value that may agree well with γ_S^d rather than the true solid surface tension γ_S, particularly where substantial contribution from γ_S^p exists.

On non-polar and low energy surfaces the third assumption, c), suggests that complete wetting can only occur when the surface tension of the wetting liquid has been reduced to a critical value, γ_c, characteristic of the substrate, e.g., 33.6 dynes/cm^2 for HOPG and about 31 dynes/cm^2 for polyethylene. This equates γ_c with $\gamma_S - \gamma_{SL}$. For many liquids, a plot of Cos θ versus γ_L is linear. Extrapolation of this plot to Cos θ = 1, that is θ = 0, yields γ_c or the critical surface tension for complete wetting. This quantity is a constant for a particular substrate irrespective of the nature of the wetting agent. This will, of course, require that $\gamma_S - \gamma_{SL}$ be reduced to the same value in all cases. Rosen[8] has suggested that the two necessary conditions to achieve a constant value of $\gamma_S - \gamma_{SL}$: (a) the free energy per unit

area, γ_S, of the surface in equilibrium with the liquid-saturated air above it be equated with γ_S, the free energy of the solid, free of adsorbed material (This implies that π_e, the equilibrium pressure, will have to vanish.); and (b) the adsorption of liquid on the substrate interface occurs with some orientation and degree of packing, producing the same value γ_{SL} (thus a constant value of $\gamma_S - \gamma_{SL}$) as the surface tension of the spreading liquid approaches γ_c.

Schwarz[13] in 1964 and Bernett[14] in 1959 have shown that the presence of highly fluorinated carbocyclic acids and their salts will lower the value of γ_c for polyethylene from its usual value of almost 31 dynes/cm^2 to about 20 dynes/cm^2. This adsorption of the fluorinated surfactants onto the polyethylene surface gives the result that solutions of these surfactants having surface tensions less than the normal γ_c for polyethylene do not spread on it.

In our work, the contact angle of Epon 828 on HOPG is about fifteen degrees, while that of DTA is thirty degrees. One would have expected some intermediate contact angle in the mixture of these two materials. In fact, the contact angle remains consistently at thirty degrees for all mixtures because the amine preferential migrates to the interface and spreads out. Although the contact angle of distilled water on HOPG is sixty degrees, in the case of a mixture of Epon 828 and distilled water, the contact angle of the mixture remains at fifteen degrees because the water phase separated as small bubbles in the droplet.

The requirement that the surface tension of the wetting liquid be reduced by the surfactant to some critical value characteristic of the substrate is thus necessary but not sufficient for complete spreading-wetting. In general, a liquid will not produce complete wetting of HOPG if its surface tension is above the critical surface tension, γ_c. For liquids with surface tension below 33.6 dynes/cm^2, complete wetting of HOPG may or may not be produced as in the case of n-butyric acid, acetic anhydride and acetonitrile.

In the fourth assumption, (d), the effect of surface roughness could be relaxed provided the plane remains basal; for instance, no significant contact angle change was observed on growth cones on HOPG (basal). The effect of non-basal planes was observed to be quite drastic. Contact angle has been observed to be reduced by as much as nineteen degrees by the presence of edges. The liquid tended to be dragged along this edge.

d) Conclusion

Our preliminary work in the study of surface energetics of the basal planes of HOPG suggests that the polar contribution to the surface is as much as ten percent. The critical surface energy of HOPG, γ_c, and Zisman slope, b, have been characterized, and we have shown that the calculated work of adhesion for various epoxies on HOPG is quite close to the maximum work obtainable from the surface.

3. Plans for the Upcoming Period

While the separation of the surface tension of HOPG into its polar and dispersive component indicates that at 20-25°C the polar contribution accounts for roughly ten percent of the total surface energy, in HMU fiber the polar contribution accounts for as much as twenty percent, according to the work of Drzal[9] et al. This separation of the surface energy component for the various epoxy and resin matrices would require about five different solid surfaces with characterized polar and dispersive components, respectively. This is one of our immediate objectives.

The relationship between contact angle of resins and their viscosity is not well know at this time. The separation of surface tension of epoxy into their polar and dispersive components, the relationship between contact angle and viscosity of resins and the various surface modifications to lower b and to increase the critical surface tension γ_c is to be performed.

4. References

1. Goan, J. C. and S. P. Prosen, "Interfaces in Composites", ASTM Special Tech. Publ., No. 452, P. 3.

2. Herrick, J. W., P. E. Gruber, Jr. and F. T. Mansur, "Treatments for Fibrous Carbon Reinforcements", AFML-TR-66-178, Part 1, Air Force Materials Laboratory, July 1966.

3. Herrick, J. W., 23rd Annual Technical Conference, Reinforced Plastics/Composites Division, Section 16A, February 1968.

4. McKee, D. W., and V. J. Mimeault, "Surface Properties of Carbon Fibers", Chemistry and Physics of Carbon, Vol. 8, Edited by P. L. Walter and P. A. Thrower, Dekker Inc., N. Y., 1973, pp. 151-245.

5. "Treatise on Adhesion and Adhesives", Vol. 1, Theory, Edited by R. Patrick, Dekker Inc., N. Y.

6. Fowkes, F. M., "Attractive Forces at Interfaces", Symposium on Interfaces, Sponsored by Ind. and Engr. Chem. and American Chem. Soc., Washington, D. C., June 15-16, 1964, ACS publ., Washington, D. C., 1965, pp. 1-12.

7. Kaeble, D. H., "Physical Chemistry of Adhesion", Wiley/Interscience, N. Y., 1971, pp. 84-188.

8. Rosen, M. J., "Surfactants and Interfacial Phenomena", John Wiley and Sons, N. Y., 1978, pp. 174-88.

9. Drzal, L. T., Carbon, Vol. 17, No. 5/A.

10. Wu, S., Journal of Colloid and Interface Science, Vol. 71, No. 3, October 1979.

11. Mark, H. F., "Adhesion and Cohesion", Proceedings of the Symposium on Adhesion and Cohesion, General Motors Research Labs., Warren, Michigan, 1961, Edited by Philip Weiss, Elsevier Publ. Co., 1962.

12. Handbook of Chemistry and Physics, 58th Edition, CRC Press, 1977-1978.

13. Schwarz, E. G. and W. G. Reid, Ind. Eng. Chem., 56, No. 9, 26, 1964.

14. Bernett, M. K. and W. A. Zisman, J. Phys. Chem., 63, 1911, 1959.

15. Graves, N. F., A. W. Moore and S. L. Strong, (Union Carbide Corp.) "Structure, Properties and Application of Highly Orientated Graphite", Paper presented at the 9th Biennial Conf. on Carbon, Boston College, Massachusetts, June 16-20, 1969.

16. Furnished by Vendor Union Carbide Corporation.

17. Sparks, Jr., C. J., O. B. Cavin, L. A. Harris and J. C. Ogle, "Simple Quantitative X-Ray Fluorescent Analysis of Trace Elements", Trace Substances in Environmental Health - VIII, A Symposium, D. D. Hamphill, Editor, Univ. Of Missouri, 1973, pp. 361-368.

IV-D FATIGUE IN COMPOSITE MATERIALS

Senior Investigator: E. Krempl

The deformation and fatigue failure behavior of composites is being studied for (essentially one-dimensional) laminate samples under uniaxial loading and, more intensively, for graphite-epoxy tubes under biaxial (tension, torsion) loading. The aim of this research is to provide basic understanding and design information on the biaxial response of advanced composites.

1. Status

The following had been accomplished prior to the start of the current reporting period: a series of fatigue tests to failure were performed, using uniaxially loaded laminate specimens, to evaluate frequency dependence and the influence of R - ratio. Specially designed test fixtures were manufactured capable of loading tubular specimens biaxially and triaxially (axial, torsional and internal pressure loading). Eight tubular graphite-epoxy specimens with four layers of $(\pm 45°)_s$ were designed and manufactured. The elastic properties of these specimens were determined, using strain measurement on the gage length.

Studies of damage accumulation models have also been performed with particular reference to the residual strength degradation model. Models in the literature have been compared

for such aspects as constant amplitude loading, rate dependence and non-deterministic properties, etc.

2. Progress During Report Period

Additional tubular test specimens have been manufactured, and their elastic properties under uniaxial, torsional and combined loading have been determined. Elastic properties were determined using an Instron biaxial extensometer attached to the gage length of the specimen under cyclic axial, torsion and combined axial-torsion loading, covering the first and third quadrant of the tension-torsion space.

Figures IV-D-1a and-1b show that the slopes of axial load versus axial strain and torque vs. engineering shear strain are unaffected by proportional loading. In the elastic range the material behaves isotropically. Figures IV-D-1a and -1b also demonstrate that the moduli are equal in tension and compression.

The small hysteresis loops in Figures IV-D-1a and -1b are probably due to friction in the extensometer. They do not appear to be a property of the tubes.

With all tubes we measured effective Poisson's ratio using an axial and a diametral MTS extensometer. The effective Poisson's ratio (negative diametral strain/axial strain), the effective Young's modulus and the effective shear modulus are listed in Table IV-D-1.

The post-elastic behavior of these tubular specimens has also been determined, including ultimate strength under

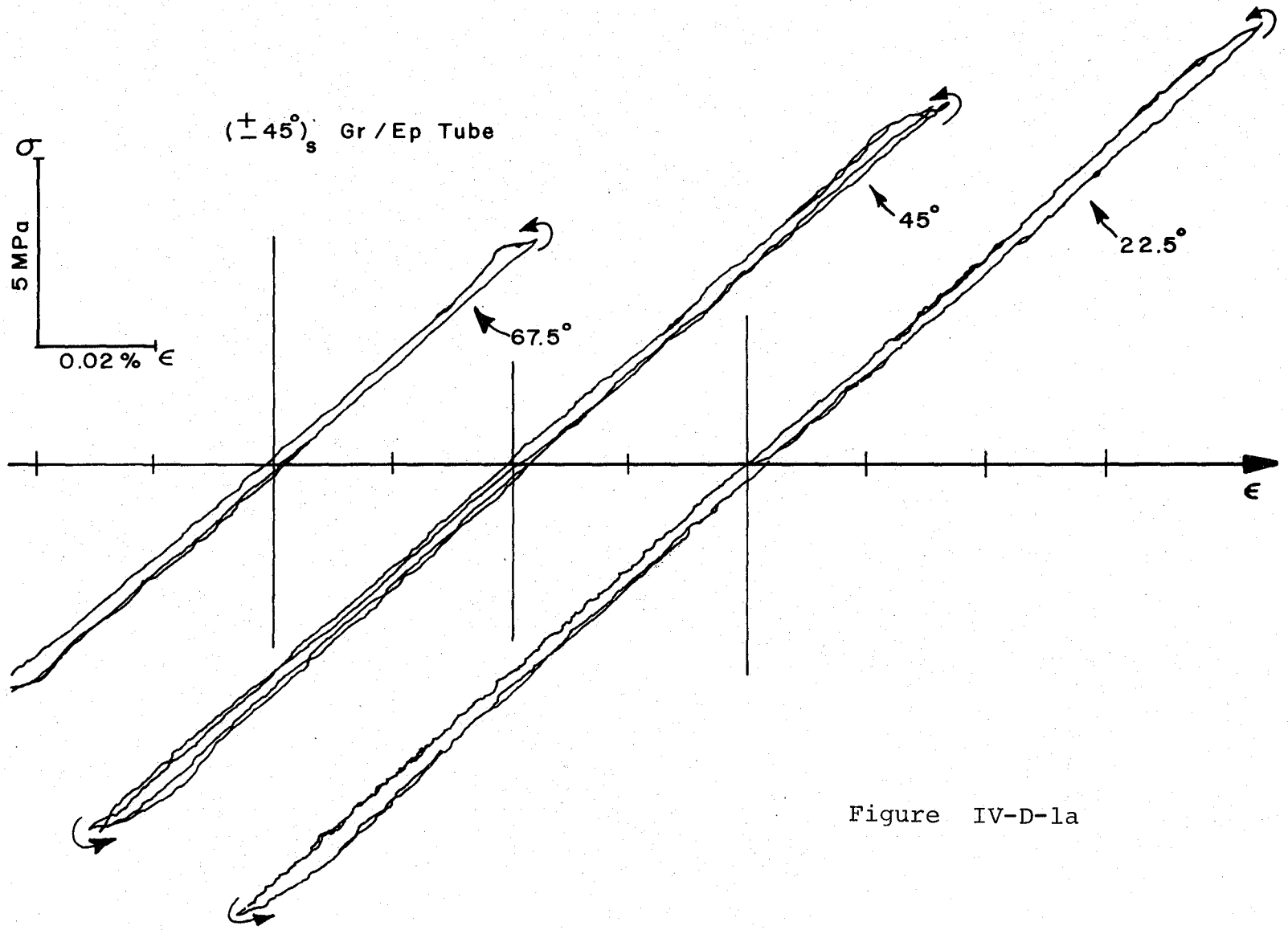

Figure IV-D-1a

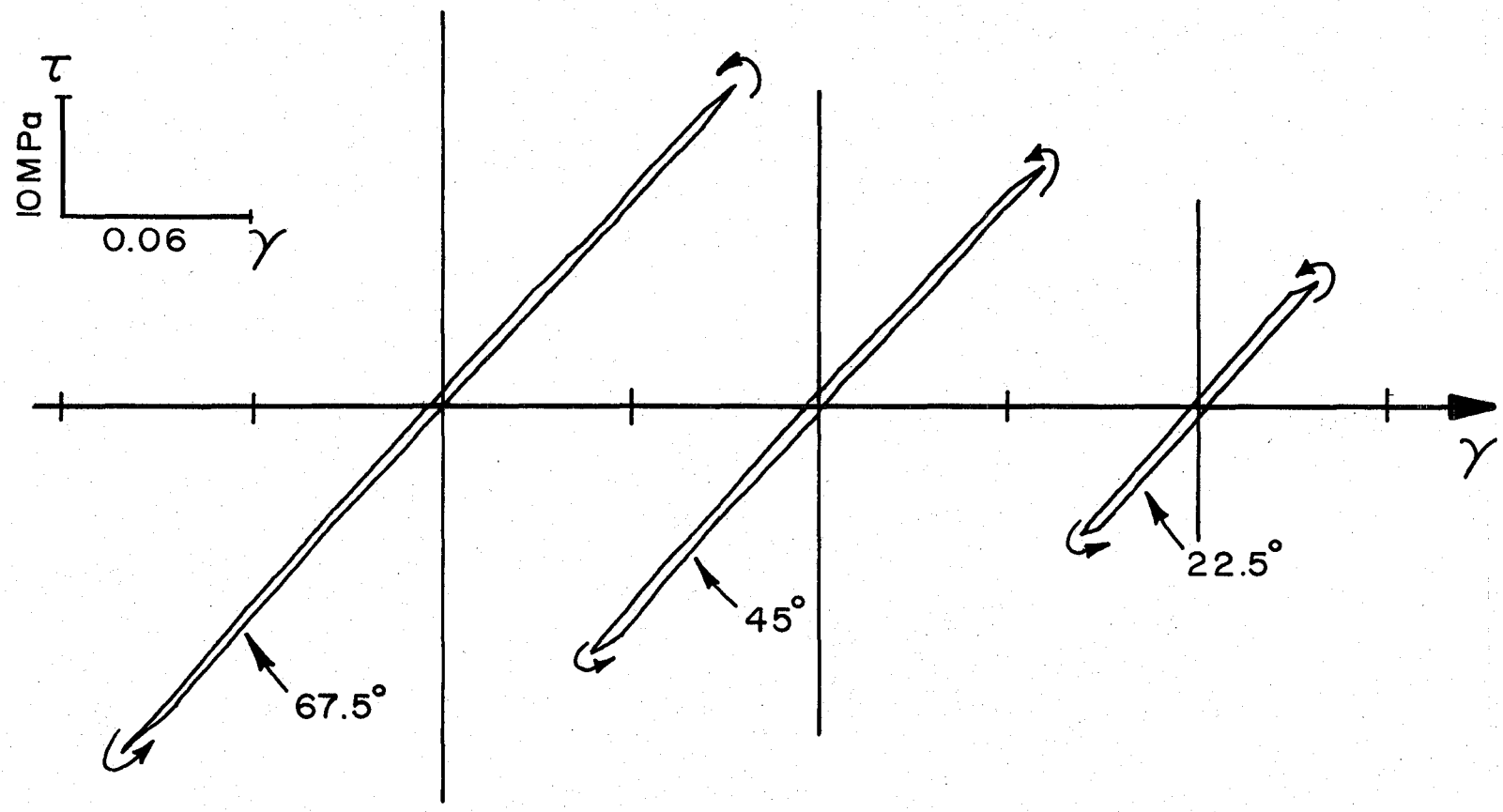

Figure IV-D-1b
(companion to Figure -1a)
Shear Stress Vs. Engineering Shear Strain (Angle Change)

TABLE IV-D-1

STATIC PROPERTIES OF GRAPHITE-EPOXY TUBES $(\pm 45°)_s$

Tube No.	Modulus E (GPa)	G (GPa)	Ultimate Strength σ_u (MPa)	τ_u (MPa)	Poisson's Ratio, ν
7	12.92	---	---	---	---
9	11.84	27.20	-148*	---	0.784
10	12.00	22.74	-166*	---	0.736
11	12.93	23.56	148**	---	0.724
12	11.40	23.14	---	180	0.752
13	12.31	23.41		---	0.738
14	13.83	27.44			0.748
15	11.34	---			0.875
16	11.76				0.722
17	11.34				0.884
18	11.34				0.696
20	11.13				0.863
21	12.86				0.447
22	12.00				0.769
23	11.88				0.745
Avg.	11.99	24.58	---	---	0.749

* Compression

** Tension

tension, compression and torsional loading.

Figures IV-D-2a and -2b show graphs of axial load versus crosshead displacement. Torque versus angle of twist of the actuator is plotted in Figure IV-D-3. For axial loading, the diagrams depart from linearity at 26 percent and at 35 percent of the ultimate in tension and compression, respectively. The nonlinear portions are characterized by time-dependent behavior as evidenced by the increase of the displacement (creep) during periods of constant load (see Figure IV-D-2a).

Fatigue testing has also been conducted, using completely reversed, load-controlled uniaxial loading. Axial and diametrical strain measurements were taken during these tests. Figure IV-D-4 shows behavior during such loading at a load amplitude of about 60 percent of the ultimate load. This demonstrates further the time dependence shown in Figure IV-D-2a. Cycles 9 and 10 (ABCD) took 240 seconds. When B was reached during the eleventh cycle the rate was reduced by a factor of 1000. A "creeping motion", BE, is evident before the load increases again. The strain range of the "slow" loop (BEFGH), which takes 66.67 hours for completion, is considerably larger than that of the "fast" loop (ABCD). The strain range increased further during the next loop which started at H and ended at I.

The torque versus angle of twist of the actuator curve, Figure IV-D-4, shows much less deviation from linearity than the axial curve due to the "fiber dominance" of this deformation. Deviations from linearity are beyond 50 percent of the ultimate load.

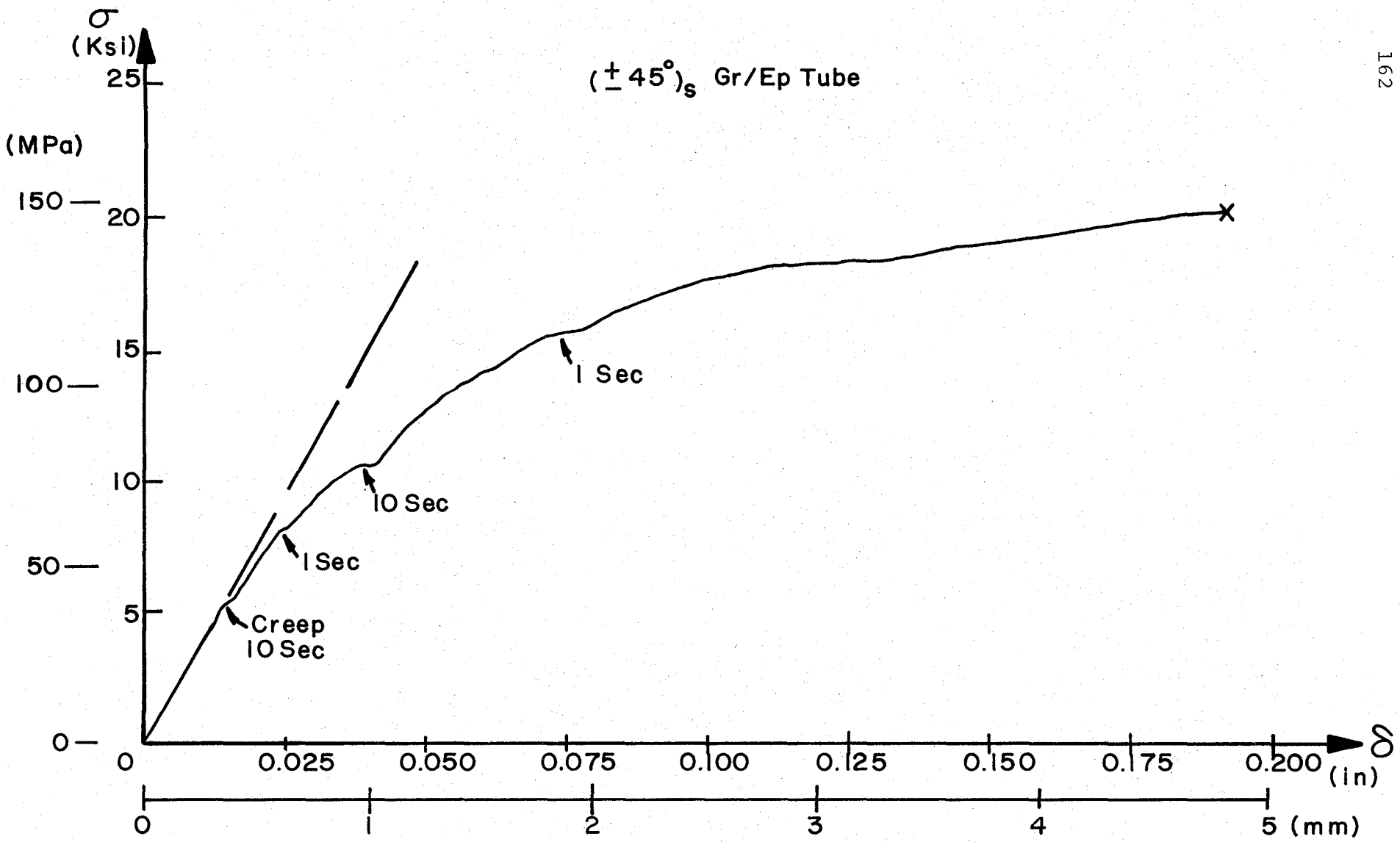

Figure IV-D-2a

Axial Load Vs. Crosshead Displacement for Tensile Loading
(The time dependence - as indicated by the creep deformation during short intervals of constant load - is noteworthy.)

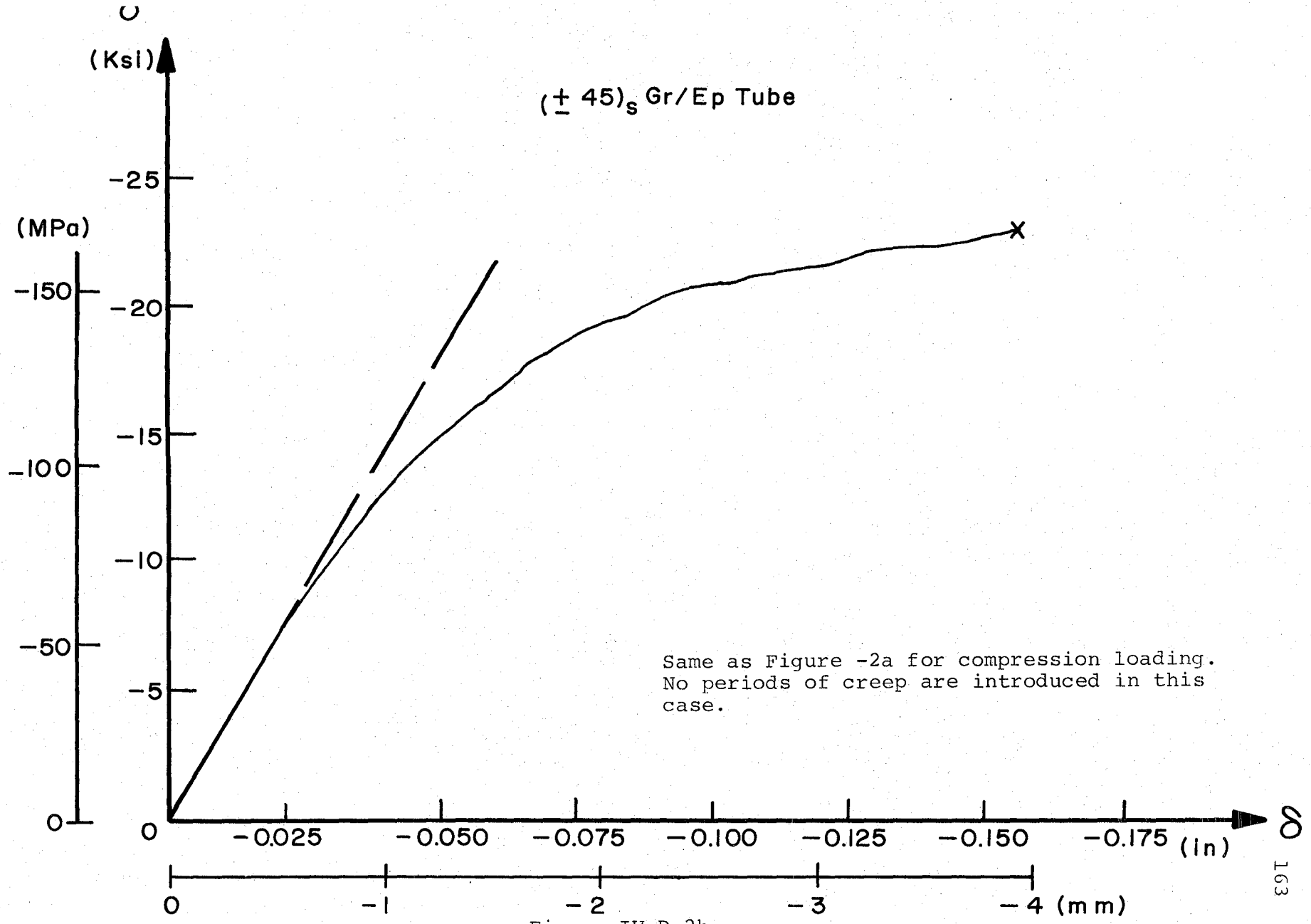

Same as Figure -2a for compression loading. No periods of creep are introduced in this case.

Figure IV-D-2b

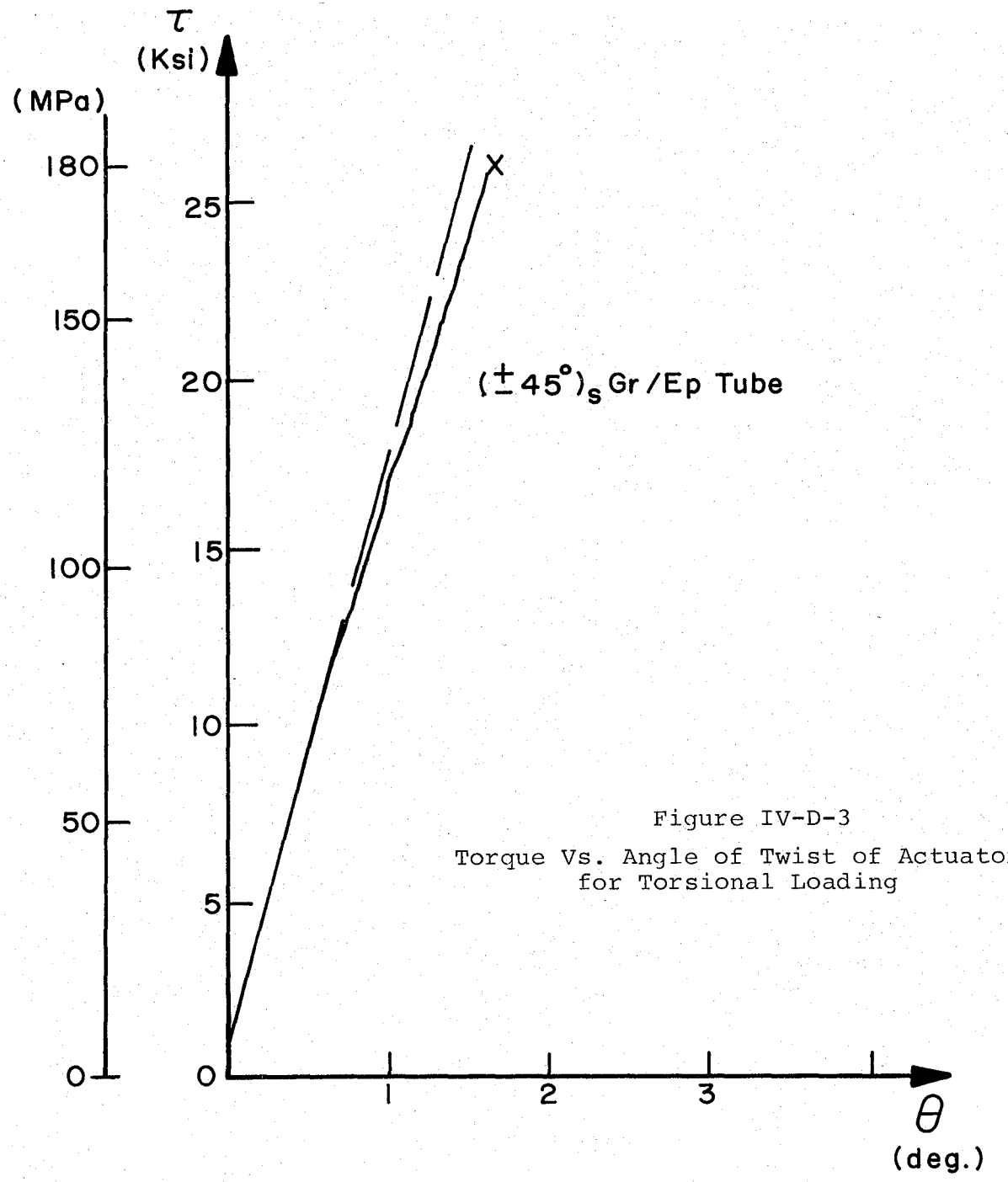

Figure IV-D-3

Torque Vs. Angle of Twist of Actuator for Torsional Loading

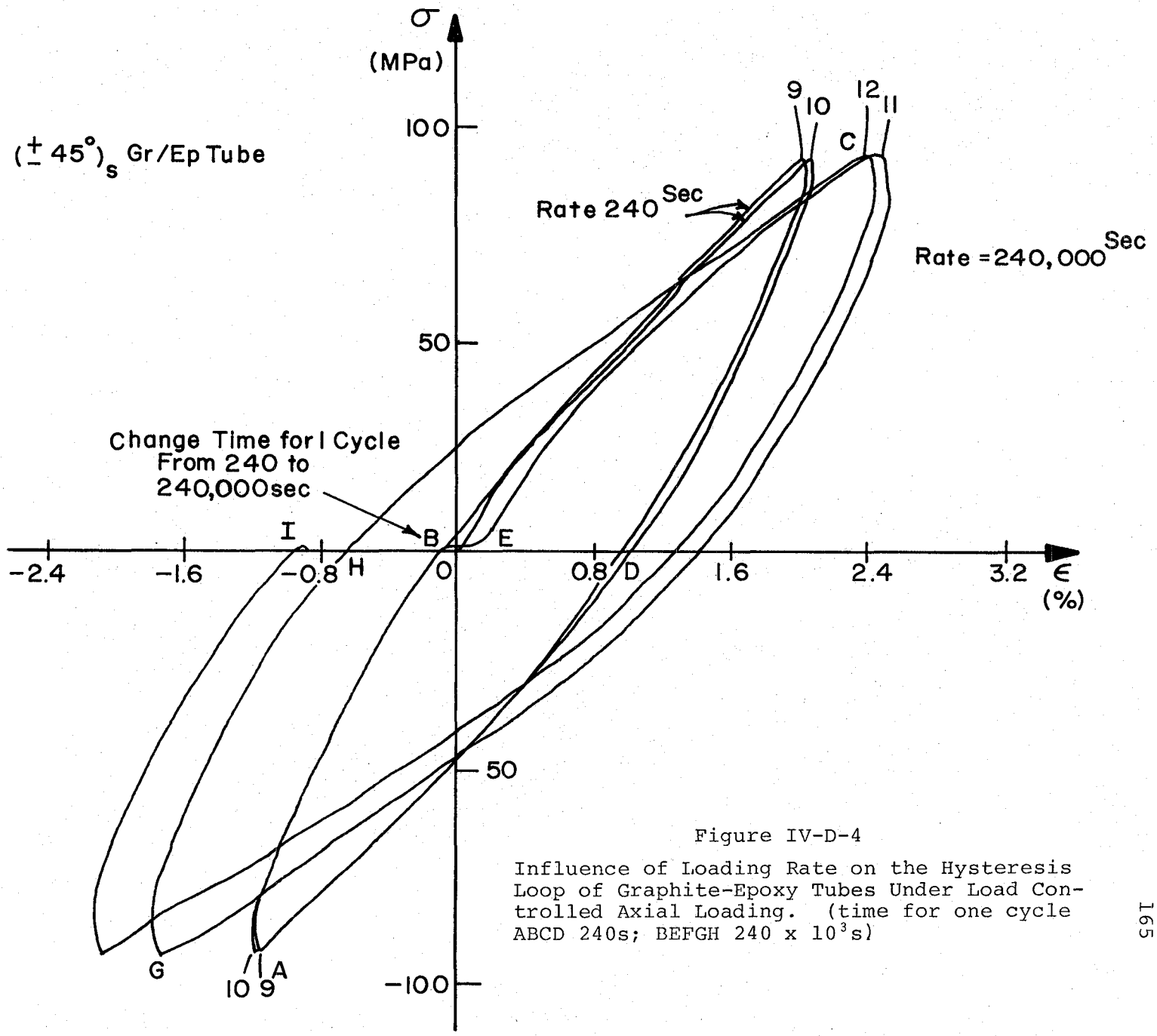

Figure IV-D-4

Influence of Loading Rate on the Hysteresis Loop of Graphite-Epoxy Tubes Under Load Controlled Axial Loading. (time for one cycle ABCD 240s; BEFGH 240 x 10^3s)

As indicated on Figures IV-D-2a, -2b and -3, the ultimate load was determined in each case. The appropriate ultimate strengths are listed in Table IV-D-1.

It is noteworthy that the tubes permit the determination of the compressive ultimate strength without any buckling problems. The ultimate compressive strength would appear to be very comparable to the ultimate tensile strength.

3. Plans for the Upcoming Period

The completely reversed, load-controlled axial tests which are now under way to ascertain the influence of loading rate on the hysteresis loop and on the fatigue life will be continued and completed. They are to be followed by torsion and combined axial-torsion tests.

A paper on biaxial deformation and fatigue behavior is scheduled to be written during the next reporting period.

IV-E ACOUSTIC EMISSION OF COMPOSITE MATERIALS UNDERGOING FATIGUE

Senior Investigators: H. Otsuka
H. A. Scarton

The Acoustic Emission (AE) technique has been shown to be useful in monitoring composite material fracture under conditions of monotonically increasing loads[1,2]*. Different signal amplitudes were shown to be associated with different AE sources; namely, a) low amplitude signals, matrix crazing; b) intermediate amplitude signals, delamination and fiber pull-out and c) large amplitude signals, fiber breakage. The current research deals with the extension of this work to include fatigue failure.

1. Status

Acoustic emission test and data analysis have been performed for composite material tensile specimens under constant load rates. Both count versus time data and length-location of acoustic emission sources have been successfully obtained for (±45°) and (0° -90°) graphite cloth epoxy composites.

2. Progress During Report Period

The shape of the specimens used in fatigue tests is shown in Figure IV-E-1. Reinforcing aluminum tabs were bonded

*Numbers in parentheses in this section refer to the references listed on page 175.

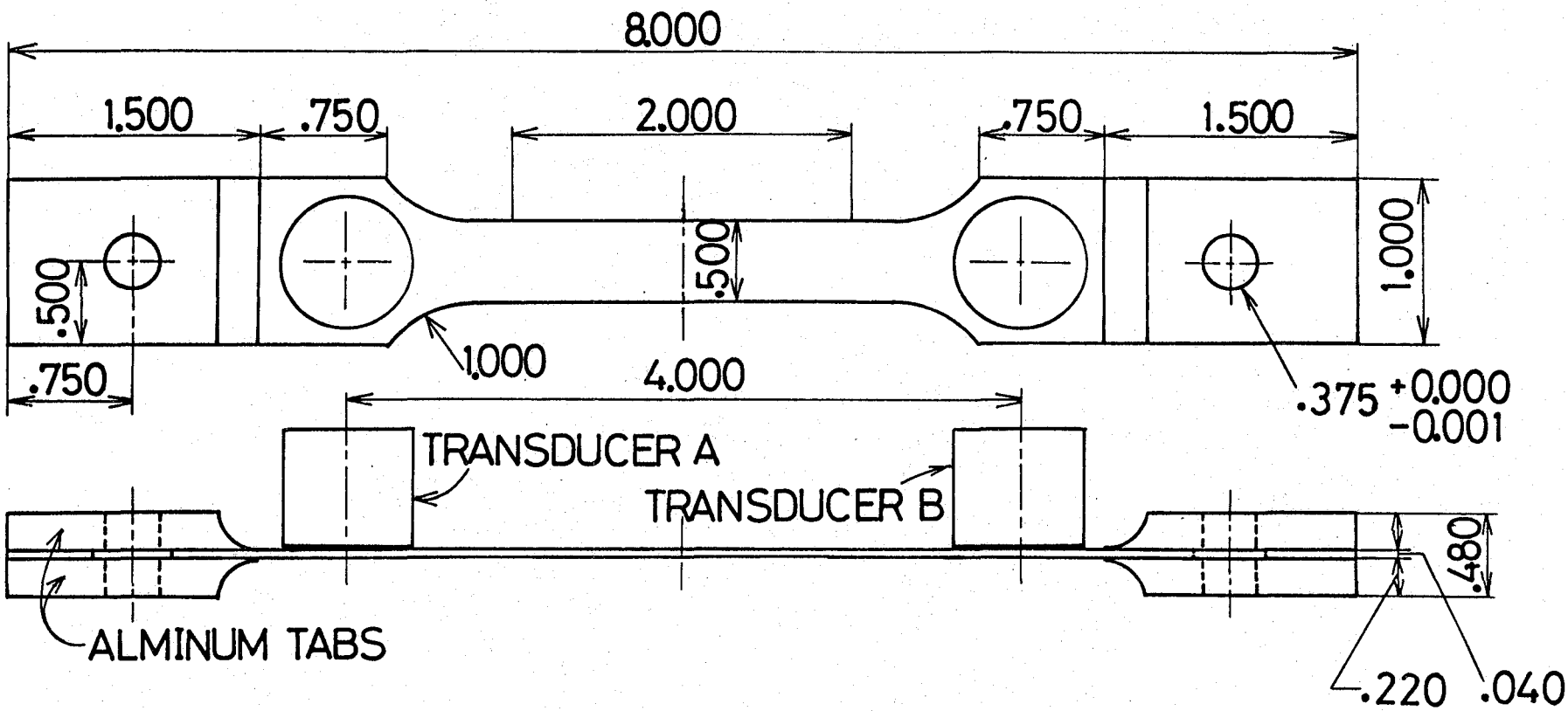

Figure IV-E-1

Test Specimen (dimensions in inches)

to the composite specimens as shown. Load was transferred from the testing machine to the specimens through mechanical, 85 dB attenuator fixtures by steel pins. The materials used in the specimens were carbon cloth-ply with a 0°-90° fiber orientation and a twelve-layer prepreg, carbon-epoxy composite with the following stacking sequence: $(0°, \pm 45°_2, 90°)_s$.

Testing was performed on an Instron 1333 (capacity 50 kN, 25 kN range) using the AE setup shown in Figure IV-E-2. Amplitude distributions of the acoustic emission signals were recorded in memory A and location distributions in memory B.

Tension-tension fatigue tests were performed using both the 0°-90° and twelve-layered graphite-epoxy composites according to the load schedule shown in Figure IV-E-3, where the specific loads undergone and fatigue strength are indicated in Table IV-E-1. Figures IV-E-4 and -5 show the AE count versus fatigue cycles for the 0°-90° and twelve-layer prepreg specimens, respectively. The previously reported static tests[2] showed sharply increasing AE signals (critically active) just prior to failure. The fatigue results presented here show (after an initial period) a linear relationship between fatigue cycles and AE count. This suggests that differences in failure mechanism may exist between these two forms of failure. Critically active behavior was observed on the 0°-90° specimens in fatigue just prior to failure, while no such activity was observed on the prepreg specimen. No defect was

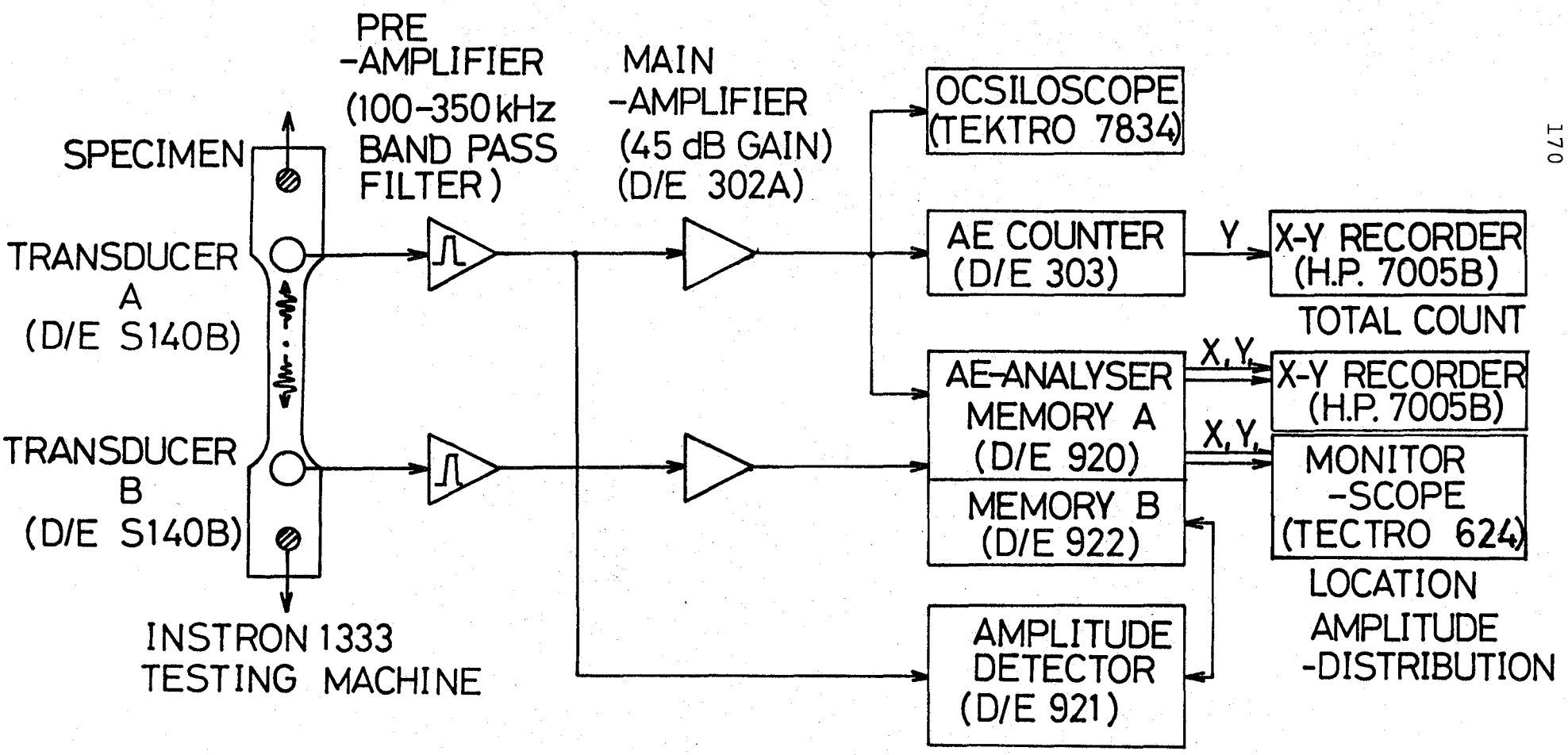

Figure IV-E-2

Acoustic Emission Instrumentation

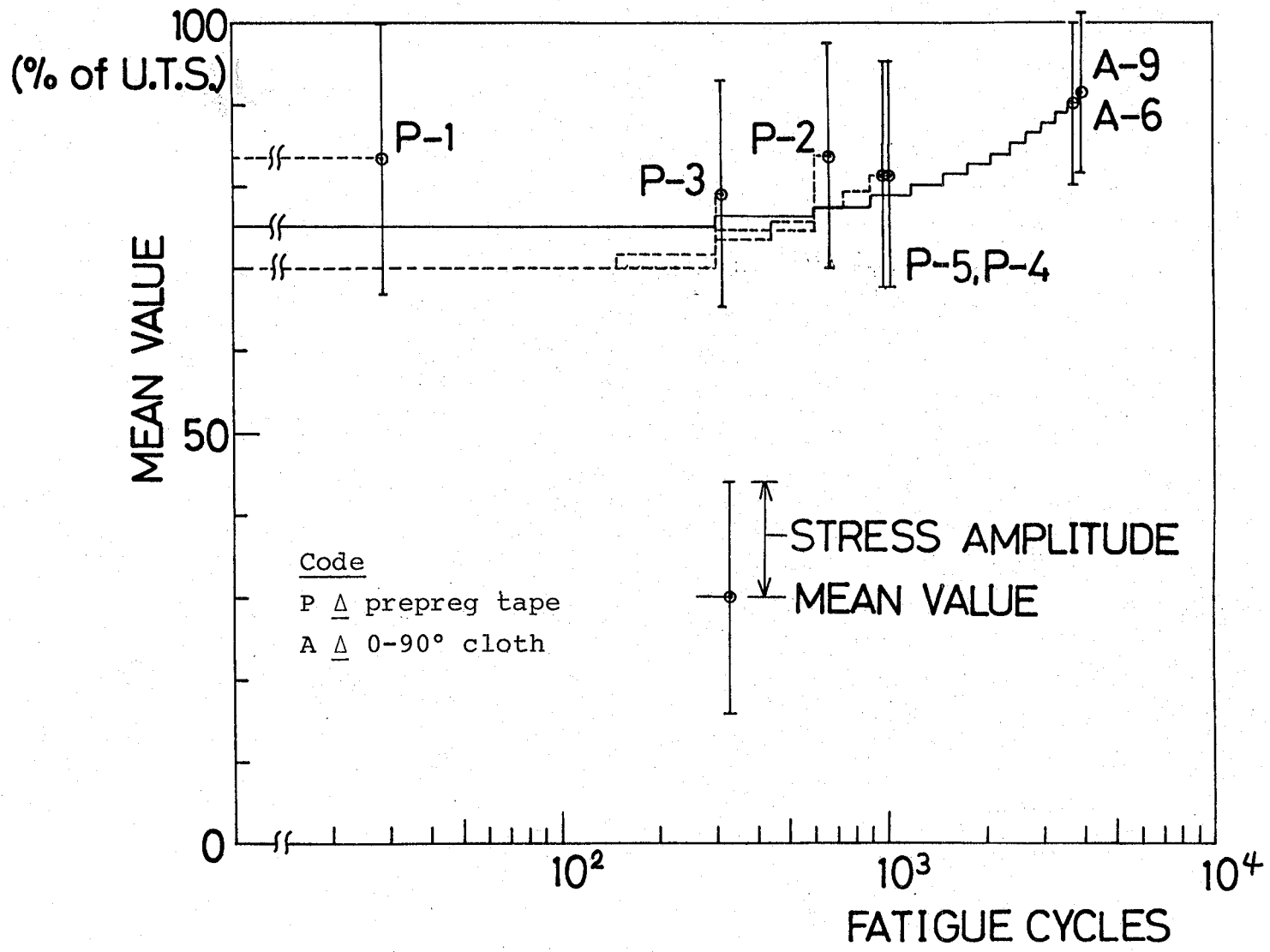

Figure IV-E-3

Load Schedule for Fatigue Test

TABLE IV-E-1

FATIGUE TEST RESULTS

Specimen	Number of Cycles	Load Mean Value ± Variation (psi)	(kg/mm²)	(% of u.T.S.)
#6, 0-90°				
	0→300	43390 ± 5784	30.27 ± 4.034	75.00 ± 10
	300→600	44130 ± 5784	30.78 ± 4.034	76.28 ± 10
	600→900	44860 ± 5784	31.29 ± 4.034	77.55 ± 10
	900→1200	45610 ± 5784	31.81 ± 4.034	78.83 ± 10
	1200→1500	46340 ± 5784	32.32 ± 4.034	80.10 ± 10
	1500→1800	47080 ± 5784	23.84 ± 4.034	81.38 ± 10
	1800→2100	47810 ± 5784	33.35 ± 4.034	82.65 ± 10
	2100→2400	48560 ± 5784	33.89 ± 4.034	83.93 ± 10
	2400→2700	49290 ± 5784	34.38 ± 4.034	85.20 ± 10
	2700→3000	50030 ± 5784	34.89 ± 4.034	86.48 ± 10
	3000→3300	50770 ± 5784	35.41 ± 4.034	87.75 ± 10
	3300→3600	51500 ± 5784	35.92 ± 4.034	89.03 ± 10
	3600→3862	52250 ± 5784	36.44 ± 4.034	90.30 ± 10
#9, 0-90°				
	$\int_{3600}^{0}$	The same as for Specimen #6.		
	3900→3997	52980 ± 5784	36.95 ± 4.034	91.58 ± 10
P-1				
12 Layer	0→29	49194 ± 9838	34.31 ± 6.86	83.33 ± 16.67
P-2				
12 Layer	0→300	41250 ± 8250	28.77 ± 5.940	69.88 ± 13.98
	300→600	44000 ± 8250	30.69 ± 5.940	74.54 ± 13.98
	600→669	49500 ± 8250	34.53 ± 5.940	83.85 ± 13.98
P-3				
12 Layer	0→300	41250 ± 8250	28.77 ± 5.940	69.88 ± 13.98
	300→322	46750 ± 8250	32.61 ± 5.940	79.19 ± 13.98
P-4				
12 Layer	0→150	41250 ± 8250	28.77 ± 5.940	69.88 ± 13.98
	150→300	42350 ± 8250	29.54 ± 5.940	71.74 ± 13.98
	300→450	43450 ± 8250	30.31 ± 5.940	73.60 ± 13.98
	450→600	44550 ± 8250	31.07 ± 5.940	75.47 ± 13.98
	600→750	45650 ± 8250	31.84 ± 5.940	77.33 ± 13.98
	750→900	46750 ± 8250	32.61 ± 5.940	79.19 ± 13.98
	900→1036	47850 ± 8250	33.38 ± 5.940	81.06 ± 13.98
P-5				
12 Layer	0→150	41250 ± 8250	28.77 ± 5.940	69.88 ± 13.98
	150→300	42350 ± 8250	29.54 ± 5.940	71.74 ± 13.98
	300→450	43450 ± 8250	30.31 ± 5.940	73.60 ± 13.98
	450→600	44550 ± 8250	31.07 ± 5.940	75.47 ± 13.98
	600→750	45650 ± 8250	31.84 ± 5.940	77.33 ± 13.98
	750→900	46750 ± 8250	32.61 ± 5.940	79.19 ± 13.98
	900→990	47850 ± 8250	33.38 ± 5.940	81.06 ± 13.98

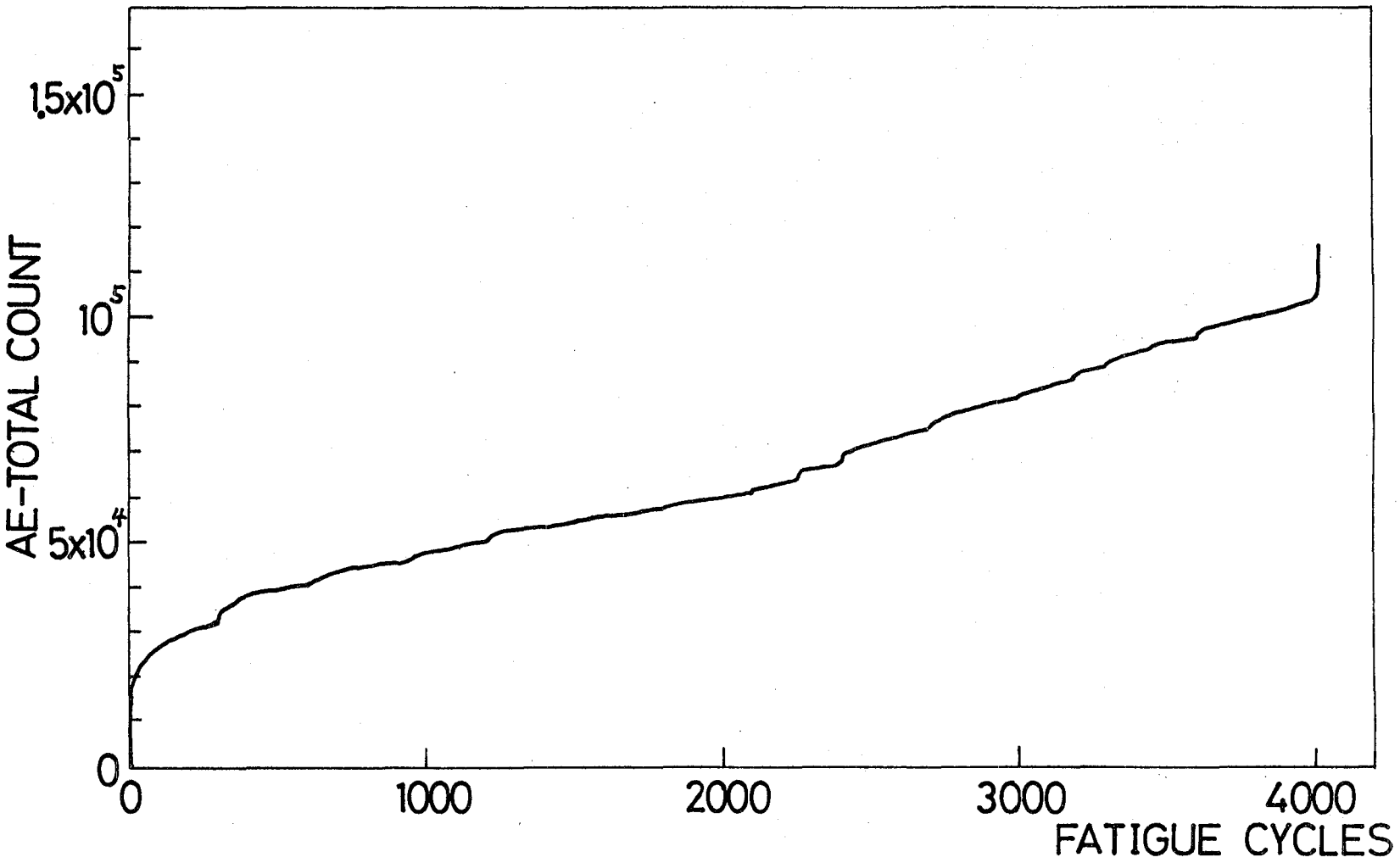

Figure IV-E-4

Acoustic Emission Counts versus Load Cycles
for 0-90° Carbon-Epoxy Specimens

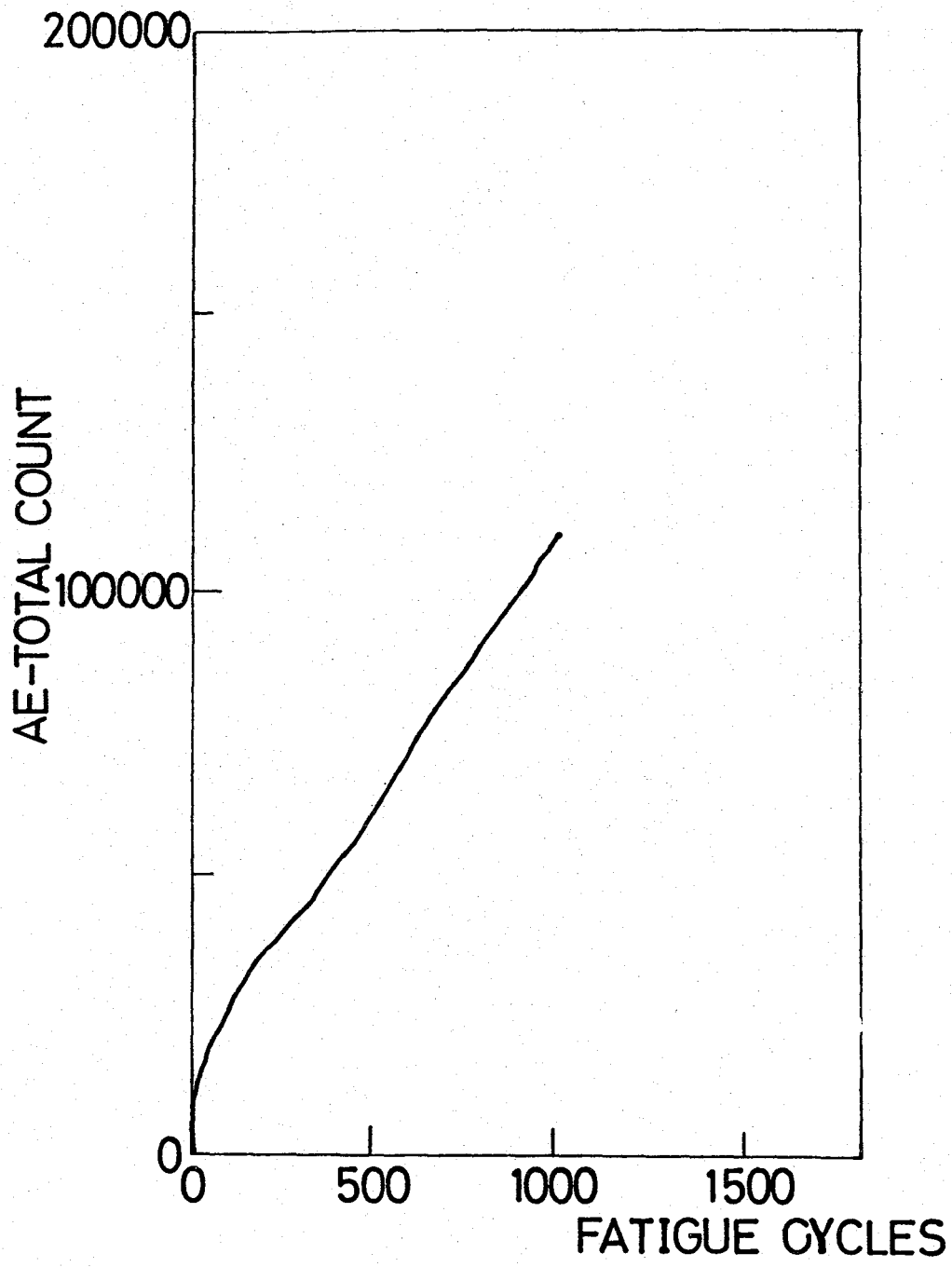

Figure IV-E-5

Acoustic Emission Counts versus Load Cycles
for the Twelve-Layer Carbon Prepreg Specimen

apparent on the 0°-90° specimen, while the twelve-layer specimen failed as a result of the growth of an easily visible defect at the center 0°-90° layers (Figure IV-E-6). The ultimate tensile strengths of the 0°-90° and twelve-layer specimens were 57,851 psi (0.399 GPa) and 59,032 psi (0.407 GPa), respectively. Amplitude distributions (Figure IV-E-7) and location distributions (Figure IV-E-8) were recorded every 150 cycles during the fatigue test. It is possible that the transitions from one given amplitude distribution to another correlate to the growth of the 0°-90° center layer defect. Note that the fixed nature of the multi-modal distribution is maintained with increasing load.

3. Plans for the Upcoming Period

Further work will be devoted to analyzing the acoustic emission process as it relates to the fatigue process as a method of evaluating composite material performance.

4. References

1) Otsuka, H. and H. A. Scarton, "Variation in Acoustic Emission between Graphite- and Glass-Epoxy Composites", Journal of Composite Materials, Submitted for publication July 1980.

2) Otsuka, H. and H. A. Scarton, "Acoustic Emission Testing of Composite Tensile Specimens", NASA/AFOSR 38th Semi-Annual Report, "Composite Structural Materials", June 1980, pp 133-139.

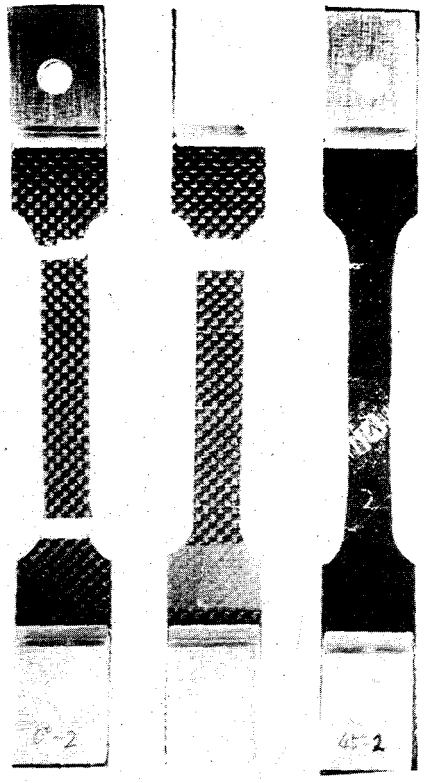

a) front view with two right most specimens used to determine elastic constants

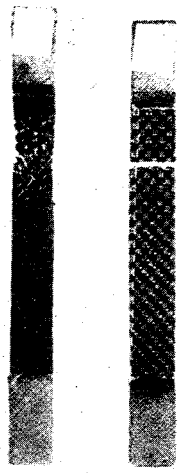

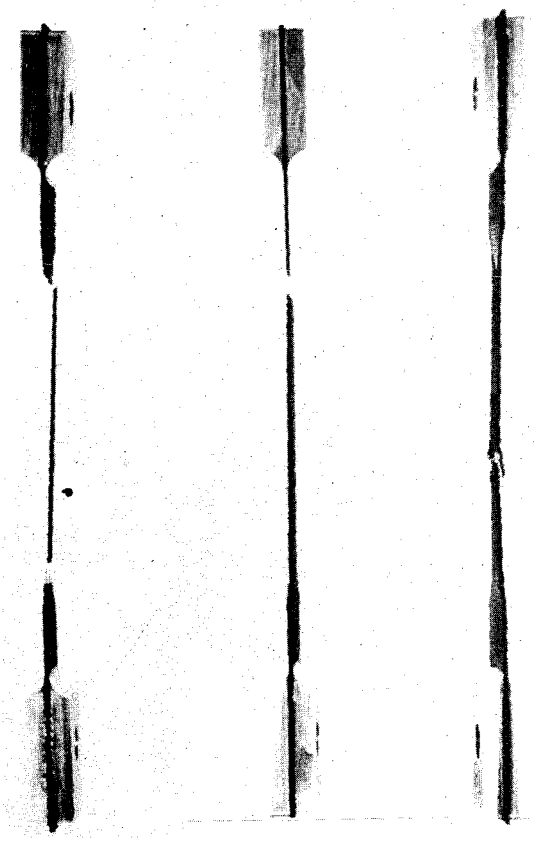

b) side view

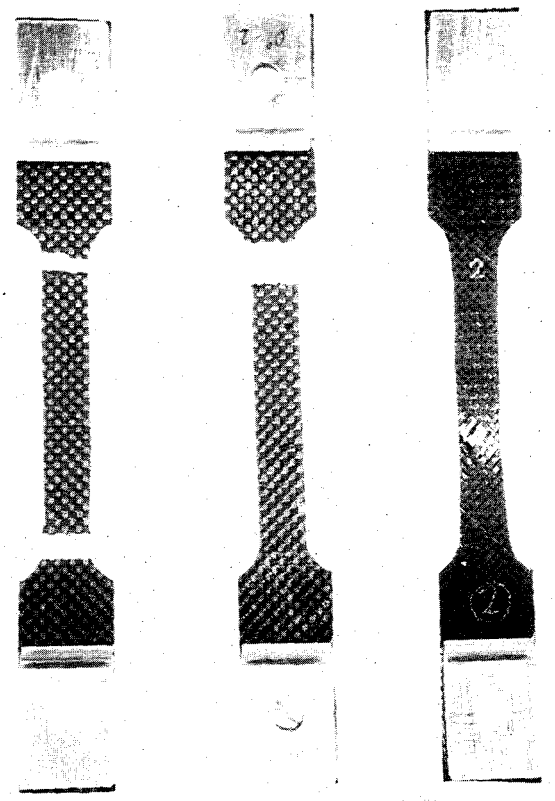

c) rear view

Figure IV-E-6

Failed 0-90° (two left most) Specimens and Twelve-Layered Carbon-Epoxy (third from left) Specimens

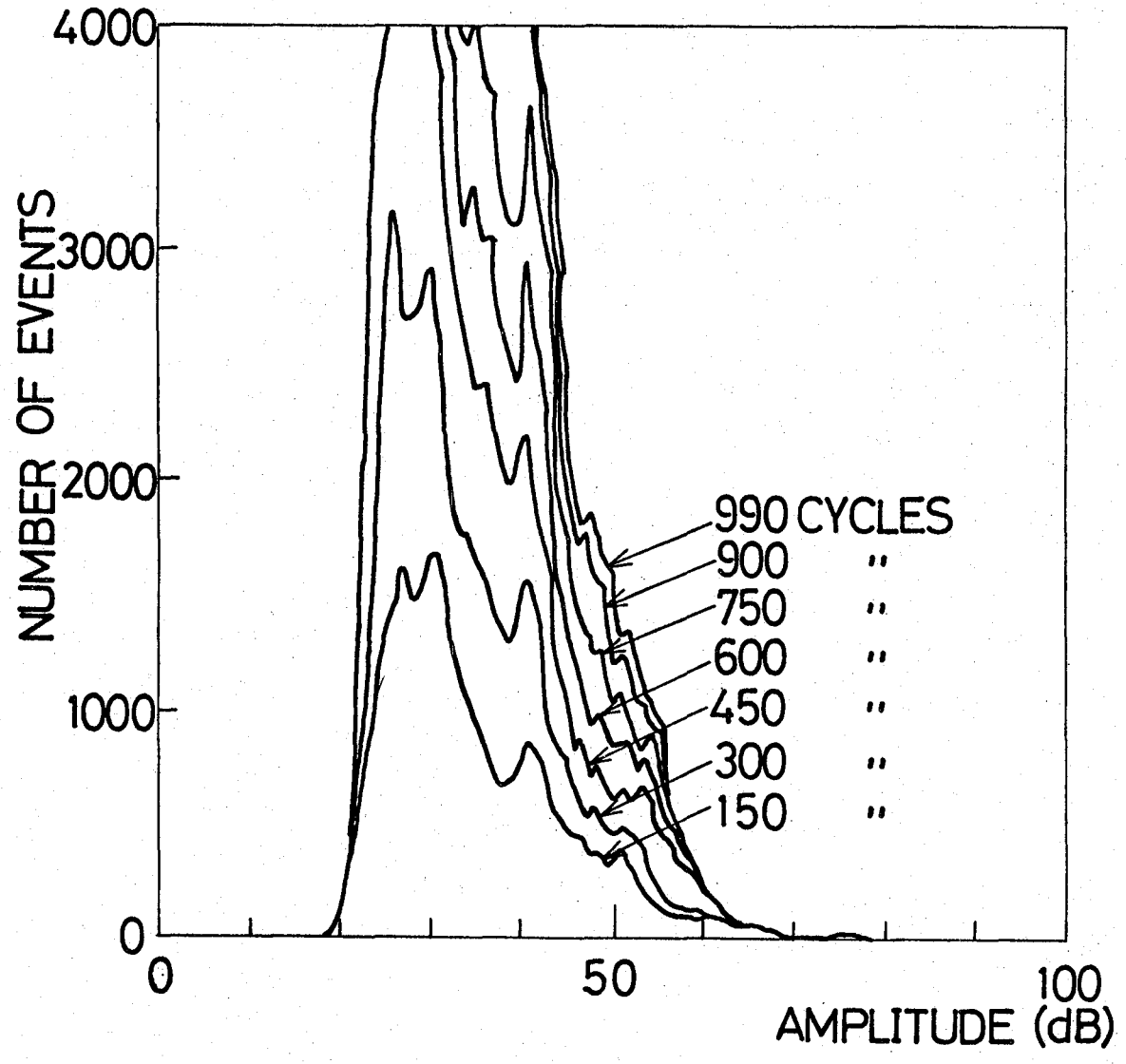

Figure IV-E-7

Transition of Amplitude Distribution for Twelve-Layer Specimen (#5) with Number of Cycles

Figure IV-E-8

Transition of Location Distribution for Twelve-Layer Specimen (#5) with Number of Cycles

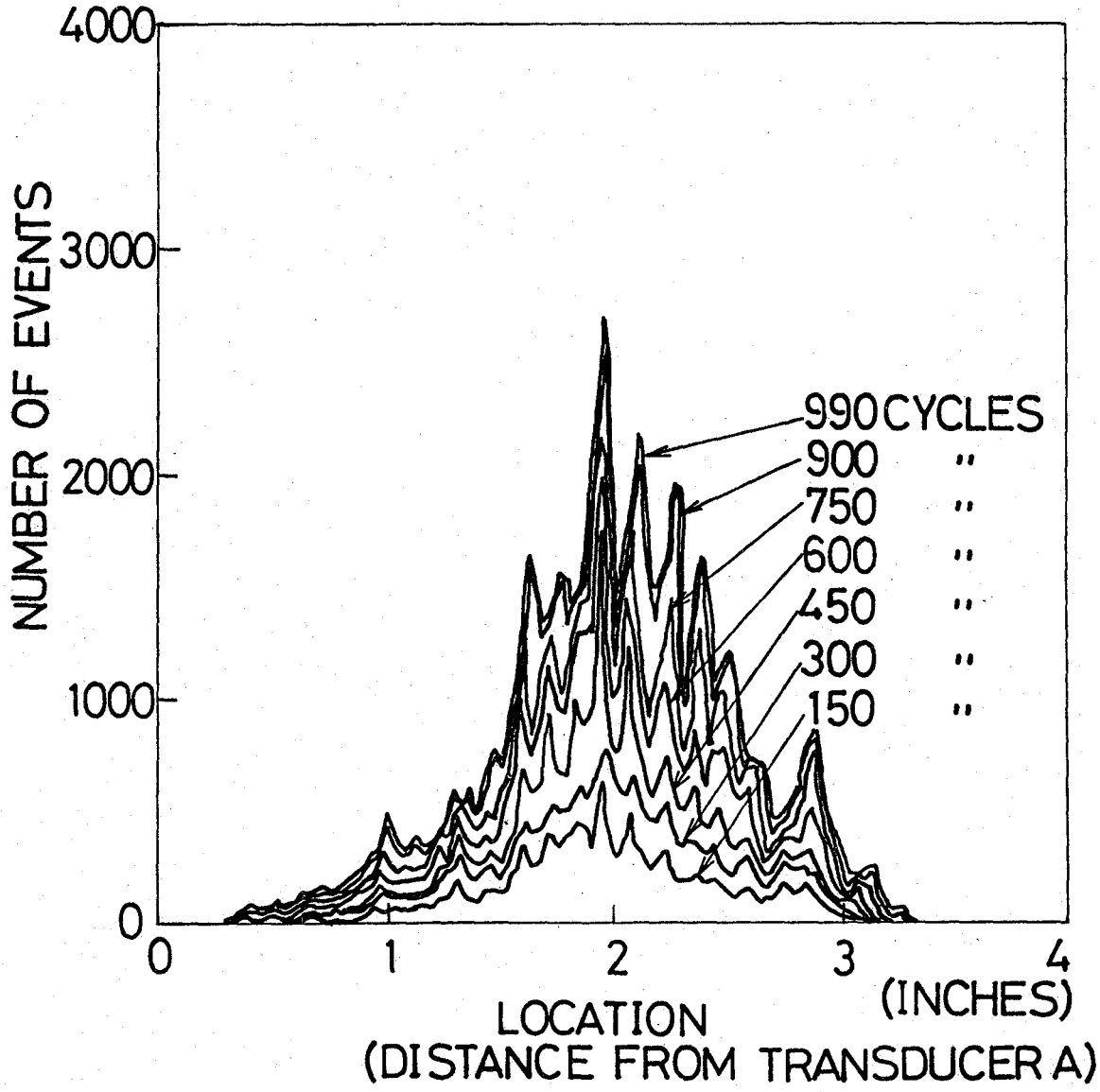

IV-F RESIN MATRIX DEPENDENT CHARACTERISTICS OF COMPOSITES

Senior Investigator: S. S. Sternstein

This project is concerned with those properties of high performance composites which are strongly dependent on the physical properties of the matrix resin. To date, the research has involved the precise viscoelastic characterization of epoxy neat resins, interlaminar failure of composites and the inhomogeneous swelling of and the effects of moisture on composites.

1. Status

Dynamic mechanical spectroscopy, creep and stress relaxation techniques have been used to determine the effect of moisture and temperature on the properties of neat resins. Non-linear plate theories have been reviewed to guide planning of tests intended to determine interlaminar failure tolerance of the epoxy layers between adjacent plies. Constitutive relations have been formulated describing the thermodynamics of water interaction with epoxy resins. The model includes a water dependent modulus of elasticity. Solutions for stress and strain around a carbon fiber in an infinite epoxy matrix have been obtained.

2. Progress During Report Period

Our activities during the current period have emphasized three areas, namely, a) the delamination failure of carbon-

epoxy laminates as a result of out-of-plane loading; b) the stress distribution in various stacking sequence laminates subjected to biaxial, out-of-plane bending; c) the viscoelastic characterization of *in situ* resin as a function of both humidity and temperature. A fourth project on resin cure rheology has been initiated with non-NASA support and is also relevant to this program.

a) Delamination Failure

This project has emphasized the development of a simple but effective test for the study of delamination failure in carbon-epoxy laminates. The test sample consists of a circular disc of roughly 1.3 inches diameter and approximately 10 to 14 plies thickness. The sample is mounted on a special anvil which is attached to an Instron compression load cell. The anvil supports the disc sample around the perimeter at a one inch diameter. The out-of-plane load is applied to the center of the sample using a large ball bearing which is loaded by the Instron movable crosshead. The test geometry may be described as a centro symmetric bend test. It is important to precisely center the ball bearing with respect to the sample anvil so as to maintain a true biaxial deformation.

The load cell circuitry of the Instron has been modified to permit external recording of the load signal. This necessitated building an amplifier, filter and buffer circuit. Crosshead motion is monitored using a highly sensitive LVDT and external amplifier. Thus, direct x-y recording of force

and displacement can be obtained with high accuracy. Finally, the compliance of the machine and load cell have been carefully measured and used to correct measured sample compliances.

The centro symmetric bend test is useful for delamination failure measurements and has been shown to give very reproducible data. It is important to note that this test always initiates failure at the center of the sample and not at the edges. Therefore, the presence of nicks and flaws due to sample preparation is of no significance. While it has these important advantages, however, the centro symmetric bend test should not be viewed as providing a polar-symmetric situation. The fact that each filament layer has non-zero thickness means that the three important moments of lamina thickness about the plate neutral axis (zero, first and second order of the depth dimension) cannot all be made identical, as one changes stacking angle from one lamina to another.

Samples were prepared in a press from prepregs. The stacking sequences used thus far include the following 12-ply laminates: (A) $[0/90]_{3S}$, (B) $[0,45,90,135,0,45]_{S}$, and (C) $[0,30,50,90,120,150]_{S}$. In choosing these, priority was given to perserving the angle between adjacent plies through the depth of a particular sample. Sample A will be referred to as a 90° sample in that each ply rotates by 90°; similarly, samples B and C are 45° and 30° samples, respectively.

The stacking sequences all contain a screw axis symmetry of 90°, 45° or 30° per ply. Note that sample B, which has more layers with filaments in the +45° direction than the -45°

direction could only have been "balanced", in that sense, by either relaxing the "equal angle between adjacent plies criterion" or changing the total number of plies from that used for samples A and C. Retaining the relationships among samples was considered more important than "balance" in that conventional sense.

A typical load versus disc (center) deflection curve is shown in Figure IV-F-1 for a 90° sample. The characteristic vertical drop around 80 kg load is the first delamination failure. Fresh samples either unloaded or loaded to less than roughly 70 kg have been examined in the Acoustic Imaging Lab of Professor Das at R.P.I. and show no signs of delamination; conversely, the sample shown in Figure IV-F-1 clearly shows a large central delamination when examined ultrasonically.

Figure IV-F-2 shows another 90° sample which was first subjected to 50 cycles of deflection between 0 kg and 50 kg. The sample was then tested to 100 kg. Clearly, the precycle test had little effect, if any, on the 80 kg load drop.

A 90° sample was preconditioned in boiling water for 1000 hours and then tested, as shown in Figure IV-F-3. The load at which failure occurs is markedly reduced to about 35 kg, but the sharp load drop as seen in Figure IV-F-1 is now an inflection with a significant drop in stiffness beyond that point.

The first cycle failure of a dry 45° sample is shown in

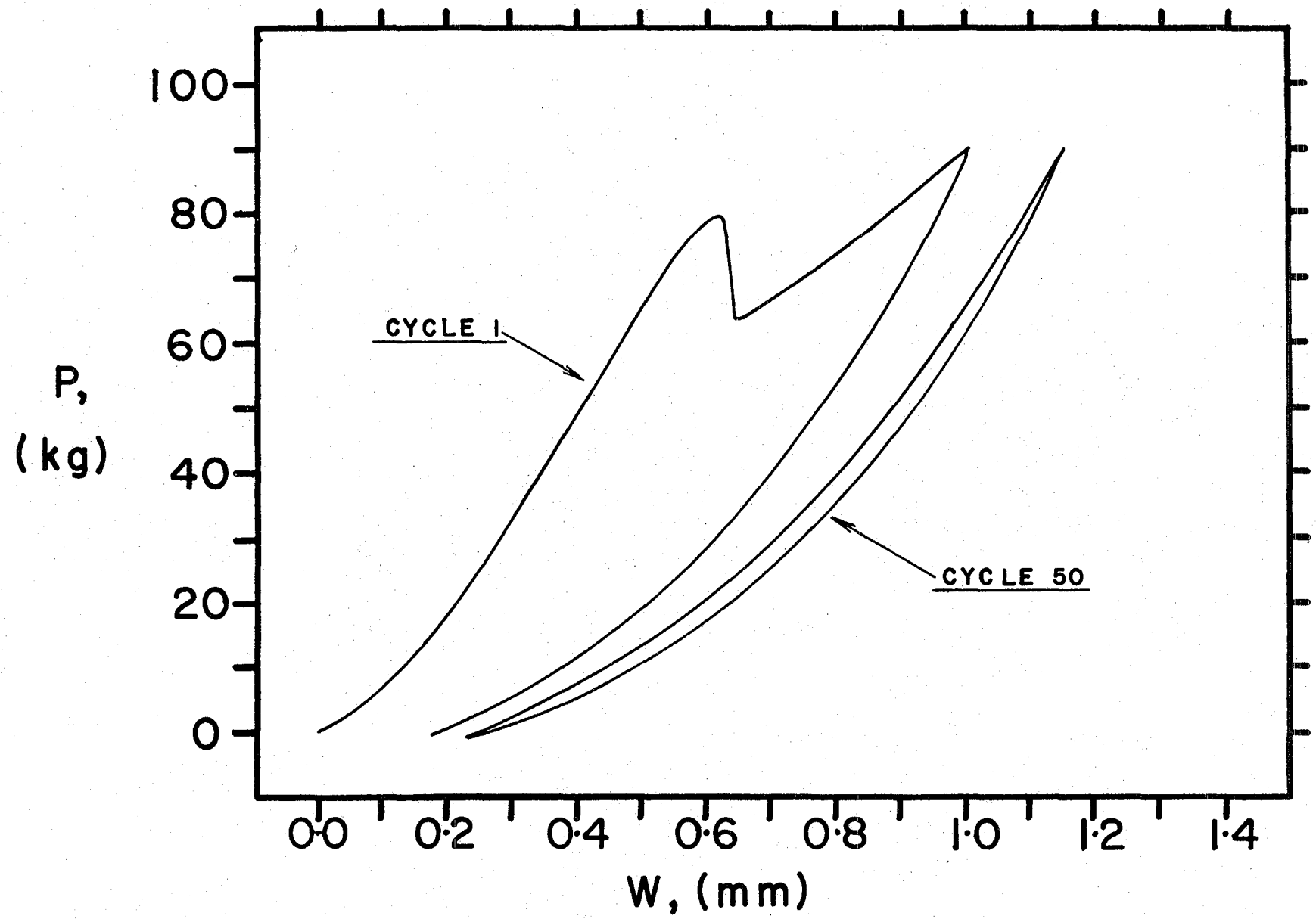

Figure IV-F-1

Load vs. Deflection at Disc Center (90° sample, no pre-conditioning)

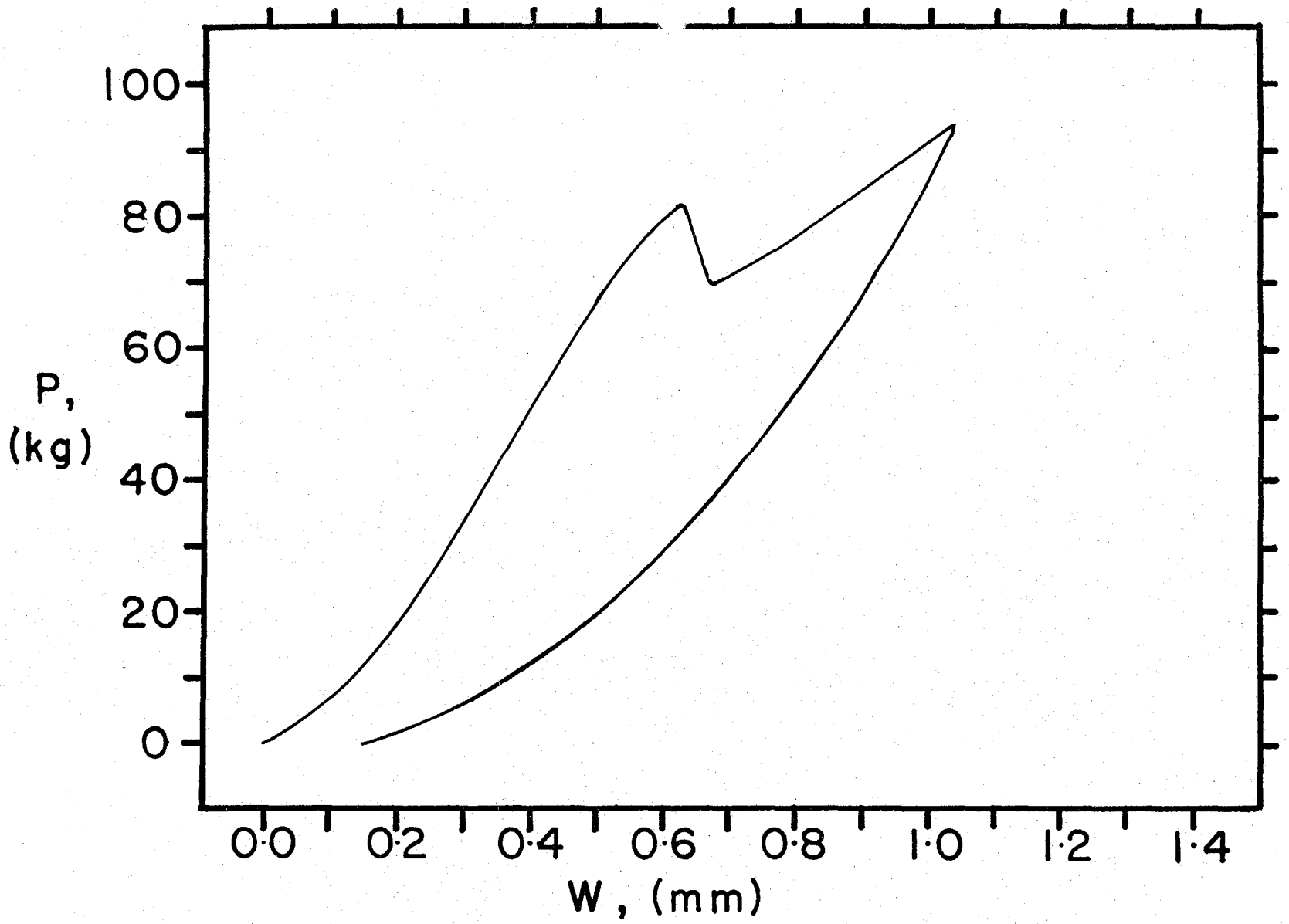

Figure IV-F-2

Load vs. Deflection at Disc Center (90° sample, prior load; 50 cycles between 0 and 50 kg)

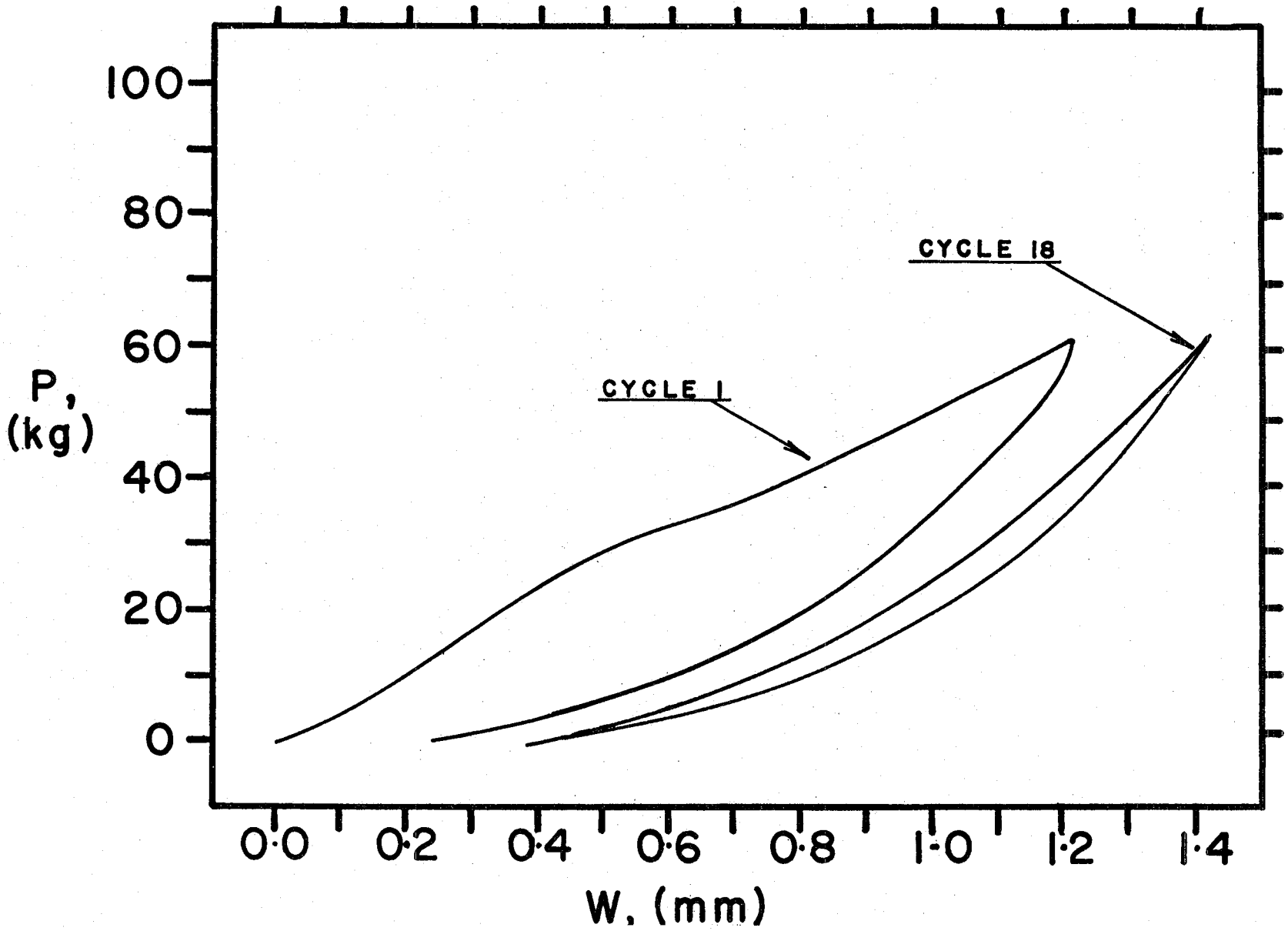

Figure IV-F-3

Load vs. Deflection at Disc Center (90° sample, preconditioned 1000 hrs. in boiling water)

Figure IV-F-4. When compared to Figure IV-F-1, it is seen that the delamination failure point is reduced to roughly 67 kg (vs. 80 kg for the 90° sample) and the load drop is much smaller.

A brief summary of a statistically significant number of samples is given in Table IV-F-1.

TABLE IV-F-1

FAILURE CHARACTERISTICS OF VARIOUS LAMINATES

Property	90° Sample	45° Sample	30° Sample
$\overline{P}_B$ (kg)	79.7	68.6	70.4
$\overline{\Delta P}_B$ (kg)	15.0	2.70	Inflection
$\overline{X}_B$ (mm)	0.683	0.619	0.669

where: $\overline{P}_B$ = mean load at first failure

$\overline{\Delta P}_B$ = mean load drop at first failure

$\overline{X}_B$ = mean deflection at first failure

Finally, we note that the results are reasonably independent of sample size. Figure IV-F-5 shows a 90° sample which was tested using an anvil $\sqrt{2}$ times the diameter used in Figure IV-F-1. The first delamination failure occurs at 87 kg and has a load drop of 14 kg which is within the statistical expectation for 90° samples.

b) Stress Analysis

A detailed analysis of the elastic stress distribution in the laminates used in section a) above is being performed

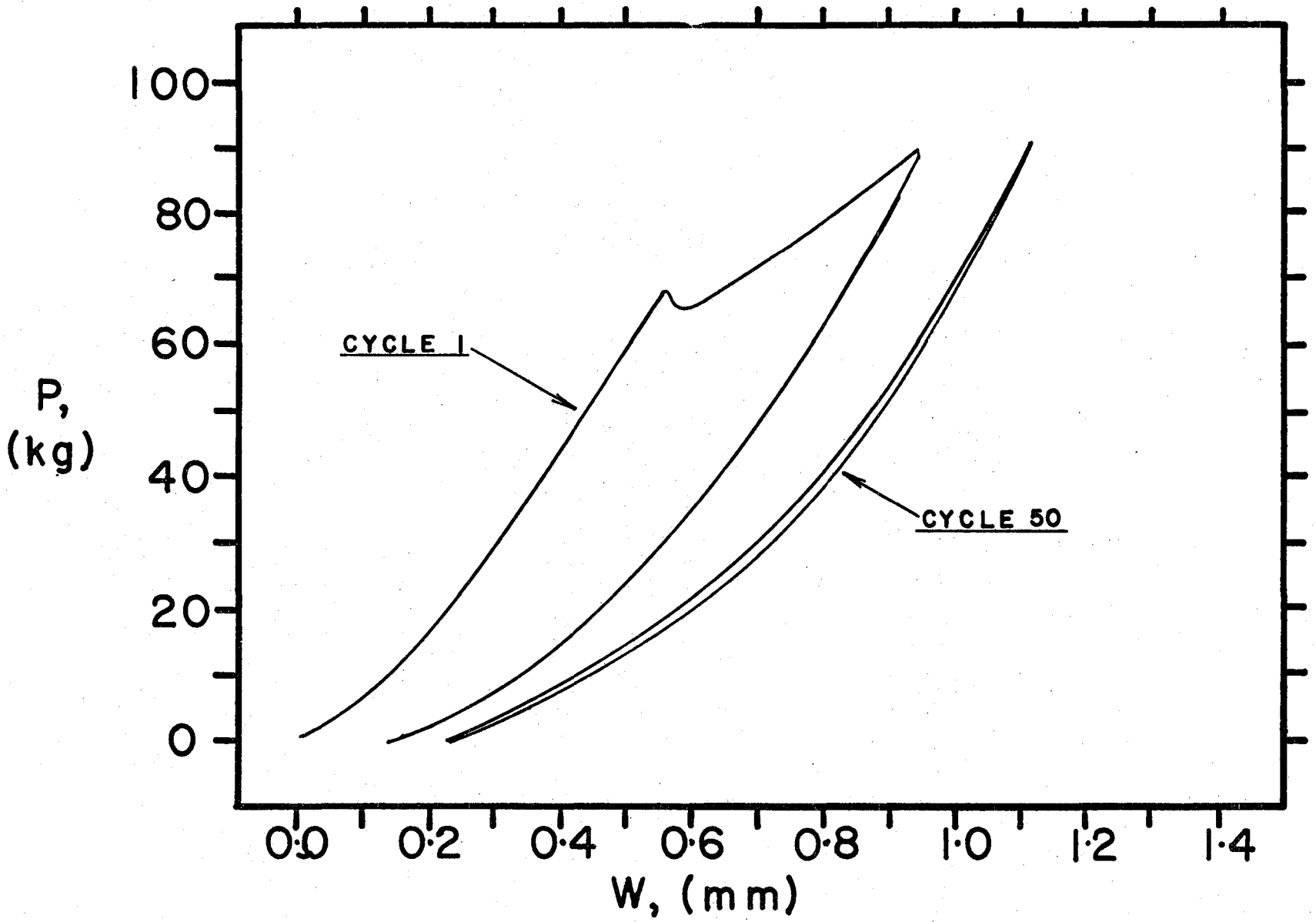

Figure IV-F-4

Load vs. Deflection at Disc Center (45° sample, no precon-ditioning)

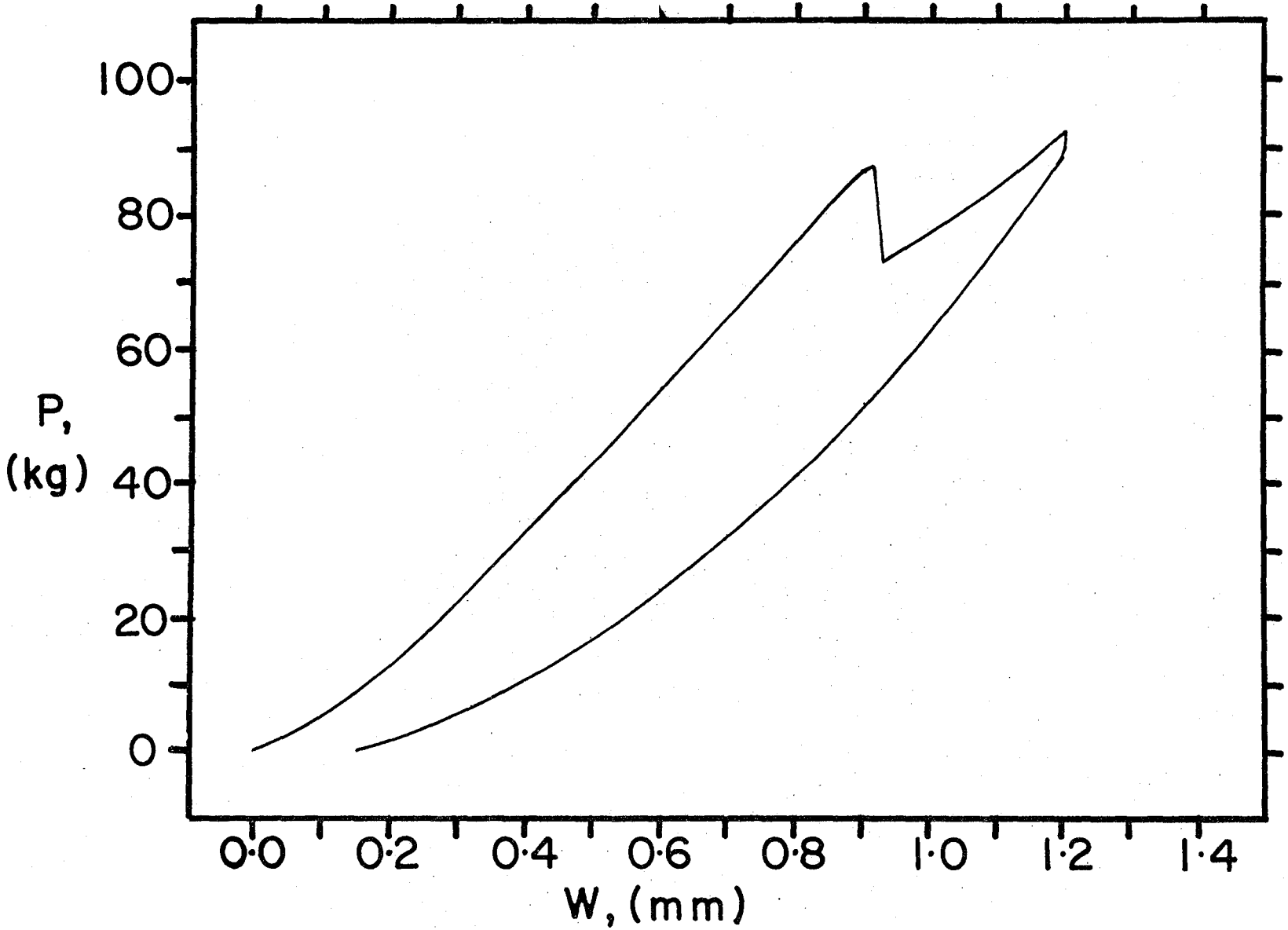

Figure IV-F-5

Load vs. Deflection at Disc Center (90° sample, no preconditioning; outer dia. $\sqrt{2}$ times standard)

using modifications of laminated plate theory. In particular, we have been concerned with the state of stress at the interfaces between plies. For this reason it has been essential to satisfy both the condition of stress equilibrium at each interface as well as the condition of displacement continuity. Simple laminated plate theory as used by many authors does not give equilibrium of the stresses at each interface. To provide such equilibrium, at least a quadratic distribution of displacement through each ply thickness is called for; a different quadratic is required for each ply.

Some results are shown here, but a complete analysis and discription of our findings will be published shortly. The out-of-plane stress component $\sigma(rz)$ is shown versus thickness (depth z) for a 90° sample in Figure IV-F-6 at angle 0°. The same stress component, $\sigma(rz)$, is shown at angle 30° in Figure IV-F-7. Similarly, the stress component, $\sigma(\phi z)$, is shown at an angle of 30° in Figure IV-F-8.

The maximum shear stress [out-of-plane resultant of $\sigma(\phi z)$ and $\sigma(rz)$] is shown versus angle for the various interfaces in Figure IV-F-9 and a polar representation is given in Figure IV-F-10.

The maximum out-of-plane shear stress resultant for a sample having a stacking sequence of $(0)_{12}$ is shown in Figure IV-F-11 and should be compared to Figure IV-F-9 for the 90° sample.

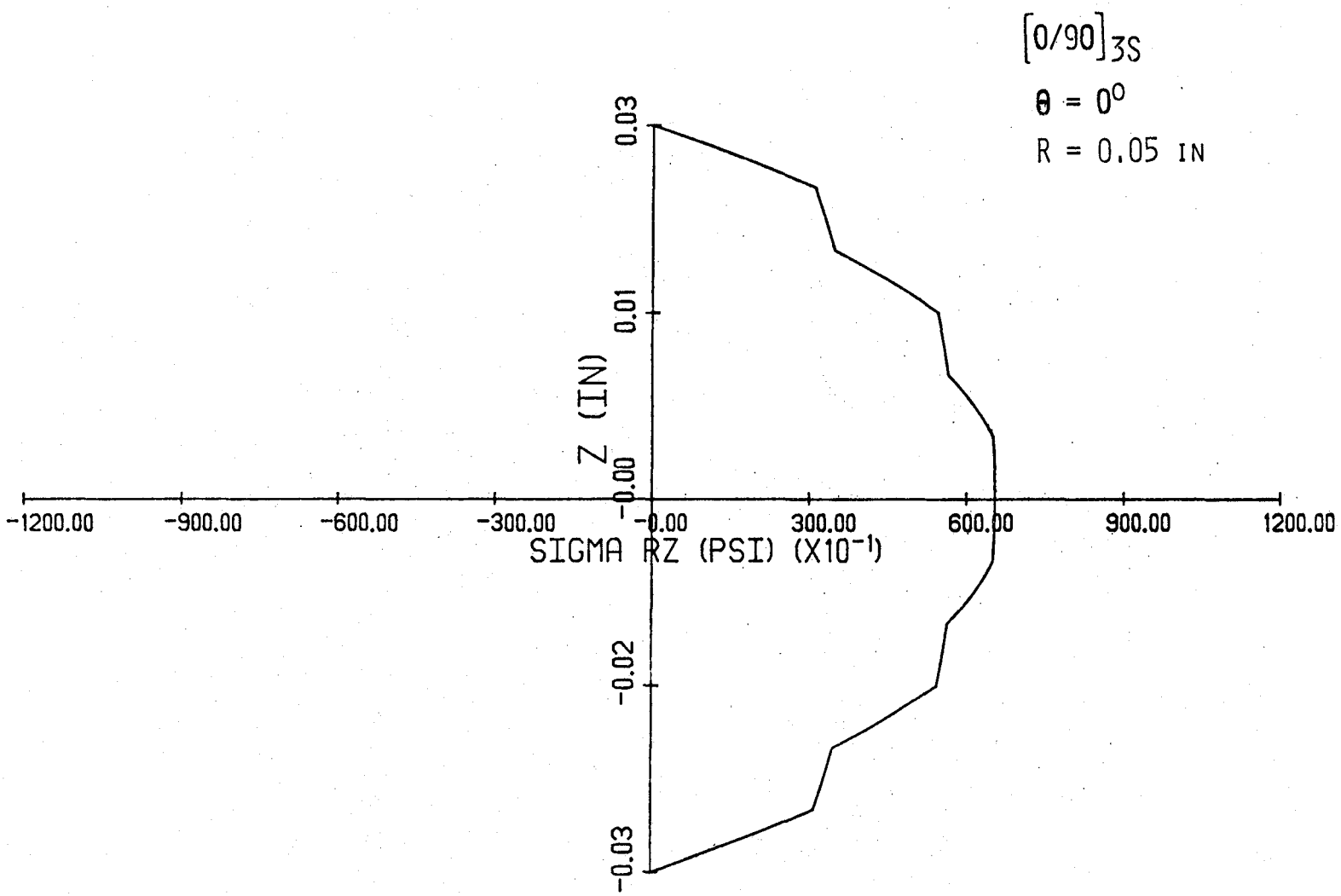

Figure IV-F-6
Out-of-Plane Stress Component (σ_{rz}) vs. Plate Depth (z)
(90° sample at angle ψ = 0)

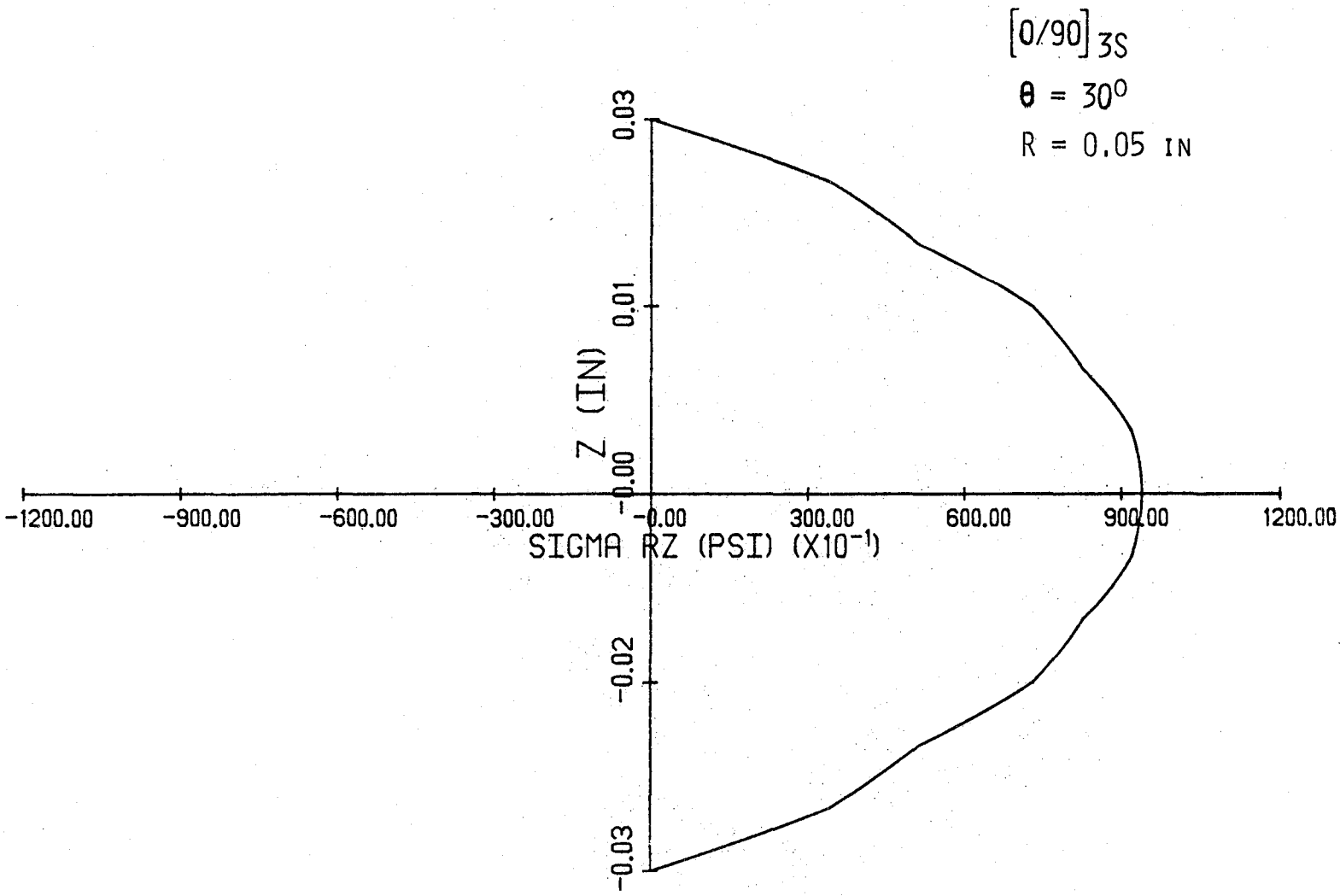

Figure IV-F-7
Out-of-Plane Stress Component (σ_{rz}) vs. Plate Depth (z)
(90° sample at angle 30°)

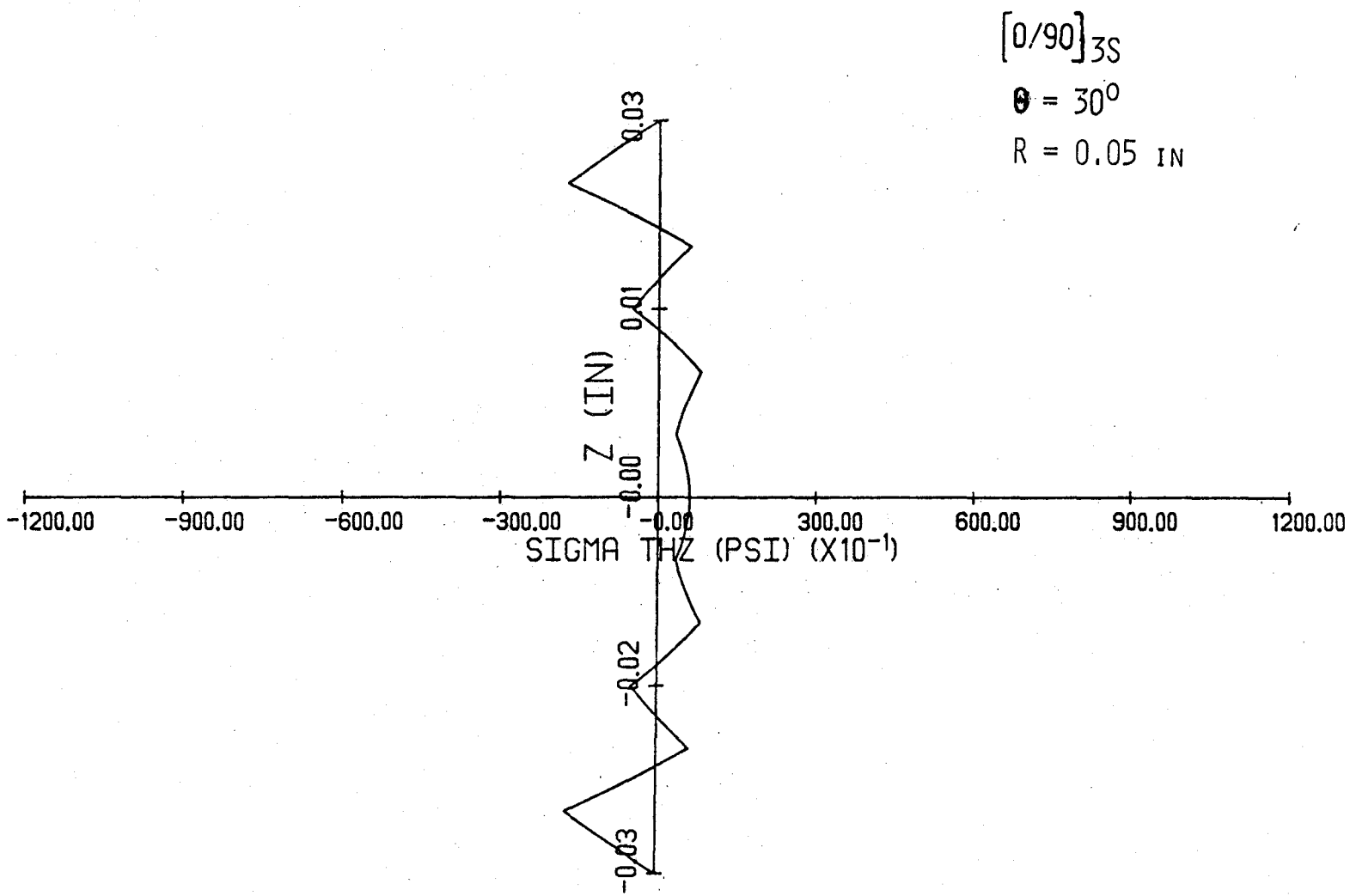

Figure IV-F-8
Out-of-Plane Stress Component ($\sigma_{\phi z}$) vs. Plate Depth (z)
(90° sample at angle 30°)

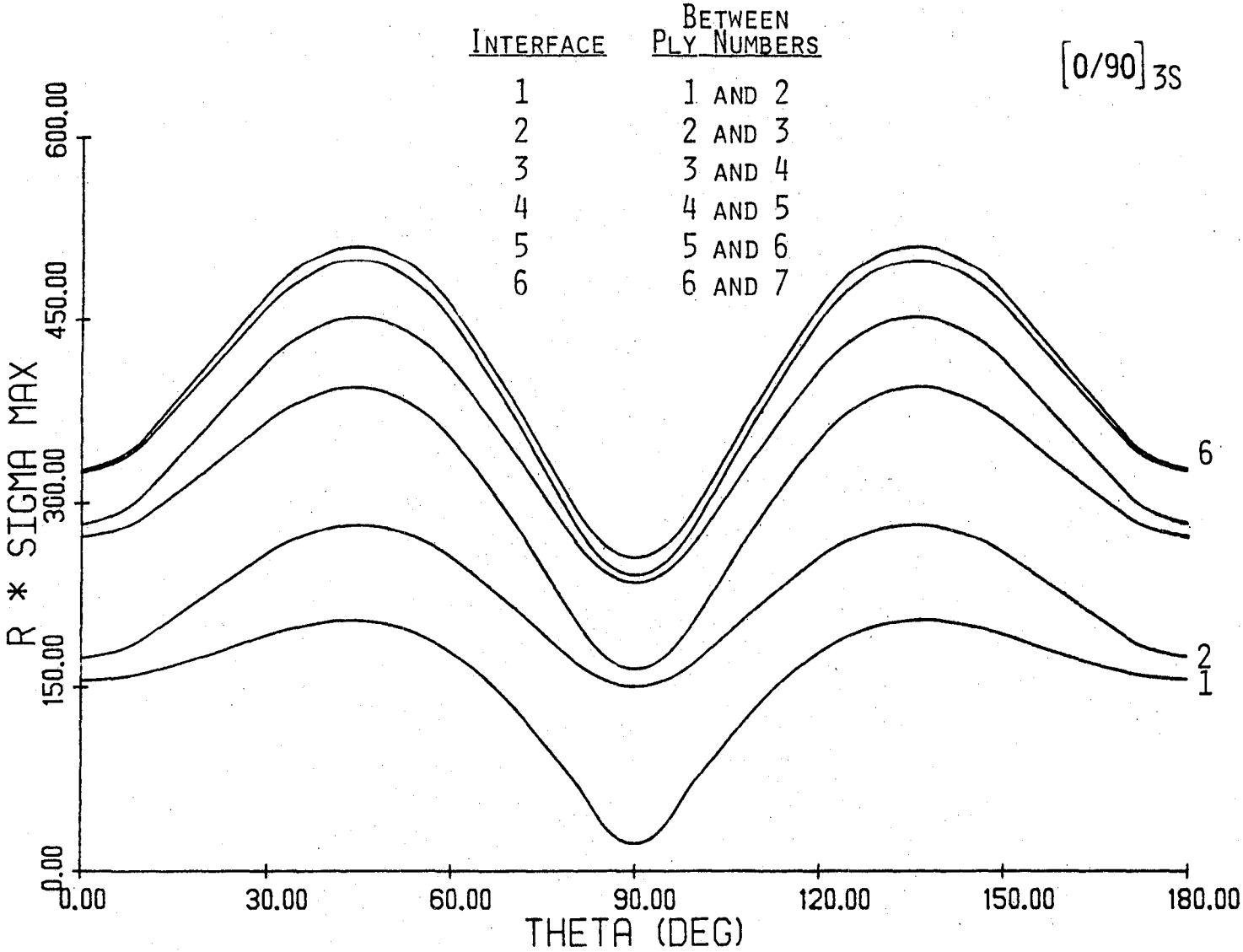

Figure IV-F-9

Maximum Shear Stress vs. Angle for Various Interfaces Between Lamina (90° sample)

$[0/90]_{3S}$

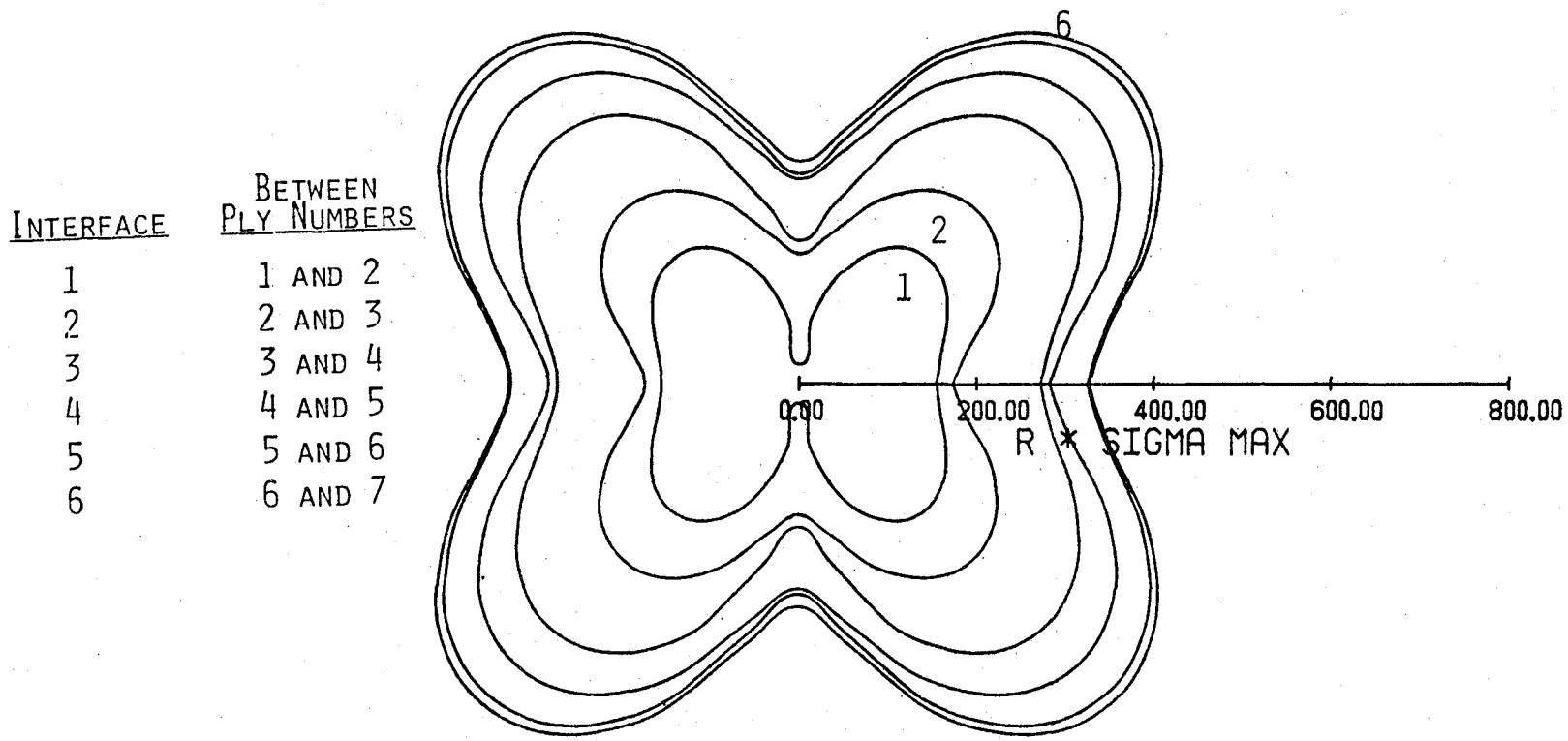

Figure IV-F-10

Polar Representation of Maximum Shear Stresses for Various Interfaces Between Lamina (90° sample)

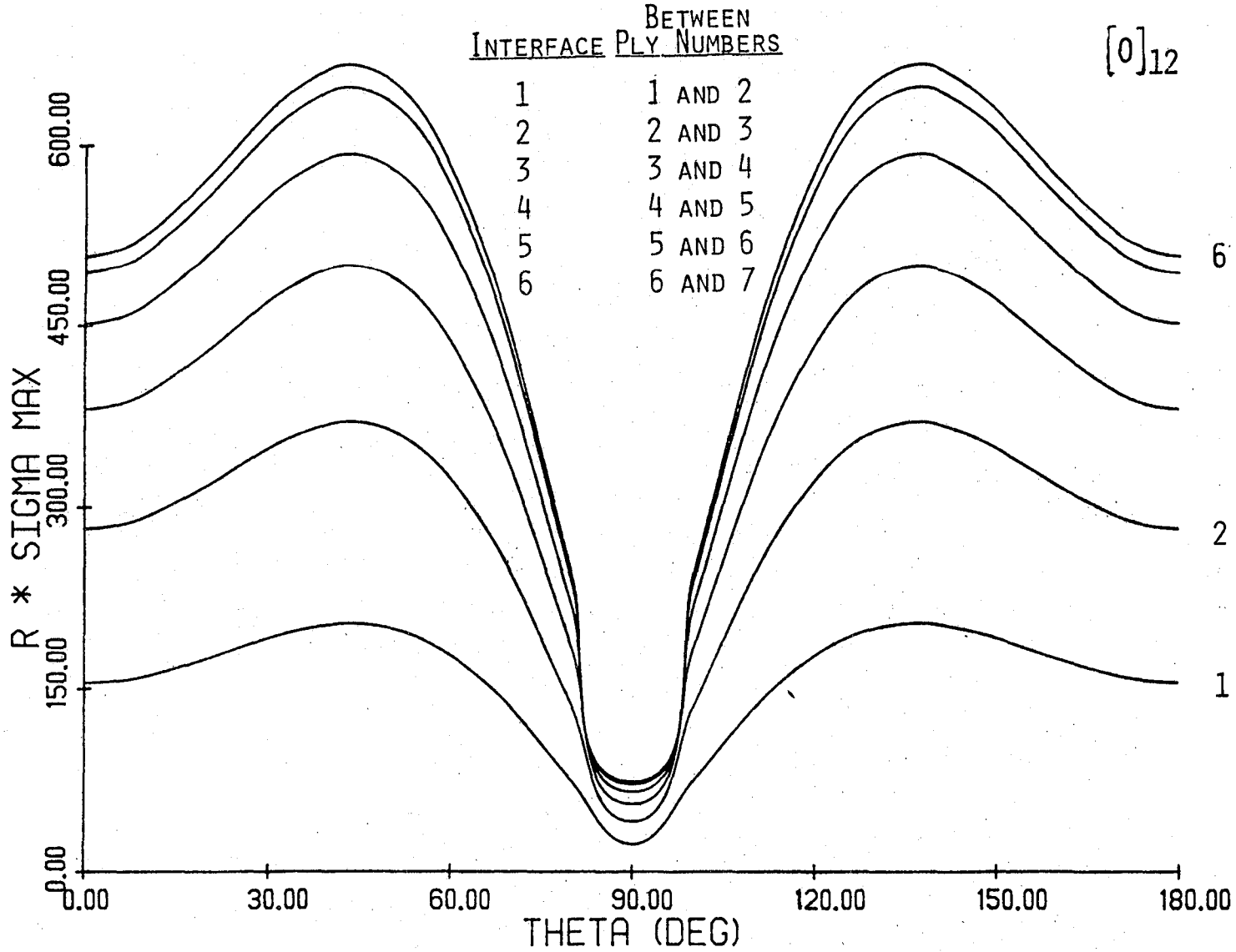

Figure IV-F-11

Maximum Shear Stress vs. Angle for Various Interfaces Between Lamina (unidirectional, $(0°)_{12}$, sample)

c) Viscoelastic Study

The sample and loading geometry described in section a) has also been used in our dynamic mechanical spectrometer to study the in situ glass transition behavior of the epoxy resin. The sample is under load servo control and is programmed with a static load of 3 kg and a dynamic load of 1 kg amplitude. Frequency and temperature are computerized and the dynamic analysis (dynamic modulus and loss factor) is performed using a Fourier type correlation in an instrument referred to as a "Dynalyzer".

Typical results for a 90° sample are given in Figures IV-F-12 and 13. Figure IV-F-12 shows the loss factor (tan delta) at 6.5 Hz versus temperature. The effect of water is quite apparent after the sample is reheated. Notice the reduction in mechanical loss at 100°C and increase by 5° of the glass transition (at 160°C) upon the second heating. This is not due to post-curing. The dynamic modulus $|E^*|$ is shown in Figure IV-F-13. These "small-strain" dynamic results are extremely useful in the characterization of samples, particularly in regard to sample batch-to-batch variations in either processing or starting materials.

3. Plans for the Upcoming Period

We intend to continue the centro symmetric bending tests using additional ply arrangements to further ascertain the effects of temperature, humidity and load rate. Further, an

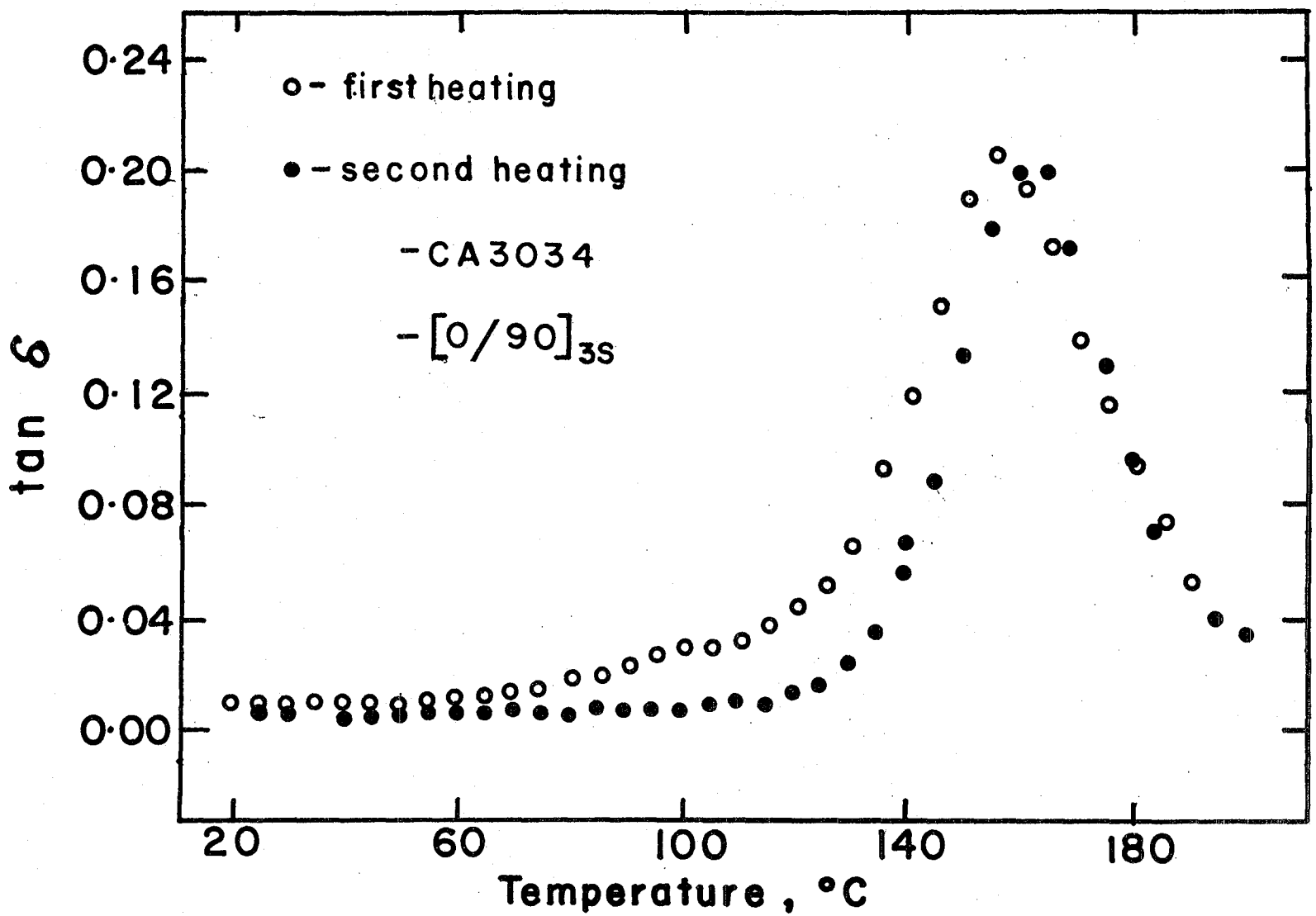

Figure IV-F-12
Loss Factor (tan δ) vs. Temperature (°C)
(90° sample at 6.5 Hz)

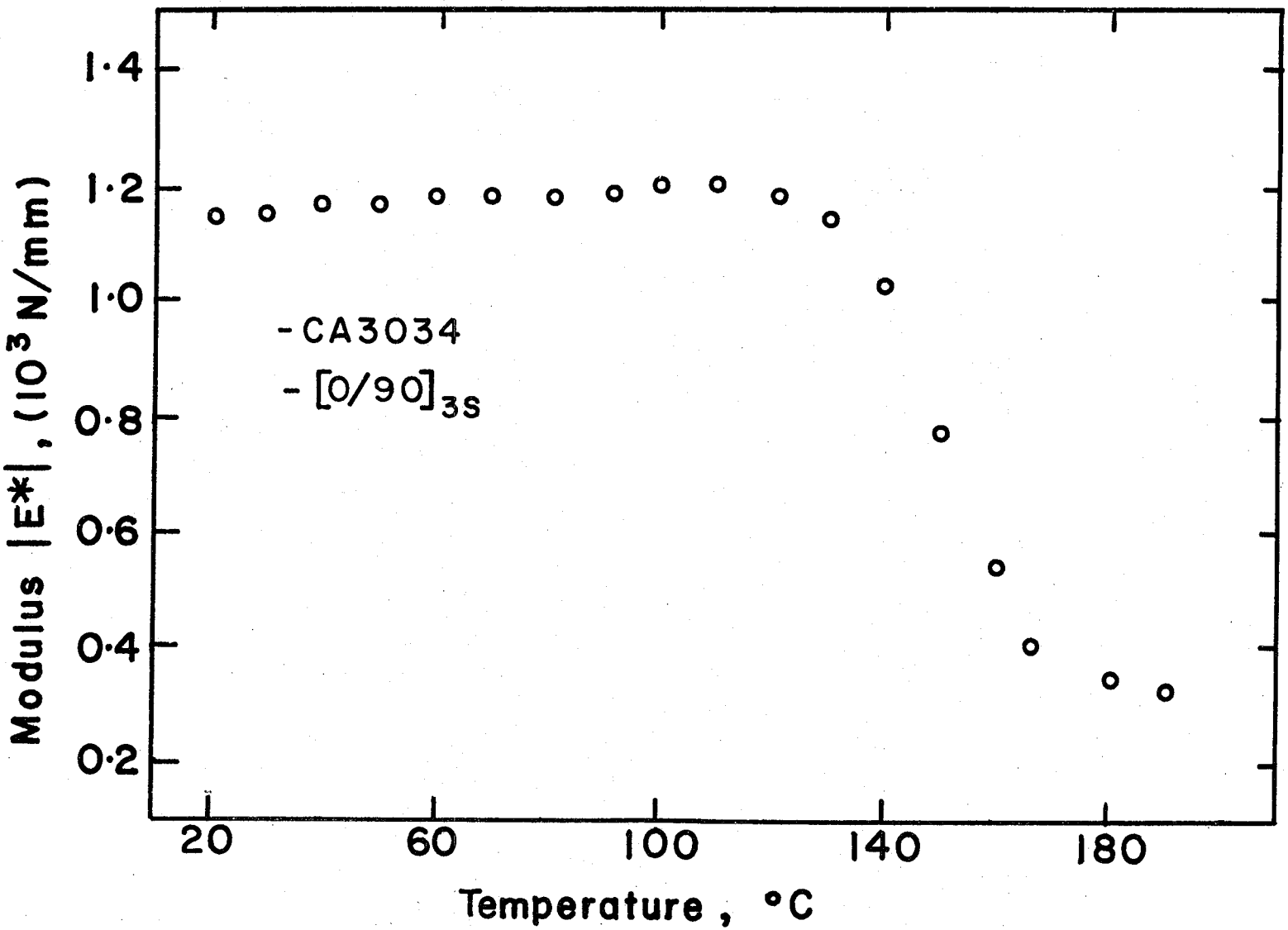

Figure IV-F-13
Dynamic Modulus |E*| vs. Temperature (°C)
(90° sample at 6.5 Hz)

attempt will be made to extend this testing technique to the evaluation of neat resins. The dynamic mechanical spectroscopy results are being obtained at frequencies from 0.1 Hz to 40 Hz and master curves will be constructed to ascertain the applicability of time-temperature superposition to the *in situ* glass transition behavior of the epoxy and also the relaxation time spectrum of *in situ* epoxy relative to neat resin.

PART V

PERSONNEL

AUTHOR INDEX

PERSONNEL

Senior Investigators

Brunelle, E. J., Jr. Sc.D. (Aeroelastic and structures design and analysis)*	Associate Professor of Aeronautical Engineering
Das, P. K., Ph.D. (Non-destructive evaluation, research)*	Professor of Electrical and Systems Engineering
Diefendorf, R. J., Ph.D. (Fabrication, CAPGLIDE, fiber behavior, research)*	Professor of Materials Engineering
Feeser, L. J., Ph.D. (Computer applications and graphics, computer aided design, optimization)*	Professor of Civil Engineering
Hagerup, H. J., Ph.D. (Aerodynamics, configuration, pilot accommodation, CAPGLIDE)*	Associate Professor of Aeronautical Engineering
Helwig, G., Dr.Ing. (Finite element methods, computer aided design, composite structure optimization, CAPGLIDE)*	Research Assistant Professor of Aeronautical Engineering
Hoff, N. J. Ph.D. (Structural design and analysis, CAPGLIDE)*	John A. Clark and Edward T. Crossan Professor of Engineering
Krempl, E., Dr.Ing. (Fatigue studies, research)*	Professor of Mechanics and Director of Cyclic Strain Laboratory
Scarton, H., Ph.D. (Acoustic emission NDE)*	Associate Professor of Mechanical Engineering and Mechanics
Shephard, M., Ph.D. (Computer graphics, finite element methods)*	Assistant Professor of Civil Engineering
Sternstein, S. S., Ph.D. (Failure analysis, matrix behavior, research)*	William Weightman Walker Professor of Polymer Engineering
Tiersten, H.F., Ph.D. (Non-destructive evaluation theory, research)*	Professor of Mechanics

---

* Fields of Speciality

Research Staff

Manager & Master Technician, Composites Laboratory

Paedelt, Volker

Research Associates

Otsuka, Hiromitsu, M.S.
Webster, R. T., M.S.

Graduate Assistants

Altman, Carl, B.A.
Bobal, Gail, M.E.
Helmer, James, B.S.
Kim, Wonsub, B.S.
Lumban Tobing, Frida, M.S.
Muser, Cristoph, Dipl.Mech.Ing.
Niu, Tyan-Min, M.S.
Oyibo, Gabriel, M.S.
Taggart, David, B.S.
Uzoh, Cyprian, B.S.
Yang, Phillip, B.S.

Undergraduate Assistants - Seniors

Biddlecorn, Charles
Borfitz, Michael H.
DeFazio, Richard
DeTaranto, Francis
Emmel, John E.
Fortune, James
Luth, James
Mirales, Nicholas
Reilly, Dominic R.
Riker, Steven
Thomas, Scott
Van Etten, Charles
Venner, Joseph D.
Werner, Ross
Wetzel, Eric
Winckler, Steven
Zahorsky, John

Undergraduate Assistants - Juniors

Cawthorne, Matthew
Coffed, Steven
Cronin, Catherine
Crowell, John
Dalzell, Scott
Dormady, Daniel
Dunlap, Daniel
Ellis, Craig
Fox, Peter
Grant, Peter
Kappeyne Van DeCoppello, Michael
Leonard, Peter
Merritt, Mark
Murawski, Michael
Paige, Ron
Paige, Russel
Pretak, David
Ryan, Jody
Ryan, Kenneth
Walker, Eric

AUTHOR INDEX

End of Document